EBM Experimental Biology and Medicine

Volume 250 | Issue 7

Experimental Biology and Medicine

Editor-in-Chief

Nicola Conran
University of Campinas, Brazil

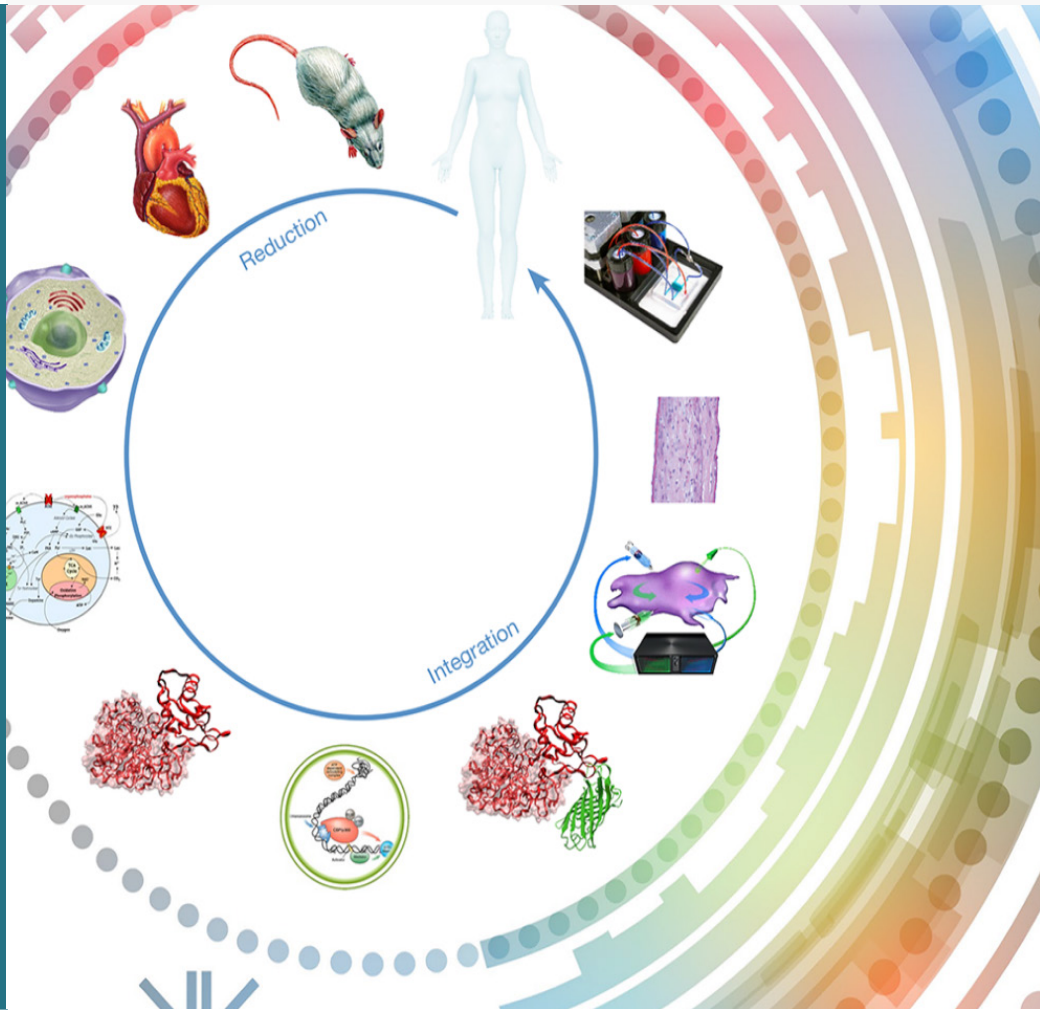

ISBN 978-2-8325-6868-2
DOI 10.3389/978-2-8325-6868-2

frontiers | Publishing Partnerships

EBM Experimental Biology and Medicine

SEBM Executive Council

Publication Committee

Society for Experimental Biology and Medicine
3220 N Street NW, #179
Washington DC 20007, USA
Executive Director – ed@sebm.org

www.sebm.org

EBM Experimental Biology and Medicine

Editorial Board

ISSN 1535-3699
ISBN 978-2-8325-6868-2
DOI 10.3389/978-2-8325-6868-2

Generative AI statement
Any alternative text (Alt text) provided alongside figures in the articles in this ebook has been generated by Frontiers with the support of artificial intelligence and reasonable efforts have been made to ensure accuracy, including review by the authors wherever possible. If you identify any issues, please contact us.

EBM Experimental Biology and Medicine

2025 | Volume 250 | Issue 7 | ISSN 1535-3699

Table of contents

Biochemistry and Molecular Biology
Highlight

Original Research

07 Mechanisms of AGE-induced VSMC phenotypic switching and macrophage modulation in human abdominal aortic aneurysms

Xiaoying Ma, Jinfang Xu, Huiying Sun, Jiajun Liu, Shibo Xia, Hao Zhang, Chaoyi Cui and Chao Song

Biochemistry and Molecular Biology
Highlight

Original Research

26 Vitamin D_3 affects liver expression of pro-/anti-inflammatory cytokines and nitric oxide synthases in type 2 diabetes

Ihor Shymanskyi, Olha Lisakovska, Mykola Veliky, Olha Mezhenska, Vasyl Bilous, Andrii Siromolot, Anna Khomenko, Dmytro Labudzynskyi, Tetyana Horid'ko and Elvira Pasichna

Genomics, Proteomics, and Bioinformatics

Original Research

42 Dietary-related characteristics and cataract risk: evidence from a mendelian randomization study

Chen Li, Yicheng Lu, Mingxuan Chen, Qing Zhang, Zhe Zhang, Wenqun Xi and Weihua Yang

Immunology/Microbiology/Virology

Original Research

52 Gestational exposure to HIV drugs alters intestinal mucosa-associated microbial diversity in adult rat offspring

Yaswanthi Yanamadala, Chandra Mohan Reddy Muthumula, Kuppan Gokulan, Kumari Karn, Vicki Sutherland, Helen Cunny, Janine H. Santos and Sangeeta Khare

Physiology and Pathophysiology

Brief Communication

64 Natural killer cell subpopulations in the peripheral blood of single ventricle/hypoplastic left heart syndrome patients via single-cell RNA sequencing

Hui-Qi Qu, Kushagra Goel, Kayleigh Ostberg, Diana J. Slater, Fengxiang Wang, James Snyder, Cuiping Hou, Garnet Eister, John J. Connolly, Michael March, Joseph T. Glessner, Charlly Kao and Hakon Hakonarson

Population Health

Original Research

73 Proximity to a hazardous waste thermal treatment facility alters human physiology: a community-driven pilot study

Avinash Kumar, Chuqi Guo, Qudus Sarumi, Christopher Courtney, Shawn Campagna, Jennifer Richmond-Bryant and Stephania A. Cormier

Stem Cell Biology

Original Research

94 Csf1^{+} AD-MSCs promote stroke repair by activating the resident microglia

Jiguang Hou, Sunfu Zhang, Shuang Luo, Xiao Zuo, Fei Ma, Huizhen Wang, Pengfei Han, Ping Zhu, Ning Wang, Xiaoming Hou and Jin Li

Translational Research

Correction

107 Corrigendum: A double-edged effect of hypoxia on astrocyte-derived exosome releases

Yang Jie Tseng, Hui-Ju Huang, Chien-Hui Lin and Anya Maan-Yuh Lin

EBM Experimental Biology and Medicine

TYPE Original Research
PUBLISHED 07 August 2025
DOI 10.3389/ebm.2025.10527

OPEN ACCESS

*CORRESPONDENCE
Chao Song,
chao.song@vip.163.com
Chaoyi Cui,
cuichoi8432@163.com

†These authors have contributed equally to this work

RECEIVED 13 February 2025
ACCEPTED 07 July 2025
PUBLISHED 07 August 2025

CITATION
Ma X, Xu J, Sun H, Liu J, Xia S, Zhang H, Cui C and Song C (2025) Mechanisms of AGE-induced VSMC phenotypic switching and macrophage modulation in human abdominal aortic aneurysms. *Exp. Biol. Med.* 250:10527. doi: 10.3389/ebm.2025.10527

Mechanisms of AGE-induced VSMC phenotypic switching and macrophage modulation in human abdominal aortic aneurysms

Xiaoying Ma[1,2†], Jinfang Xu[3†], Huiying Sun[1†], Jiajun Liu[4], Shibo Xia[1], Hao Zhang[1], Chaoyi Cui[5*] and Chao Song[1*]

[1]Department of Vascular Surgery, Changhai Hospital, Shanghai, China, [2]Hepatobiliary Surgery Center, Tongji Hospital, School of Medicine, Tongji University, Shanghai, China, [3]Department of Health Statistics, Naval Medical University, Shanghai, China, [4]School of Pharmacy, East China University of Science and Technology, Shanghai, China, [5]Department of Vascular Surgery, Shanghai Ninth People's Hospital, School of Medicine, Shanghai Jiao Tong University, Shanghai, China

Abstract

Advanced glycation end products (AGEs) have been associated with vascular pathologies including abdominal aortic aneurysms (AAAs), although their causal role remains unclear. In this study, we observed significant accumulation of AGEs in human AAAs, particularly in cases associated with intraluminal thrombus (ILT). *In vitro*, AGE exposure induced vascular smooth muscle cell (VSMC) migration and suppressed contractility, accompanied by reduced expression of contractile markers (α-SMA and MYH11) and elevated MMP-2. This phenotypic transformation was linked to the activation of the NLRP3 inflammasome and RAGE/RhoA/ROCK signaling, and was reversible upon inhibition of RAGE, RhoA, or ROCK. In macrophages, AGE pretreatment had minimal effects on basal cytokine secretion but attenuated LPS-induced IL-6 and IL-1β release and NF-κB activation. Co-culture experiments further revealed that AGE-pretreated macrophages reduced LPS-driven pro-migratory effects on VSMCs. Spatial transcriptomics demonstrated enriched AGE-RAGE signaling in αSMA+ VSMCs and CD68+αSMA+ macrophage-like VSMCs in ILT-containing AAAs. Overall, these associative findings implicate AGE-RAGE signaling in AAA pathogenesis and warrant further investigation to establish causality.

KEYWORDS

abdominal aortic aneurysms, AGE-RAGE, VSMC phenotypic switch, NLRP3, macrophages

Impact statement

This study reports on the association between advanced glycation end products (AGEs) and vascular smooth muscle cell (VSMC) dysfunction/macrophage responses in abdominal aortic aneurysms (AAAs), particularly within the intraluminal thrombus. Using spatial transcriptomics (GeoMx® DSP), we detected the co-localization of AGE-RAGE signaling in VSMC niches and demonstrated *in vitro* that AGE exposure correlates with VSMC phenotypic transformation via the RAGE/RhoA/ROCK pathways, along with the modification of macrophage responses. Pharmacological reversal of AGE-induced changes provides mechanistic hypotheses for AAA pathogenesis and merits future causal studies of the AGE-RAGE axis in vascular remodeling.

Introduction

Advanced glycation end products (AGEs) encompass a diverse array of irreversible adducts formed through the nonenzymatic glycosylation of proteins, lipids, and nucleic acids by reducing sugars [1]. Normally, AGE formation occurs at a low rate, but accelerates significantly in both microvascular and macrovascular diseases [2]. Vascular smooth muscle cells (VSMCs) are located in the middle layer of arterial vessels, playing a crucial role in maintaining arterial structure and regulating vascular tone. Under normal physiological conditions, VSMCs exhibit a contractile phenotype. However, in response to harmful stimuli, VSMCs lose their contractile properties and transition to a synthetic phenotype. This transformation is pivotal in the development and progression of abdominal aortic aneurysms (AAAs) [3].

Studies have confirmed that AGEs can stimulate the proliferation of VSMCs [4]. The receptor for AGEs (RAGE) is particularly important as it mediates the proliferation and migration of VSMCs induced by AGEs [5, 6]. In response to stress, AGEs accumulate and bind to RAGE with high affinity, triggering oxidative stress, inflammation, and procoagulant responses. These processes ultimately contribute to vascular wall lesions, including remodeling of the aortic vasculature and dysfunction of the aortic endothelium.

The intraluminal thrombus (ILT) within abdominal aortic aneurysms is a complex fibrin structure comprised mainly of canaliculi, platelets, erythrocytes, and other hematopoietic cells [7]. Clinically, ILT is found in 75% of AAA sacs and is associated with arterial wall hypoxia, cellular inflammation, and apoptosis of the extracellular matrix, and can contribute significantly to aneurysm growth, potentially leading to rupture [8–12]. While the AGE-RAGE axis has been implicated in vascular pathologies, its role in ILT-associated AAA remains underexplored. Characterizing this association could offer insights into the mechanisms of aneurysm progression.

The Rho GTPase protein family, which includes RhoA, Rac1, and Cdc42, plays a critical role in cellular functions such as contraction, migration, and the organization of the actin cytoskeleton. Rho-associated kinase (ROCK), a key downstream effector protein of Rho GTPases, phosphorylates various targets to influence these cellular processes. Studies have demonstrated that the RhoA/ROCK pathway is involved in regulating the phenotype of VSMCs induced by platelet-derived growth factor BB (PDGF-BB) [13]. Activation of the Rho/ROCK pathway can lead to the phosphorylation of threonine 696 on the Myosin Phosphatase Target subunit-1 (MYPT1), resulting in abnormal contraction of vascular smooth muscle [14]. Inhibition of the RAGE/RhoA/ROCK signaling pathway has been shown to protect the integrity of the aortic wall [15]. *However, whether Rho GTPases and their downstream signals are implicated in the regulation of VSMC phenotype mediated by AGEs has not been conclusively established.*

The NOD-like receptor family pyrin domain 3 (NLRP3) inflammasome is a key cytosolic complex involved in initiating inflammatory responses. It consists of NLRP3, apoptosis-associated speck-like protein (ASC), and procaspase-1, which together regulate the maturation and secretion of pro-inflammatory cytokines such as IL-1β and IL-18. An increasing number of studies have provided conclusive evidence that the NLRP3 inflammasome can be activated by AGEs [16]. AGEs upregulate the mRNA or protein expression of inflammasome-related molecules (such as NLRP3, caspase-1, and IL-1β) in non-myeloid cells (such as podocytes, nucleus pulposus cells, and placental cells) [17]. Understanding how AGEs may influence VSMC inflammatory responses could elucidate pathways relevant to vascular complications.

This research suggests a potential role for AGEs in the pathogenesis of abdominal aortic aneurysms, particularly by modulating the interactions between vascular smooth muscle cells and macrophages. By characterizing context-dependent responses to AGEs in VSMCs and macrophages, this study provides mechanistic insights into AAA pathophysiology and identifies signaling pathways that warrant further investigation.

Materials and methods

Cell culture and reagents

THP-1 cells and HA-VSMC were procured from Pricella Life Science & Technology Co., Ltd. HA-VSMC is a cell line exhibiting fibroblast-like morphology that was isolated from the smooth muscle of the aorta of an 11-month-old white female patient. The cell identification results are shown in Supplementary Figure S1. HA-VSMCs were cultured in F-12K medium (Cat. No. 30-2004, ATCC, Manassas, United states)

TABLE 1 Primer sequences in qRT-PCR.

Primers	Sequences
ACTA2	F: AGTTCCGCTCCTCTCTCCAA R: AACGCTGGAGGACTTGCTTT
MMP-2	F: GAGTGCATGAACCAACCAGC R: GTCTGGGGCAGTCCAAAGAA
NLRP3	F: CTTGGAGACATCCTGTCAGGG R: AGTCACAAGACCAGGCATATTCT
TNF	F: GACAAGCCTGTAGCCCATGT R: GGAGGTTGACCTTGGTCTGG
IL-6	F: TTCGGTCCAGTTGCCTTCTC R: TGTTTTCTGCCAGTGCCTCT
IL1B	F: AACCTCTTCGAGGCACAAGG R: AGATTCGTAGCTGGATGCCG
NOS2	F: GCCATAGAGATGGCCTGTCC R: GGGGACTCATTCTGCTGCTT
GAPDH	F: AATGGGCAGCCGTTAGGAAA R: GCGCCCAATACGACCAAATC

Abbreviations: F, forward; R, reverse.

supplemented with 0.05 mg/ml L-ascorbic acid, 0.01 mg/mL insulin, 0.01 mg/mL transferrin, 10 ng/mL sodium selenite, 0.03 mg/mL endothelial cell growth supplement, 10% FBS, 10 mM HEPES, 10 mM TES, and 1% penicillin/streptomycin. Third- to fourth-generation HA-VSMCs were used in the cell-based experiments of this study. THP-1 cells were maintained in RPMI 1640 medium (Cat. No. SH30809.01, HyClone, MA, United states) supplemented with 10% fetal bovine serum (FBS) (Cat. No. FBSSR-01021-50, Cyagen, CA, United states). Prior to experimentation, THP-1 cells were differentiated using 100 ng/mL phorbol 12-myristate 13-acetate (PMA) Cat. No. P1585, Sigma, MA, United states). Z-VAD-FMK (pyroptosis inhibitor, Cat. No. HY-16658B), CY-09 (NLRP3 inhibitor, Cat. No. HY-103666), FPS-ZM1 (RAGE inhibitor, Cat. No. HY-19370), CCG-1423 (RhoA inhibitor, Cat. No. HY-13991), Y-27632 (ROCK inhibitor, Cat. No. HY-10071) and Lipopolysaccharides (Cat. No. HY-D1056) were all purchased from MedChemExpress LLCNJ, United states. Advanced glycation end product-BSA (AGE-BSA) was purchased from Abcam (Cat. No. ab51995, Abcam, Cambridge, United kingdom).

Real-time quantitative reverse transcription-polymerase chain reaction (qRT-PCR)

As previously reported [18], total RNA was extracted using the FastPure Cell/Tissue Total RNA Isolation Kit (Cat. No. RC112-01, Vazyme, Nanjing, China). Subsequently, cDNA synthesis was performed using AceQ qPCR SYBR Green Master Mix (Vazyme, Cat. No. Q121-02). For quantitative real-time PCR (qPCR), the HiScript III SuperMix for qPCR (Vazyme, Cat. No. R323-01) was employed, and the reactions were analyzed using a CFX96 Fluorescence quantitative PCR instrument (Bio-Rad, CA, United states). The primer sequences utilized are detailed in Table 1. Gene expression data were normalized to GAPDH as an internal reference and quantified using the $2^{-\Delta\Delta CT}$ method.

Digital space profiling (DSP)

Six biopsies were obtained from AAA patients (3 with ILT and 3 without ILT) from Shanghai Changhai Hospital following approval by the Ethics Committee (approval number: CHEC2022-052). Detailed clinicopathological characteristics can be found in Table 2. Whole-exome sequencing was conducted on specific regions of interest (ROIs) using the GeoMX Digital Spatial Profiling platform, with subsequent data analysis and processing performed using the R language. Differentially expressed mRNA was identified using criteria of adjusted p-value <0.05 and |Log2Fold Change| > 1.

ELISA assay of AGE/CCL2/IL-6/MMP-2

A total of 16 specimens from AAA patients were collected and stored in liquid nitrogen for future experiments. Non-AAA samples (N = 5) were obtained during aorta-bifemoral bypass surgery for aorta-iliac occlusive disease. The clinicopathological characteristics of the AAA patients are detailed in Table 3. Ethical approval for this study was obtained from the Ethics Committee of the Shanghai Changhai Hospital. Aortic tissue lysates were prepared using cell lysis buffer to determine protein concentrations. The competitive AGE-ELISA procedure was conducted using an AGE Assay kit (Abcam, Cat. No. ab238539) to assess advanced glycation end-products. Inflammatory factors, including MMP2, IL-6, and MCP-1, were quantified using specific ELISA kits: MMP2 Human ELISA Kit (Cat. No. KHC3082, Invitrogen, CA, United states), IL-6 Human ELISA Kit (Invitrogen, Cat. No. EH2IL6), and MCP-1 Human Instant ELISA™ Kit (Invitrogen, Cat. No. BMS281INST), respectively. All of these assays were performed according to the manufacturers' instructions.

Western blot

As previously reported [19], the total proteins were separated on a 10% SDS-PAGE gel (Cat. No. PG212, Epizyme, MA, United states) and subsequently transferred onto PVDF membranes (Bio-Rad Laboratories Inc., CA, United States). After blocking with 1x protein-free fast blocking buffer (Epizyme, Cat. No. PS108P) for 1 h, the membranes were incubated overnight at 4°C with various primary antibodies, including a smooth muscle actin Polyclonal antibody (Cat. No. 14395-1-AP, Proteintech,

TABLE 2 Demographic data of AAA patients with and without intraluminal thrombus.

Patient ID	G1-1	G2-1	G1-2	G2-2	G1-3	G2-3
ILT	Y	N	Y	N	Y	N
Age, years	66	68	73	66	65	71
Sex	Female	Male	Male	Female	Male	Male
AAA diameter, mm	52	54	68	48	65	58
Hypertension	Y	Y	Y	N	Y	N
Diabetes mellitus	N	N	N	N	N	N
Smoking history	N	N	Y	N	Y	Y
CAD	Y	N	N	N	N	N
COPD	N	Y	N	N	N	N
PAD	N	N	N	N	N	N

Abbreviations: AAA, abdominal aortic aneurysm; CAD, coronary artery disease; COPD, chronic obstructive pulmonary disease; PAD, peripheral arterial disease.

TABLE 3 Demographic data of AAA patients with and without intraluminal thrombus.

Variables	AAA with ILT	AAA without ILT
No.	8	8
Age, years	68.9 ± 5.6	70.6 ± 4.4
Male patients	8/8	7/8
AAA diameter, mm	66.4 ± 1.0	63.2 ± 0.4
Hypertension	5/8	3/8
Diabetes mellitus	1/8	0/8
Smoking history	5/8	3/8
CAD	1/8	2/8
COPD	0/8	0/8
PAD	0/8	0/8
Antiplatelet therapy	1/8	4/8
Statins	0/8	1/8

Continuous variables are reported as mean ± standard deviation.
Abbreviations: AAA, abdominal aortic aneurysm; CAD, coronary artery disease; COPD, chronic obstructive pulmonary disease; PAD, peripheral arterial disease.

Wuhan, China), NLRP3 Polyclonal antibody (Proteintech, Cat. No. 27458-1-AP), MMP-2 Antibody (Cat. No. 4022S, CST, MA, United states), Phospho-IκBα (Ser32) (14D4) Rabbit mAb (CST, Cat. No. 2859T), and GAPDH (14C10) Rabbit mAb (CST, Cat. No. 2118T). Subsequently, the membranes were incubated with Peroxidase AffiniPure Goat Anti-Rabbit IgG (H + L) (1:10000, Cat. No. FZ111-035-003, Jackson ImmunoResearch Inc., PA, United states) for 1.5 h. Detection of protein bands was performed using the Omni-ECL™ basic chemiluminescence detection kit (Epizyme, Cat. No. SQ202), and imaging was conducted with the ChemiDocTM MP chemiluminescence image analysis system (BIO-RAD).

Transwell migration assay

VSMCs were treated with AGE-BSA and/or inhibitors. Then 2×10^5 cells in serum-free medium were seeded onto 6.5-mm Transwell® inserts with an 8.0-μm Pore Polycarbonate Membrane (Cat. No. 3422, Corning, NY, United states). The lower chamber contained a culture medium supplemented with 10% FBS to serve as a chemoattractant. After incubation for 24 or 72 h, the cells that had migrated to the underside of the membrane were fixed using 4% paraformaldehyde, stained with 0.1% crystal violet (Cat. No. MS4006-100ML, Maokangbio, Shanghai, China), and subsequently

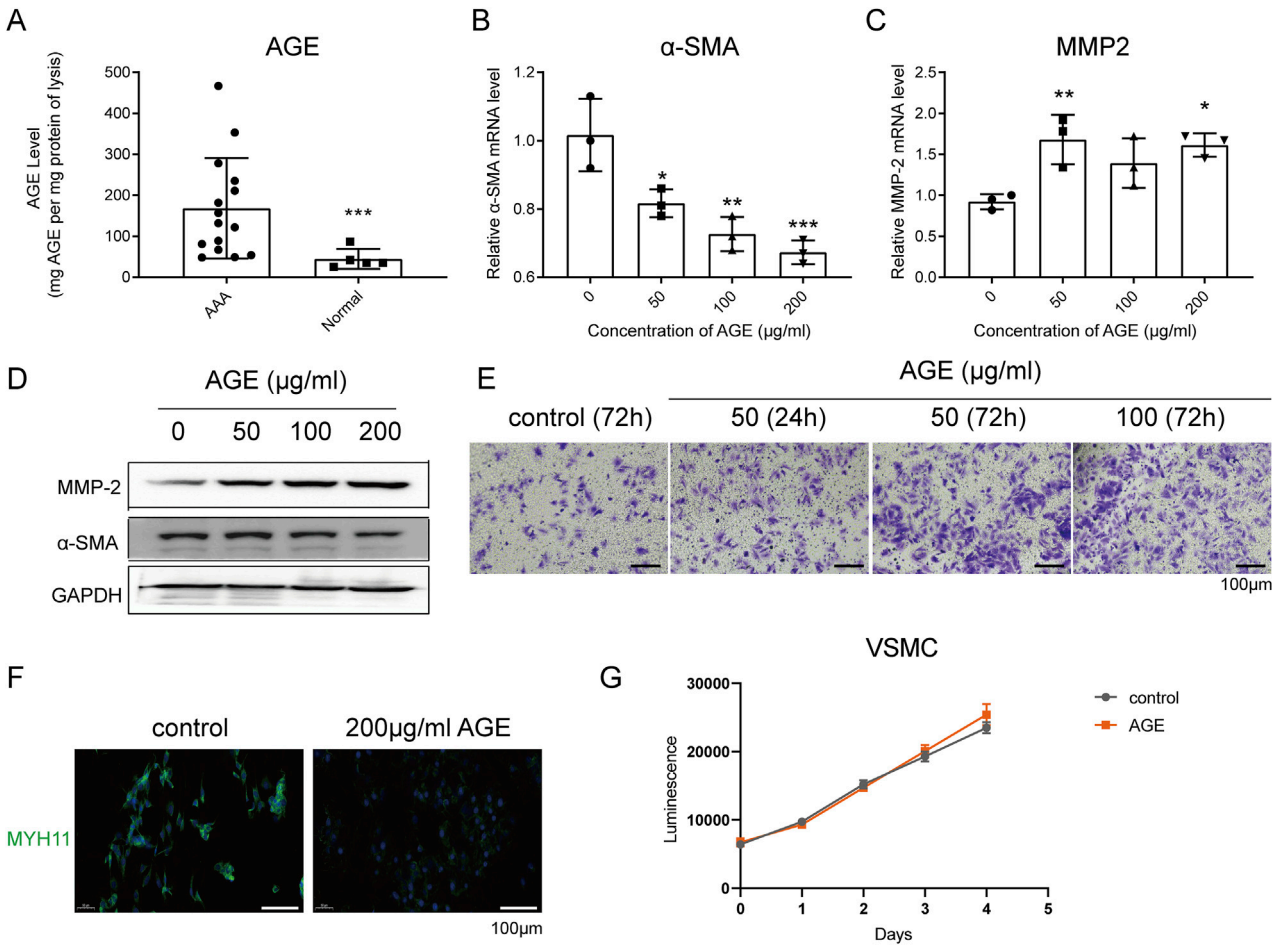

FIGURE 1
AGE Effects on Human VSMCs: Promotion of Migration and Inhibition of Contraction. **(A)** ELISA analysis detected the accumulation of AGEs in lysates of human aortic tissues. **(B–D)** RT-qPCR **(B,C)** and Western blot **(D)** detected the expression of the contraction marker α-SMA and the migration marker MMP-2 in human VSMCs after AGE treatment for 24 h; **(E)** Transwell migration experiment detected the migration of human VSMCs after AGE treatment for 24 h or 72 h; **(F)** Immunofluorescence detected the expression of the contraction marker MYH11 in human VSMCs after AGE treatment for 24 h. Blue fluorescence indicates DAPI staining, and green indicates MYH11 staining. **(G)** The CTG assay detected the growth curve of human VSMCs under the treatment with 200 μg/mL AGE. Data are presented as the mean ± SD from three independent experiments and were analyzed with a one-way ANOVA followed by a Dunnett's multiple comparisons test. Asterisks indicate significant differences (*P < 0.05, **P < 0.01, ***P < 0.001) between the treatment group and the control group.

photographed under a microscope. This Transwell® migration assay allows for the assessment of cell migration in response to different treatments, providing insights into the migratory behavior of VSMCs under experimental conditions.

Immunofluorescence

VSMCs were fixed with 4% paraformaldehyde at room temperature for 15 min, followed by three washes with PBS. Subsequently, they were incubated with 0.3% Triton X-100 at room temperature for 30 min and washed again three times with PBS. The cells were then treated with a 3% hydrogen peroxide solution at room temperature for 25 min in the dark, followed by another three washes with PBS. After blocking with 3% BSA at room temperature for 30 min, the cells were incubated overnight at 4°C with MYH11 Antibody (1:100, Proteintech, Cat. No. 21404-1-AP). Following three washes with PBS, the cells were incubated with an anti-rabbit HRP-labeled secondary antibody at room temperature for 1 h in the dark, again followed by three washes with PBS. A freshly prepared fluorescent chromogenic solution (Cat. No. SD0155, Simuwubio, Shanghai, China) was applied and allowed to develop color for several minutes, with the reaction being stopped with PBS. The cells were then incubated with a DAPI dye solution at room temperature for 10 min in the dark,

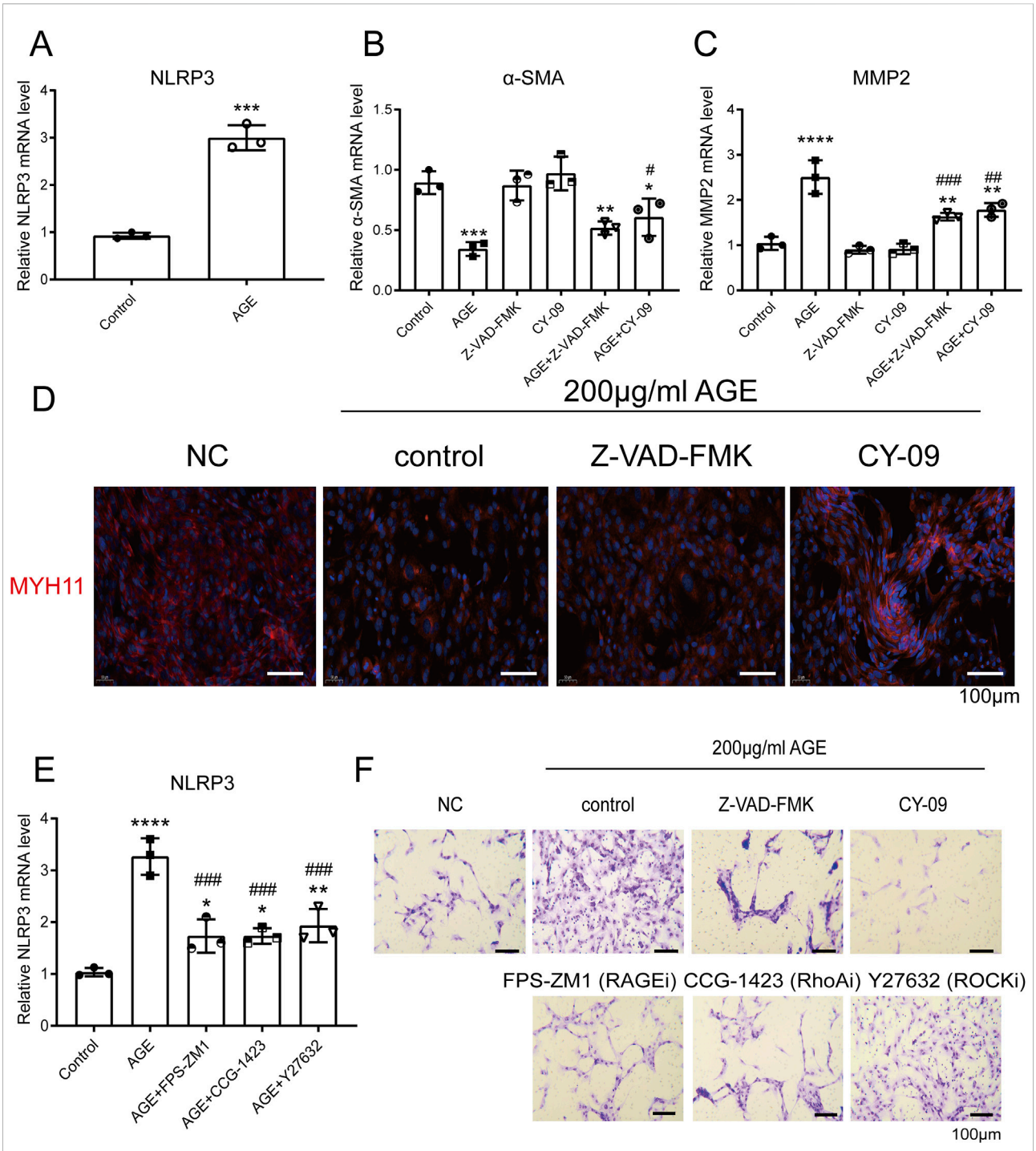

FIGURE 2
AGE-Mediated Transformation of VSMCs from Contractile to Migratory Phenotype via NLRP3 Activation. **(A)** RT-qPCR detected the expression of NLRP3 in human VSMCs after AGE treatment for 48 h; **(B,C)** RT-qPCR detected the expression of α-SMA **(B)** and MMP-2 **(C)** in human VSMCs. The cells were pretreated with 10 μM CY-09 (an NLRP3 inhibitor) or Z-VAD-FMK (a pyroptosis inhibitor) for 2 h, then incubated with 200 μg/mL AGE for 48 h; **(D)** Immunofluorescence demonstrated that the pyroptosis inhibitor Z-VAD-FMK and the NLRP3 inhibitor CY-09 could reverse the effect of AGE on the phenotypic transformation of VSMCs. The cells were pretreated with 10 μM CY-09 (NLRP3 inhibitor) or Z-VAD-FMK (pyroptosis inhibitor) for 2 h, then incubated with 200 μg/mL AGE for 48 h; **(E)** RT-qPCR detected the expression of NLRP3 in human VSMCs. The cells were pretreated with 10 μM FPS-ZM1 (a RAGE inhibitor) or CCG-1423 (a RhoA inhibitor) or Y-27632 (a ROCK inhibitor) for 2 h, then incubated with 200 μg/mL AGE for 48 h. **(F)** A Transwell migration experiment demonstrated that pretreatment with the pyroptosis inhibitor Z-VAD-FMK, the NLRP3 inhibitor CY-09, the RAGE inhibitor FPS-ZM1, the RhoA inhibitor CCG-1423, and the ROCK inhibitor Y27632 could reverse the pro-migration effect of 200 μg/mL AGE on VSMCs. The cells were pretreated with 10 μM CY-09 (NLRP3 inhibitor), Z-VAD-FMK (pyroptosis inhibitor), FPS-ZM1
(*Continued*)

FIGURE 2 (Continued)
(RAGE inhibitor), CCG-1423 (RhoA inhibitor), or Y-27632 (ROCK inhibitor) for 2 h, then incubated with 200 μg/mL AGE for 48 h. Data are presented as the mean ± SD from three independent experiments and were analyzed with a one-way ANOVA followed by a Dunnett's multiple comparisons test. Asterisks indicate significant differences (*P < 0.05, **P < 0.01, ***P < 0.001, ****P < 0.0001) between the treatment group and the control group. Pound signs indicate a significant difference (#P < 0.05, ##P < 0.01, ###P < 0.001) between the treatment group and the AGE group.

washed three times with PBS, and finally mounted with an anti-fluorescence quenching mounting medium for observation under a microscope.

Lactate dehydrogenase (LDH) release assay

LDH release was quantified using a lactate dehydrogenase cytotoxicity assay kit (Cat. No. C0016, Beyotime Biotech, Shanghai, China) following the manufacturer's instructions. VSMCs were cultured in a 96-well plate until they reached 80–90% confluence. The LDH detection working solution was then added to each well, and the plate was incubated at room temperature in the dark for 30 min. Absorbance was measured at a wavelength of 490 nm using a BioTek microplate reader (H1MFD). This assay provides a quantitative assessment of LDH release, indicating cellular cytotoxicity or membrane damage.

NF-κB transcription factor assay

Nuclear proteins were extracted using the Nuclear Extract Kit (Cat. No. 40010, Active Motif, Inc., CA, United states). Subsequently, cRel, p52, and p62 levels were assessed using TransAM NF-κB Transcription Factor Assays (Active Motif, Inc., Cat. No. 43296). The experimental protocol proceeded as follows: First, 30 μL of Complete Binding Buffer was added to each well of the TransAM plate, followed by the addition of 10 μg of nuclear protein (diluted to 20 μL). The plate was then incubated at room temperature for 1 h with gentle shaking at 100 rpm. After incubation, each well was washed three times with 200 μL of 1X Wash Buffer. Subsequently, 100 μL of the primary antibody solution (diluted 1:1000) was added to each well and the mixtures were incubated at room temperature for 1 h. Following another set of three washes with 1X Wash Buffer, 100 μL of HRP-conjugated secondary antibody solution (diluted 1:1000) was added to each well and the mixtures were incubated at room temperature for an additional hour. After a final round of washing, 100 μL of Developing Solution was added to each well, which was incubated at room temperature in the dark for 5 min. The reaction was terminated by adding 100 μL of Stop Solution to each well, and the absorbance was measured at a wavelength of 450 nm using a BioTek microplate reader (H1MFD). This procedure enabled the quantification of NF-κB transcription factors (cRel, p52, and p62) bound to DNA in the nuclear extracts, providing insight into NF-κB activity in the samples.

ELISA detection of cytokines

After incubating the cells with different concentrations of advanced glycation end products (AGEs) for 24 h, 1 μg/mL of lipopolysaccharide (LPS) was added for an additional 4 h. The cell culture supernatant was then collected and centrifuged at 10,000 rpm for 5 min. Subsequently, the levels of IL-6 and IL-1β were quantified using the QuantiCyto® Human IL-6 ELISA kit, (Cat. No. EHC007.96, NeoBioscience, Shenzhen, China) and the human IL-1β ELISA kit (Abcam, Cat. No. ab214025), following the respective kit instructions. These assays were employed to assess the secretion of IL-6 and IL-1β cytokines under these experimental conditions.

Cell viability assay

VSMCs were seeded in 96-well plates at a density of 5000 cells per well. After 4 h of incubation, 200 μg/mL of advanced glycation end products (AGEs) was added to each well. Cell viability was assessed using the Cell Titer-Glo 2.0 Cell Viability Assay (Cat. No. G9242, Promega, WI, United states) from days 1–5 following treatment. This assay measures cellular ATP levels as an indicator of cell viability and metabolic activity over the specified time course.

NFκB dual luciferase reporter assay

The 293FT cells in the logarithmic growth phase were adjusted to a density of 4×10^5 cells/mL and seeded into a 6-well plate. The cells were incubated overnight at 37°C in a 5% CO2 incubator. To transfect the cells, 2 μg of the NFκB Luciferase Reporter Plasmid (Cat. No. 11501ES03, Yeasen, Shanghai, China) was diluted in 125 μL of Opti-MEM medium and mixed gently. Similarly, 10 μL of Lipofectamine 2000 (Invitrogen, Cat. No. 10668018) was diluted in 125 μL of Opti-MEM medium, mixed gently, and incubated at room temperature for 5 min before being combined with the plasmid DNA. The mixture was allowed to stand for an additional 20 min. The resulting complex (250 μL) was added

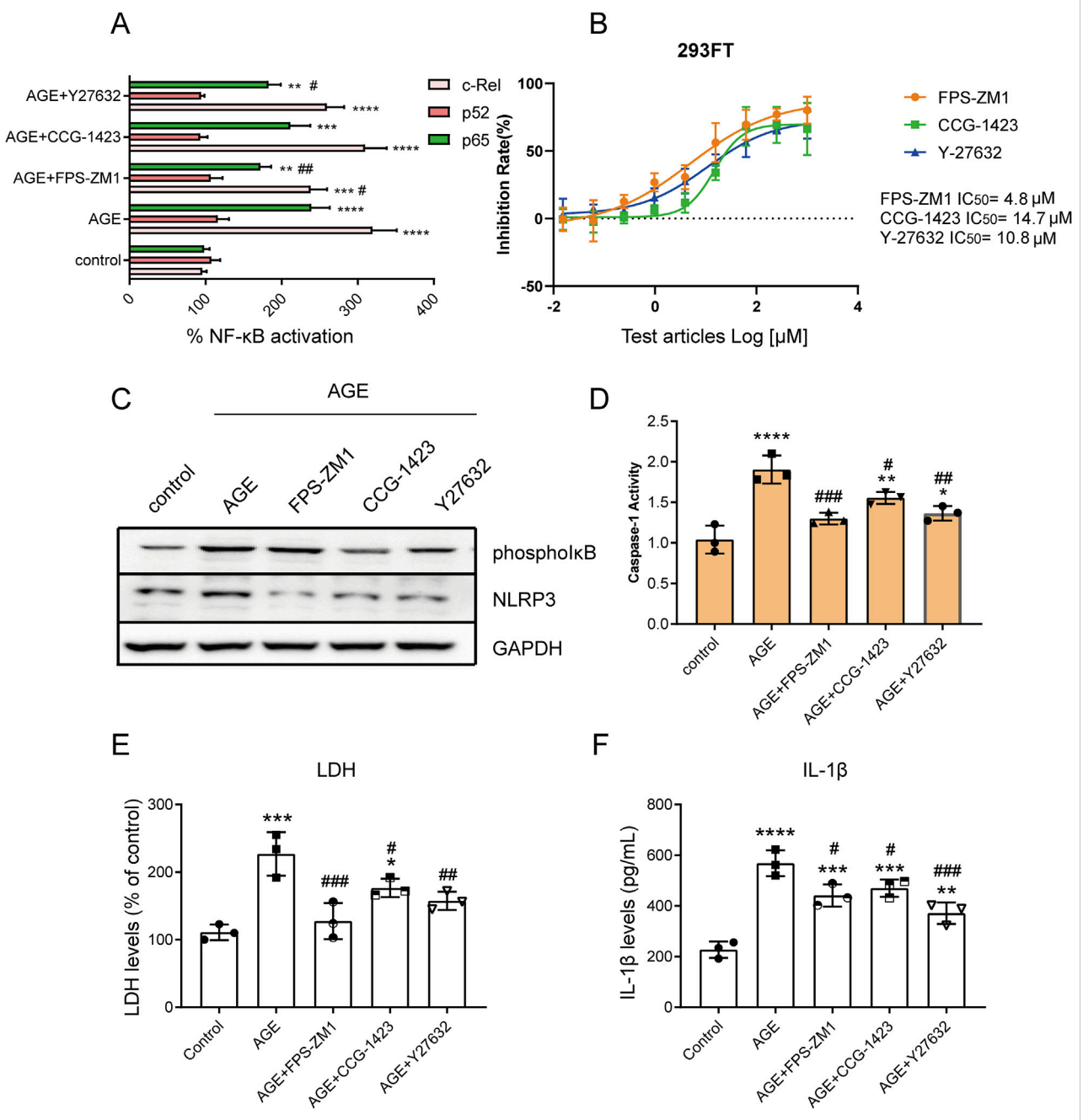

FIGURE 3
AGEs Activate the NF-κB Pathway and NLRP3 Inflammasome via the RAGE/RhoA/ROCK Pathway. **(A)** The TransAM NF-κB Transcription Factor Assay detected the effect of the RAGE/RhoA/ROCK inhibitor on the nuclear translocation of c-Rel, p52, and p65; **(B)** The NF-κB dual luciferase reporter gene system assessed the impact of RAGE/RhoA/ROCK inhibitors on AGE-induced NF-κB signaling; **(C)** Western blot analysis showed that AGEs regulate the expression of NLRP3 via the RAGE/RhoA/ROCK/NF-κB signaling pathway; **(D)** The effects of the inhibitors on caspase-1 activation were assessed using a caspase-1 assay kit; **(E)** An LDH release assay showed that AGE promoted VSMC cell pyroptosis, but it could be reversed by RAGE, RhoA, and ROCK inhibitors; **(F)** An ELISA assay demonstrated that AGE promoted the release of the inflammatory factor IL-1β through RAGE/RhoA/ROCK. Data are presented as the mean ± SD from three independent experiments and were analyzed with a one-way ANOVA followed by a Dunnett's multiple comparisons test. Asterisks indicate significant differences (*P < 0.05, **P < 0.01, ***P < 0.001, ****P < 0.0001) between the treatment group and the control group. Pound signs indicate a significant difference (#P < 0.05, ##P < 0.01, ###P < 0.001) between the treatment group and the AGE group.

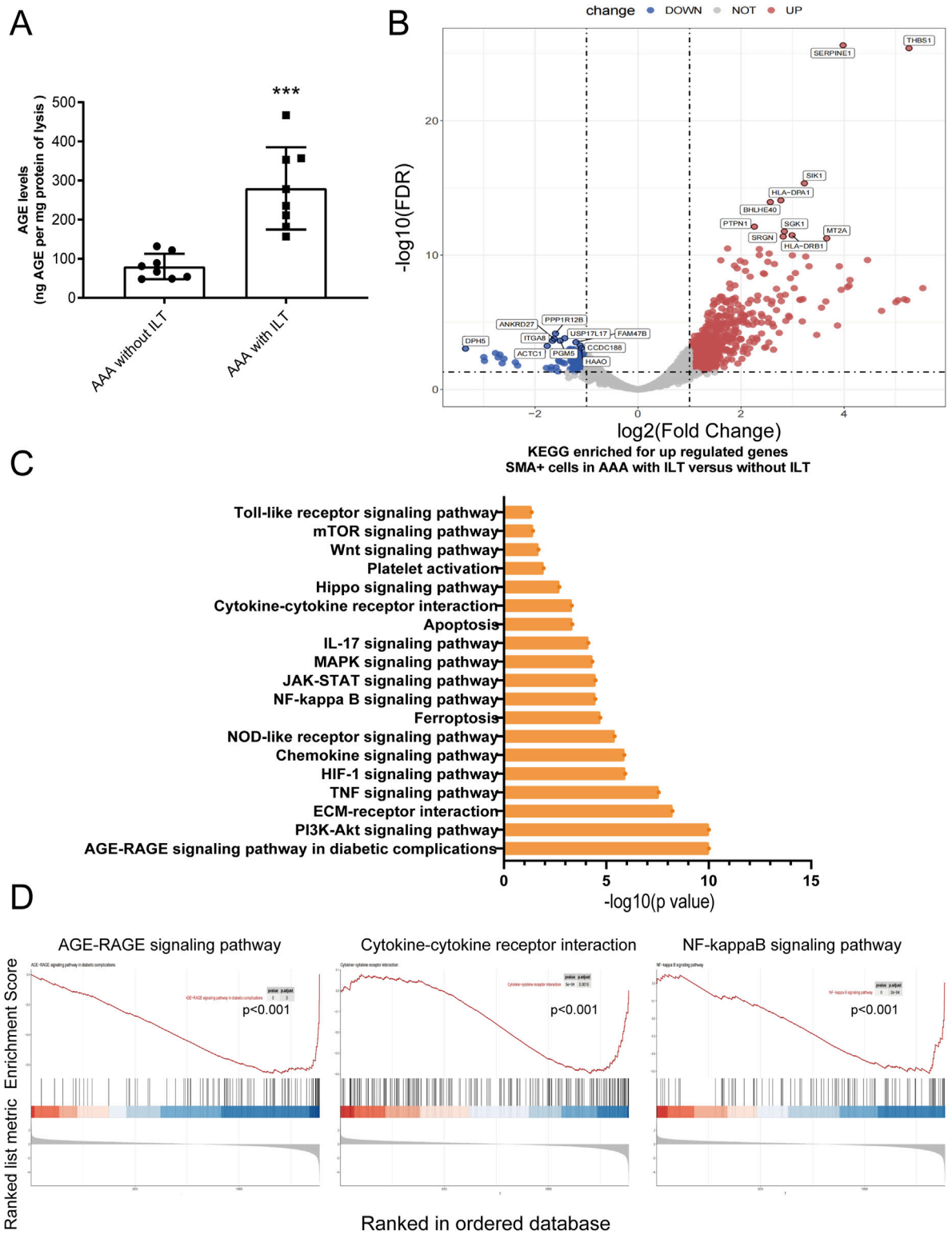

FIGURE 4
AGE-RAGE signaling pathway is highly activated in SMA-positive cells within abdominal aortic aneurysm featuring intraluminal thrombus. **(A)** An ELISA analysis detected an accumulation of AGEs in lysates of human aortic tissues. **(B–D)** Digital Spatial Profiling revealed strong enrichment of the AGE-RAGE signaling pathway in SMA-positive cells from AAAs with ILT compared to those without ILT. **(B)** The Volcano map of the gene expression profile; **(C,D)** the KEGG analysis of DEGs.

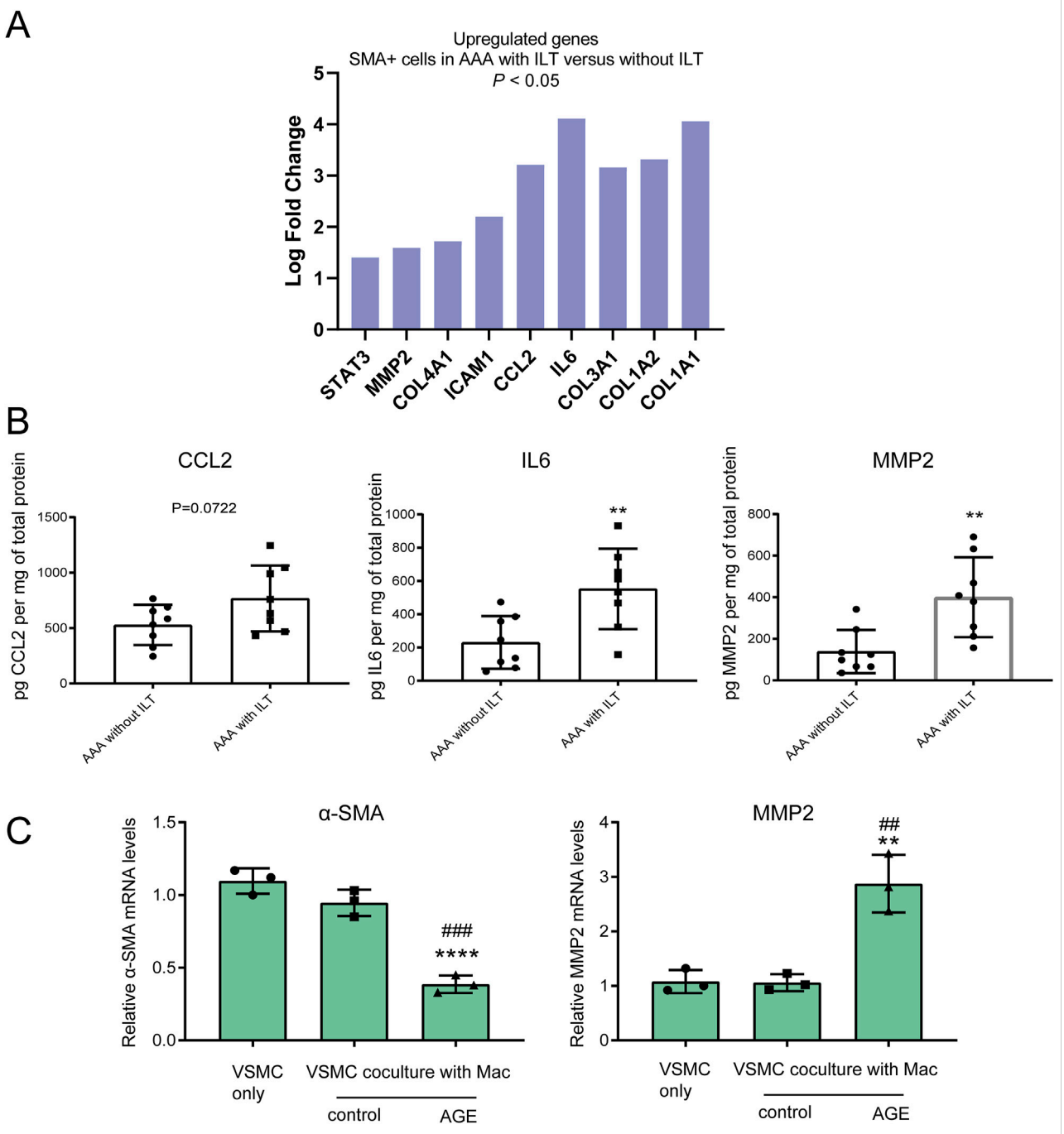

FIGURE 5
Inflammatory and migration phenotypes are featured in an abdominal aortic aneurysm with an intraluminal thrombus. **(A)** Using an adjusted p-value <0.05 and a |Log2Fold Change| > 1 as the criteria, we identified significantly differentially expressed mRNA, including elevated levels of critical genes involved in the AGE-RAGE signaling pathway; **(B)** ELISA assays confirmed increased expression of CCL-2, IL-6, and MMP-2 in aortas covered with ILT; **(C)** RT-qPCR detected the expression of the contraction marker α-SMA and the migration marker MMP-2 in human VSMCs after AGE treatment for 24 h in the co-culture system. Data are presented as the mean ± SD from three independent experiments and were analyzed with a one-way ANOVA followed by a Dunnett's multiple comparisons test. ~ versus VSMC only. Asterisks indicate a significant difference (**P < 0.01, ****P < 0.0001); ~ versus VSMC co-culture with macrophages. Pound signs indicate a significant difference (##P < 0.01, ###P < 0.001).

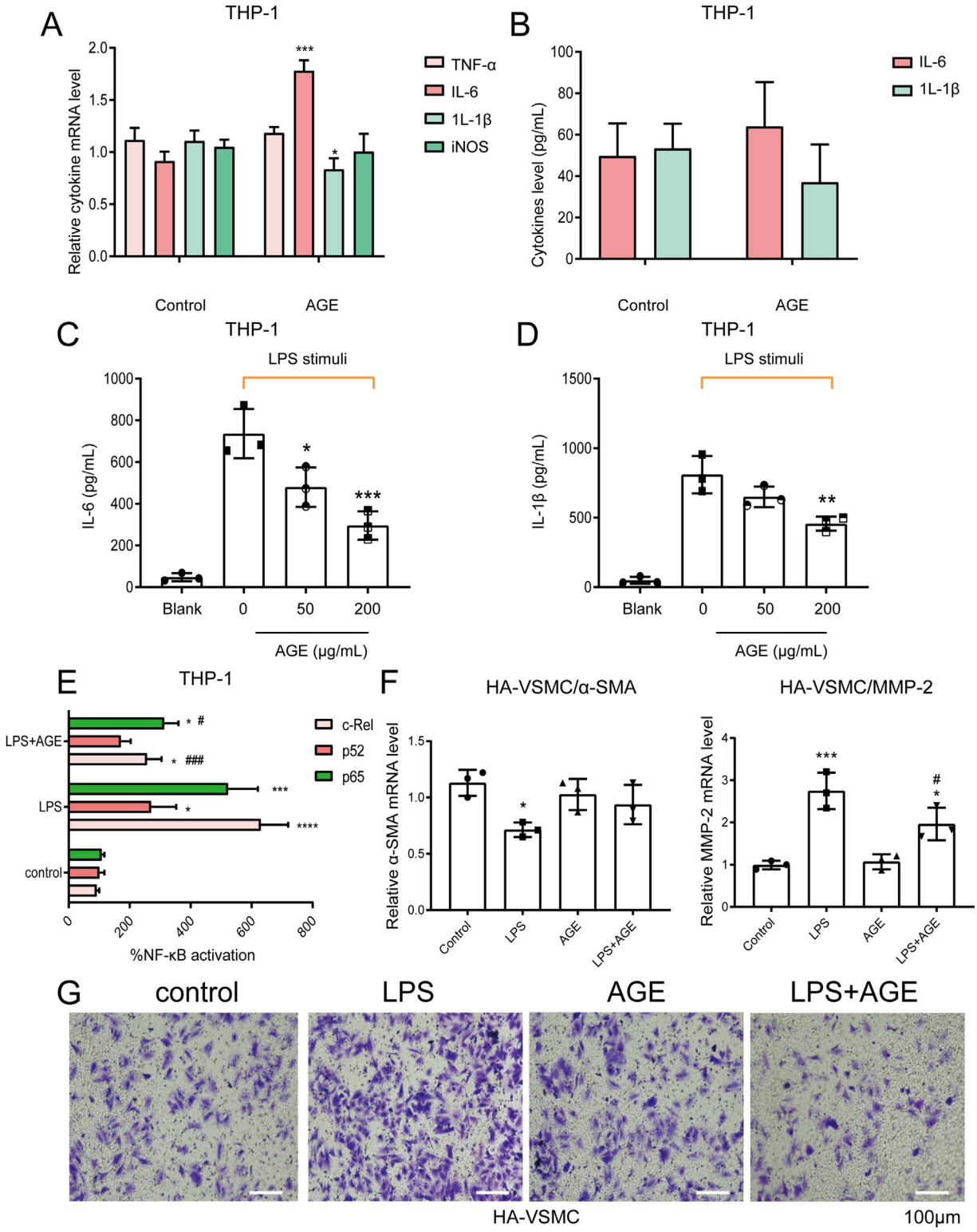

FIGURE 6
AGE Pretreatment Reverses the Effect of LPS-Stimulated Macrophages on VSMC Phenotypic Transformation. **(A,B)** qPCR **(A)** and ELISA **(B)** assays showed that in human macrophages THP-1, 200 μg/mL AGEs had little effect on the expression and secretion of cytokines TNF-α, IL-1β, and iNOS, and had a weak promoting effect on IL-6; **(C,D)** The ELISA assay demonstrated that pretreatment with AGE could inhibit the secretion of IL-6 and IL-1β induced by 1 μg/mL LPS stimulation; **(E)** The TransAM NF-κB Transcription Factor Assay showed that in human macrophage THP-1

(*Continued*)

FIGURE 6 (Continued)
cells, pretreatment with AGE could inhibit the NF-κB signaling pathway activated by LPS stimulation; **(F,G)** Human macrophage THP-1 cells were cultured in the lower layer. The cells were first pretreated with 200 μg/mL AGE for 18 h, and then stimulated with 1 μg/mL LPS for 4 h. After replacing the fresh medium, VSMCs were cultured in the upper layer of macrophages for 24 h before collection. RT-qPCR **(F)** detected the expression of the contraction marker α-SMA and the migration marker MMP-2 in human VSMCs; Transwell migration experiment **(G)** detected the migration of human VSMCs. Data are presented as the mean ± SD from three independent experiments and were analyzed with a one-way ANOVA followed by a Dunnett's multiple comparisons test. Asterisks indicate significant differences (*P < 0.05, **P < 0.01, ***P < 0.001) between the treatment group and the control group. Pound signs indicate a significant difference (#P < 0.05) between the treatment group and the LPS group.

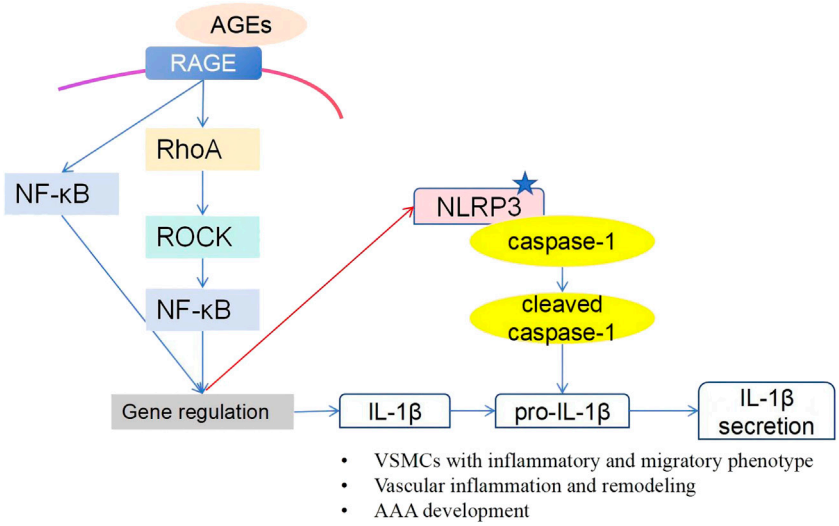

FIGURE 7
Schematic overview of the AGE-induced phenotypic switch in human VSMCs. Our research demonstrated that, in human VSMCs, AGEs activate the NLRP3 inflammasome through the RAGE/RhoA/ROCK/NF-κB signaling pathway, inducing an inflammatory and migratory phenotype.

to each well, and the cells were incubated for 24 h. After transfection, the cells were adjusted to a density of 2 × 10^5 cells/100 μL and seeded into a 96-well plate, and incubated overnight at 37°C in a 5% CO2 incubator. In 293T cells, AGEs were used to activate the NFκB signaling pathway. Through concentration screening, the EC50 was determined to be 52.7 μg/mL (Supplementary Figure S2), and a concentration of 100 μg/mL was selected to activate the NFκB signaling pathway. The test compounds (FPS-ZM1/CCG-1423/Y-27632) were prepared at the following final concentrations: 1, 10, and 10 μM (4-fold serial dilutions, with 9 concentration points in total). After 2 h of treatment, 100 μg/mL of AGEs was added, and the cells were co-incubated for 24 h. Dual luciferase reporter gene assays were performed following the instructions provided in the Dual Luciferase Reporter Gene Assay Kit (Yeasen, Cat. No. 11402ES60) and using an Envision 2105 multimode plate reader (PerkinElmer). The results were calculated using the following formula: 1). Experimental Group Ratio = (Experimental Group Firefly Luminescence (F) - Background Firefly Luminescence (F))/(Experimental Group Renilla Luminescence (R) - Background Renilla Luminescence (R)); 2). Control Group Ratio = (Control Group Firefly Luminescence (F) - Background Firefly Luminescence (F))/(Control Group Renilla Luminescence (R) - Background Renilla Luminescence (R)); 3). Fold Change = Experimental Group Ratio/Control Group Ratio.

Note:

a) Background F: Untransfected cells + Firefly luciferase assay reagent
b) Background R: Transfected cells + Firefly luciferase assay reagent + Renilla luciferase assay reagent
c) Experimental Group: Transfected cells treated with compounds
d) Control Group: Transfected cells without treatment, used for standardization of results

Caspase-1 activity assay

The enzymatic activity of caspase-1 was assayed using a Caspase-1 Colorimetric Assay Kit (MCE, Cat. No. HY-K2610-

100T) according to the manufacturer's protocol. Absorbance was measured at 405 nm by using a plate reader.

Statistical analysis

The data were analyzed using GraphPad Prism 8.0 software (GraphPad Software Inc., USA) and are presented as the mean ± standard deviation (SD). Statistical significance was determined using a One-way ANOVA followed by a Dunnett's multiple comparisons test. A p-value <0.05 was considered statistically significant.

Results

AGE effects on human VSMCs: promotion of migration and inhibition of contraction

We initiated our research by investigating whether AGE expression differs between AAA specimens and normal arteries. ELISA assays revealed a significant increase in AGE accumulation in human AAA specimens (Figure 1A). RT-qPCR and Western blot analyses revealed that AGEs, administered at varying concentrations (50, 100, 200 μg/mL), significantly suppressed the expression of the contraction marker α-SMA, while concurrently enhancing the expression of the migration marker MMP-2 in human VSMCs following a 24-h treatment period, exhibiting a concentration-dependent response (Figures 1B–D). Results from the Transwell migration assay demonstrated that compared to VSMCs treated with AGEs for 24 h, a higher number of cells migrated following a 72-h treatment (Figure 1E). Immunofluorescence analysis further confirmed that AGEs (200 μg/mL) markedly attenuated the expression of the contraction marker MYH11 (Figure 1F). However, CTG results demonstrated that higher concentrations of AGEs did not significantly promote VSMC proliferation, contrary to previous reports [20, 21] (Figure 1G).

AGE-mediated transformation of VSMCs from contractile to migratory phenotype via NLRP3 activation

RT-qPCR and Western blot results demonstrated that AGEs enhance the expression of NLRP3 (Figures 2A, 3C). Furthermore, RT-qPCR, Transwell migration assays, and immunofluorescence analyses indicated that pre-incubation with the pyroptosis inhibitor Z-VAD-FMK and the NLRP3 inhibitor CY-09 could reverse the AGE-induced phenotypic transformation of VSMCs (from contractile to a migratory phenotype). Specifically, this treatment increased the expression of the contraction markers α-SMA and MYH11 while reducing the expression of the migration marker MMP-2 (Figures 2B–D). To exclude the possibility of drug-induced toxicity affecting cell behavior, cell growth was monitored under a microscope 48 h after treatment with AGEs, revealing no inhibition of cell growth or induction of apoptosis due to AGEs or inhibitor treatments (data not shown).

AGE-induced transition of VSMCs to a migratory phenotype via the RAGE/RhoA/ROCK/NLRP3 pathway

RT-qPCR and Western blot analyses revealed that AGEs regulate NLRP3 expression through the RAGE/RhoA/ROCK pathway (Figures 2E, 3C). Additionally, Transwell migration assay results demonstrated that pre-incubation with the RAGE inhibitor FPS-ZM1, the RhoA inhibitor CCG-1423, and the ROCK inhibitor Y27632 could reverse the pro-migration effect induced by 200 μg/mL AGEs on VSMCs (Figure 2F).

AGEs Activate the NF-κB Pathway and NLRP3 Inflammasome via the RAGE/RhoA/ROCK Pathway

TransAM NF-κB Transcription Factor Assay results demonstrated that AGEs activate the NF-κB signaling pathway via the RAGE/RhoA/ROCK pathway. Specifically, inhibition of RAGE/RhoA/ROCK suppressed the nuclear translocation of c-Rel and p65 without affecting p52 (Figure 3A). We then applied the NF-κB dual luciferase reporter gene system to assess the impact of RAGE/RhoA/ROCK inhibitors on AGE-induced NF-κB signaling. After 2 h of inhibitor treatment, 100 μg/mL AGEs were added, and the cells were incubated for an additional 48 h. The RAGE/RhoA/ROCK inhibitors significantly inhibited the NF-κB pathway, with IC_{50} values of 4.8, 14.7, and 10.8 μM, respectively (Figure 3B). A characteristic feature of inflammasome priming signals involves the activation of the NF-κB pathway to upregulate NLRP3. Western blot analysis revealed that AGEs regulate the expression of phospho-IκB and NLRP3 through the RAGE/RhoA/ROCK signaling pathway (Figure 3C). Activation of the NLRP3 inflammasome leads to Caspase-1 cleavage, triggering Caspase-1-dependent inflammatory cell death known as pyroptosis. Next, we investigated whether inhibitors of RAGE, RhoA, and ROCK can suppress the activation of caspase-1 triggered by AGEs. The cells were pretreated with the inhibitors for 2 h and then treated with AGEs for an additional 48 h. The effects of the inhibitors on caspase-1 activation were assessed using a caspase-1 assay kit. We found that the enhanced caspase-1 activity was significantly suppressed by inhibitors of RAGE, RhoA, and ROCK (Figure 3D). Levels of LDH release were used to assess pyroptosis induced by

NLRP3 inflammasome activation, showing that AGEs promote VSMC cell pyroptosis, which can be reversed by inhibitors of RAGE, RhoA, and ROCK (Figure 3E). As caspase-1 activity is known to generate IL-1β, we also investigated the effect of inhibitors of RAGE, RhoA, and ROCK on IL-1β production. ELISA results indicated that AGEs enhance the release of the inflammatory factor IL-1β through RAGE/RhoA/ROCK signaling (Figure 3F).

The AGE-RAGE signaling pathway is highly activated in αSMA-positive cells within abdominal aortic aneurysms featuring intraluminal thrombus (ILT)

Next, we investigated whether AGE expression differs between AAAs with ILT and AAAs without ILT. ELISA assays revealed a significant increase in AGE accumulation in human AAA tissues featuring ILT (Figure 4A). Using Digital Spatial Profiling, we found that several signaling pathways are enriched in SMA-positive cells (VSMCs) within AAAs with ILT compared to those without ILT (Figures 4B–D), including the AGE-RAGE signaling pathway, Cytokine-cytokine receptor interaction, and NF-kappaB signaling pathway, among others. We employed an adjusted p-value <0.05 and a |Log2Fold Change| > 1 as criteria to identify differentially expressed mRNAs. Among these, critical genes involved in the AGE-RAGE signaling pathway such as COL1A1, IL6, CCL2, MMP-2, and STAT3, among others, exhibited notably higher expression in SMA-positive cells of AAAs with ILT, showing statistical significance (Figure 5A; Supplementary Table S1). Additionally, ELISA confirmed elevated levels of IL-6 (inflammatory factor) and MMP2 (migration phenotype marker) in aortas covered with ILT (Figure 5B). Macrophage-like VSMCs are named for their similar surface markers and functions to macrophages. These cells contribute to chronic inflammation and may participate in the destruction of the aortic wall. Consistent with our expectations, the proportion of CD68+SMA+ double-positive cells (macrophage-like VSMCs) was significantly increased in AAAs with thrombus (data not shown). In AAAs with thrombus, we compared the molecular phenotypes of the CD68+SMA+ and CD68-SMA+ cell subpopulations. Notably, MMP-9 (logFC = 1.7) and IL-1β (logFC = 2.3) were significantly upregulated in AAAs with thrombus (data not shown). Further functional annotation through Gene Ontology (GO) and KEGG pathway enrichment analysis (using both ORA and GSEA methods) revealed significant enrichment in pathways related to inflammatory response regulation, cytokine-cytokine receptor interactions, NF-κB signaling, the AGE-RAGE signaling pathway, etc. (data not shown). *In vitro*, we co-cultured human macrophages (THP-1) and VSMCs. The macrophages were cultured in the lower chamber of a Transwell, while the VSMCs were cultured in the upper chamber. The results indicated that AGEs promoted the transformation of VSMCs into a migratory phenotype in the co-culture system, characterized by a decrease in α-SMA expression and an increase in MMP2 expression (Figure 5C).

AGEs inhibit LPS-stimulated IL-6 and IL-1β secretion in human macrophage THP-1 cells

Vascular inflammation plays a crucial role in the pathogenesis of vascular diseases. Inflammatory mediators originating from inflammatory cells (such as macrophages) within vascular lesions promote the development of stenotic lesions through the proliferation and migration of vascular smooth muscle cells [22, 23]. Macrophages exhibit both pathogenic and protective functions in the pathophysiology of abdominal aortic aneurysms by participating in inflammation. Results from RT-qPCR and ELISA demonstrated that in human macrophage THP-1 cells, treatment with 200 μg/mL AGEs had minimal effect on the expression and secretion of the cytokines TNF-α, IL-1β, and iNOS, with a modest stimulatory effect observed on IL-6 (Figures 6A,B), which is the opposite of what has been implicated in VSMCs. Moreover, unexpectedly, ELISA results indicated that pre-incubation with AGEs could attenuate the secretion of IL-6 and IL-1β induced *by LPS stimulation* (Figures 6C,D). Experimental findings from TransAM NF-κB Transcription Factor Assays showed that pre-incubation with AGEs inhibited the NF-κB signaling pathway activated by LPS in THP-1 cells (Figure 6E).

AGE pretreatment reverses the effect of LPS-stimulated macrophages on VSMC phenotypic transformation

THP-1 cells were cultured in the lower layer of a co-culture system. Initially, the cells were pretreated with 200 μg/mL AGEs for 18 h, followed by stimulation with 1 μg/mL LPS for an additional 4 h. After replacing the medium, vascular smooth muscle cells were cultured in the upper layer of the co-culture system. RT-qPCR results revealed that AGE pretreatment reversed the inhibitory effect of LPS-stimulated macrophages on the contraction phenotype of VSMCs. Specifically, the expression of the contraction marker protein α-SMA increased, while the expression of the migration marker protein MMP2 decreased (Figure 6F). Furthermore, Transwell migration assay results demonstrated that AGE pretreatment attenuated the promotional effect of LPS-stimulated macrophages on VSMC migration (Figure 6G). In summary, AGEs exert

markedly different effects on macrophages compared to VSMCs, which highlights the cell-type-specific immunomodulatory effects of macrophages in AAAs. This refers to the two opposing or complementary roles that macrophages may play in different environments or contexts. For example, they can either promote or inhibit inflammation and immune responses.

Discussion

Vascular smooth muscle cells (VSMCs) are one of the most important components of the human aortic wall, and their normal structure and function are essential to the intact biomechanical properties of the aortic wall [24]. Many damaging factors, such as hemodynamic changes and the inflammatory response, can stimulate VSMCs to undergo phenotypic transformation [25, 26]. VSMCs play a pivotal role in the pathogenesis of vascular diseases due to their ability to transition from a contractile to a synthetic phenotype. This phenotypic switch enables VSMCs to proliferate, migrate, and produce pro-inflammatory cytokines, contributing significantly to vascular disease processes [27].

Zhang et al. [28] demonstrated significantly higher levels of advanced glycation end products (AGEs) in the aortas of abdominal aortic aneurysm (AAA) patients compared to healthy subjects using immunohistochemistry and ELISA. They also found elevated expression levels of the receptor for AGEs (RAGE) in human and mouse AAA tissues compared to normal aortic tissues. Prasad et al. showed a positive correlation between serum AGE levels and IL-1β, IL-6, and MMP-2 levels in patients with thoracic aortic aneurysms (TAA). Additionally, AGE-RAGE stress in TAA patients was positively correlated with MMP-2 levels [29]. Our study revealed a significant accumulation of AGEs in human AAA specimens, especially those covered with intraluminal thrombus (ILT). To avoid the influence of antiplatelet therapy on AGE levels, we analyzed clinical sample data that did not include antiplatelet therapy, and our conclusions remained consistent. Furthermore, the AGE-RAGE signaling pathway was highly enriched in smooth muscle actin (SMA)-positive cells (VSMCs) in AAAs with ILT compared to AAAs without ILT. Before this study, the molecular mechanisms by which the AGE-RAGE axis promotes inflammatory responses and migratory phenotypes in AAA, particularly in AAA with ILT, were not well understood.

The Rho family of small GTPase proteins, particularly RhoA, plays a critical role in regulating various cellular processes. RhoA acts through its effector Rho kinase (ROCK) to modulate the organization of the actin cytoskeleton, thereby influencing cellular functions such as contraction, motility, proliferation, and apoptosis. Zhao et al. [30] showed that high glucose stimulation increases the permeability of human umbilical vein endothelial cells and upregulates myosin light chain (MLC) phosphorylation. Rao et al. [31] reported that the RhoA/ROCK pathway is crucial for regulating cell migration and that ROCK inhibitors suppress the release of adhesion molecules such as intercellular cell adhesion molecule-1 (ICAM-1) and monocyte chemoattractant protein-1 (MCP-1). Based on these findings, we hypothesized that the RhoA/ROCK pathway might serve as a key downstream signaling pathway for AGEs-RAGE in regulating inflammatory responses and phenotypic transformation. Our study demonstrated that pretreatment with the RAGE inhibitor FPS-ZM1, the RhoA inhibitor CCG-1423, and the ROCK inhibitor Y27632 could reverse the pro-migration effect induced by AGEs on human VSMCs.

The interaction between advanced glycation end products and their receptor RAGE leads to the generation of reactive oxygen species (ROS) by activating nicotinamide adenine dinucleotide phosphate (NADPH) oxidase [32], which in turn activates the transcription factor NF-κB [33], thereby inducing an inflammatory response [34]. Canonical activation of the NLRP3 inflammasome involves an initial signal regulated by NF-κB to transcribe NLRP3 and pro-IL-1β, followed by a second signal to assemble the NLRP3 inflammasome. This assembly facilitates the cleavage of caspase-1 and the subsequent maturation and secretion of IL-1β [35]. Song et al. demonstrated that the RAGE/NF-κB pathway can activate the NLRP3 inflammasome, leading to the maturation of IL-1β in nucleus pulposus cells [36]. Our research has demonstrated that AGEs regulate the expression of NLRP3 through the RAGE/RhoA/ROCK/NF-κB signaling pathway and pretreatment of VSMCs with the pyroptosis inhibitor Z-VAD-FMK and the NLRP3 inhibitor CY-09 for 24 h can reverse the effects of AGEs on the phenotypic transformation of VSMCs.

In addition to RAGE, AGEs bind to and signal through TLR4 [37], which acts as a receptor for multiple pathogen-associated molecular patterns (PAMPs), including lipopolysaccharides from Gram-negative bacteria (LPS), which can induce inflammatory effects [38]. AGEs interacting with RAGE or TLR4 can stimulate multiple transcription factors; among these, NF-κB is crucial for M1 polarization and mediates pro-inflammatory responses in macrophages and other cell types [39]. In our study using human macrophage THP-1 cells, we observed that a high concentration of AGEs had a minimal impact on the expression and secretion of the cytokines TNF-α, IL-1β, and iNOS, and had a modest promoting effect on IL-6. Interestingly, AGEs inhibited the secretion of IL-6 and IL-1β induced by LPS stimulation in THP-1 macrophages. Furthermore, a TransAM NF-κB Transcription Factor Assay demonstrated that AGEs inhibited the NF-κB signaling pathway activated by LPS in THP-1 macrophages.

Multiple studies have indicated the presence of macrophages in the walls of aneurysmal aortas, as observed in both human aortic sections and animal models of abdominal aortic aneurysms [40–42]. The accumulation of macrophages in the aneurysmal

aortic wall plays a vital role in driving inflammation, extracellular matrix degradation, and tissue remodeling during the healing process. Numerous studies have provided *in vitro* evidence suggesting potential crosstalk between macrophages and smooth muscle cells via cytokine secretion, including PDGF, IL-6, TNF-α, and MCP-1 [43]. Human macrophages strongly induce VSMC apoptosis through direct cell-to-cell interactions mediated by Fas/Fas-L, which contributes to plaque rupture [44]. Additionally, another study demonstrated that macrophages promote VSMC apoptosis and influence VSMC phenotype switching through a circRNA-mediated mechanism [45]. In our previous study, we demonstrated that overexpression of hsa_circ_0087352 in macrophages induced smooth muscle cell apoptosis in a co-culture system, likely due to the release of pro-apoptotic cytokines such as IL-6, TNF-α, and IL-1β [19]. Initially, we speculated that macrophages pretreated with AGEs might promote the transition of VSMCs to a migratory phenotype. Notably, our data demonstrate that AGE pretreatment attenuates LPS-induced proinflammatory cytokine production and NF-κB activation in macrophages. This immunomodulatory effect aligns with the established mechanism reported by Son et al. [46], in which AGEs suppress NLRP3 inflammasome assembly and TLR signaling via non-RAGE pathways, specifically inhibiting M1 polarization. Then, in our experimental setup, human macrophage THP-1 cells were cultured in the lower chamber of a coculture system. We pretreated these cells with 200 μg/mL AGEs for 18 h, followed by stimulation with 1 μg/mL LPS for 4 h. After replacing the medium with fresh medium, VSMCs were cultured in the upper chamber above the macrophages. Unexpectedly, the results showed that pretreatment with AGEs reversed the pro-migration effect of LPS-stimulated macrophages on VSMCs. While some previous studies have reported that AGEs do not significantly promote cytokine production [46–48], other findings suggest that AGEs can indeed increase cytokine secretion [49–51]. Further detailed studies are needed to fully understand the complex role of AGEs in the macrophage-mediated inflammatory responses in abdominal aortic aneurysms.

In diabetic vascular disease—where AGE accumulation is pronounced—clinical trials of AGE-RAGE inhibitors (e.g., Alagebrium) have demonstrated reduced vascular stiffness and improved endothelial function [52, 53]. While these findings highlight the pathway's biological relevance, they do not directly support the therapeutic efficacy in AAA. Mechanistically, inhibition of RAGE or downstream RhoA/ROCK signaling may modulate processes implicated in AAA pathogenesis, such as VSMC phenotypic transformation. However, the absence of *in vivo* AAA outcome data precludes conclusions about clinical benefits. Substantial challenges remain, including: a) the complexity of AGE formation and cross-tissue involvement, raising concerns about therapeutic specificity; b) the potential for off-target effects when inhibiting RAGE/RhoA/ROCK in non-vascular tissues; c) a lack of evidence regarding dosing, timing, or patient selection in AAA contexts—particularly in cases with comorbidities such as diabetes; and d) the critical need for long-term safety/efficacy studies in AAA-specific models before considering clinical translation.

Limitations of this study

First, the current research primarily relies on *in vitro* models, which may not fully capture the complexity of AAAs in a living organism. Thus, future studies are critical for validating the therapeutic effects of AGE-RAGE signaling pathway inhibitors in animal models of AAAs, especially those with thrombus.

Second, our study used the HA-VSMC cell line, which was derived from an 11-month-old female donor, representing a significant biological mismatch with the predominant elderly male demographic in AAAs. While this model provides standardized insights into VSMC behavior, it fails to capture critical age- and sex-specific pathways that influence AAA pathogenesis, such as senescence-associated secretory phenotypes and androgen-mediated signaling. Future studies should prioritize primary VSMCs from age- and sex-matched AAA patients.

Third, our use of PMA-differentiated THP-1 macrophages represents a significant limitation in our ability to model human AAA pathophysiology. While this system revealed that AGE pretreatment attenuated LPS-induced IL-6/IL-1β release and reduced macrophage-driven VSMC migration in co-culture, PMA differentiation fails to replicate critical aspects of ILT-associated macrophage heterogeneity in AAAs. Consequently, our observed anti-inflammatory effect of AGEs on LPS-challenged macrophages may not translate to the complex AAA microenvironment, where thrombus hypoxia, erythrocyte lysis, and matrix remodeling create unique signaling milieus. Future studies must validate these interactions using the following: a) macrophages isolated from human AAAs; b) ILT-integrated AAA animal models with single-cell RNA sequencing; c) spatial multi-omics to resolve AGE-RAGE effects on *bona fide* disease-associated macrophage subsets.

Fourth, the small cohort size reduced statistical power for subgroup analyses and precluded the formal correlation of AGE levels with clinical severity markers (e.g., aneurysm size/growth rate). Additionally, while our aorto-iliac occlusive disease controls provide age- and comorbidity-matched comparisons for AAA patients, they do not represent true healthy aortic biology. As explicitly demonstrated in the landmark study by Zhang et al. [28] comparing AAA to autopsy-derived normal aortas, the use of truly healthy controls remains the gold standard for establishing disease-specific biomolecular changes. We emphasize the need for cautious interpretation until independent validation in larger cohorts is performed.

Fifth, while this study establishes cell-type-specific immunomodulatory effects of AGEs - activating RAGE-dependent pro-inflammatory pathways in VSMCs versus suppressing NLRP3 inflammasome activation in macrophages via non-RAGE

mechanisms (Son et al. [46]) - key mechanistic aspects remain unresolved. Specifically, the identity of the alternative receptors mediating AGE immunosuppression in macrophages (e.g., scavenger receptors) remains undefined in our experimental system. Future investigations should: a) employ receptor-knockout macrophages to validate non-RAGE pathways; b) develop spatial-omics approaches to map AGE-receptor interactomes across vascular niches; and c) define temporal thresholds for the transition from AGE-mediated immunosuppression to inflammation.

Collectively, our data reveal cell-type-specific modulation by AGE-RAGE signaling: promoting inflammatory pathways in VSMCs (e.g., ROCK/NF-κB/NLRP3; Figure 7) while attenuating inflammatory responses in macrophages. This observed dichotomy advances our understanding of metabolic influences in AAAs, but it requires rigorous causal validation in disease-relevant models before considering clinical applications.

Author contributions

XM: Formal analysis, Methodology, Funding acquisition, Investigation, and Writing – original draft. JX, HS, JL, SX, and HZ: Investigation. CC: Funding acquisition, and Writing – reviewing and editing. CS: Resources, Conceptualization, Funding acquisition, Supervision, and Writing – reviewing and editing. All authors contributed to the article and approved the submitted version.

Data availability

The datasets presented in this article are not readily available because the authors are affiliated with Changhai Hospital, an institution designated with a national security classification level, and institutional policy strictly prohibits the public deposition of raw research data. Requests to access the datasets should be directed to the corresponding author, CS.

Ethics statement

The studies involving humans were approved by the Ethics Committee of Shanghai Changhai Hospital. The studies were conducted in accordance with the local legislation and institutional requirements. The participants provided their written informed consent to participate in this study.

Funding

The author(s) declare that financial support was received for the research and/or publication of this article. This work was supported by the Young Scientists Fund of the National Natural Science Foundation of China (Grant Nos 82100456 and 82400164), and the Health Clinical Research Project of the Shanghai Municipal Health Commission (No. 202040328).

Conflict of interest

The author(s) declared no potential conflicts of interest with respect to the research, authorship, and/or publication of this article.

Generative AI statement

The author(s) declare that no Generative AI was used in the creation of this manuscript.

Supplementary material

The Supplementary Material for this article can be found online at: https://www.ebm-journal.org/articles/10.3389/ebm.2025.10527/full#supplementary-material

References

1. Bucala R, Cerami A. Advanced glycosylation: chemistry, biology, and implications for diabetes and aging. *Adv Pharmacol (San Diego, Calif)* (1992) **23**:1–34. doi:10.1016/s1054-3589(08)60961-8

2. Kalea AZ, Schmidt AM, Hudson BI. RAGE: a novel biological and genetic marker for vascular disease. *Clin Sci (London, Engl : 1979)* (2009) **116**:621–37. doi:10.1042/cs20080494

3. Wang L, Zhang J, Fu W, Guo D, Jiang J, Wang Y. Association of smooth muscle cell phenotypes with extracellular matrix disorders in thoracic aortic dissection. *J Vasc Surg* (2012) **56**:1698–709.e1. doi:10.1016/j.jvs.2012.05.084

4. Yamagishi S, Matsui T. Pathologic role of dietary advanced glycation end products in cardiometabolic disorders, and therapeutic intervention. *Nutrition (Burbank, Los Angeles County, Calif)* (2016) **32**:157–65. doi:10.1016/j.nut.2015.08.001

5. Wang R, Kudo M, Yokoyama M, Asano G. Roles of advanced glycation Endoproducts(AGE) and receptor for AGE on vascular smooth muscle cell growth. *J Nippon Med Sch* (2001) **68**:472–81. doi:10.1272/jnms.68.472

6. Simard E, Söllradl T, Maltais JS, Boucher J, D'Orléans-Juste P, Grandbois M. Receptor for advanced glycation end-products signaling interferes with the vascular smooth muscle cell contractile phenotype and function. *PloS one* (2015) **10**:e0128881. doi:10.1371/journal.pone.0128881

7. Adolph R, Vorp DA, Steed DL, Webster MW, Kameneva MV, Watkins SC. Cellular content and permeability of intraluminal thrombus in abdominal aortic aneurysm. *J Vasc Surg* (1997) **25**:916–26. doi:10.1016/s0741-5214(97)70223-4

8. Harter LP, Gross BH, Callen PW, Barth RA. Ultrasonic evaluation of abdominal aortic thrombus. *J Ultrasound Med* (1982) **1**:315–8. doi:10.7863/jum.1982.1.8.315

9. Vorp DA, Federspiel WJ, Webster MW. Does laminated intraluminal thrombus within abdominal aortic aneurysm cause anoxia of the aortic wall? *J Vasc Surg* (1996) **23**:540–1. doi:10.1016/s0741-5214(96)80027-9

10. Vorp DA, Lee PC, Wang DH, Makaroun MS, Nemoto EM, Ogawa S, et al. Association of intraluminal thrombus in abdominal aortic aneurysm with local hypoxia and wall weakening. *J Vasc Surg* (2001) **34**:291–9. doi:10.1067/mva.2001.114813

11. Siegel CL, Cohan RH, Korobkin M, Alpern MB, Courneya DL, Leder RA. Abdominal aortic aneurysm morphology: CT features in patients with ruptured and nonruptured aneurysms. *Am J Roentgenology* (1994) **163**:1123–9. doi:10.2214/ajr.163.5.7976888

12. Ma X, Xia S, Liu G, Song C. The detrimental role of intraluminal thrombus outweighs protective advantage in abdominal aortic aneurysm pathogenesis: the implications for the anti-platelet therapy. *Biomolecules* (2022) **12**:942. doi:10.3390/biom12070942

13. Valencia JV, Mone M, Zhang J, Weetall M, Buxton FP, Hughes TE. Divergent pathways of gene expression are activated by the RAGE ligands S100b and AGE-BSA. *Diabetes* (2004) **53**:743–51. doi:10.2337/diabetes.53.3.743

14. Liu B, Lee YC, Alwaal A, Wang G, Banie L, Lin CS, et al. Carbachol-induced signaling through Thr696-phosphorylation of myosin phosphatase-targeting subunit 1 (MYPT1) in rat bladder smooth muscle cells. *Int Urol Nephrol* (2016) **48**:1237–42. doi:10.1007/s11255-016-1303-2

15. Stockton RA, Shenkar R, Awad IA, Ginsberg MH. Cerebral cavernous malformations proteins inhibit rho kinase to stabilize vascular integrity. *J Exp Med* (2010) **207**:881–96. doi:10.1084/jem.20091258

16. Deng X, Huang W, Peng J, Zhu TT, Sun XL, Zhou XY, et al. Irisin alleviates advanced glycation end products-induced inflammation and endothelial dysfunction *via* inhibiting ROS-NLRP3 inflammasome signaling. *Inflammation* (2018) **41**:260–75. doi:10.1007/s10753-017-0685-3

17. Shahzad K, Bock F, Dong W, Wang H, Kopf S, Kohli S, et al. Nlrp3-inflammasome activation in non-myeloid-derived cells aggravates diabetic nephropathy. *Kidney Int* (2015) **87**:74–84. doi:10.1038/ki.2014.271

18. Ma X, Liu J, Yang X, Fang K, Zheng P, Liang X, et al. Mesenchymal stem cells maintain the stemness of Colon cancer stem cells *via* interleukin-8/mitogen-activated protein kinase signaling pathway. *Exp Biol Med (Maywood, NJ)* (2020) **245**:562–75. doi:10.1177/1535370220910690

19. Ma X, Xu J, Lu Q, Feng X, Liu J, Cui C, et al. Hsa_circ_0087352 promotes the inflammatory response of macrophages in abdominal aortic aneurysm by adsorbing hsa-miR-149-5p. *Int immunopharmacology* (2022) **107**:108691. doi:10.1016/j.intimp.2022.108691

20. Cai Q, Li BY, Gao HQ, Zhang JH, Wang JF, Yu F, et al. Grape seed procyanidin b2 inhibits human aortic smooth muscle cell proliferation and migration induced by advanced glycation end products. *Biosci Biotechnol Biochem* (2011) **75**:1692–7. doi:10.1271/bbb.110194

21. Hwang AR, Nam JO, Kang YJ. Fluvastatin inhibits advanced glycation end products-induced proliferation, migration, and extracellular matrix accumulation in vascular smooth muscle cells by targeting connective tissue growth factor. *Korean J Physiol and Pharmacol* (2018) **22**:193–201. doi:10.4196/kjpp.2018.22.2.193

22. Galis ZS, Khatri JJ. Matrix metalloproteinases in vascular remodeling and atherogenesis: the good, the bad, and the ugly. *Circ Res* (2002) **90**:251–62. doi:10.1161/res.90.3.251

23. Waitkus-Edwards KR, Martinez-Lemus LA, Wu X, Trzeciakowski JP, Davis MJ, Davis GE, et al. $\alpha_4\beta_1$ integrin activation of L-Type calcium channels in vascular smooth muscle causes arteriole vasoconstriction. *Circ Res* (2002) **90**:473–80. doi:10.1161/hh0402.105899

24. Zhang Z, Wang M, Fan XH, Chen JH, Guan YY, Tang YB. Upregulation of TRPM7 channels by angiotensin II triggers phenotypic switching of vascular smooth muscle cells of ascending aorta. *Circ Res* (2012) **111**:1137–46. doi:10.1161/circresaha.112.273755

25. Majesky MW. Vascular smooth muscle cells. *Arteriosclerosis, Thromb Vasc Biol* (2016) **36**:e82–6. doi:10.1161/atvbaha.116.308261

26. Milewicz DM, Trybus KM, Guo DC, Sweeney HL, Regalado E, Kamm K, et al. Altered smooth muscle cell force generation as a driver of thoracic aortic aneurysms and dissections. *Arteriosclerosis, Thromb Vasc Biol* (2017) **37**:26–34. doi:10.1161/atvbaha.116.303229

27. Ackers-Johnson M, Talasila A, Sage AP, Long X, Bot I, Morrell NW, et al. Myocardin regulates vascular smooth muscle cell inflammatory activation and disease. *Arteriosclerosis, Thromb Vasc Biol* (2015) **35**:817–28. doi:10.1161/atvbaha.114.305218

28. Zhang F, Kent KC, Yamanouchi D, Zhang Y, Kato K, Tsai S, et al. Anti-receptor for advanced glycation end products therapies as novel treatment for abdominal aortic aneurysm. *Ann Surg* (2009) **250**:416–23. doi:10.1097/SLA.0b013e3181b41a18

29. Prasad K, Sarkar A, Zafar MA, Shoker A, Moselhi HE, Tranquilli M, et al. Advanced glycation end products and its soluble receptors in the pathogenesis of thoracic aortic aneurysm. *Aorta (Stamford, Conn)* (2016) **04**:1–10. doi:10.12945/j.aorta.2015.15.018

30. Zhao XY, Wang XF, Li L, Zhang L, Shen DL, Li DH, et al. Effects of high glucose on human umbilical vein endothelial cell permeability and myosin light chain phosphorylation. *Diabetology and Metab Syndr* (2015) **7**:98. doi:10.1186/s13098-015-0098-0

31. Rao J, Ye Z, Tang H, Wang C, Peng H, Lai W, et al. The RhoA/ROCK pathway ameliorates adhesion and inflammatory infiltration induced by AGEs in glomerular endothelial cells. *Scientific Rep* (2017) **7**:39727. doi:10.1038/srep39727

32. Wautier MP, Chappey O, Corda S, Stern DM, Schmidt AM, Wautier JL. Activation of NADPH oxidase by AGE links oxidant stress to altered gene expression *via* RAGE. *Am J Physiol Endocrinol Metab* (2001) **280**:E685–94. doi:10.1152/ajpendo.2001.280.5.E685

33. Gloire G, Legrand-Poels S, Piette J. NF-κB activation by reactive oxygen species: fifteen years later. *Biochem Pharmacol* (2006) **72**:1493–505. doi:10.1016/j.bcp.2006.04.011

34. Reznikov LL, Waksman J, Azam T, Kim SH, Bufler P, Niwa T, et al. Effect of advanced glycation end products on endotoxin-induced TNF-a, IL-1b and IL-8 in human peripheral blood mononuclear cells. *Clin Nephrol* (2004) **61**:324–36. doi:10.5414/cnp61324

35. Latz E, Xiao TS, Stutz A. Activation and regulation of the inflammasomes. *Nat Rev Immunol* (2013) **13**:397–411. doi:10.1038/nri3452

36. Song Y, Wang Y, Zhang Y, Geng W, Liu W, Gao Y, et al. Advanced glycation end products regulate anabolic and catabolic activities *via* NLRP3-inflammasome activation in human nucleus pulposus cells. *J Cell Mol Med* (2017) **21**:1373–87. doi:10.1111/jcmm.13067

37. Chen YJ, Sheu ML, Tsai KS, Yang RS, Liu SH. Advanced glycation end products induce peroxisome proliferator-activated receptor γ down-regulation-related inflammatory signals in human chondrocytes *via* toll-like Receptor-4 and receptor for advanced glycation end products. *PloS one* (2013) **8**:e66611. doi:10.1371/journal.pone.0066611

38. Patel MC, Shirey KA, Pletneva LM, Boukhvalova MS, Garzino-Demo A, Vogel SN, et al. Novel drugs targeting toll-like receptors for antiviral therapy. *Future Virol* (2014) **9**:811–29. doi:10.2217/fvl.14.70

39. Stirban A, Gawlowski T, Roden M. Vascular effects of advanced glycation endproducts: clinical effects and molecular mechanisms. *Mol Metab* (2014) **3**:94–108. doi:10.1016/j.molmet.2013.11.006

40. Tieu BC, Lee C, Sun H, Lejeune W, Recinos A, 3rd, Ju X, et al. An adventitial IL-6/MCP1 amplification loop accelerates macrophage-mediated vascular inflammation leading to aortic dissection in mice. *J Clin Invest* (2009) **119**:3637–51. doi:10.1172/jci38308

41. Wang Y, Ait-Oufella H, Herbin O, Bonnin P, Ramkhelawon B, Taleb S, et al. TGF-Beta activity protects against inflammatory aortic aneurysm progression and complications in angiotensin II-infused mice. *J Clin Invest* (2010) **120**:422–32. doi:10.1172/jci38136

42. Daugherty A, Manning MW, Cassis LA. Angiotensin II promotes atherosclerotic lesions and aneurysms in apolipoprotein E-deficient mice. *J Clin Invest* (2000) **105**:1605–12. doi:10.1172/jci7818

43. Koga J, Aikawa M. Crosstalk between macrophages and smooth muscle cells in atherosclerotic vascular diseases. *Vasc Pharmacol* (2012) **57**:24–8. doi:10.1016/j.vph.2012.02.011

44. Boyle JJ, Bowyer DE, Weissberg PL, Bennett MR. Human blood-derived macrophages induce apoptosis in human plaque-derived vascular smooth muscle cells by fas-Ligand/fas interactions. *Arteriosclerosis, Thromb Vasc Biol* (2001) **21**:1402–7. doi:10.1161/hq0901.094279

45. Lv P, Yin YJ, Kong P, Cao L, Xi H, Wang N, et al. SM22*α* loss contributes to apoptosis of vascular smooth muscle cells *via* macrophage-derived circRasGEF1B. *Oxidative Med Cell longevity* (2021) **2021**:5564884. doi:10.1155/2021/5564884

46. Son S, Hwang I, Han SH, Shin JS, Shin OS, Yu JW. Advanced glycation end products impair NLRP3 inflammasome-mediated innate immune responses in macrophages. *J Biol Chem* (2017) **292**:20437–48. doi:10.1074/jbc.M117.806307

47. Liu J, Zhao S, Tang J, Li Z, Zhong T, Liu Y, et al. Advanced glycation end products and lipopolysaccharide synergistically stimulate proinflammatory

cytokine/chemokine production in endothelial cells *via* activation of both mitogen-activated protein kinases and nuclear factor-κB. *FEBS J* (2009) **276**:4598–606. doi:10.1111/j.1742-4658.2009.07165.x

48. Mone M, Koehne C, Rediske J, Hughes TE, Valencia JV. Binding of receptor for advanced glycation end products (RAGE) ligands is not sufficient to induce inflammatory signals: lack of activity of endotoxin-free albumin-derived advanced glycation end products. *Diabetologia* (2004) **47**:844–52. doi:10.1007/s00125-004-1392-9

49. Pertyńska-Marczewska M, Kiriakidis S, Wait R, Beech J, Feldmann M, Paleolog EM. Advanced glycation end products upregulate angiogenic and pro-inflammatory cytokine production in human monocyte/macrophages. *Cytokine* (2004) **28**:35–47. doi:10.1016/j.cyto.2004.06.006

50. Rasheed Z, Akhtar N, Haqqi TM. Advanced glycation end products induce the expression of interleukin-6 and interleukin-8 by receptor for advanced glycation end product-mediated activation of mitogen-activated protein kinases and nuclear factor- B in human osteoarthritis chondrocytes. *Rheumatology (Oxford, England)* (2011) **50**:838–51. doi:10.1093/rheumatology/keq380

51. Miyata T, Inagi R, Iida Y, Sato M, Yamada N, Oda O, et al. Involvement of beta 2-microglobulin modified with advanced glycation end products in the pathogenesis of hemodialysis-associated amyloidosis. Induction of human monocyte chemotaxis and macrophage secretion of tumor necrosis factor-alpha and interleukin-1. *J Clin Invest* (1994) **93**:521–8. doi:10.1172/jci117002

52. Zieman SJ, Melenovsky V, Clattenburg L, Corretti MC, Capriotti A, Gerstenblith G, et al. Advanced glycation endproduct crosslink breaker (alagebrium) improves endothelial function in patients with isolated systolic hypertension. *J Hypertens* (2007) **25**:577–83. doi:10.1097/HJH.0b013e328013e7dd

53. Bakris GL, Bank AJ, Kass DA, Neutel JM, Preston RA, Oparil S. Advanced glycation end-product cross-link breakers. A novel approach to cardiovascular pathologies related to the aging process. *Am J Hypertens* (2004) **17**:23s–30s. doi:10.1016/j.amjhyper.2004.08.022

EBM Experimental Biology and Medicine

TYPE Original Research
PUBLISHED 24 July 2025
DOI 10.3389/ebm.2025.10456

OPEN ACCESS

*CORRESPONDENCE
Ihor Shymanskyi,
ihorshym@gmail.com

RECEIVED 05 December 2024
ACCEPTED 08 July 2025
PUBLISHED 24 July 2025

CITATION
Shymanskyi I, Lisakovska O, Veliky M, Mezhenska O, Bilous V, Siromolot A, Khomenko A, Labudzynskyi D, Horid'ko T and Pasichna E (2025) Vitamin D_3 affects liver expression of pro-/anti-inflammatory cytokines and nitric oxide synthases in type 2 diabetes. *Exp. Biol. Med.* 250:10456. doi: 10.3389/ebm.2025.10456

Vitamin D_3 affects liver expression of pro-/anti-inflammatory cytokines and nitric oxide synthases in type 2 diabetes

Ihor Shymanskyi[1]*, Olha Lisakovska[1], Mykola Veliky[1], Olha Mezhenska[1], Vasyl Bilous[2], Andrii Siromolot[3], Anna Khomenko[1], Dmytro Labudzynskyi[1], Tetyana Horid'ko[4] and Elvira Pasichna[1]

[1]Department of Biochemistry of Vitamins and Coenzymes, Palladin Institute of Biochemistry of the National Academy of Sciences of Ukraine, Kyiv, Ukraine, [2]Department of Enzyme Chemistry and Biochemistry, Palladin Institute of Biochemistry of the National Academy of Sciences of Ukraine, Kyiv, Ukraine, [3]Department of Molecular Immunology, Palladin Institute of Biochemistry of the National Academy of Sciences of Ukraine, Kyiv, Ukraine, [4]Department of Lipids Biochemistry, Palladin Institute of Biochemistry of the National Academy of Sciences of Ukraine, Kyiv, Ukraine

Abstract

Our objective was to study the effect of vitamin D_3 (VD) on hepatocellular oxidative-nitrosative stress and pro/anti-inflammatory cytokines in relation to nitric oxide (NO) formation and NO synthase (NOS) levels in type 2 diabetes mellitus (T2DM). After T2DM induction by high-fat diet and a single streptozotocin injection (25 mg/kg b. w.), male Wistar rats were treated with/without VD (1,000 IU/kg b. w., 30 days). Oxidative stress/inflammation and NOS/NO were assessed by flow cytometry, RT-qPCR, western blotting, and ELISA. A 3.3-fold decrease in serum 25(OH)D_3 was established in diabetic rats, suggesting their VD deficient status. T2DM was associated with excess reactive oxygen species (ROS; 2.4-fold) and NO (2.5-fold) production in hepatocytes paralleled by elevated levels of myeloperoxidase (1.7-fold), carbonylated (2.8-fold) and nitrotyrosylated (1.7-fold) proteins in liver tissue vs. control, indicative of oxidative-nitrosative stress. Low-grade inflammation in diabetic liver was confirmed by increased NF-κB transcriptional activity (1.24-fold) and mRNA expression of proinflammatory cytokines TNF-α (3.5-fold) and IL-1β (2.2-fold) with alleviating mRNAs of anti-inflammatory cytokines IL-4 (1.7-fold) and IL-10 (2.6-fold), while TGF-β1 expression raised 1.4-fold vs. control. Higher iNOS and eNOS mRNAs (2.7- and 3.3-fold, respectively) and protein (2.1- and 3.2-fold, respectively) levels, as well as NOS activity (1.6-fold) were found in diabetic liver. VD supplementation restored 25(OH)D_3, partially normalized NF-κB transcriptional activity and pro/anti-inflammatory cytokines, lowered hepatocellular ROS/NO, and oxidative protein modifications. However, VD had no effect on eNOS, IL-10 and TGF-β1 mRNAs. It also led to a further increase in myeloperoxidase, eNOS and iNOS proteins and NOS activity compared to diabetes. In conclusion, abnormal oxidative metabolism in

T2DM is associated with enhanced NF-κB/NOS/NO response, which can be partially attenuated by VD treatment via normalization of pro-oxidative/pro-inflammatory processes. The paradoxical sustained increase in NOS expression in the presence of VD antioxidant activity likely improves hepatocellular NO bioavailability, ultimately reducing T2DM-associated liver injury.

KEYWORDS

type 2 diabetes mellitus, liver dysfunction, vitamin D_3, nitric oxide, oxidative-nitrosative stress, inflammatory cytokines

Impact statement

Progression of liver damage associated with type 2 diabetes mellitus (T2DM) is a major health concern, but the underlying mechanisms remain unclear. Several epidemiological studies have highlighted a significant association between low vitamin D3 levels and an increased risk of metabolic dysfunction-associated steatotic liver disease (MASLD). We hypothesized that excessive NO synthesis could exert protective or detrimental effects on hepatocellular function depending on the intensity of prooxidant and/or proinflammatory processes in the liver in diabetes. Vitamin D3 may increase NO bioavailability by modulating oxidative metabolism and pro-/anti-inflammatory status. Therefore, we investigated for the first time, to our knowledge, the regulatory effects of vitamin D3 on T2DM-induced experimental uncoupling of NO synthase (eNOS, iNOS) expression and NO generation in relation to hyperglycemic state, oxidative stress and chronic inflammation. The obtained findings may have novel implications for preventive strategies against diabetes-induced T2DM and its associated liver complications.

Introduction

Type 2 diabetes mellitus (T2DM) is currently recognized as a global non-infectious epidemic [1]. The number of adults worldwide suffering from the disease is estimated to reach 650 million by 2045. Hyperglycemia, as a consequence of T2DM, leads to the development of various comorbidities, such as glycemic hepatopathy and metabolic dysfunction-associated steatotic liver disease (MASLD) [2]. According to

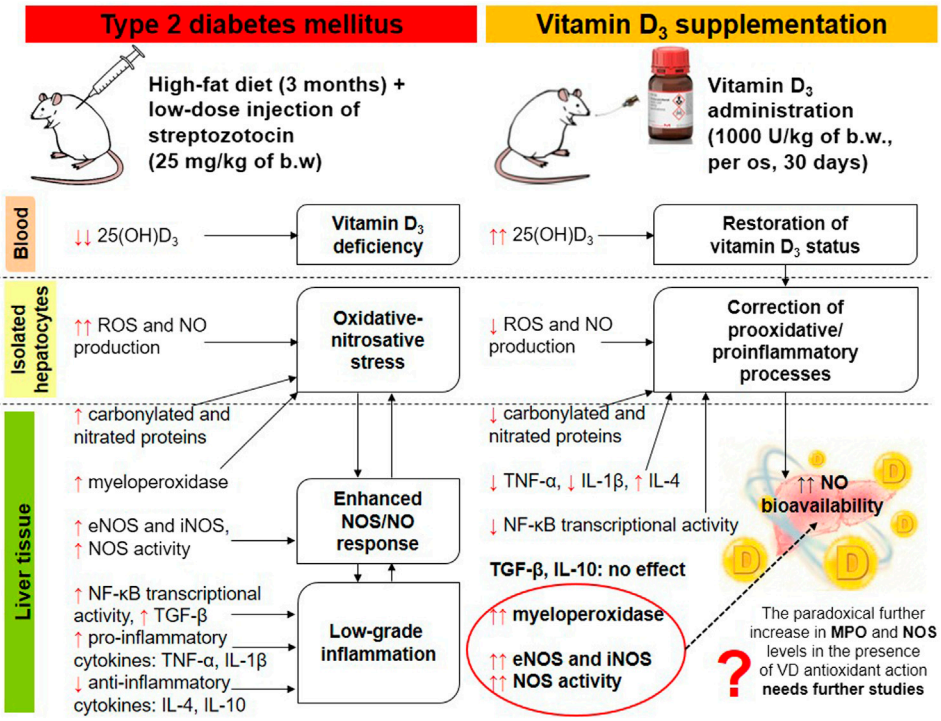

GRAPHICAL ABSTRACT

multiple clinical studies, the prevalence of MASLD is up to 60%–70% of all individuals with type 2 diabetes [3]. It has been shown that the accumulation of triacylglycerols in the liver is an important and early sign of metabolic disorder. At the cellular level, liver damage in T2DM involves glycotoxic and oxidative stress, impaired autophagy and unfolded protein response in the endoplasmic reticulum (ER) during ER stress, alongside with mitochondrial dysfunction [4–6]. In turn, various types of stress can lead to the development of inflammation, induction of apoptotic cell death and enhancement, especially against the background of fibrotic processes, of liver cell proliferation due to activation of the nuclear factor kappa B (NF-κB) signaling pathway [7, 8].

Metastable free radical nitric oxide (NO) production is associated with MASLD and is essential for adequate glucose and lipid homeostasis [9, 10]. This gaseous substance is known to be synthesized by nitric oxide synthases (NOSs). Three isoforms with distinct functions have been identified for the NOS enzyme, namely neuronal (NOS-1; nNOS), endothelial (NOS-3; eNOS), and inducible (NOS-2; iNOS) [11]. Both neuronal and endothelial isoforms generate low levels of nitric oxide as a signaling molecule and are Ca^{2+}-dependent. Instead, iNOS activation occurs at the transcriptional level under the influence of endotoxins or inflammatory cytokines, particularly in cells such as macrophages and neutrophils, and is independent of cytoplasmic Ca^{2+} levels. Given that iNOS is a highly yielding enzyme that generates toxic amounts of nitric oxide, it represents a crucial component of the antiparasitic/antimicrobial and antitumor activities of the innate immune system. Nitric oxide is also an important regulator and mediator of numerous processes in the nervous and cardiovascular system. In particular, relaxation of vascular smooth muscles, leading to arterial vasodilation, occurs due to binding to the heme of cytosolic guanylate cyclase. Activation of the latter promotes an increase in the intracellular level of cyclic guanosine-3′,5′-monophosphate (cGMP). In turn, activated cGMP-dependent protein kinase phosphorylates the myosin phosphatase-targeting subunit and the inositol triphosphate receptor-associated cGMP kinase substrate, ultimately resulting in vascular smooth muscle relaxation [12]. Nitric oxide can also act in a cGMP-independent manner, for example, by altering the activity of proteins by covalent nitrosylation of thiol groups of specific cysteine residues in their molecules [13].

In addition to mediating normal functions, NO is involved in a variety of pathophysiological conditions such as hypertension, stroke, neurodegenerative diseases, septic shock, diabetes mellitus and its complications, etc. [9, 14]. Nitric oxide has a significant impact on the liver, playing a pivotal role in regulating metabolism and the immune response [15]. Liver functions depend on complex interactions of heterogeneous subpopulations of its cells. Hepatic nitric oxide is produced primarily by eNOS and iNOS and is responsible for most of the physiological and pathophysiological reactions involving the liver. While nitric oxide formed by eNOS exhibits mainly protective functions in the liver due to the regulation of blood flow and cell interactions, NO synthesized by iNOS can exhibit both protective and damaging effects on liver homeostasis [15]. Experimental models have shown that hepatocytes produce iNOS in response to inflammatory cytokines [16]. Immunohistochemical methods have shown that the eNOS isoform is detected in endothelial cells of arteries and terminal veins of the liver, sinusoids, and in epithelial cells of the bile ducts. Distinct iNOS expression can be observed in the periportal region with decreasing intensity towards the perivenous areas of the hepatic ducts [17]. Liver cells can be exposed to the action of NO generated by neighboring Kupffer cells, endothelial cells, as well as to the influence of autoendogenous NO. It has been shown that iNOS expression is also observed under physiological conditions in the liver and, possibly, through this mechanism, hepatocytes control the degree of apoptosis [18]. Since NO is a multifunctional signaling molecule that plays a striking role in health and disease, adverse changes in the NO system caused by diabetes may be considered as an important link between the diabetic state and liver pathology.

Although there are currently no pharmacological agents specifically approved for the treatment of T2DM-associated liver disease, numerous drug candidates are being studied in clinical trials to address lipotoxic liver injury and insulin resistance, inflammation, fibrosis, and metabolism on a case-by-case basis.

A limited amount of experimental and clinical data is available on the hepatoprotective effect of vitamin D_3 (cholecalciferol) in T2DM-associated chronic liver diseases [19, 20]. Traditional concepts of the regulatory role of vitamin D_3 in bone remodeling and mineralization have currently been supplemented by new data that expand the understanding of the pleiotropic effects of this bioactive steroid, which regulates various pathways of cellular metabolism, exhibits anti-inflammatory, immunomodulatory effects and has a powerful impact on cell proliferation, differentiation and death [19–21]. This compound accomplishes its biological effects through the mechanism of hormonal action of the bioactive cholecalciferol derivative, 1α,25-dihydroxyvitamin D_3 ($1\alpha,25(OH)_2D_3$, calcitriol), which is mediated by a specific vitamin D_3 receptor (VDR). The latter serves as a transcription factor in regulating the expression of numerous genes [22]. The molecular mechanisms of vitamin D_3 action in the diabetic liver remain largely unclear. However, it can be speculated that its hepatoprotective efficacy is, at least in part, mediated by the regulation of oxidative-nitrosative stress, NF-κB-associated inflammation, and cell proliferation/death [21, 23]. Vitamin D_3 was shown to be a promising pharmacological agent for the treatment of metabolic and cardiovascular disturbances, and nitric oxide may play an essential role in mediating these effects [24, 25].

As NO signaling pathway is not only affected by vitamin D_3 levels but also closely related to MASLD through a series of

mechanisms, such as pro/anti-inflammatory imbalance, immune disorders, and oxidative stress, the effect of cholecalciferol on T2DM-elicited liver abnormalities may be achieved via regulation of the NO system. The trial was therefore performed to explore the effects of vitamin D_3 on hepatocellular oxidative-nitrosative stress and NF-κB-mediated expression of pro/anti-inflammatory cytokines in association with the levels of NO synthases (eNOS, iNOS) and nitric oxide generation in experimental T2DM.

Materials and methods

Experimental animals and treatments

We conducted an investigator-blinded, vehicle-controlled study on 35 male Wistar rats weighing 202.5 ± 15.8 g. All rats underwent a 1-week adaptation period to the animal facility environment (temperature +22 ± 2°C, air humidity 50–60%, natural day/night cycle). Food and water were available freely. At the beginning of the experiment, the first random allocation of the animals to two groups was performed: (1) the control rats (n = 10) without somatic pathology, kept on a standard diet for rodents (REZON-1, Ukraine); (2) the T2DM group (n = 25) – animals with experimental T2DM induced by keeping them for 60 days on a homemade high-fat diet (HFD) followed by a single administration of streptozotocin (STZ; Sigma-Aldrich, USA) at a low dose. The HFD was a mixture of a standard vivarium diet (REZON-1, Ukraine) with the addition of vitamins and minerals (based on the daily requirement for animals) – 54%, pork lard prepared by rendering visceral fat – 25%, fructose (Golden Pharm, Ukraine) – 20%, supplemented with bile acids – 1% (Pharma Cherkas, Ukraine). Baseline 25-hydroxyvitamin D_3 ($25(OH)D_3$) levels were measured in all animals in both groups. On day 61 of high-fat diet, rats were intraperitoneally injected with freshly prepared STZ solution after 12 h of fasting (25 mg/kg b.w. dissolved in 0.5 mL of 0.1 M citrate buffer, pH 4.5). Group 1 received an equal (0.5 mL) volume of vehicle (citrate buffer) treatment intraperitoneally. On the 75th day of experiment, the glucose levels were measured by OneTouch Select glucometer (LifeScan Europe GmbH, Switzerland). From the second part of the experiment, we had to exclude 9 animals without or with mild features of diabetes (fasting blood glucose level less than 7.5 mmol/L). At the final stage of the trial, the following groups of rodents were formed: (1) control (n = 7), (2) diabetic (T2DM; n = 7) and (3) diabetic, whose animals were orally (through a gavage) administered 0.1 mL of a solution of vitamin D_3 (cholecalciferol; SigmaAldrich, USA) in sunflower oil at a dose of 1,000 IU/kg of b. w. daily for 30 days (T2DM + VD; n = 7). The baseline fasting blood glucose levels in the experimental groups were 4.40 ± 0.15, 10.35 ± 1.93 and 10.51 ± 2.02 mmol/L, respectively. Groups 1 and 2 were orally given an equal (0.1 mL) volume of the vehicle (sunflower oil). After the final group formation, all animals were transferred to a standard diet. On day 105, an intraperitoneal insulin tolerance test (ipITT) was performed. The rats were then decapitated under deep ether anesthesia. Blood samples were collected and livers were excised for further analysis. Serum was obtained by centrifugation of whole blood at 3,000 g (+4°C) for 10 min.

All animal procedures were performed in accordance with bioethical principles and international standards concerning animal welfare, including the European Convention for the Protection of Vertebrate Animals Used for Experimental and Other Scientific Purposes (Strasbourg, France; 1986) and the Guidelines for Bioethical Evaluation of Preclinical and Other Scientific Research Conducted on Animals (Kyiv, Ukraine; 2006).

Assessment of intraperitoneal insulin tolerance test

Experimental rats were fasted for 12 h before performing the intraperitoneal insulin tolerance test. Baseline blood glucose levels (at 0 min) were measured, after that rats were injected intraperitoneally with insulin solution (Actrapid HM Penfill, Novo Nordisk, Denmark) at a dose of 0.7 U/kg b. w. Glucose was monitored at time intervals of 30, 45, 60, 90, and 120 min after insulin administration. Microsoft Excel was used to calculate the total area under the curves in response to insulin injection.

HOMA-IR determination

HOMA-IR was determined based on the results of fasting blood glucose and insulin measurements using the following formula:

$$\text{HOMA-IR} = \text{serum insulin (mmol/L)} * (\text{blood glucose (mmol/L)}/22.5$$

Serum insulin content was measured by Rat insulin ELISA kit (MBS724709, MyBioSource, USA) following the manufacturer's protocol.

Detection of 25-hydroxyvitamin D_3 content in blood serum

Assessment of vitamin D_3 status in animals was based on serum $25(OH)D_3$ levels. Vitamin D ELISA kit (DE1971, Demeditec Diagnostics GmbH, Germany) was used to determine $25(OH)D_3$ according to the manufacturer's instruction.

Isolation of primary rat hepatocytes and determination of reactive oxygen species and nitric oxide

To isolate primary rat hepatocytes, the oxygenated perfusion solution was slowly infused through the cannulated portal vein and inferior vena cava. After perfusion, the left lobe of the liver was excised and treated with liver digestion medium supplemented with 0.05% collagenase (Sigma, USA) for 1 h (+37°C). Cells were then harvested, washed, and resuspended after centrifugation.

Intracellular generation of reactive oxygen species (ROS) and nitric oxide in isolated hepatocytes was detected using the ROS- and NO-sensitive probes 2′,7′- dichlorodihydrofluorescein diacetate (DCFH-DA; Sigma, USA) and 4,5-diaminofluorescein diacetate (DAF-2DA) (Sigma, USA), respectively. Briefly, hepatocytes (0.5×10^6 cells) were incubated immediately after their isolation in Hank's balanced salt solution with 10 μM DCFH-DA or DAF-2DA for 30 min (+37°C) in the dark and a humidified atmosphere of 5% CO_2. After washing by centrifugation and resuspension of the cells, fluorescence was measured using an EPICS XLTM flow cytometer (Beckman Coulter, USA) at 485/530 nm or 495/515 nm (excitation/emission wavelengths for DCFH-DA and DAF-2DA, respectively). Flow cytometric data were then analyzed with FCS Express V3 software. The results were expressed in arbitrary units as the relative fluorescence of the samples compared to the control.

Nitric oxide synthase activity quantitative assessment

Total nitric oxide synthase activity was determined in liver tissue samples using the NOS Assay Kit (MAK532-1KT, Sigma-Aldrich, USA) in accordance with the manufacturer's instructions. In brief, liver samples were homogenized in 1x PBS (pH 7.4) and centrifuged at 10,000g (+4°C) to obtain supernatants for NOS activity assay. The step of nitric oxide formation in the NOS reaction of the samples was followed by nitrate reduction to nitrite using the Griess method. The OD was read at 500–570 nm (peak 540 nm).

Quantitative real-time polymerase chain reaction (RT-qPCR)

Total RNA was isolated from rat liver tissue using the NucleoZOL® single-phase RNA purification kit (Macherey-Nagel, Germany). The extracted RNA was then reverse-transcribed into cDNA with the iScript gDNA Clear cDNA synthesis kit (Bio-Rad, USA). The following primers for RT-qPCR: TGF-β1-Forward: 5′-TGCTGAGAAAAAGCAGCAGA′, TGF-β1Reverse: 5′-AGTACGTCGTTGCAGATGTC-3′; TNF-a-Forward: 5′TCAGCGAGGACACCAAGG-3′, TNF-a-Reverse: 5′-CTCTGCCAGTTCCACATCTC-3′; IL-1β-Forward: 5′-AAT CTCACAGCAGCATCTCG-3′, IL-1β-Reverse: 5′CATCATCCC ACGAGTCACAG-3′; IL-4-Forward: 5′-GATGTAACGACA GCCCTCTG-3′, IL-4-Reverse: 5′-TGGTACAAACATCTC GGTGC-3′; IL-10-Forward: 5′-ATTTTAATAAGCTCCAAG ACAAAGG-3′, IL-10-Reverse: 5′-GGAGAGAGGTACAAA CGAGG-3′; NOS2 (iNOS)-Forward: 5′-TTGGTGAGGGGA CTGGACTTT-3′, NOS2 (iNOS)-Reverse: 5′-TGAAGAGAA ACTTCCAGGGGC-3′; NOS3 (eNOS)-Forward:5′-GTTGACCAAGGCAAACCACC-3′, NOS3 eNOS-Reverse:5′-GCTGACTCCCTCCCAGTCTA-3′; β-actin-Forward: 5′-CCG TGAGTTAGGTCGAGC-3′, βactin-Reverse: 5′-GTACATGCA GCCTTCGTTG-3′; Mrpl32-Forward: 5′- CAAAAACAGACG CACCATCG-3′, Mrpl32-Reverse: 5′-GCTTCAGGTGACCAC ATTCA- 3′. PCR was performed using a SsoAdvanced Universal SYBR Green Supermix kit (Bio-Rad, USA) by CFX Opus 96 Real-Time PCR System (Bio-Rad, USA). Expression levels of β-actin and Mrpl32 were used as double internal standards. Each experiment was performed in triplicate.

Western blot analysis

The relative levels of target proteins (MPO, iNOS, eNOS, protein carbonyl and 3-nitrotyrosine groups) were determined by western blot analysis. Protein lysates were prepared from liver samples in RIPA lysis buffer containing a cocktail of protease and phosphatase inhibitors (Sigma-Aldrich, USA) according to a standard protocol with subsequent sonication on ice and final addition of Laemmli buffer. Depending on the molecular weight of the target proteins, lysate proteins (60 μg per track) were separated by 10%–15% SDS-PAGE. After transferring the proteins to a nitrocellulose membrane, it was blocked with 5% skim milk or BSA for 1 h and then incubated overnight (+4°C) with the corresponding primary antibodies: MPO (1:1000; ab208670, Abcam, UK); 3-nitrotyrosine (1:500; A21285, Invitrogen, Thermo Fisher Scientific, USA); iNOS (1:500; ab15323, Abcam, UK), eNOS (1:500; ab76198, Abcam, UK). Afterwards, the membranes were incubated for 1 h at room temperature with the appropriate secondary antibodies conjugated with horseradish peroxidase (HRP) and then developed with HRP substrate-specific chemiluminescent agents, namely p-coumaric acid (Sigma-Aldrich, USA) and luminol (AppliChem GmbH, Germany). To measure protein carbonyl groups generated by protein oxidation, a Protein Carbonyl Assay Kit (ab178020, Abcam, UK) for western blot was used according to the manufacturer's protocol. Quantitation of immunoreactive signals was performed using Gel-Pro Analyzer v3.1 software and corrected for the corresponding β-actin levels, which were determined with anti-β-actin antibody (1:10000; A3854, Sigma-Aldrich, USA).

TABLE 1 Body weight, fasting blood glucose and HOMA-IR in rats with T2DM and after vitamin D_3 administration (1,000 IU/kg body weight, 30 days).

Parameter	Control	T2DM	T2DM + Vitamin D3
Weight, g	369.7 ± 12.7	383.4 ± 12.2	372.3 ± 10.5
Blood glucose, mmol/L	5.32 ± 0.12	13.10 ± 1.44*	11.00 ± 0.61#
HOMA-IR	0.70 ± 0.05	2.93 ± 0.17*	1.95 ± 0.12#

Note. All data are presented as means ± SD, n = 7; *$p < 0.05$, the T2DM group vs. the control group, #$p < 0.05$, the T2DM + VD group vs. the T2DM group.

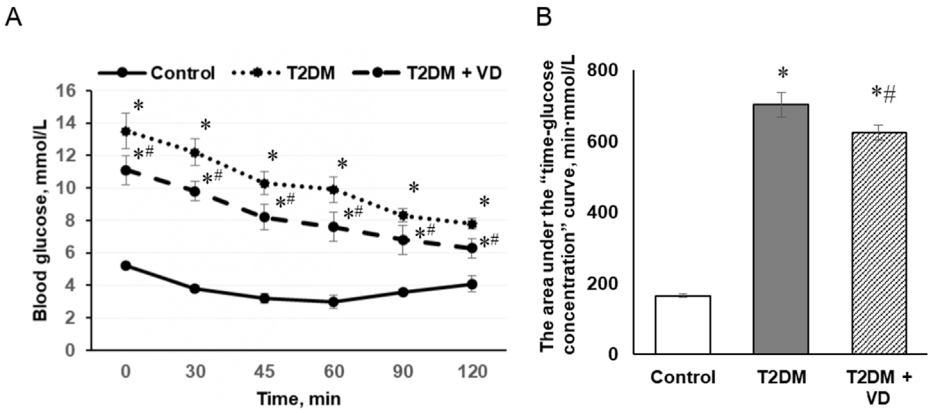

FIGURE 1
The effect of vitamin D_3 treatment (1,000 IU/kg body weight, 30 days) on the insulin tolerance test in male Wistar rats after 3-month HFD and a single injection of streptozotocin (25 mg/kg). **(A)** The concentration of blood glucose in dynamics after intraperitoneal injection of insulin (0.7 units/kg) to rats; **(B)** Bar graphs represent the area under the "time-glucose concentration" curve. The data are presented as means ± SD, n = 7; *$p < 0.05$, the T2DM group vs. the control group, #$p < 0.05$, the T2DM + vitamin D_3 group vs. the T2DM group.

NF-κB transcriptional activity

NF-κB p65 transcriptional activity was measured by a sensitive ELISA-based method using the NF-κB p65 Transcription Factor Assay Kit (ab133112, Abcam, UK). Briefly, freshly isolated rat liver nuclear extracts were added to the wells of a 96-well plate, incubated overnight at +4°C and washed. To determine the amount of NF-κB p65 bound to the NF-κB response elements of double-stranded DNA adsorbed at the bottom of the wells, samples were incubated for 1 h with NF-κB p65 primary antibody. After washing and subsequent 1 h incubation with HRP-conjugated secondary antibody followed by the development solution (for 45 min), OD (450 nm) was analyzed using a microplate reader.

Statistical analysis

We expressed the obtained data as the mean ± standard deviation (SD). For comparison of two experimental groups, Student's t-test was used, and one-way ANOVA followed by Tukey's post-hoc test was used to compare more than two groups. Differences were considered significant at $p < 0.05$.

Results

Vitamin D_3 partially improves hyperglycemia and insulin resistance in type 2 diabetes

In experimental type 2 diabetes, we observed a significant deterioration of carbohydrate homeostasis, which was confirmed by more than twofold increase in blood glucose levels (Table 1) and the development of insulin resistance (Figures 1A,B). Insulin resistance was assessed using an intraperitoneal exogenous insulin tolerance test. In diabetic animals, basal blood glucose levels after an overnight fast were shown to increase markedly at all time points following insulin administration (0.7 U/kg). Blood glucose in control rats after insulin injection reached a minimum at 45 min (2.63 mmol/L), while in animals with T2DM it was minimal only after 120 min (7.50 mmol/L). Calculations based on the ipITT revealed a nearly fourfold increase in the area under the curve in diabetes compared to the control group (Figure 1B), indicating a significant slowdown in glucose uptake by peripheral tissues as a result of insulin resistance. Furthermore, we found a 4.2-fold enhancement of HOMA-IR in rats fed a high-fat diet and given a single injection of STZ compared to control animals

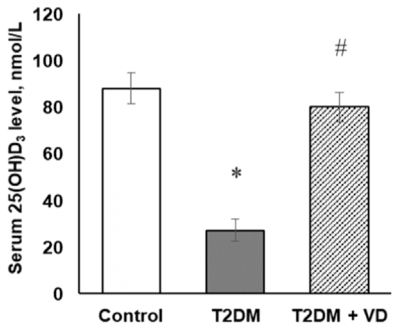

FIGURE 2
The serum level of 25-hydroxyvitamin D_3 (25(OH)D_3) of diabetic rats and after supplementation of vitamin D_3 (1,000 IU/kg body weight, 30 days). The data are presented as means ± SD, n = 7; *$p < 0.05$, the T2DM group vs. the control group, #$p < 0.05$, the T2DM + vitamin D_3 vs. the T2DM group.

(Table 1). This corresponds to increased resistance of cells and tissues to insulin and the progression of T2DM. Pharmacotherapy with vitamin D_3 (1000 IU/kg b.w., for 30 days), partially recovering the sensitivity of peripheral tissues to insulin, contributed to enhanced tissue utilization of glucose, which was manifested by mild compensation of hyperglycemia in animals with T2DM. Thus, the basal glucose level decreased by 16% in vitamin D_3-treated rats (Table 1). The study of glycemic response during the ipITT showed a 12% decrease in the area under the curve after cholecalciferol administration compared to the diabetic group of animals (Figure 1B). Vitamin D_3 also partially diminished the HOMA-IR index (by 33%).

Experimental type 2 diabetes is accompanied by vitamin D_3 deficiency

Maintaining adequate vitamin D_3 status prevents the development of numerous diseases, including both types of diabetes [26]. Therefore, we assessed serum 25(OH)D_3 levels as a main marker of vitamin D_3 bioavailability in animals. Measurement of baseline 25(OH)D_3 during random assignment of animals to control and diabetic groups before the onset of diabetes revealed no between-group differences. All animals were characterized by vitamin D_3 sufficiency (92.8 ± 6.3 nmol/L). Such homogeneity of the initial values of 25(OH)D_3 indicates the absence of systemic disturbances in the metabolism of vitamin D_3 and its bioavailability before experimental interventions, which allowed us to reliably assess the contribution of each factor (vitamin D_3 deficiency, prooxidation/inflammation, vitamin D_3 supplementation) to T2DM-induced changes in the liver. It was found that T2DM progression is accompanied by a threefold decrease in circulating 25(OH)D_3 compared to control rats, indicating the development of a D_3-deficient state in diabetic animals (Figure 2). Therapeutic intervention with vitamin D_3 in animals with type 2 diabetes almost completely normalized serum 25(OH)D_3 levels.

Vitamin D_3 inhibits reactive oxygen species formation and oxidative protein modifications in type 2 diabetic liver

Excessive formation of ROS and reactive nitrogen species (RNS) and the associated oxidative-nitrosative stress are currently considered as universal mechanism of detrimental changes in diabetes-related complications [27]. In order to clarify the possible contribution of prooxidative processes to hepatocellular dysfunction induced by type 2 diabetes, the level of free radical generation in primary hepatocyte culture, using the ROS-sensitive probe DCFH-DA, was investigated. We found that T2DM leads to elevated ROS formation in isolated hepatocytes (Figures 3A,B). This is evidenced by an increase in the fluorescence intensity of the oxidized form of the probe, DCF, by more than twofold compared to control animals. Pharmacotherapeutic application of vitamin D_3 reduced the level of hepatocellular ROS generation almost to the control level, which is consistent with available data on the protective antioxidant effect of this compound [28].

It is known that T2DM-associated hyperglycemia significantly increases the rate of formation of oxidatively modified (carbonylated) proteins, which reliably reflects the degree of oxidative stress. Intensification of carbonylated protein formation may be an important indicator of damage to cell structures in liver pathology. In this regard, we studied the level of covalently modified (carbonylated) proteins in the liver of diabetic animals that was 2.8-fold elevated compare to intact controls (Figures 3C,E). Cholecalciferol supplementation caused a moderate decrease in the level of protein carbonylation compared to diabetic rats.

An important enzyme that may play a role in oxidative stress is myeloperoxidase (MPO). Being directly involved in the antimicrobial activity of neutrophils and the defense of the body against various pathogens, primarily through participation in phagocytosis, MPO is released from leukocytes and catalyzes the formation of several reactive compounds, including hypochlorous acid (HOCl) and hypothiocyanic acid [29]. These compounds are involved in oxidative stress and post-translational modification of target proteins. Despite the importance of the antimicrobial function of innate immunity, unregulated release of MPO leads to tissue damage. Determination of the amount of MPO protein, one of the common markers of oxidative stress/inflammation, in the diabetic liver showed its increase by 1.7 times compared to the control (Figures 3D,E). An unexpected observation was that the administration of cholecalciferol further increased the expression of this prooxidant enzyme. The inconsistency of the obtained results necessitates the need for further studies to clarify the full

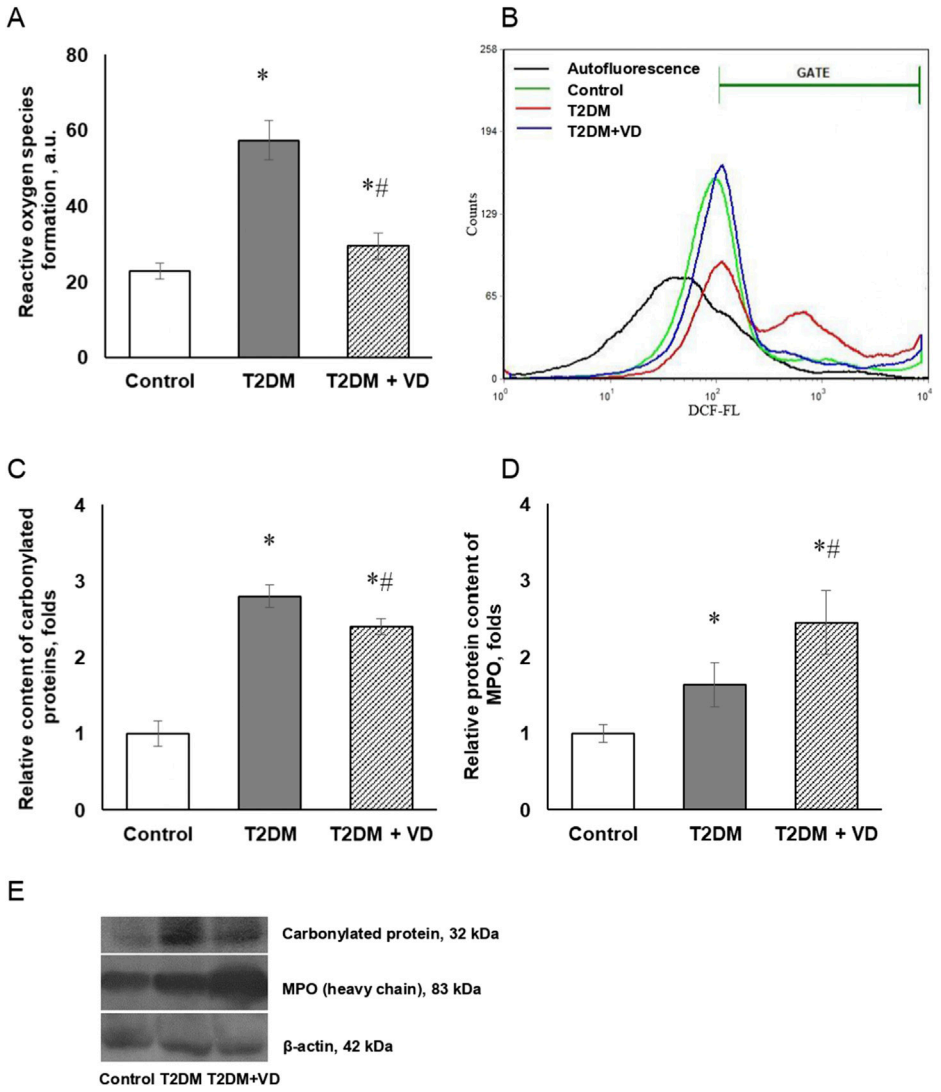

FIGURE 3
Reactive oxygen species formation and oxidative protein modifications in type 2 diabetic liver. Quantification of DCFH-DA oxidation in isolated rat hepatocytes documented by flow cytometry analysis **(A)** and representative histograms of DCF fluorescence **(B)** are shown. Relative content of carbonylated proteins **(C)** and MPO **(D)** in the liver of diabetic rats and after supplementation of vitamin D_3 (1,000 IU/kg body weight, 30 days) was determined by western blot analysis. Representative immunoblots **(E)** are shown. The data are presented as means ± SD, n = 7; $^*p < 0.05$, the T2DM group vs. the control group, $^{\#}p < 0.05$, the T2DM + vitamin D_3 vs. the T2DM group.

potential of vitamin D_3 in regulating myeloperoxidase activity in the studied pathology.

Vitamin D_3 attenuates nitric oxide and 3-nitrotyrosine levels while increasing iNOS and eNOS protein synthesis and NOS activity in diabetic rat liver

Using the NO-sensitive probe DAF-2DA, we demonstrated that T2DM induces a more than twofold elevation of NO synthesis in isolated hepatocytes (Figures 4A,B). Vitamin D_3 partially suppressed the intensity of nitric oxide formation. In accordance with the synergistic ability of NO and ROS to covalently modify protein molecules, tyrosine residues in the latter are sensitive targets for the active nitrating agent, peroxynitrite. Thus, the content of 3-nitrotyrosine is considered as a specific marker of peroxynitrite activity and associated oxidative-nitrosative stress [30]. Figures 4C,E shows immunoblotograms of the relative content of nitrated proteins in the liver tissue of diabetic animals, as well as under the action of vitamin D_3. In

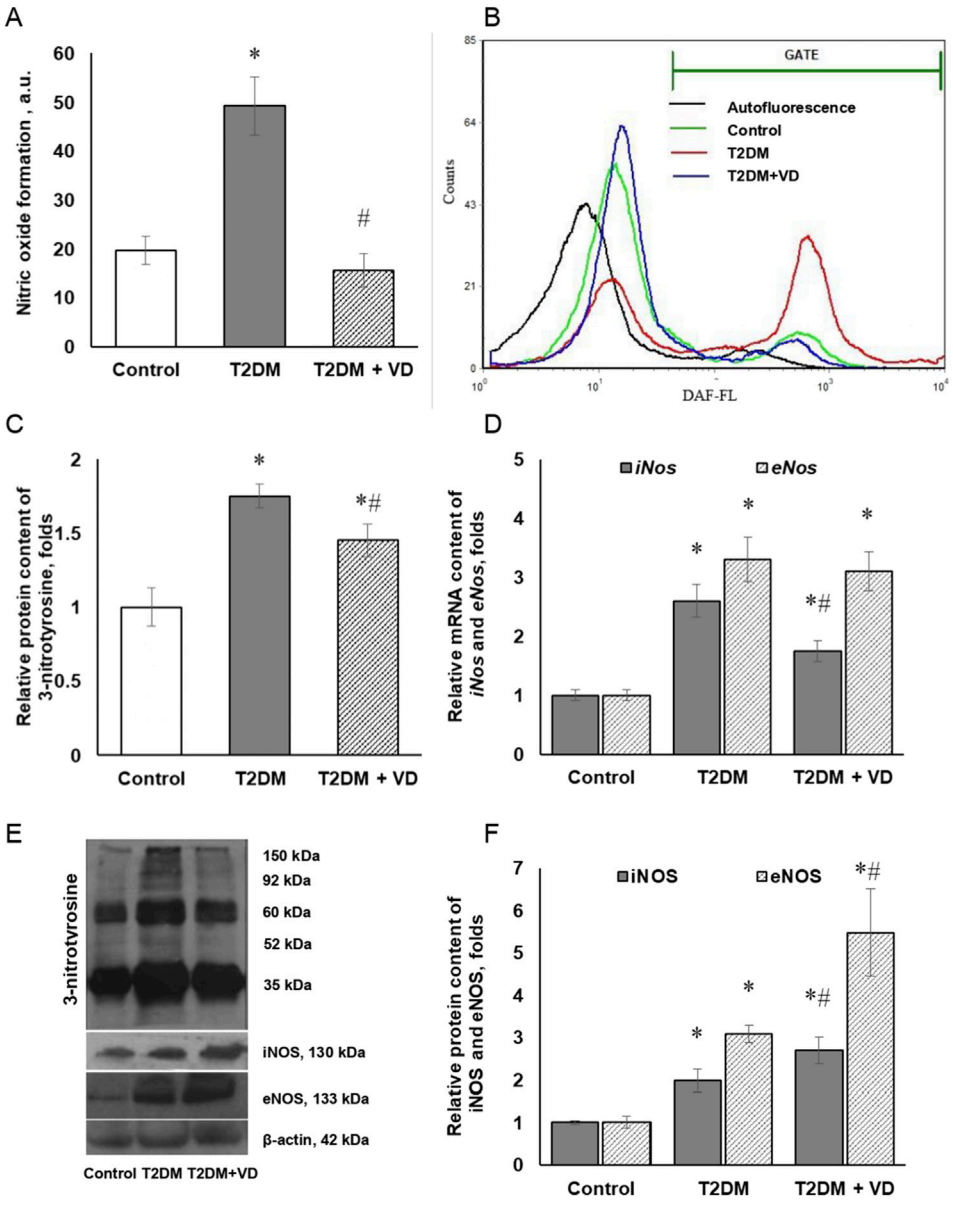

FIGURE 4
Nitric oxide formation in isolated rat hepatocytes in type 2 diabetic liver and effect of vitamin D_3 administration. Quantification of DAF oxidation documented by flow cytometry analysis **(A)** and representative histograms of DAF fluorescence **(B)** are shown. Relative protein level of 3-nitrotyrosine **(C)**, iNOS and eNOS mRNA **(D)** and protein content **(F)**, as well as their representative immunoblots **(E)** are shown in the liver of diabetic rats and after vitamin D_3 treatment (1,000 IU/kg body weight, 30 days). The data are presented as means ± SD, n = 7; *p < 0.05, the T2DM group vs. the control group, #p < 0.05, the T2DM + vitamin D_3 group vs. the T2DM group.

the liver of diabetic rats, an increased content of protein macromolecules with 3-nitrotyrosine moieties (1.7 times) was found compared to the control group, clearly highlighting the development of oxidative-nitrosative stress. Cholecalciferol supplementation reduced the content of nitrotyrosylated proteins by 20% compared to the diabetic group. Remarkably, the findings of other authors showed a link between vitamin D_3 deficiency in rats and the development of nitrosative stress, associated with increased formation of 3-nitrotyrosine [31].

In the liver, the inducible and endothelial NO synthase isoforms are the key enzymes responsible for nitric oxide synthesis. Diabetes-associated liver disorders were characterized by a strong elevation of their expression at both transcriptional and translational levels. We showed, respectively, a 2.7- and 3.3-fold upregulation of iNOS and

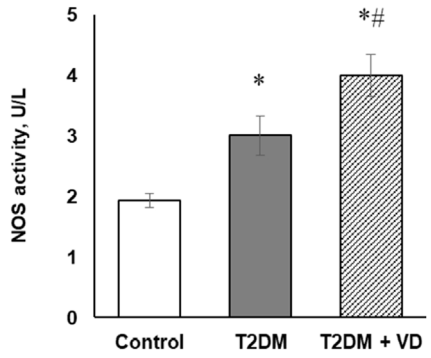

FIGURE 5
The enzymatic NOS activity in the liver of diabetic rats and after supplementation of vitamin D_3 (1,000 IU/kg body weight, 30 days). The data are presented as means ± SD, n = 7; *p < 0.05, the T2DM group vs. the control group, #p < 0.05, the T2DM + vitamin D_3 group vs. the T2DM group.

eNOS mRNA expression (Figure 4D) in the liver of diabetic rats that paralleled by an equally profound increase in their protein levels (2.1- and 3.2-fold, respectively), Figures 4E,F. The upregulated NOS levels align with our findings of increased NO production as well as the formation of 3-nitrotyrosine residues within oxidatively modified proteins. These changes were also found to positively correlate with the enhancement of overall NOS enzymatic activity (1.5-fold) in the liver tissue of diabetic rats (Figure 5). While partially abrogating T2DM-associated increase in iNOS mRNA (1.58-fold) and leaving eNOS mRNA expression unchanged (Figure 4D), vitamin D_3 supplementation contributed to a further significant enhancement of iNOS and eNOS protein synthesis (1.45- and 1.92-fold, respectively) in comparison with the diabetic state (Figures 4E,F). As shown in Figure 5, the discovered increase in iNOS and eNOS protein synthesis correlated with the elevated NOS enzymatic activity in diabetes and under the influence of vitamin D_3.

Vitamin D_3 hepatoprotective effects involve modulation of pro-inflammatory/anti-inflammatory cytokine and transforming growth factor expression

Cytokines and growth factors are capable of inducing different cellular mechanisms leading to NOS induction. In particular, inflammatory cytokines can act as triggers that switch NO synthesis from constitutive to inducible [15]. Cytokine involvement and disruption of inflammatory cell interactions are also among the "kindling mechanisms" of the concept of eNOS uncoupling in the development of inflammation and vascular dysfunction [12]. We have shown that diabetes-associated upregulation of the iNOS and eNOS mRNA and protein expression (Figure 4), described in the previous section, correlated with significantly higher mRNA transcript levels of pro-inflammatory cytokines such as TNF-α (tumor necrosis factor alpha) and IL-1β (interleukin 1 beta) by 3.5- and 2.2-fold, respectively (Figures 6A,B). Another important pro-inflammatory factor, which belongs to the group of CC-chemokines (β-chemokines), is MCP-1 (monocyte chemoattractant protein), or CCL2 (C-C motif ligand). This bioregulatory compound is the most potent factor of monocyte chemotaxis in mammals that controls the egress of cells from hematopoietic organs and their trafficking to the foci of inflammation [32]. MCP-1 was established to be involved in some mechanisms of insulin resistance, as well as liver fibrosis and a number of other pathologies associated with chronic inflammation. The results of our study indicate a profound increase in the protein content of this pro-inflammatory chemokine in the liver of diabetic rats, while it was not detected at all in control rats under these experimental conditions (data not shown).

The advanced diabetes-evoked synthesis of pro-inflammatory factors could be rescued by the formation of anti-inflammatory cytokines. In light of this, gene expression of such anti-inflammatory cytokines as IL-4 and IL-10, as well as TGF-β1 (transforming growth factor beta) in liver tissue was investigated. Our findings indicate that the diabetic state, against the background of intensified pro-inflammatory cytokines formation, is characterized by a significant 1.72- and 2.56-fold lowering of IL-4 (Figure 6C) and IL-10 (Figure 6D) mRNAs, respectively, with a 1.40-fold increase in the level of TGF-β1 mRNA (Figure 6E). Vitamin D_3 shifted the pro-inflammatory/anti-inflammatory balance towards the anti-inflammatory profile. The increase in the mRNA expression of IL-10 following vitamin D_3 administration was accompanied by a decrease in the levels of TNF-α and IL-1β mRNAs and MCP-1 protein. The expression level of IL-4 and TGF-β did not change under the influence of cholecalciferol compared to the diabetic group of animals.

Nuclear factor κB activation is implicated in type 2 diabetes-induced liver disorder and in the mechanism of hepatoprotection associated with vitamin D_3 treatment

Free radicals are known to activate the transcription factor NF-κB regardless of the mechanism and source of their formation [33]. Nuclear factor κB affects the function of many genes responsible for the immune response, inflammation, survival and programmed cell death, as well as for their proliferative activity. In particular, NF-κB has also been shown to indirectly or directly target induction of NOS

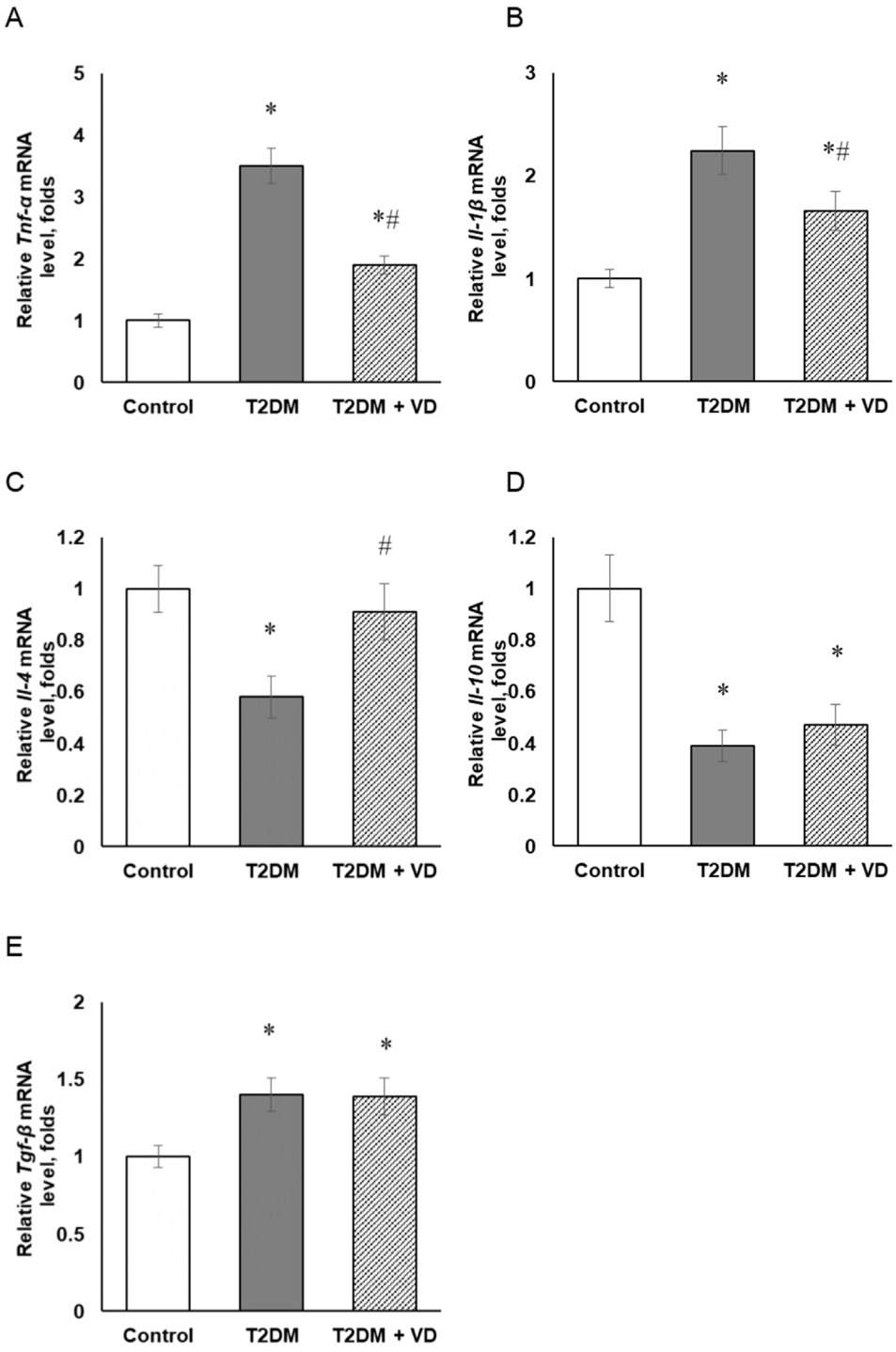

FIGURE 6
The relative gene expression of pro/anti-inflammatory cytokines in the liver tissue of rats with T2DM and after vitamin D_3 treatment (1,000 IU/kg body weight, 30 days). Relative mRNA content of *Tnf-α* **(A)**, *Il-1β* **(B)**, *Il-4* **(C)**, *Il-10* **(D)**, and *Tgf-β* **(E)** was determined by RT-qPCR. mRNA levels were adjusted to *β-actin* and *Mrpl32* expression. The data are presented as means ± SD, n = 7; *$p < 0.05$, the T2DM group vs. the control group, $^{\#}p < 0.05$, the T2DM + vitamin D_3 group vs. the T2DM group.

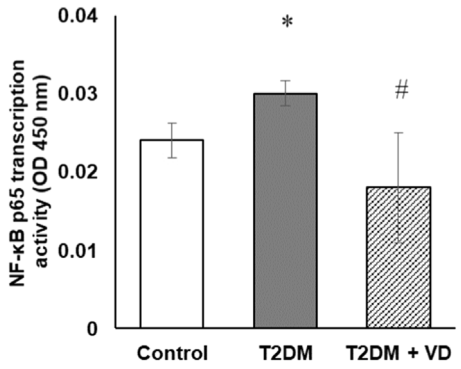

FIGURE 7
The NF-κB p65 transcription activity in the nuclear fraction of liver extracts of rats with T2DM and after vitamin D_3 treatment (1,000 IU/kg body weight, 30 days). Data are shown as means ± SD, n = 7; *$p < 0.05$, the T2DM group vs. the control group, #$p < 0.05$, the T2DM + vitamin D_3 group vs. the T2DM group.

promoters and downstream expression of NO synthases [34]. To confirm the potential involvement of NF-κB in the mechanism of liver dysfunction associated with T2DM, it was important to investigate the transcriptional activity of NF-κB and its correlation with the delineated changes in the expression of NO synthases and key cytokines involved in inflammation. The transcriptional activity of NF-κB was determined in nuclear extracts of liver cells by the ELISA method according to the level of its binding to the NF-κB-response element of double-stranded DNA fragments. Our study revealed a 24% increase in NF-κB transcriptional activity in diabetes compared to controls (Figure 7). Vitamin D_3 effectively reduced this activity to near control values.

Discussion

Oxidative stress, which is associated with a shift in the balance between reactive oxygen/nitrogen species generation and the efficiency of the antioxidant defense system towards the predominance of prooxidant processes, attracts the attention of researchers as one of the cornerstones of undesirable changes in the development of numerous chronic complications of T2DM, and MASLD is no exception. In the present study, we attempted to confirm the hypotheses that unbalanced nitric oxide metabolism in type 2 diabetes mellitus may facilitate and exacerbate oxidative damage to hepatocellular structures, and vitamin D_3 could be proposed as a therapeutic agent to manage diabetes-evoked liver disorders.

The ability of the NO molecule to exhibit cytoprotective or cytotoxic effects is known to depend on the cell type, its development phase and biochemical potential, as well as on the local concentration of NO and the presence of ROS. As recent studies highlight, the balance between the protective and cytotoxic effects of NO may be determined, among other factors, by the redox status of the cell [35, 36]. The cytotoxicity of the NO seems to be associated with excessive accumulation of superoxide anions in the lesion site, which, interacting with the NO molecule, form a potent mediator of oxidative cellular damage – peroxynitrite [30]. The latter is capable of oxidizing NH- and SH- groups of proteins, lipoproteins, DNA, leading to the loss of the native properties of these biomolecules. Reacting with metal ions, as part of SOD (superoxide dismutase), peroxynitrite causes the production of a reactive and highly toxic nitrosonium ion (NO_2^+), which, in turn, forms nitrophenols [37–39]. As a result, the functions of highly specialized protein molecules are disrupted. In the presence of peroxynitrite or its decay product, glutathiyl radical (GS·) is formed and, as a consequence, the latter is converted from an antioxidant into a prooxidant, initiating lipid peroxidation [40]. All this determines the cytotoxic effect of peroxynitrite, leading to cell death through apoptosis or necrosis [30, 38].

The level of 3-nitrotyrosine moieties within protein macromolecules is considered a specific and reliable marker of peroxynitrite activity [41]. The significant accumulation of nitrated proteins in liver tissue that we discovered, associated with overproduction of ROS and NO, along with an increase in the content of proteins with carbonylated groups and myeloperoxidase level, is quite convincing evidence of the development of oxidative-nitrosative stress in T2DM. In addition, increased peroxynitrite formation caused by diabetes most likely reduces the bioavailability of nitrogen oxide and interferes with the physiological effects of the latter in liver cells.

Nuclear factor κB, as a potent cellular redox sensor, appears to be highly sensitive to free radical formation. ROS and NO, regardless of the mechanism and source of their generation, activate NF-κB [33]. It is known that iNOS expression, which is mainly regulated at the transcriptional level, can be directly induced by activated NF-κB through its binding to the iNOS promoter containing NF-κB-binding sequence [42]. Moreover, multiple NF-κB enhancer elements have also been found upstream to the iNOS promoter, conferring inducibility to several signaling molecules [43]. Among such iNOS inducers, NF-κB mediates the expression of a number of growth factors, chemokines, and cytokines [34, 44]. Specifically, iNOS can be activated either by IFN-γ (interferon gamma) signal alone or by TNF-α in the presence of other signals [45, 46]. At the same time, the action of TGF-β is associated with a strong inhibitory effect on iNOS, whereas IL-4 and IL-10 are weak inhibitory signals [47, 48].

In contrast to iNOS, whose production is largely affected at the transcriptional level, constitutively expressed eNOS is subject to subtle post-transcriptional regulation according to its physiological role in signal transduction. These eNOS-mediated mechanisms link NO signaling cascades to its physiological functions in vascular endothelium, including vasorelaxation, angiogenesis, pro/anti-inflammatory balance of

endothelial cells, etc. [49]. In particular, eNOS expression is increased by TGF-β, estrogens, and, in some experiments, by exposure of endothelial cells to high glucose concentrations [50, 51]. Several studies have provided evidence that TNF-α and NF-κB activation can repress eNOS synthesis through post-transcriptional destruction of its mRNA without affecting eNOS promoter activity. Mechanistically, this involves NF-κB-dependent formation of specific microRNA targeting eNOS mRNA [52]. Whether activation of the NF-κB is a necessary step for eNOS induction at the transcriptional level is still debatable. However, several experimental studies have demonstrated that NF-κB activation is required for eNOS gene induction, and corresponding binding sites in the iNOS promoter have been identified [53].

Our study further develops the hypothesis that activation of NF-κB-associated signaling pathways may be one of the key events resulting in liver dysfunction at the cellular level in T2DM. In particular, insufficient nitric oxide bioavailability could be compensated by even greater intensification of its production, involving NF-κB-mediated expression of NO synthases and contributing to the formation of a vicious circle of amplified oxidative damage to biomolecules and inflammation with much more dangerous consequences for cellular function. In the present study, we found enhanced NF-κB activity accompanied by upregulated mRNA synthesis of pro-inflammatory cytokines and downregulated mRNA levels of anti-inflammatory cytokines in T2DM. These changes correlated with elevated expression of iNOS and eNOS at both transcriptional and translational levels. The findings are consistent with the data of other researchers on diabetes-evoked expression of the inducible form of NOS [54]. Regarding the expression of eNOS, the available literature data are contradictory and range from upregulated expression of this enzyme to reduced levels [55, 56]. Our results are not in line with the aforementioned role of TNF-induced NF-κB activation, which post-transcriptionally reduces eNOS levels [52]. Rather, they are consistent with the possibility of eNOS promoter activation by NF-κB at the transcriptional level of regulation. Although TGF-β expression increased under our experimental conditions, the level of its production is probably insufficient to effectively counteract the increased synthesis of NOSs.

Notably, nitric oxide is able to inhibit the expression of the iNOS gene by reducing the level of NF-κB in a culture of primary human and rat hepatocytes [57, 58]. These cells can produce NO in large quantities, and such physiological response seems to involve a negative feedback mechanism that serves to prevent unrestrained tissue damage. A similar mechanism is likely also relevant to the regulation of NF-κB activity in vascular endothelium mediated by eNOS. The resulting NO reduces the expression of the NOS genes, limiting the excessive formation of this metabolite under pathophysiological conditions. Apparently, this mechanism of switching off the stimulating effect of NF-κB on gene expression can be impaired under conditions of T2DM-associated liver pathology. Furthermore, it has been shown that NF-κB transcriptional activity largely depends on the intracellular redox state. In particular, the redox state of intracellular glutathione is believed to determine hepatocellular iNOS synthesis both *in vivo* and *in vitro* and this correlates with NF-κB activation [59]. Glutathione depletion prevented iNOS induction in hepatocytes, although this phenomenon has not been established in cells involved in the immune response during inflammation.

Our investigation revealed a significant, but not entirely unambiguous, modulating effect of vitamin D_3 on the functioning of the NO system in the diabetic liver. Vitamin D_3 appears to be effective in reducing ROS and NO generation in primary hepatocyte culture, which occurs in parallel with attenuation of 3-nitrotyrosine in liver tissue of diabetic rats.

However, the impact of cholecalciferol on the synthesis of eNOS and iNOS at the translational level, as well as on total NOS activity in liver tissue, was potentiating in relation to the effects of T2DM on these parameters. Although the increased production of nitric oxide by hepatocytes in diabetes was reduced by the action of vitamin D_3, its enhanced formation is possible due to the contribution of other types of liver cells. However, it remains unclear by which cells this generation of nitric oxide could occur and which NOS isoforms are involved in the intensification of its synthesis. Elevated NO levels are most likely not toxic for cells, because their formation takes place against the background of mitigated oxidative stress under the action of vitamin D_3. This is evidenced by a decrease in the intensity of ROS/NO generation in hepatocytes, as well as the accumulation of carbonylated and nitrated proteins in diabetic liver tissue after cholecalciferol treatment. Simultaneously, available literature highlights the ability of vitamin D_3 to positively affect the antioxidant capacity and the redox state of cells, in particular, the glutathione redox system [60]. The delineated upregulation of key NO-generating isoforms of liver NO synthase and an increase in the total activity of NOS are probably aimed at compensating for the reduced bioavailability of nitrogen oxide in diabetes and more effectively accomplishing its physiological functions in hepatocellular signaling.

Indeed, growing line of evidence suggests that NO is an important physiological regulator of hepatocyte function [15–17]. As is known, when hepatocytes are stimulated by inflammatory mediators or glucocorticoids, these cells secrete proteins characteristic of the acute phase of inflammation. It has been shown that NO generated by hepatocytes and resident macrophages (Kupffer cells) reduces the total production of these proteins [61]. Other studies confirm that in hepatocytes nitric oxide exerts an inhibitory effect on glucose metabolism that may have relevance in the context of its antidiabetic action. In particular, *in vitro* experiments have shown significant NO-dependent inhibition of glyceraldehyde-3-phosphate dehydrogenase in the liver of rats expressing high levels of

iNOS [62]. The ability of NO to inhibit hepatic gluconeogenesis in cell culture was also demonstrated [63]. Furthermore, hepatocyte-specific eNOS knockout was found to impair the energy-sensing ability of these cells and suppress the activation of the autophagy initiating factor ULK1, indicative of the novel role of eNOS in liver cell mitochondrial adaptation [64]. Higher amounts of NO produced by iNOS or exogenous nitric oxide are known to prevent apoptosis. Stimulated glutathione oxidation is thought to be a possible mechanism by which NO induces Hsp70 protein and provides protection against apoptosis triggered by TNF-α in cultured rat hepatocytes [65]. The ability of nitric oxide to nitrosylate thiols in the active sites of caspases and inhibit their activity is another potential mechanism for the modulation of apoptosis [66]. Finally, some evidence suggests the existence of a negative feedback mechanism by which DNA damage elicited by NO activates p53 expression that, in turn, blocks the iNOS gene promoter and iNOS expression [67].

The positive hepatoprotective effect of vitamin D_3 in the liver is in line with its inhibitory action on NF-κB transcriptional activity and the activity-dependent expression of pro-inflammatory cytokines. This function, on the one hand, can be mediated by the direct inhibitory effect of cholecalciferol on NF-κB, and also indirectly due to the normalization of oxidative metabolism and the suppression of ROS/RNS formation as strong inducers of this transcription factor. In turn, reduced expression and transcriptional activity of NF-κB attenuates the synthesis of pro-inflammatory cytokines and slows down cytokine-evoked nitric oxide formation. Studies by other authors also show that vitamin D_3 is a negative regulator of NF-κB transcriptional activity at the genomic level, the effects of which are mediated by vitamin D_3 receptor [68]. They demonstrated that VDR, through direct interaction with the IKKβ (inhibitory kappa B kinase beta), suppresses the canonical pathway of NF-κB activation. The uncovered discrepancy between iNOS protein and mRNA levels after taking vitamin D_3, respectively upregulate and downregulated, can be explained by probable changes in the stability of iNOS mRNA and protein at the post-transcriptional and post-translational levels of regulation [12].

We finally turn to the unexpected observation of a sustainable increase in myeloperoxidase protein expression after vitamin D_3 supplementation, which deserves a more detailed insight. Although the available scientific data generally describes an inverse correlation between $25(OH)D_3$ and myeloperoxidase levels, the detected elevation of MPO expression after vitamin D_3 treatment was not accompanied by an intensification of oxidative stress/inflammation, so we can conclude that MPO-mediated oxidation may play a minor role in the overall oxidative stress and low-grade metabolic inflammation in the liver of diabetic rats. Presumably, increased MPO synthesis under the influence of cholecalciferol can be associated with the functional activation of non-resident and resident macrophages, whose elevated phagocytic activity can help regenerative processes in liver tissue and improve insulin sensitivity. In particular, several lines of evidence implicate MPO and RNS in the oxidative modification of low-density lipoproteins, leading to their increased uptake by macrophages [69]. This suggestion aligns with our previous findings that vitamin D_3 may prevent the immunosuppressive effects of glucocorticoids by enhancing the efficiency of oxygen-dependent phagocytic mechanisms in peripheral blood neutrophils and monocytes, thereby increasing the functional activity of phagocytic cells [70]. Thus, the reduction in the propagation of prooxidative/inflammatory processes, in our opinion, may partly justify the stimulation of MPO sufficient to maintain adequate functioning of the innate immune system without MPO-associated tissue damage.

Notably, all metabolic disorders caused by T2DM were observed against the background of vitamin D_3 deficiency in diabetic rats, which can independently, as an additional pathogenic factor, contribute to the development of liver failure associated with diabetes. It should also be emphasized that, according to the most recent data, a link has been established between vitamin D_3 deficiency in animals and the propagation of nitrosative stress associated with increased formation of 3-nitrotyrosine in various tissues [31].

We conclude that experimental T2DM is associated with increased ROS and NO formation in primary hepatocyte culture, which is closely related to an increased NF-κB-dependent expression of inflammation markers and NOSs and is accompanied by the intensification of oxidative-nitrosative stress in rat liver. Our findings shed light on the hepatoprotective role of vitamin D_3 intervention, which modulates NF-kappaB activity and NOS expression/NO production, key hepatocellular responses to inflammatory mediators and oxidative stress associated with T2DM. These changes are likely to improve the bioavailability of NO for liver cells during vitamin D_3 supplementation. Further studies are required to definitively decipher the true significance of the aggravated stimulation of MPO, iNOS and eNOS synthesis following vitamin D_3 treatment that could help to better understand its protective effects in diabetes.

Author contributions

IS and MV designed the study; IS, OL, OM, VB, AS, AK, DL, TH, EP conducted the experiments; OL and DL processed and analyzed the obtained data; IS and MV provided the necessary reagents and animals; IS and OL drafted the manuscript; MV edited the manuscript. All authors contributed to the article and approved the submitted version.

Data availability

The raw data supporting the conclusions of this article will be made available by the authors, without undue reservation.

Ethics statement

All procedures with animals were carried out in accordance with national and international legislation and approved by the Animal Ethics Committee of the Palladin Institute of Biochemistry, Kyiv, Ukraine (protocol #5 dated 06/08/2022).

Funding

The author(s) declare that financial support was received for the research and/or publication of this article. This work was supported by the National Research Foundation of Ukraine (grant number 2021.01/0417).

Conflict of interest

The author(s) declared no potential conflicts of interest with respect to the research, authorship, and/or publication of this article.

Generative AI statement

The author(s) declare that no Generative AI was used in the creation of this manuscript.

References

1. Tinajero MG, Malik VS. An update on the epidemiology of type 2 diabetes: a global perspective. *Endocrinol Metab Clin North America* (2021) **50**(3):337–55. doi:10.1016/j.ecl.2021.05.013

2. Ciardullo S, Muraca E, Vergani M, Invernizzi P, Perseghin G. Advancements in pharmacological treatment of NAFLD/MASLD: a focus on metabolic and liver-targeted interventions. *Gastroenterol Rep* (2024) **12**:goae029. doi:10.1093/gastro/goae029

3. Qadri S, Yki-Järvinen H. Surveillance of the liver in type 2 diabetes: important but unfeasible? *Diabetologia* (2024) **67**(6):961–73. doi:10.1007/s00125-024-06087-7

4. Scoditti E, Sabatini S, Carli F, Gastaldelli A. Hepatic glucose metabolism in the steatotic liver. *Nat Rev Gastroenterol Hepatol* (2024) **21**(5):319–34. doi:10.1038/s41575-02300888-8

5. Hayashi T, Oe S, Miyagawa K, Kusanaga M, Ogino N, Honma Y, et al. Excess glucose alone induces hepatocyte damage due to oxidative stress and endoplasmic reticulum stress. *Exp Cell Res* (2024) **442**(2):114264. doi:10.1016/j.yexcr.2024.114264

6. Jakubek P, Pakula B, Rossmeisl M, Pinton P, Rimessi A, Wieckowski MR. Autophagy alterations in obesity, type 2 diabetes, and metabolic dysfunction-associated steatotic liver disease: the evidence from human studies. *Intern Emerg Med* (2024) **19**(5):1473–91. doi:10.1007/s11739-024-03700-w

7. Neira G, Becerril S, Valentí V, Moncada R, Catalán V, Gómez-Ambrosi J, et al. FNDC4 reduces hepatocyte inflammatory cell death via AMPKα in metabolic dysfunctionassociated steatotic liver disease. *Clin Nutr* (2024) **43**(9):2221–33. doi:10.1016/j.clnu.2024.08.007

8. Syed AA, Reza MI, Shafiq M, Kumariya S, Singh P, Husain A, et al. Naringin ameliorates type 2 diabetes mellitus-induced steatohepatitis by inhibiting RAGE/NF-κB mediated mitochondrial apoptosis. *Life Sci* (2020) **257**:118118. doi:10.1016/j.lfs.2020.118118

9. Kumar S, Duan Q, Wu R, Harris EN, Su Q. Pathophysiological communication between hepatocytes and non-parenchymal cells in liver injury from NAFLD to liver fibrosis. *Adv Drug Deliv Rev* (2021) **176**:113869. doi:10.1016/j.addr.2021.113869

10. Hu S, Han M, Rezaei A, Li D, Wu G, Ma X. L-Arginine modulates glucose and lipid metabolism in obesity and diabetes. *Curr Protein and Pept Sci* (2017) **18**(6):599–608. doi:10.2174/1389203717666160627074017

11. Santolini J. What does ldquo NO-Synthase rdquo stand for. *Front Biosci Landmark Ed* (2019) **24**(1):133–71. doi:10.2741/4711

12. Pautz A, Li H, Kleinert H. Regulation of NOS expression in vascular diseases. *Front Biosci Landmark Ed* (2021) **26**(5):85–101. doi:10.52586/4926

13. Martínez-Ruiz A, Araújo IM, Izquierdo-Álvarez A, Hernansanz-Agustín P, Lamas S, Serrador JM. Specificity in S-nitrosylation: a short-range mechanism for NO signaling? *Antioxid and Redox Signaling* (2013) **19**(11):1220–35. doi:10.1089/ars.2012.5066

14. Maher A, Abdel Rahman MF, Gad MZ. The role of nitric oxide from neurological disease to cancer. *Adv Exp Med Biol* (2017) **1007**:71–88. doi:10.1007/978-3-319-60733-7_5

15. Iwakiri Y, Kim MY. Nitric oxide in liver diseases. *Trends Pharmacol Sci* (2015) **36**(8):524–36. doi:10.1016/j.tips.2015.05.001

16. Zhang B, Lakshmanan J, Du Y, Smith JW, Harbrecht BG. Cell-specific regulation of iNOS by AMP-activated protein kinase in primary rat hepatocytes. *J Surg Res* (2018) **221**:104–12. doi:10.1016/j.jss.2017.08.028

17. McNaughton L, Puttagunta L, Martinez-Cuesta MA, Kneteman N, Mayers I, Moqbel R, et al. Distribution of nitric oxide synthase in normal and cirrhotic human liver. *Proc Natl Acad Sci U S A* (2002) **99**(26):17161–6. doi:10.1073/pnas.0134112100

18. Jin L, Gao H, Wang J, Yang S, Wang J, Liu J, et al. Role and regulation of autophagy and apoptosis by nitric oxide in hepatic stellate cells during acute liver failure. *Liver Int* (2017) **37**(11):1651–9. doi:10.1111/liv.13476

19. Aggeletopoulou I, Tsounis EP, Triantos C. Vitamin D and metabolic dysfunctionassociated steatotic liver disease (MASLD): novel mechanistic insights. *Int J Mol Sci* (2024) **25**(9):4901. doi:10.3390/ijms25094901

20. Argano C, Mirarchi L, Amodeo S, Orlando V, Torres A, Corrao S. The role of vitamin D and its molecular bases in insulin resistance, diabetes, metabolic syndrome, and cardiovascular disease: state of the art. *Int J Mol Sci* (2023) **24**(20):15485. doi:10.3390/ijms242015485

21. MacGirlley R, Phoswa WN, Mokgalaboni K. Modulatory properties of vitamin D in type 2 diabetic patients: a focus on inflammation and dyslipidemia. *Nutrients* (2023) **15**(21):4575. doi:10.3390/nu15214575

22. Carlberg C, Raczyk M, Zawrotna N. Vitamin D: a master example of nutrigenomics. *Redox Biol* (2023) **62**:102695. doi:10.1016/j.redox.2023.102695

23. Gong J, Gong H, Liu Y, Tao X, Zhang H. Calcipotriol attenuates liver fibrosis through the inhibition of vitamin D receptor-mediated NF-κB signaling pathway. *Bioengineered* (2022) **13**(2):2658–72. doi:10.1080/21655979.2021.2024385

24. Quan QL, Yoon KN, Lee JS, Kim EJ, Lee DH. Impact of ultraviolet radiation on cardiovascular and metabolic disorders: the role of nitric oxide and vitamin D. *Photodermatol Photoimmunology and Photomed* (2023) **39**(6):573–81. doi:10.1111/phpp.12914

25. Lisakovska O, Shymanskyy I, Mazanova A, Khomenko A, Veliky M. Vitamin D_3 protects against prednisolone-induced liver injury associated with the impairment of the hepatic NF-κB/iNOS/NO pathway. *Biochem Cell Biol* (2017) **95**(2):213–22. doi:10.1139/bcb-20160070

26. Kawahara T, Okada Y, Tanaka Y. Vitamin D efficacy in type 1 and type 2 diabetes. *J Bone Miner Metab* (2024) **42**(4):438–46. doi:10.1007/s00774-024-01509-3

27. Jomova K, Raptova R, Alomar SY, Alwasel SH, Nepovimova E, Kuca K, et al. Reactive oxygen species, toxicity, oxidative stress, and antioxidants: chronic diseases and aging. *Arch Toxicol* (2023) **97**(10):2499–574. doi:10.1007/s00204-023-03562-9

28. Vázquez-Lorente H, Herrera-Quintana L, Jiménez-Sánchez L, Fernández-Perea B, Plaza-Diaz J. Antioxidant Functions of Vitamin D and CYP11A1-derived vitamin D, tachysterol, and lumisterol metabolites: mechanisms, clinical implications, and future directions. *Antioxidants (Basel)* (2024) **13**(8):996. doi:10.3390/antiox13080996

29. Degotte G, Frederich M, Francotte P, Franck T, Colson T, Serteyn D, et al. Targeting myeloperoxidase activity and neutrophil ROS production to modulate redox process: effect of ellagic acid and analogues. *Molecules* (2023) **28**(11):4516. doi:10.3390/molecules28114516

30. Pérez-Torres I, Manzano-Pech L, Rubio-Ruíz ME, Soto ME, Guarner-Lans V. Nitrosative Stress and its association with cardiometabolic disorders. *Molecules* (2020) **25**(11):2555. doi:10.3390/molecules25112555

31. Keeney JTR, Förster S, Sultana R, Brewer LD, Latimer CS, Cai J, et al. Dietary vitamin D deficiency in rats from middle to old age leads to elevated tyrosine nitration and proteomics changes in levels of key proteins in brain: implications for low vitamin Ddependent age-related cognitive decline. *Free Radic Biol Med* (2013) **65**:324–34. doi:10.1016/j.freeradbiomed.2013.07.019

32. Ji X, Yang L, Zhang Z, Zhang K, Chang N, Zhou X, et al. Sphingosine 1phosphate/microRNA-1249-5p/MCP-1 axis is involved in macrophage-associated inflammation in fatty liver injury in mice. *Eur J Immunol* (2020) **50**(11):1746–56. doi:10.1002/eji.201948351

33. Morgan MJ, Liu ZG. Crosstalk of reactive oxygen species and NF-κB signaling. *Cell Res* (2011) **21**(1):103–15. doi:10.1038/cr.2010.178

34. Xie QW, Kashiwabara Y, Nathan C. Role of transcription factor NF-kappa B/Rel in induction of nitric oxide synthase. *J Biol Chem* (1994) **269**(7):4705–8. doi:10.1016/s0021-9258(17)37600-7

35. Chakraborty S, Choudhuri A, Mishra A, Bhattacharyya C, Billiar TR, Stoyanovsky DA, et al. Nitric oxide and thioredoxin modulate the activity of caspase 9 in HepG2 cells. *Biochim Biophys Acta (BBA) - Gen Subjects* (2023) **1867**(11):130452. doi:10.1016/j.bbagen.2023.130452

36. Magnifico MC, Xhani M, Popov M, Saso L, Sarti P, Arese M. Nonylphenol and octylphenol differently affect cell redox balance by modulating the nitric oxide signaling. *Oxidative Med Cell Longevity* (2018) **2018**:1684827. doi:10.1155/2018/1684827

37. Piacenza L, Zeida A, Trujillo M, Radi R. The superoxide radical switch in the biology of nitric oxide and peroxynitrite. *Physiol Rev* (2022) **102**(4):1881–906. doi:10.1152/physrev.00005.2022

38. Campolo N, Issoglio FM, Estrin DA, Bartesaghi S, Radi R. 3-Nitrotyrosine and related derivatives in proteins: precursors, radical intermediates and impact in function. *Essays Biochem* (2020) **64**(1):111–33. doi:10.1042/ebc20190052

39. Hughes MN. Relationships between nitric oxide, nitroxyl ion, nitrosonium cation and peroxynitrite. *Biochim Biophys Acta (BBA) - Bioenerg* (1999) **1411**(2-3):263–72. doi:10.1016/s0005-2728(99)00019-5

40. Madrasi K, Joshi MS, Gadkari T, Kavallieratos K, Tsoukias NM. Glutathiyl radical as an intermediate in glutathione nitrosation. *Free Radic Biol Med* (2012) **53**(10):1968–76. doi:10.1016/j.freeradbiomed.2012.08.013

41. Bandookwala M, Sengupta P. 3-Nitrotyrosine: a versatile oxidative stress biomarker for major neurodegenerative diseases. *Int J Neurosci* (2020) **130**(10):1047–62. doi:10.1080/00207454.2020.1713776

42. Li Y, Li X, He K, Li B, Liu K, Qi J, et al. C-peptide prevents NF-κB from recruiting p300 and binding to the iNOS promoter in diabetic nephropathy. *FASEB J* (2018) **32**(4):2269–79. doi:10.1096/fj.201700891R

43. Guo Z, Shao L, Du Q, Park KS, Geller DA. Identification of a classic cytokineinduced enhancer upstream in the human iNOS promoter. *FASEB J* (2007) **21**(2):535–42. doi:10.1096/fj.06-6739com

44. Schwentker A, Vodovotz Y, Weller R, Billiar TR. Nitric oxide and wound repair: role of cytokines? *Nitric Oxide* (2002) **7**(1):1–10. doi:10.1016/s1089-8603(02)00002-2

45. Lubina-Dąbrowska N, Stepień A, Sulkowski G, Dąbrowska-Bouta B, Langfort J, Chalimoniuk M. Effects of IFN-β1a and IFN-β1b treatment on the expression of cytokines, inducible NOS (NOS type II), and myelin proteins in animal model of multiple sclerosis. *Arch Immunol Ther Exp (Warsz)* (2017) **65**(4):325–38. doi:10.1007/s00005-017-0458-6

46. Wahl SM, McCartney-Francis N, Chan J, Dionne R, Ta L, Orenstein JM. Nitric oxide in experimental joint inflammation. *Cells Tissues Organs* (2003) **174**(1-2):26–33. doi:10.1159/000070572

47. Takaki H, Minoda Y, Koga K, Takaesu G, Yoshimura A, Kobayashi T. TGF-β1 suppresses IFN-γ-induced NO production in macrophages by suppressing STAT1 activation and accelerating iNOS protein degradation. *Genes to Cells* (2006) **11**(8):871–82. doi:10.1111/j.1365-2443.2006.00988.x

48. Saini R, Singh S. Inducible nitric oxide synthase: an asset to neutrophils. *J Leukoc Biol* (2018) **105**(1):49–61. doi:10.1002/JLB.4RU0418-161R

49. Janaszak-Jasiecka A, Płoska A, Wierońska JM, Dobrucki LW, Kalinowski L. Endothelial dysfunction due to eNOS uncoupling: molecular mechanisms as potential therapeutic targets. *Cell Mol Biol Lett* (2023) **28**(1):21. doi:10.1186/s11658-023-00423-2

50. Wei Y, Yuan P, Zhang Q, Fu Y, Hou Y, Gao L, et al. Acacetin improves endothelial dysfunction and aortic fibrosis in insulin-resistant SHR rats by estrogen receptors. *Mol Biol Rep* (2020) **47**(9):6899–918. doi:10.1007/s11033-020-05746-3

51. Lin F, Yang Y, Wei S, Huang X, Peng Z, Ke X, et al. Hydrogen sulfide protects against high glucose-induced human umbilical vein endothelial cell injury through activating PI3K/Akt/eNOS pathway. *Drug Des Dev Ther* (2020) **14**:621–33. doi:10.2147/DDDT.S242521

52. Kim S, Shim S, Kwon J, Ryoo S, Byeon J, Hong J, et al. Alleviation of preeclampsia-like symptoms through PlGF and eNOS regulation by hypoxia- and NF-κB-responsive miR-214-3p deletion. *Exp Mol Med* (2024) **56**(6):1388–400. doi:10.1038/s12276-024-01237-8

53. Davis ME, Grumbach IM, Fukai T, Cutchins A, Harrison DG. Shear stress regulates endothelial nitric-oxide synthase promoter activity through nuclear factor κB binding. *J Biol Chem* (2004) **279**(1):163–8. doi:10.1074/jbc.M307528200

54. Bahadoran Z, Mirmiran P, Ghasemi A. Adipose organ dysfunction and type 2 diabetes: role of nitric oxide. *Biochem Pharmacol* (2024) **221**:116043. doi:10.1016/j.bcp.2024.116043

55. Shati AA, Maarouf A, Dawood AF, Bayoumy NM, Alqahtani YA, A Eid R, et al. Lower extremity arterial disease in type 2 diabetes mellitus: metformin inhibits femoral artery ultrastructural alterations as well as vascular tissue levels of AGEs/ET-1 axis-mediated inflammation and modulation of vascular iNOS and eNOS expression. *Biomedicines* (2023) **11**(2):361. doi:10.3390/biomedicines11020361

56. Desrois M, Clarke K, Lan C, Dalmasso C, Cole M, Portha B, et al. Upregulation of eNOS and unchanged energy metabolism in increased susceptibility of the aging type 2 diabetic GK rat heart to ischemic injury. *Am J Physiology-Heart Circulatory Physiol* (2010) **299**(5):H1679–86. doi:10.1152/ajpheart.00998.2009

57. Siendones E, Fouad D, Díaz-Guerra MJM, de la Mata M, Boscá L, Muntané J. PGE1induced NO reduces apoptosis by D-galactosamine through attenuation of NF-kappaB and NOS-2 expression in rat hepatocytes. *Hepatology* (2004) **40**(6):1295–303. doi:10.1002/hep.20448

58. Smith BC, Fernhoff NB, Marletta MA. Mechanism and kinetics of inducible nitric oxide synthase auto-S-nitrosation and inactivation. *Biochemistry* (2012) **51**(5):1028–40. doi:10.1021/bi201818c

59. Tirmenstein MA, Nicholls-Grzemski FA, Schmittgen TD, Zakrajsek BA, Fariss MW. Glutathione-dependent regulation of nitric oxide production in isolated rat hepatocyte suspensions. *Antioxid and Redox Signaling* (2000) **2**(4):767–77. doi:10.1089/ars.2000.2.4-767

60. Fathi FEZM, Sadek KM, Khafaga AF, Al Senosy AW, Ghoniem HA, Fayez S, et al. Vitamin D regulates insulin and ameliorates apoptosis and oxidative stress in pancreatic tissues of rats with streptozotocin-induced diabetes. *Environ Sci Pollut Res* (2022) **29**(60):90219–29. doi:10.1007/s11356-022-22064-2

61. Curran RD, Ferrari FK, Kispert PH, Stadler J, Stuehr DJ, Simmons RL, et al. Nitric oxide and nitric oxide-generating compounds inhibit hepatocyte protein synthesis. *FASEB J* (1991) **5**(7):2085–92. doi:10.1096/fasebj.5.7.1707021

62. Muronetz VI, Medvedeva MV, Sevostyanova IA, Schmalhausen EV. Modification of glyceraldehyde-3-phosphate dehydrogenase with nitric oxide: role in signal transduction and development of apoptosis. *Biomolecules* (2021) **11**(11):1656. doi:10.3390/biom11111656

63. Dai Z, Wu Z, Yang Y, Wang J, Satterfield MC, Meininger CJ, et al. Nitric oxide and energy metabolism in mammals. *Biofactors* (2013) **39**(4):383–91. doi:10.1002/biof.1099

64. Cunningham RP, Moore MP, Dashek RJ, Meers GM, Jepkemoi V, Takahashi T, et al. Hepatocyte-specific eNOS deletion impairs exercise-induced adaptations in hepatic mitochondrial function and autophagy. *Obesity (Silver Spring)* (2022) **30**(5):1066–78. doi:10.1002/oby.23414

65. Kim YM, de Vera ME, Watkins SC, Billiar TR. Nitric oxide protects cultured rat hepatocytes from tumor necrosis factor-alpha-induced apoptosis by inducing heat shock protein 70 expression. *J Biol Chem* (1997) **272**(2):1402–11. doi:10.1074/jbc.272.2.1402

66. Maejima Y, Adachi S, Morikawa K, Ito H, Isobe M. Nitric oxide inhibits myocardial apoptosis by preventing caspase-3 activity via S-nitrosylation. *J Mol Cell Cardiol* (2005) **38**(1):163–74. doi:10.1016/j.yjmcc.2004.10.012

67. Zhang YQ, Ding N, Zeng YF, Xiang YY, Yang MW, Hong FF, et al. New progress in roles of nitric oxide during hepatic ischemia reperfusion injury. *World J Gastroenterol* (2017) **23**(14):2505–10. doi:10.3748/wjg.v23.i14.2505

68. Chen Y, Zhang J, Ge X, Du J, Deb DK, Li YC. Vitamin D receptor inhibits nuclear factor κB activation by interacting with IκB kinase β protein. *J Biol Chem* (2013) **288**(27):19450–8. doi:10.1074/jbc.M113.467670

69. Delporte C, Van Antwerpen P, Vanhamme L, Roumeguère T, Zouaoui Boudjeltia K. Low-density lipoprotein modified by myeloperoxidase in inflammatory pathways and clinical studies. *Mediators Inflamm* (2013) **2013**:1–18. doi:10.1155/2013/971579

70. Shymanskyy IO, Lisakovska OO, Mazanova AO, Riasniy VM, Veliky MM. Effects of vitamin D_3 and vitamin E on prednisolone-induced alterations of phagocyte function. *Eur Rev Med Pharmacol Sci* (2016) **20**(7):1379–83.

EBM Experimental Biology and Medicine

TYPE Original Research
PUBLISHED 04 August 2025
DOI 10.3389/ebm.2025.10544

OPEN ACCESS

*CORRESPONDENCE
Wenqun Xi,
xiwq125@126.com
Weihua Yang,
benben0606@139.com

RECEIVED 24 February 2025
ACCEPTED 18 July 2025
PUBLISHED 04 August 2025

CITATION
Li C, Lu Y, Chen M, Zhang Q, Zhang Z, Xi W and Yang W (2025) Dietary-related characteristics and cataract risk: evidence from a mendelian randomization study.
Exp. Biol. Med. 250:10544.
doi: 10.3389/ebm.2025.10544

Dietary-related characteristics and cataract risk: evidence from a mendelian randomization study

Chen Li[1], Yicheng Lu[1], Mingxuan Chen[2], Qing Zhang[3], Zhe Zhang[3], Wenqun Xi[3]* and Weihua Yang[3]*

[1]Department of Ophthalmology, The First Affiliated Hospital of Soochow University, SuZhou, Jiangsu, China, [2]School of Clinical Medicine, Medical College of Soochow University, SuZhou, Jiangsu, China, [3]Shenzhen Eye Hospital, Shenzhen Eye Medical Center, Southern Medical University, Shenzhen, China

Abstract

Cataract is the leading cause of blindness globally, imposing a significant socioeconomic burden. While diet is associated with various eye diseases, the causal relationship between dietary-related characteristics (DRCs) and cataract remains unclear. This study investigates the causal associations between DRCs and cataract using Mendelian randomization (MR) to provide insights into potential dietary interventions for cataract prevention. We conducted a two-sample MR analysis using data from the open GWAS database, focusing on individuals of European descent. Instrumental variables were selected based on stringent criteria, and multiple MR methods were applied to estimate causal effects. Sensitivity analyses assessed the robustness of the findings. Significant causal associations were found between oily fish intake (OR = 0.86) and variation in diet (OR = 1.26) with cataract. Sensitivity analyses supported the robustness of these findings. Mediation effect analysis suggested that the intake of oily fish might indirectly influence cataract risk through metabolites. This study provides evidence for causal relationships between specific DRCs and cataract, highlighting the potential role of dietary interventions in cataract prevention.

KEYWORDS

cataract, dietary-related characteristics, mendelian randomization, causal relationship, prevention strategy

Impact statement

This study provides the first Mendelian randomization evidence for causal relationships between oily fish intake, dietary variation, and cataract, enabling targeted dietary strategies for high-risk populations.

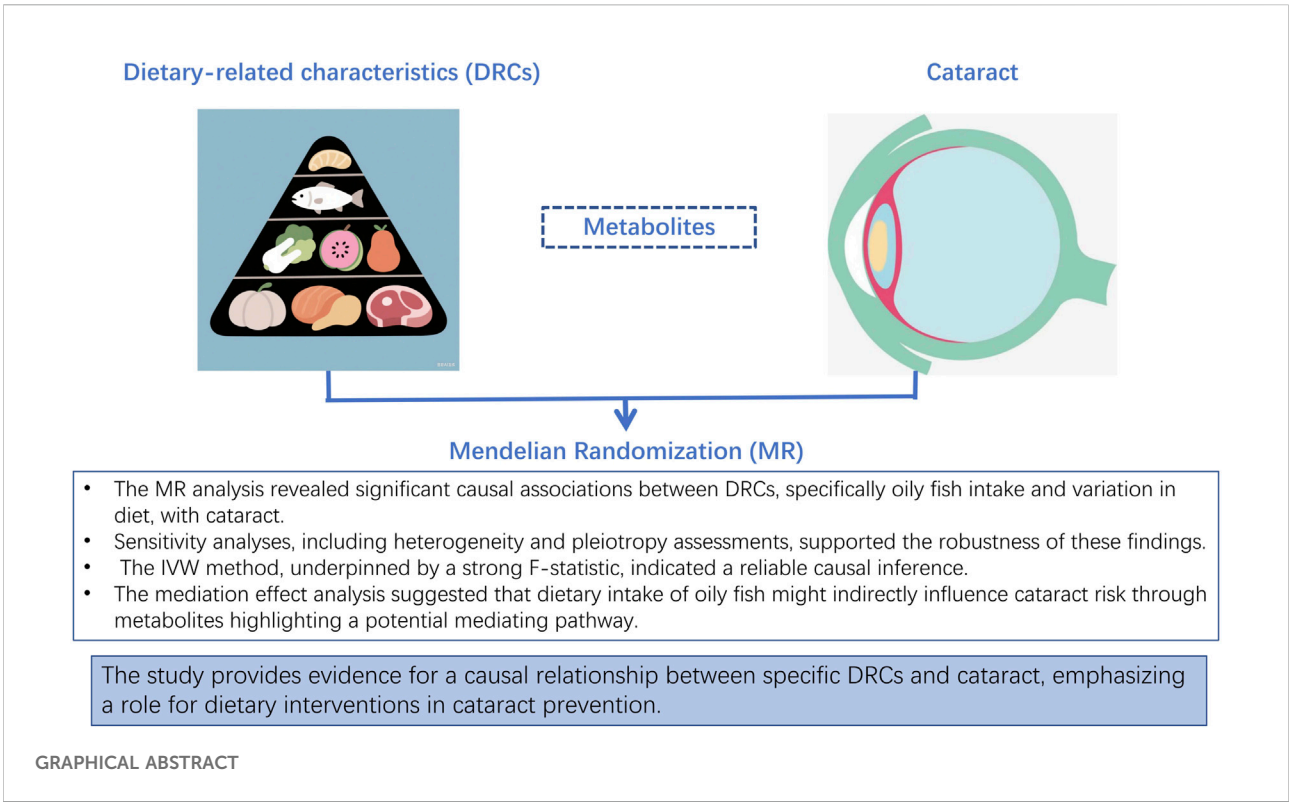

GRAPHICAL ABSTRACT

Introduction

Cataracts are a leading cause of blindness globally, affecting approximately 17.01 million people and causing severe visual impairment in 83.48 million individuals by 2020. They impose a substantial burden on patients and society [1]. Aging is the primary cause of cataract development, but genetic predisposition, environmental factors, and lifestyle choices also increase the risk. Currently, cataracts are mainly treated surgically, which involves risks and economic burdens. There are no effective medications to prevent or treat moderate to severe cataracts [2].

Dietary intake is associated with various eye diseases, including cataracts [3–7]. Studies have shown that a high intake of carbohydrates and polyunsaturated fatty acids increases the risk of cortical and nuclear cataracts, while a high intake of protein, especially animal protein, has a protective effect against posterior subcapsular cataracts [6]. Compared with those who consume large amounts of meat, vegetarians have a lower risk of cataracts, indicating that plant-based diets are protective [8]. The dietary pattern of "dairy and vegetables" and traditional dietary patterns are negatively correlated with the occurrence of cataracts. In contrast, high-carbohydrate and monosaccharide diets increase the risk [9]. Dietary factors may influence cataracts by affecting lens oxidative stress, and higher antioxidant intake may reduce the incidence and severity of cataracts [10]. However, the causal relationship between diet and cataracts remains unclear.

In this study, we used data from the GWAS database and employed a two-sample Mendelian randomization (MR) approach to investigate the causal relationship between dietary-related characteristics (DRCs) and cataract risk, focusing on individuals of European descent. Our analysis included selecting single nucleotide polymorphisms (SNPs) associated with DRCs as instrumental variables (IVs), using various MR methods to estimate causal relationships, and conducting sensitivity analyses to ensure robustness. This study aims to identify dietary factors that influence cataract risk and provide strategies for dietary interventions and non-surgical treatments.

Materials and methods

Data sources

All data in this study were obtained from publicly available databases. The GWAS data were downloaded from the Open GWAS database[1] [11]. GWAS data for dietary-related

Abbreviations: MR, Mendelian randomization; DRCs, dietary-related characteristics; SNPs, single nucleotide polymorphisms; IVs, instrumental variables; MVMR, Multivariable Mendelian Randomization.

1 https://gwas.mrcieu.ac.uk/

TABLE 1 Data sources and characteristics.

Data type	Description	Sample size	Source	Validation method
DRCs	Genetic variants associated with dietary habits (e.g., "Oily fish intake"; "Variation in diet")	Oily fish intake (N = 460,443); Variation in diet (N = 460,884)	Open GWAS database	GWAS data analysis
Cataracts	Case-control data for cataracts derived from GWAS database (GBE ID: ebi-a-GCST90018814)	39,519 cases and 452,358 controls	Open GWAS database	GWAS data analysis
Covariates (e.g., diabetes, age, smoking)	Data sources and validation methods for covariates including diabetes, age, and smoking	finn-b-DIABETES_FG (218,792 (36,219 cases and 182,573 controls)); ukb-b-8727 (N = 170,248); finn-b-SMOKING (138,088 (1321 cases and 136,767 controls))	Literature and public databases	Literature review and GWAS data analysis

characteristics were acquired by searching for the keywords "diet" or "intake" and were derived from European ancestry samples. The relevant data are in Supplementary Table S1. The cataract GWAS data (ebi-a-GCST90018814) included 39,519 cases and 452,358 controls, also based on European ancestry populations. We identified cataract risk factors through a literature review and obtained data for diabetes, age, and smoking [12–14], all based on European samples. Additionally, we acquired data for 249 metabolites by searching for "met-d," selecting European individuals, and presented the data in Supplementary Table S2. Table 1 provides an overview of the GWAS data characteristics, including population information, sample size, sources, and validation approaches. The report follows the STROBE-MR Statement guidelines. This study uses open-source data, so there are no ethical issues or conflicts of interest. The study design is shown in Figure 1.

Instrument selection and strength assessment

Initially, SNPs from the exposure GWAS with a statistical significance threshold of $P < 5 \times 10^{-6}$ were considered, prioritizing those with the strongest evidence of association. Additionally, we identified SNPs in linkage disequilibrium. To mitigate the potential bias introduced by weak IVs, the F-statistic was employed as a quantitative measure of instrument strength. An F-statistic threshold of 10 was established and the formula for the F-statistic is as follows:

$$F = \frac{N-k-1}{k} \times \frac{R^2}{1-R^2}$$

Where R^2 is the coefficient of determination from the regression of the exposure on the IV, k denotes the number of IV used, and N is the sample size.

MR causal effect estimation

Multiple two-sample MR methods were employed to estimate the causal effect of DRCs on cataract, including IVW, MR-Egger, weighted median, simple mode, and weight mode. Besides, we use the Steiger directionality test from the TwoSampleMR package to determine the direction of causality. The same methods are applied to assess the potential causal effect of the outcome on the exposure for reverse causality.

Sensitivity analysis

Sensitivity analysis includes heterogeneity assessment, pleiotropy assessment, and leave-one-out analysis. First, we used the Cochran Q test to evaluate the heterogeneity between SNP estimates. The statistically significant result of the Cochran Q test suggests the presence of significant heterogeneity in our analysis results. We further quantified the proportion of heterogeneity using the I^2 statistic. The calculation formula for I^2 values is as follows:

$$I^2 = \frac{Q-df}{Q} \times 100\%$$

Subsequently, we employed the MR-Egger method to test for pleiotropy in the IVs. In addition, by sequentially removing individual SNPs and calculating the MR results for the remaining IVs, we assessed whether the SNP affects the association between DRCs and cataract.

Multivariable mendelian randomization (MVMR) analysis and mediation effect estimation

We conducted individual and overall MVMR analyses on cataract-related risk factors, such as diabetes, age, and smoking, along with DRCs obtained post-screening, to determine the direct

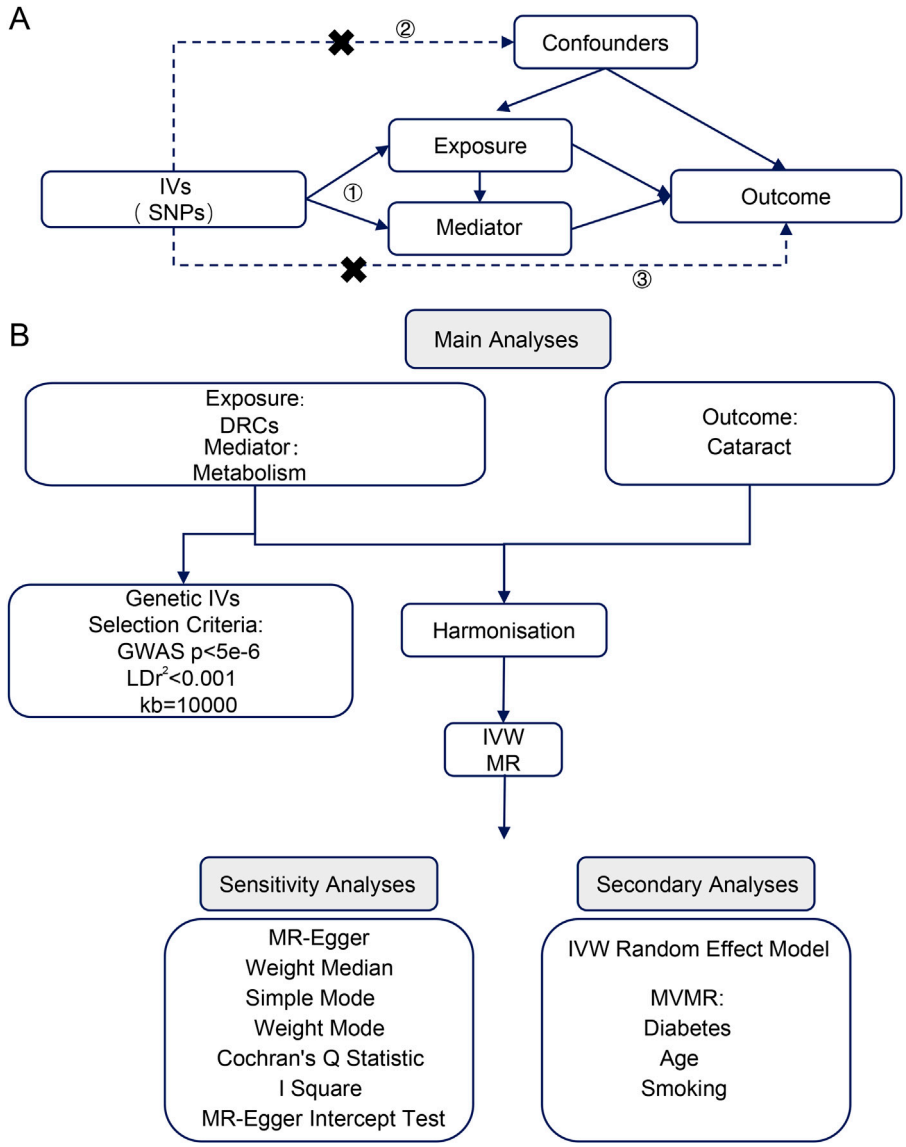

FIGURE 1
(A) Key assumptions of Mendelian randomization analysis. **(B)** Flowchart of the analytical methodology in this study. IVs, instrumental variables; SNPs, single nucleotide polymorphisms; DRCs, dietary-related characteristics; IVW, inverse variance weighted; MR, Mendelian randomization; GWAS, genome wide association study; LD, linkage disequilibrium; MR-Egger, Mendelian randomization-Egger. MVMR, multivariable Mendelian randomization.

effects of these DRCs on cataract. The mediation effect's estimates and standard errors are calculated using the following formula:

$$\beta_M = \beta_A \times \beta_B$$

$$SE_M = \sqrt{(\beta_A \times SE_B)^2 + (\beta_B \times SE_A)^2 + SE_A^2 \times SE_B^2}$$

β_M represent the mediated effect size, β_A represent the MR effect of DRCs on metabolites, β_B represent the direct effect of metabolites on cataract obtained via MVMR, SE_M represent the standard error of the mediation effect, SE_A represent the standard error of the MR analysis for DRCs on metabolites, and SE_B represent the standard error of the MR analysis for metabolites on cataract.

Statistical analysis

All computations and statistical evaluations were conducted utilizing R (version 4.2.2) [15]. In the context of MR analysis examining the effects of exposures on outcomes, OR and 95%

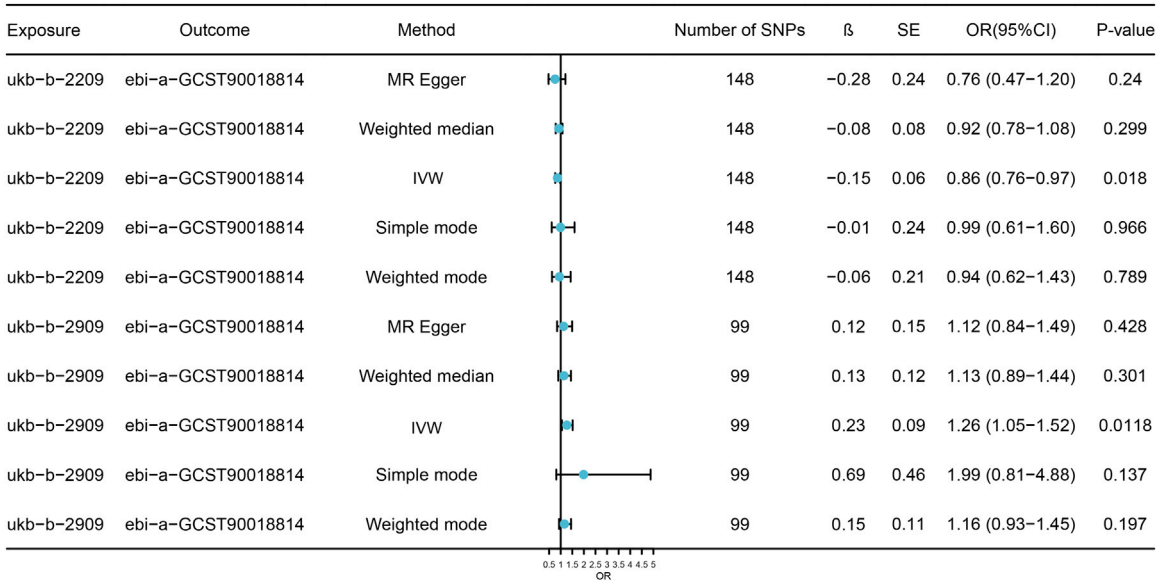

FIGURE 2
Model analysis results of the MR analysis of DRCs and cataract. Forest figure displays MR model related to DRC and the causal relation analysis result of cataract, effect evaluation value with the OR and 95% CI show, at the same time show the model using IV number and calculating the Beta values and standard error. SNPs, single nucleotide polymorphisms; SE, standard error; OR, odds ratio; CI, confidence interval; β, Mendelian randomization analysis effect coefficient; IVW, Inverse variance weighted.

confidence intervals served as the primary metrics for evaluation. All statistical P-values were obtained from two-tailed tests; SNPs identified in GWAS were deemed statistically significant at a threshold of $P < 5 \times 10^{-6}$, whereas other statistical assessments were considered significant at $P < 0.05$.

Results

Tool variable selection

Figure 1 illustrates the technical roadmap of this study. Based on the selection criteria for IVs in this study, SNPs with linkage disequilibrium were excluded, and SNPs related to DRC that matched the GWAS data for cataract were included as IVs. Supplementary Table S3 presents the outcomes of the IV selection for each indicator, highlighting only those indicators that exhibited significant results in the MR analysis. The F-statistic associated with the IVs for these indicators exceeds the threshold of 10, suggesting that the majority of SNPs identified in this study function as robust effect IVs.

Estimation of causal effects

The IVW model results for the relationship between DRCs and cataract indicate that oily fish intake (OR = 0.86, 95%CI: 0.76–0.97) and variation in diet (OR = 1.26, 95%CI:1.05–1.52), two DRCs have a significant causal association with cataract. These results indicate that increased intake of oily fish is associated with a reduced risk of cataracts, suggesting a protective effect. In contrast, greater dietary diversity is significantly associated with an elevated risk of cataracts, with statistical significance (Supplementary Table S4; Figure 2). Funnel plots (Figures 3A,B) and scatter plots (Figures 3C,D) for the five models of the relationship between DRCs and cataract illustrate the linear relationship between the effects of two DRCs with a high number of SNPs and the effects on cataract. It could be observed that the fit lines of the scatter plots for the five models are generally in the same direction, with most models having consistent slopes, and the intercept of the IVW model is close to zero.

Sensitivity analysis

The Cochran Q test and I^2 statistic evaluated heterogeneity of significant results (Supplementary Table S5), showing moderate heterogeneity in MR findings for oily fish intake and diet variation related to cataract (both $P < 0.05$). MR-Egger regression tested horizontal pleiotropy at the IV level; each indicator's intercept P-values exceeded 0.05 and were near zero, indicating study causal inferences were unaffected by horizontal pleiotropy (Supplementary Table S6). A leave-one-out sensitivity analysis revealed no substantial changes in DRC effect estimates, suggesting result stability (Supplementary Table S7). The

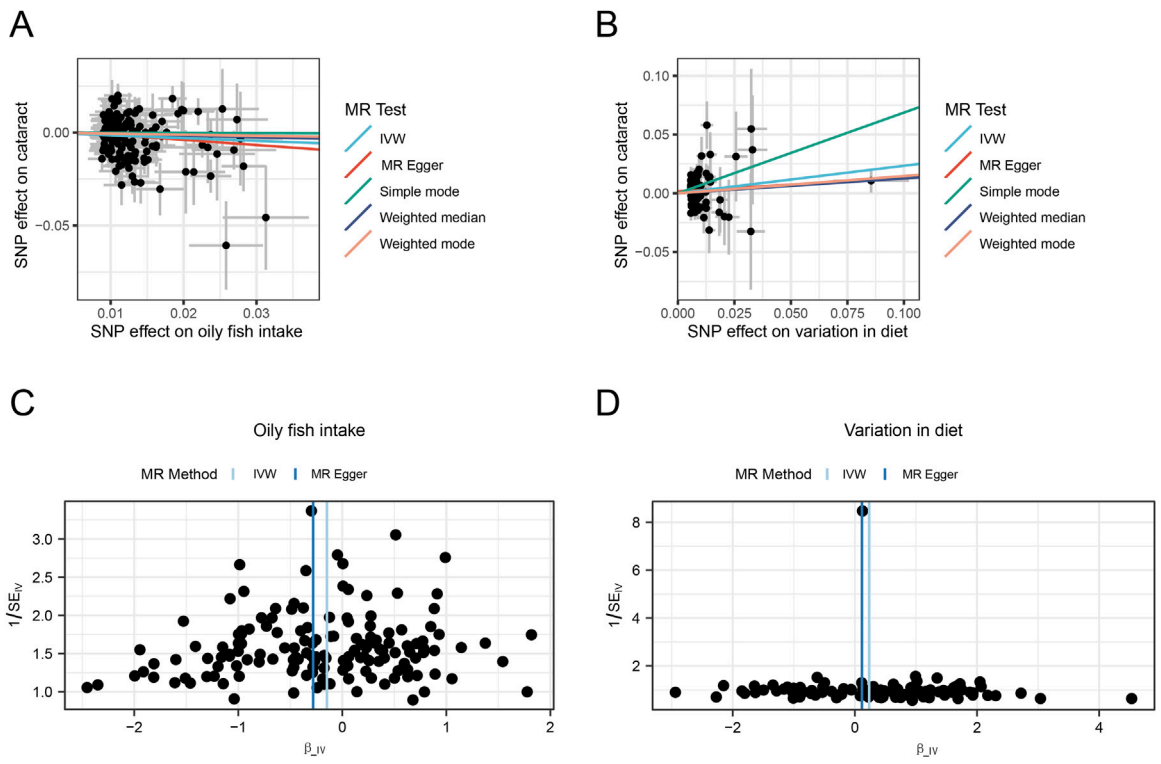

FIGURE 3
MR analysis of the causal relationship between DRCs and cataract. **(A,B)** Scatter plot showing the causal relationship between dietary patterns and cataract, with the slope of the line indicating the magnitude of the causal relationship predicted by the different models; **(C,D)** Funnel chart showing dietary pattern and causation of cataract. SNPs, single nucleotide polymorphisms; SE, standard error; OR, odds ratio; CI, confidence interval; IVW, Inverse variance weighted.

Steiger directionality test assessed the causal link from DRCs to cataract (Supplementary Table S8). Results indicated SNPs explained more variance for exposure than for the outcome, with a TRUE direction and $P < 0.05$, signifying significant and accurate directionality.

Reverse MR analysis

To assess reverse causality, we utilized cataract as the exposure and DRCs as the outcome, employing a GWAS of cataract with a SNP selection criterion of $P < 5 \times 10^{-6}$; SNPs in linkage disequilibrium were selected. The results of the reverse MR analysis indicate that cataract does not have a significant causal effect on DRCs ($P > 0.05$), as shown in Figure 4; Supplementary Table S9.

MVMR analysis

We incorporated relevant risk factors for cataract, including diabetes, age, and smoking, into multivariate MR analysis along with two DRCs to assess the direct effects of these DRCs on cataract. We constructed models by pairing each of the cataract-related risk factors with the two DRCs to predict the relationship with the outcome, resulting in MVMR models. We obtained three meaningful MVMR models (Supplementary Table S10), and the results showed that these risk factors have significant causal effects on cataract in Models 1, 2, and 3 ($P < 0.05$).

Mediation effect analysis

We first used the Steiger directionality test to determine the causal direction from two DRCs through metabolites (Supplementary Table S11). Results showed that for both DRCs, SNPs explained more variance for exposure than for outcome risk factors, with a TRUE direction and $P < 0.05$. We then assessed the mediation effect in MVMR models where the mediator significantly affected the outcome (Supplementary Table S12). In Models 1–4, DRCs significantly impacted cataract ($P < 0.05$), indicating a partial mediation effect via metabolites. Using univariate MR results, we determined the causal effect sizes of DRCs

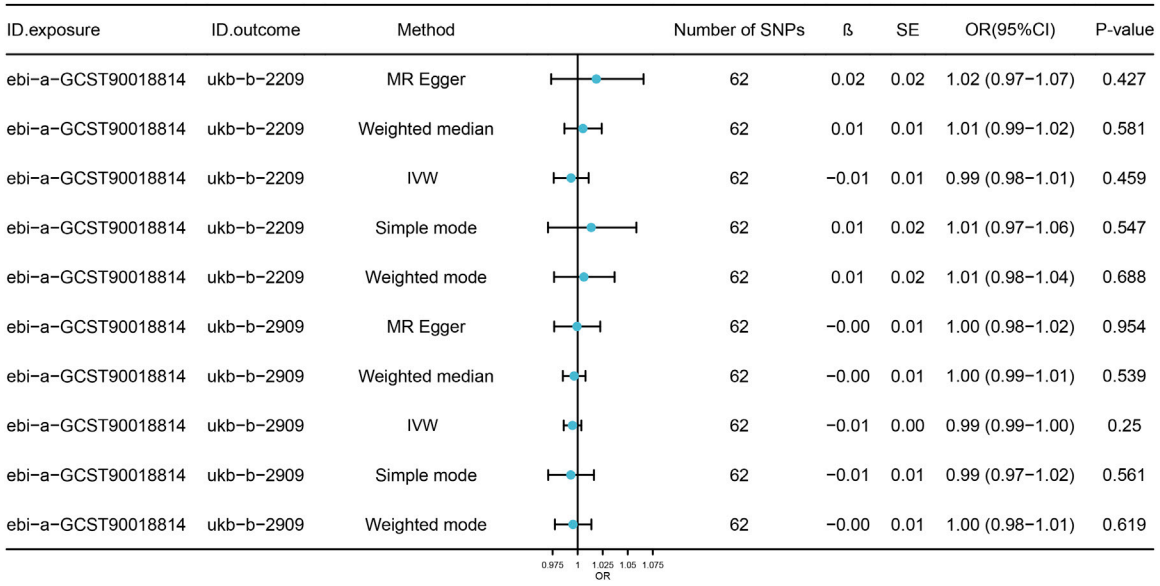

ID.exposure	ID.outcome	Method	Number of SNPs	ß	SE	OR(95%CI)	P-value
ebi-a-GCST90018814	ukb-b-2209	MR Egger	62	0.02	0.02	1.02 (0.97-1.07)	0.427
ebi-a-GCST90018814	ukb-b-2209	Weighted median	62	0.01	0.01	1.01 (0.99-1.02)	0.581
ebi-a-GCST90018814	ukb-b-2209	IVW	62	-0.01	0.01	0.99 (0.98-1.01)	0.459
ebi-a-GCST90018814	ukb-b-2209	Simple mode	62	0.01	0.02	1.01 (0.97-1.06)	0.547
ebi-a-GCST90018814	ukb-b-2209	Weighted mode	62	0.01	0.02	1.01 (0.98-1.04)	0.688
ebi-a-GCST90018814	ukb-b-2909	MR Egger	62	-0.00	0.01	1.00 (0.98-1.02)	0.954
ebi-a-GCST90018814	ukb-b-2909	Weighted median	62	-0.00	0.01	1.00 (0.99-1.01)	0.539
ebi-a-GCST90018814	ukb-b-2909	IVW	62	-0.01	0.00	0.99 (0.99-1.00)	0.25
ebi-a-GCST90018814	ukb-b-2909	Simple mode	62	-0.01	0.01	0.99 (0.97-1.02)	0.561
ebi-a-GCST90018814	ukb-b-2909	Weighted mode	62	-0.00	0.01	1.00 (0.98-1.01)	0.619

FIGURE 4
Model analysis results of reverse causality MR analysis of DRCs. The forest plots show the results of reverse causality analysis of multiple MR models for cataract and DRCs. The estimated effect values are presented as OR and 95%CI. The number of IVs used in each model, as well as the calculated Beta values and standard errors, are also shown. SNPs, single nucleotide polymorphisms; OR, odds ratio; SE, standard error; CI, confidence interval; β, Mendelian randomization analysis effect coefficient; IVW, Inverse variance weighted.

on metabolites. From the MVMR analysis, we obtained direct and indirect effect sizes of metabolites on cataract development. We calculated the mediation effect sizes of DRCs on cataract incidence through metabolites (Supplementary Table S13). The results show that oily fish intake has an indirect effect on cataract through total lipids in medium high-density lipoprotein with an effect size of −0.00419. The indirect effect accounts for 2.84% of the direct effect (|−0.00419/−0.05798|*100%).

Discussion

Cataract is the leading cause of blindness globally, significantly impacting individuals' quality of life and socio-economic frameworks. However, the influence of dietary factors on cataract incidence and progression remains unclear. This study employed MR to investigate the causal relationships between dietary risk factors and cataract development. Our findings revealed a significant causal link between oily fish consumption and cataract formation, suggesting a protective effect. Oily fish is a rich source of long-chain omega-3 polyunsaturated fatty acids, such as eicosapentaenoic acid and docosahexaenoic acid [16]. Previous studies have shown that higher consumption of long-chain omega-3 fats, particularly in women, reduces the risk of cataract extraction surgery [17]. In contrast, dietary variation increased cataract risk. Monolithic dietary structures, like the Mediterranean diet and the Korean Balanced Diet, rich in unsaturated fatty acids, antioxidants, and plant-based products, have been shown to reduce ARC incidence [18–20]. Additionally, specific vitamin dosages may slow cataract formation [21]. The MVMR analysis indicated that diabetes, age, and smoking significantly impact cataract development. Diabetes approximately doubles cataract occurrence, while smoking cessation reduces its incidence, especially among the elderly [22]. Mediation analysis suggested that oily fish intake indirectly affects cataract risk through total lipids in medium HDL. Higher HDL cholesterol levels, influenced by long-chain n-3 PUFAs, are beneficial in reducing ARC risk [23].

In this two-sample MR study, the IVW method was primarily used to assess the causal relationship between dietary risk factors and cataract. The IVW model's intercept was close to zero, and fitting curves were consistent across models, indicating a robust causal relationship [24]. The Weighted median and MR-Egger methods were used as supplementary tests. The MR-Egger regression intercept was close to zero, indicating no horizontal pleiotropy and good independence of selected SNPs.

To further validate the authenticity and robustness of our results, we conducted multiple sensitivity analyses, including Cochran's Q test to assess heterogeneity, the MR-Egger method to detect horizontal pleiotropy, and leave-one-out analysis to confirm result consistency. Additionally, we

performed Steiger directionality tests, which demonstrated that the variance explained by our selected IVs aligned with the expected causal direction, further strengthening the credibility of our causal inference. Simultaneously, in the reverse MR analysis, we evaluated the potential effect of cataracts on dietary-related characteristics. No significant causal relationship was observed, supporting the reliability of our findings. Furthermore, in MVMR analyses, we accounted for confounding factors such as diabetes, age, and smoking, which further confirmed the direct effects of dietary-related characteristics on cataract risk.

Heterogeneity testing revealed moderate heterogeneity in the MR analysis of oily fish intake and dietary variation, possibly due to gene-environment interactions. Gene-environment interactions may be an important contributing factor. For example, genetic variations in the metabolism of omega-3 fatty acids from fish differ across populations [25, 26], and dietary diversity can also lead to interindividual differences in nutrient absorption and utilization efficiency [27]. Additionally, environmental factors such as geographic location, cultural dietary habits, and lifestyle behaviors (e.g., smoking, alcohol consumption) may further exacerbate heterogeneity. For instance, specific genetic variants interact with fish intake in influencing metabolic disease risk-such as the association between fish consumption and TM6SF2 gene variants in modulating non-alcoholic fatty liver disease risk. Conversely, in other populations, environmental exposures may attenuate these effects [28]. Future studies should incorporate additional environmental covariates and gene-environment interaction terms to more comprehensively elucidate the sources of heterogeneity.

Our MVMR analysis identified smoking as an independent risk factor for cataracts, an association potentially mediated through chronic inflammation and epigenetic mechanisms. Emerging evidence indicates that smoking significantly upregulates GPR15 (an orphan receptor involved in immune regulation) and induces its hypomethylation [29]. Genome-wide transcriptomic analyses further demonstrate elevated GPR15 expression in peripheral blood of both male and female smokers, where this receptor promotes systemic chronic inflammation by modulating T-cell migration [30]. Given that lens oxidative stress and protein denaturation are central to cataract pathogenesis, GPR15-mediated sustained inflammatory microenvironments may accelerate lens epithelial cell damage. This molecular mechanism strongly aligns with our observed smoking-cataract association and concurrently provides a theoretical basis for the protective effects of dietary factors (e.g., ω-3 fatty acids in oily fish) through anti-inflammatory pathways. Future studies should explore GPR15's potential as both a biomarker and therapeutic target for smoking-associated cataracts.

Notably, although obesity or body weight (e.g., BMI) is considered a potential confounder in the relationship between certain dietary factors and cataract risk, our analysis-based on publicly available GWAS databases-primarily centered on dietary-related exposures and outcomes, precluding direct adjustment for BMI or weight. However, the strength of MR lies in its ability to mitigate phenotypic confounding bias, including obesity, at the genetic level. The independence of our selected instrumental variables helps reduce potential bias arising from unadjusted weight-related factors. Furthermore, obesity is closely correlated with other included risk factors like diabetes, the effects of which are partially accounted for in the multivariable model. Future studies with larger samples and more comprehensive multivariable analyses may further elucidate the joint effects of weight/BMI and dietary factors on cataract risk, providing deeper insights into the complex interplay between diet, obesity, and cataract development. It is noteworthy that other modifiable lifestyle factors, such as BMI and physical activity, have also been implicated in cataract risk. However, the analytical framework of this study primarily focused on elucidating the causal relationship between dietary-related characteristics and cataracts, and thus did not conduct in-depth analyses of BMI, physical activity, or other related factors. Future research should further investigate the causal associations and underlying mechanisms linking BMI, physical activity, and other lifestyle factors to cataract risk, thereby strengthening the scientific foundation for comprehensive cataract prevention and control strategies.

The study's limitations include a limited sample size, focus on European descent, and reliance on MR methods without wet-lab validation. Future research should include larger, multi-ethnic cohorts, longitudinal designs, and wet-lab experiments to verify the molecular pathways through which dietary factors influence cataract development.

In conclusion, this study provides new insights into the relationship between dietary risk factors and cataract, highlighting the protective role of oily fish and the potential risk associated with dietary variation. These findings offer a foundation for future prevention strategies and emphasize the need to explore the mediating roles of metabolites and their biological mechanisms.

Author contributions

CL: Writing – original draft, Writing – review and editing, Methodology, Supervision. YL: Writing – original draft, Writing – review and editing, Conceptualization, Investigation, Software. MC: Data curation, Methodology, Writing – original draft, Writing – review and editing. QZ: Data curation, Methodology, Writing – original draft, Writing – review and editing. ZZ: Data curation, Methodology,

Writing – original draft, Writing – review and editing. WX: Conceptualization, Investigation, Software, Writing – original draft, Writing – review and editing. WY: Conceptualization, Investigation, Software, Writing – original draft, Writing – review and editing.

Data availability

The original contributions presented in the study are included in the article/Supplementary Material, further inquiries can be directed to the corresponding authors.

Funding

The author(s) declare that no financial support was received for the research and/or publication of this article.

Conflict of interest

The author(s) declared no potential conflicts of interest with respect to the research, authorship, and/or publication of this article.

Generative AI statement

The author(s) declare that no Generative AI was used in the creation of this manuscript.

Supplementary material

The Supplementary Material for this article can be found online at: https://www.ebm-journal.org/articles/10.3389/ebm.2025.10544/full#supplementary-material

References

1. Pesudovs K, Lansingh VC, Kempen JH, Tapply I, Fernandes AG, Cicinelli MV, et al. Global estimates on the number of people blind or visually impaired by cataract: a meta-analysis from 2000 to 2020. *Eye (Lond).* (2024) **38**:2156–72. doi:10.1038/s41433-024-02961-1

2. Liu Y-C, Wilkins M, Kim T, Malyugin B, Mehta JS. *The Lancet* (2017) **390**:600–12. doi:10.1016/s0140-6736(17)30544-5

3. Gastaldello A, Giampieri F, Quiles JL, Navarro-Hortal MD, Aparicio S, García Villena E, et al. Adherence to the mediterranean-style eating pattern and macular degeneration: a systematic review of observational studies. *Nutrients* (2022) **14**:2028. doi:10.3390/nu14102028

4. Cundiff DK, Nigg CR. Diet and diabetic retinopathy: insights from the diabetes control and complications trial (DCCT). *MedGenMed* (2005) **7**:3.

5. Lu Z-Q, Yan J, Sun W-H, Jiang T-X, Zhai S-N, Li Y, et al. Relationship between dietary macronutrient intake and the risk of age-related cataract in middle-aged and elderly patients in northeast China. *Int J Ophthalmol* (2013) **6**:805–10. doi:10.3980/j.issn.2222-3959.2013.06.12

6. Appleby PN, Allen NE, Key TJ. Diet, vegetarianism, and cataract risk. *The Am J Clin Nutr* (2011) **93**:1128–35. doi:10.3945/ajcn.110.004028

7. Fan H, Han X, Shang X, Zhu Z, He M, Xu G, et al. Fruit and vegetable intake and the risk of cataract: insights from the UK biobank study. *Eye (Lond).* (2023) **37**:3234–42. doi:10.1038/s41433-023-02498-9

8. García-Layana A, Ciufo G, Toledo E, Martínez-González M, Corella D, Fitó M, et al. The effect of a mediterranean diet on the incidence of cataract surgery. *Nutrients* (2017) **9**:453. doi:10.3390/nu9050453

9. Amini S, Jafarirad S, Abiri B, Delgarm P, Mohamad-Zadeh Y, Ghomi MR, et al. Traditional and dairy products and vegetables dietary patterns are inversely associated with the risk of cataract in the middle age and aged population: a case-control study. *The J Nutr Health Aging* (2021) **25**:1248–54. doi:10.1007/s12603-021-1707-2

10. Barker F. Dietary supplementation: effects on visual performance and occurrence of AMD and cataracts. *Curr Med Res Opin* (2010) **26**:2011–23. doi:10.1185/03007995.2010.494549

11. Hemani G, Zheng J, Elsworth B, Wade KH, Haberland V, Baird D, et al. The MR-Base platform supports systematic causal inference across the human phenome. *Elife* (2018) **7**:e34408. doi:10.7554/elife.34408

12. Drinkwater JJ, Davis WA, Davis TME. A systematic review of risk factors for cataract in type 2 diabetes. *Diabetes/Metabolism Res Rev* (2019) **35**:e3073. doi:10.1002/dmrr.3073

13. Chang JR, Koo E, Agrón E, Hallak J, Clemons T, Azar D, et al. Risk factors associated with incident cataracts and cataract surgery in the Age-related eye disease study (AREDS): AREDS report number 32. *Ophthalmology* (2011) **118**:2113–9. doi:10.1016/j.ophtha.2011.03.032

14. Delcourt C, Cristol JP, Tessier F, Leger CL, Michel F, Papoz L. Risk factors for cortical, nuclear, and posterior subcapsular cataracts: the POLA study. *Am J Epidemiol* (2000) **151**:497–504. doi:10.1093/oxfordjournals.aje.a010235

15. Hemani G, Tilling K, Davey Smith G. Orienting the causal relationship between imprecisely measured traits using GWAS summary data. *Plos Genet* (2017) **13**:e1007081. doi:10.1371/journal.pgen.1007081

16. Łuczyńska J, Paszczyk B, Nowosad J, Łuczyński M. Mercury, fatty acids content and lipid quality indexes in muscles of freshwater and marine fish on the Polish market. Risk assessment of fish consumption. *Int J Environ Res Public Health* (2017) **14**:1120. doi:10.3390/ijerph14101120

17. Lu M, Cho E, Taylor A, Hankinson SE, Willett WC, Jacques PF. Prospective study of dietary fat and risk of cataract extraction among US women. *Am J Epidemiol* (2005) **161**:948–59. doi:10.1093/aje/kwi118

18. Pastor-Valero M. Fruit and vegetable intake and vitamins C and E are associated with a reduced prevalence of cataract in a Spanish mediterranean population. *BMC Ophthalmol* (2013) **13**:52. doi:10.1186/1471-2415-13-52

19. Theodoropoulou S, Samoli E, Theodossiadis PG, Papathanassiou M, Lagiou A, Lagiou P, et al. Diet and cataract: a case-control study. *Int Ophthalmol* (2014) **34**:59–68. doi:10.1007/s10792-013-9795-6

20. Huang G, Wu L, Qiu L, Lai J, Huang Z, Liao L. Association between vegetables consumption and the risk of age-related cataract: a meta-analysis. *Int J Clin Exp Med* (2015) **8**:18455–61.

21. Falkowska M, Młynarczyk M, Micun Z, Konopińska J, Socha K. Influence of diet, dietary products and vitamins on age-related cataract incidence: a systematic review. *Nutrients* (2023) **15**:4585. doi:10.3390/nu15214585

22. Wang D, Tang T, Li P, Zhao J, Shen B, Zhang M. The global burden of cataracts and its attributable risk factors in 204 countries and territories: a systematic analysis of the global burden of disease study. *Front Public Health* (2024) **12**:1366677. doi:10.3389/fpubh.2024.1366677

23. Hagen IV, Helland A, Bratlie M, Brokstad KA, Rosenlund G, Sveier H, et al. High intake of fatty fish, but not of lean fish, affects serum concentrations of TAG and HDL-Cholesterol in healthy, normal-weight adults: a randomised trial. *Br J Nutr* (2016) **116**:648–57. doi:10.1017/s0007114516002555

24. Xu S, Wang P, Fung WK, Liu Z. A novel penalized inverse-variance weighted estimator for Mendelian randomization with applications to COVID-19 outcomes. *Biometrics* (2023) **79**:2184–95. doi:10.1111/biom.13732

25. Yang C, Hallmark B, Chai JC, O'Connor TD, Reynolds LM, Wood AC, et al. Impact of amerind ancestry and FADS genetic variation on omega-3 deficiency and cardiometabolic traits in Hispanic populations. *Commun Biol* (2021) **4**:918. doi:10.1038/s42003-021-02431-4

26. Vallée Marcotte B, Guénard F, Marquis J, Charpagne A, Vadillo-Ortega F, Tejero ME, et al. Genetic risk score predictive of the plasma triglyceride response to an Omega-3 fatty acid supplementation in a Mexican population. *Nutrients* (2019) **11**:737. doi:10.3390/nu11040737

27. Ajomiwe N, Boland M, Phongthai S, Bagiyal M, Singh J, Kaur L. Protein nutrition: understanding structure, digestibility, and bioavailability for optimal health. *Foods* (2024) **13**:1771. doi:10.3390/foods13111771

28. Kalafati IP, Dimitriou M, Borsa D, Vlachogiannakos J, Revenas K, Kokkinos A, et al. Fish intake interacts with TM6SF2 gene variant to affect NAFLD risk: results of a case-control study. *Eur J Nutr* (2019) **58**:1463–73. doi:10.1007/s00394-018-1675-4

29. Kõks S, Kõks G. Activation of GPR15 and its involvement in the biological effects of smoking. *Exp Biol Med (Maywood)* (2017) **242**:1207–12. doi:10.1177/1535370217703977

30. Kõks G, Uudelepp ML, Limbach M, Peterson P, Reimann E, Kõks S. Smoking-induced expression of the GPR15 gene indicates its potential role in chronic inflammatory pathologies. *The Am J Pathol* (2015) **185**:2898–906. doi:10.1016/j.ajpath.2015.07.006

EBM Experimental Biology and Medicine

TYPE Original Research
PUBLISHED 13 August 2025
DOI 10.3389/ebm.2025.10564

OPEN ACCESS

*CORRESPONDENCE
Sangeeta Khare,
sangeeta.khare@fda.hhs.gov

†PRESENT ADDRESS
Vicki Sutherland,
J&J Innovative Medicine, Spring House, PA, United States

‡These authors have contributed equally to this work

RECEIVED 03 March 2025
ACCEPTED 07 July 2025
PUBLISHED 13 August 2025

CITATION
Yanamadala Y, Muthumula CMR, Gokulan K, Karn K, Sutherland V, Cunny H, Santos JH and Khare S (2025) Gestational exposure to HIV drugs alters intestinal mucosa-associated microbial diversity in adult rat offspring. *Exp. Biol. Med.* 250:10564. doi: 10.3389/ebm.2025.10564

Gestational exposure to HIV drugs alters intestinal mucosa-associated microbial diversity in adult rat offspring

Yaswanthi Yanamadala[1‡], Chandra Mohan Reddy Muthumula[1‡], Kuppan Gokulan[1], Kumari Karn[1], Vicki Sutherland[2†], Helen Cunny[2], Janine H. Santos[2] and Sangeeta Khare[1*]

[1]Division of Microbiology, National Center for Toxicological Research, U.S. Food and Drug Administration, Jefferson, AR, United States, [2]Division of Translational Toxicology, National Institute of Environmental Health Sciences, Research Triangle Park, NC, United States

Abstract

The antiretroviral (ARV) drug combination of abacavir sulfate, dolutegravir, and lamivudine [ABC/DTG/3TC; Tri combination Anti-retroviral therapy (TC-ART)] has revolutionized HIV treatment by effectively targeting different stages of viral replication. Despite its therapeutic efficiency for maintaining low viremia in the mother during pregnancy, there are concerns for long-term liabilities in offspring that are indirectly exposed during vulnerable periods of development. The commensal microbiota plays a crucial role in maintaining overall gut health, and disruption of the microbiome is often linked to various extraintestinal effects such as immune dysregulation and inflammation. We recently reported the effects of this drug combination in altering fecal microbiome composition of aged rats perinatally exposed to ABC/DTG/3TC-ART. The fecal microbiome can provide only a snapshot of the composition of microbial community at the end of the digestive tract, which may not reflect the microbial population interacting with ileal mucosa. Thus, the current work reports the effects of this drug combination in the gut mucosa-associated microbiome of the same animals, which showed significant microbial diversity and species richness in high dose exposed female adult offspring, along with dose-dependent changes in Firmicutes/Bacteroidetes ratio. The high dose exposure also showed an increase in opportunistic bacterial species in male animals. Overall, we found that, similar to the fecal microbiome, perinatal exposure to TC-ART led to sex- and dose-dependent alterations in the gut mucosa-associated microbial population in aged rats, suggesting that early life exposure to these drugs may influence gut mucosa-associated immune responses and intestinal permeability.

KEYWORDS

antiretroviral therapy (ART), ARV, abacavir, lamivudine, dolutegravir, microbiome, gut mucosa-associated microbes

Impact statement

This study shows that prenatal and lactational exposure to the Anti-retroviral therapy (TC-ART) drug combination (ABC/3TC/DTG) is associated with sex-dependent alterations in the ileal mucosa-associated microbiome composition when offspring are evaluated at 12 months of age. These findings emphasize the importance of including microbiome analyses in studies aiming at evaluating the long-term health effects of TC-ART exposure during early development.

Introduction

Human immunodeficiency virus (HIV) is a retrovirus that primarily targets the immune system, making it difficult for the body to fight against infections and diseases [1]. Without treatment, HIV can progress to AIDS (acquired immunodeficiency syndrome), which can be fatal [2]. Anti-retroviral (ARV) drugs have revolutionized HIV treatment by suppressing the replication of HIV, preventing it from progressing to AIDS. They have turned HIV from a fatal disease into a manageable chronic condition [2]. One such combination of drugs that has been used is abacavir sulphate, dolutegravir, and lamivudine [3]. Abacavir and lamivudine inhibit HIV reverse transcriptase and cause premature termination of viral DNA synthesis by incorporating non-functional nucleotide analogs into growing DNA chain [3, 4], while also having off target effects on the mitochondria [5, 6]. Millions of individuals globally are on Tri combination Anti-retroviral therapy (TC-ART), including pregnant women, to reduce the risk of mother to child transmission [7–9].

The gut microbiome is important due to its beneficial functions and its involvement in maintaining gastrointestinal homeostasis, health, and disease progression [10]. ARV drugs particularly nucleoside reverse transcriptase inhibitors (NRTIs) (lamivudine), are known to affect host mitochondria by inhibiting mitochondrial DNA polymerase γ, leading to mitochondrial DNA depletion and dysfunction [11, 12]. Considering the evolutionary origin of mitochondria from symbiotic bacteria and similar biochemical pathways between mitochondria and prokaryotes, it is plausible that gut microbiome can be inadvertently affected by ARV drugs. However, most of the anti-retroviral drugs are not investigated for changes in gut bacterial community and overall gut health. Recent studies have shown that exposure to ARV's can have an impact on the host's gastrointestinal health including altered microbiome and cytokine profiles [13, 14]. Microbial dysbiosis can have several downstream effects, including changes in immune function, intestinal mucosal permeability, and imbalance in other functional organs [15–17]. For instance, dysbiosis in the ratio of Firmicutes and Bacteroidetes is associated with cardiac diseases [18], while increased *Bacteroides* levels are observed in liver ailments, with the degree of alteration correlating to the severity of the condition [19]. Similarly, decreases in butyrate producing bacteria have been associated with increased immune activation and microbial translocation [20], suggesting a relationship between microbial dysbiosis, and changes in cytokine profiles, and intestinal permeability.

The intestinal barrier is a complex multilayer system with an external physical "mucosal barrier," epithelial cells, and an internal immunological functional barrier in the form of Payer's patches [21]. The mucus layer on the top of the gut mucosa hosts several commensal bacteria and serves as a defense line along with the tight epithelial layer. Disruption in the barrier can compromise the integrity of the gut ecosystem, which is associated with several pathological conditions including lung, cardiac, neuronal, and autoimmune diseases [22, 23]. It is widely accepted that newborns are sterile at their birth, and they develop the microbiota through maternal exposure, surrounding environment, and through feeding practices [22]. Interestingly, the gut microbiome also plays a major role in infant immune system development, highlighting the importance of maternal gut health in shaping the offspring health [24, 25]. It is becoming increasingly evident that changes in the gut microbiome influence the development of various diseases in later life [26]. While most of the research is primarily focused on the direct effect of the drug on the host, there is limited information on the effect of the drug on the gut health of the progeny. We recently showed that perinatal exposure to this ARV combination altered the fecal microbiome of aged rats (12 months old) in a sex- and dose-dependent manner [27]. This study expanded those findings by exploring the changes in gut mucosal microbiota of the same animals, providing knowledge on the effects of drug exposure in the intestinal mucosa associated microbiome rather than focusing on the fecal -microbiome at the distal end of the intestinal tract.

Materials and methods

Animal housing, care, treatment, euthanasia, and sample collection

Time-mated Sprague Dawley rats (Hsd:SD) were obtained from Envigo (Indianapolis, IN). All animals (pregnant female rats and their male and female offspring) were housed in the animal facility at AmplifyBio, West Jefferson, OH, an independent, scientific contract research organization. Rats were approximately 11–14 weeks of age upon receipt. The facility's Institutional Animal Care and Use Committee (IACUC) reviewed the protocol and approved it. The IACUC number for this protocol is T06055. Animals were housed in polycarbonate cages with irradiated hardwood bedding chips (Sani Chips®; Envigo, Madison, WI). During gestation and lactation, rats were provided natural crinkled

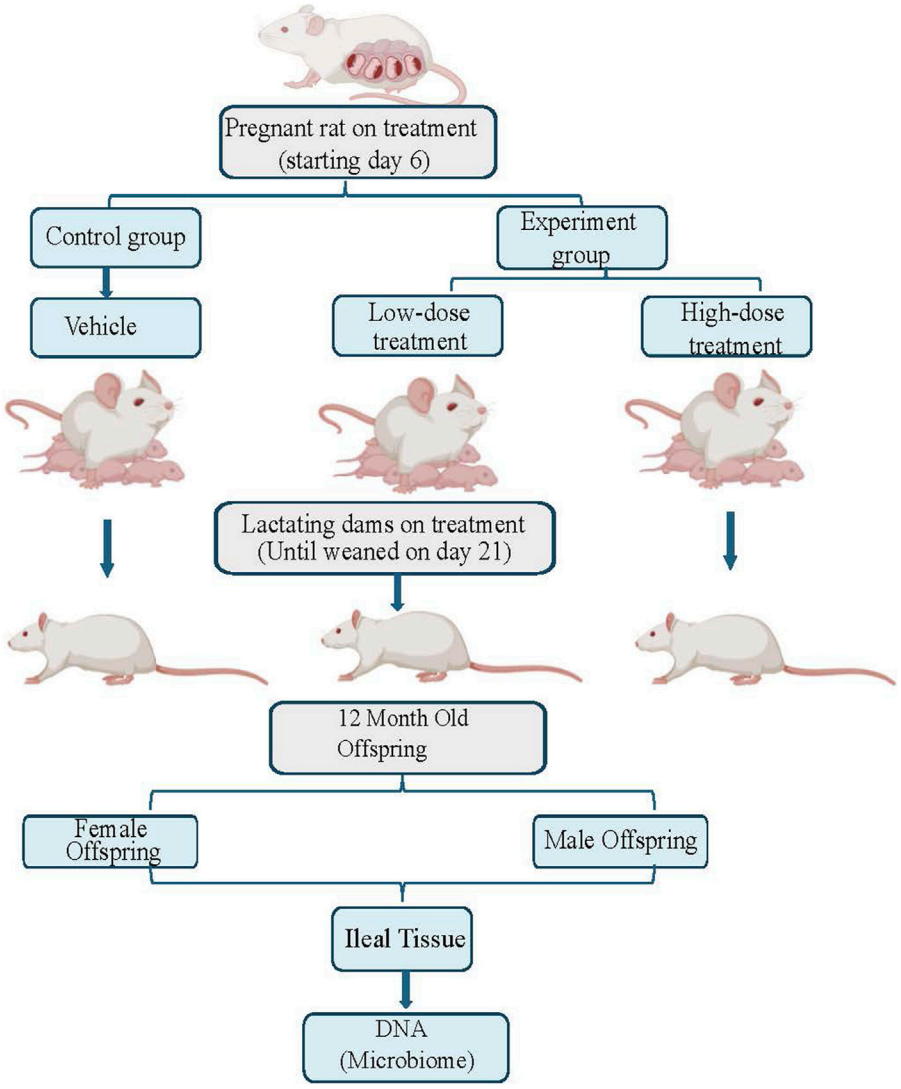

FIGURE 1
This figure illustrates the experimental flow for this study, which includes three treatment groups: control, low dose, and high dose of tricombo drug treatment. Pregnant rats were treated until the rat pups were weaned on postnatal day 21. DNA, was collected from the ileal tissue of 12-month-old rat offspring for microbiome analysis.

kraft paper for enrichment (Crink-l'nest™, The Andersons; Maumee, Ohio). Offspring remained with their respective dams until postnatal day (PND) 21. After weaning, F1 offspring were provided polycarbonate rectangular shelters (Rat Retreats™, Bio-Serve; Flemington, NJ) as enrichment and were group housed by sex, up to 5 per cage. During gestation and lactation, animals were fed irradiated NIH-07 pellets or wafers (Zeigler Bros., Gardners, PA). After weaning, animals were fed NTP-2000 (Zeigler Bros., Gardners, PA). Rats were provided municipal water *ad libitum* from an automatic watering system; both water and feed were analyzed for known contaminants that could interfere with or affect the outcome of the study, and none were found. Animals used in this investigation of the mucosa-associated microbiome were from a larger toxicology study that will be reported elsewhere (manuscript under preparation). The experimental design is outlined in Figure 1.

HIV dose selection and exposure to animals

There were 3 groups in this study (n = 5 per group). Group 1 (control): 0 mg/kg/day dosed with vehicle; Group 2 (low dose): 150/12.5/75 mg/kg ABC/DTG/3TC; Group 3 (high

dose): 300/25/150 mg/kg ABC/DTG/3TC. Vehicle was 0.2% methylcellulose/0.1% Tween 80. The treatment regimen and administered doses were based on our previously published study, which used the same animal cohort and provided detailed justification for dose selection [27]. In summary, the doses were chosen based on human therapeutic relevance and previously established toxicological data.

TC-ART was administered via oral gavage to time-mated female Sprague Dawley rats (Hsd:SD) starting on gestational day 6 (GD6) and continued through gestation, and lactation (PND21) (NTP study T06055). F1 offspring were never directly dosed in this study. Dams were weighed approximately every 3 days, and dosing volumes (5 mL/kg) were based on the most recent body weight. One male and one female offspring from each dam were used for the study.

Collection of ileal tissue for DNA extraction

After the pups were weaned from the dams, they were housed up to five per sex per cage and provided food and water *ad libitum*. Once the offspring reached 12 months of age, which is comparable to approximately 26 years in humans [28], they were euthanized by exposure to carbon dioxide, strictly adhering to the guidelines set by the IACUC. In a sterile environment, the ileum was exposed and flushed with sterile PBS to remove feces. The samples were immediately placed in pre-labelled tubes, frozen in liquid nitrogen and transported overnight on dry ice to the National Center for Toxicological Research (NCTR), Jefferson, AR, for analysis.

Ileal mucosa-associated microbial DNA extraction for population analysis

Maintaining the sterile conditions, a small section of the ileal tissue was placed in CTAB extraction solution and finely minced using a scalpel. The minced tissue was transferred into bead-beating tubes (lysing matrix B) and processed using a Fast prep Machine at 6 m/s for 45 s. Thus, obtained lysate was incubated with proteinase k (at 65°C for 20 min), followed by RNase-A (at 37°C for 15 min) as described earlier [29]. To this an equal volume of phenol-chloroform-isopropanol (PCI) solution was added and centrifuged at 12,000xg. The supernatant aqueous solution was separated, and the DNA was precipitated using sodium acetate, isopropanol, and a polyacryl carrier. The DNA pellet was washed with 70% ethanol and then dissolved in nuclease-free water. The DNA was quantified with a Qubit fluorometer (Thermo Fisher Scientific, Waltham, Massachusetts) and subsequently used for sequencing.

Rat mucosa-associated microbial population amplicon sequencing

The samples were processed and standardized using a modified methodology based on Gohl et al. 2016 [30]. The KAPA HiFi Polymerase from KAPA Biosystems was used to amplify the variable region 4 (515f/806r) of the 16S rRNA gene. The libraries were subjected to sequencing on a MiSeq (Illumina) instrument, with paired-end 2 × 250 reads, using the MiSeq Reagent Kit V3 (Illumina, 600 cycle kit), aiming to achieve a target depth of 50,000 reads. The sequencing reads underwent adapter and primer removal using Cutadapt, and any reads with a Q score below 30 were discarded. The amplicon sequence variations (ASVs) were generated using dada2 v1.16.0, using quality-controlled reads. As part of the dada2 workflow, the paired FASTQ reads underwent trimming and filtering to eliminate reads that had ambiguous nucleotides (represented by "N"s) or more than 2 sequencing mistakes per read. The dada2 learn error rate model was utilized to estimate the error profile prior to employing the core dada2 algorithm for inferring the sample composition. The forward and reverse readings were combined, and any chimeras were eliminated prior to taxonomy classification. The ASV taxonomy was determined up to the level of species using the SILVA v.138 database, following the technique developed earlier [31]. A minimum bootstrapping support of 50% was required for taxonomic assignment. Species-level taxonomy was awarded to ASVs based only on 100% identity and unambiguous reference matching.

Statistical/data analysis

Microbiome data was visualized using either microbiome analyst [32] or metaboanalyst websites [33]. For the microbiome analysis, the software used an ANOVA, followed by *post hoc* pairwise comparisons using Mann-Whitney and Kruskal-Wallis statistical tests. For the comparison between two groups either EdgeR or student T-tests were conducted. The samples for the microbiome analyst were normalized to remove 19 low abundance and 11 low variance values based on mean and standard deviation respectively. While for the metaboanalyst the samples normalization was performed using the normalization by sum. Following that the data scaling was applied using mean centering and log transformation options to ensure approximate normal distribution.

Results

Comparative analysis of the treatment groups (n = 5 per group) was conducted to assess the impact of gestational and lactational exposure of TC-ART on microbial profiles, focusing on sex-specific impacts on the offspring. During the analysis one control female and one high dose female animal showed

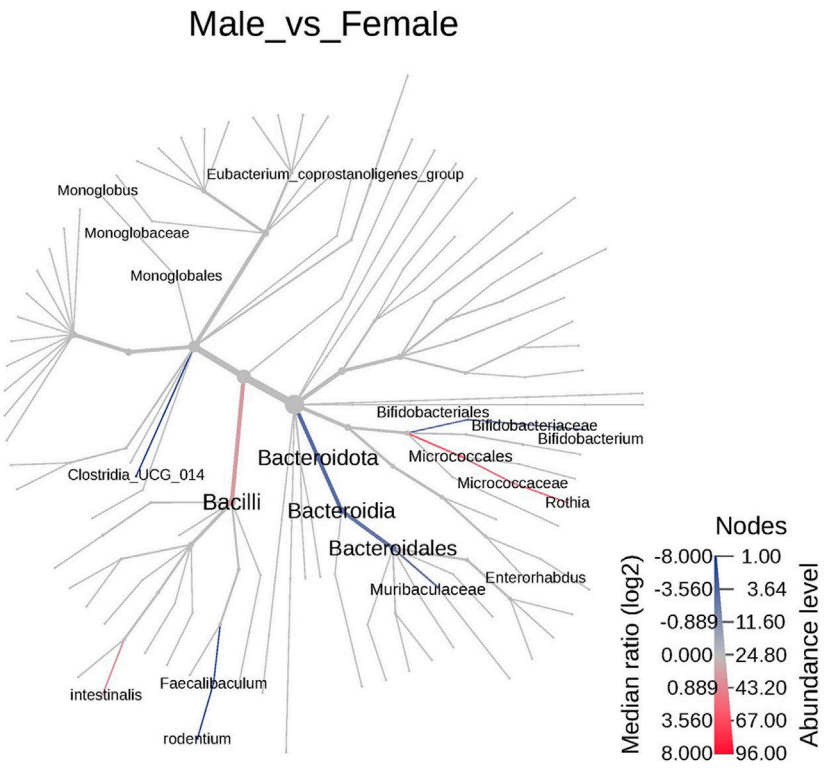

FIGURE 2
The cladogram represents the phylogenetic relationship between the male and the female animals between different taxa. The blue or highlighted branches represent significant decreased taxa in females while the red represent the significantly increased taxa. The branches are colored based on median log2 ratios and the intensity of color represents the abundance. Significant differences were observed in *Bacteroidales* and *Bacili*.

deviation in the microbial profile compared to the other animals in respective experimental groups. However, the outlier test showed the two animals are not statistically classified outliers. We have excluded the animals for the alpha diversity but to maintain the integrity, we have included the animals in our dataset for the rest of the analysis. The inclusion of these animals for later analysis did not alter our conclusions, rather it highlights the natural variability within the controlled experimental groups.

Sex-specific microbiota differences and differential response to exposure are observed in male and female animals

Sex-specific differences were observed between the microbiota of the control animals. A total of 37 significant features were differentiated between the female and male animals (Supplementary Table S1). At the phyla and species level 2 significant features were identified, 3 at family level, and 32 features varied at the genus level. The cladogram analysis revealed notable differences between the male and the female animals at the genus level (Figure 2). Notably the *Bacteroidota* and *Bifidobacteriales* were significantly increased in the female animals compared to the male animals while the *Clostridia, Bacilli,* and *Eubacterium coprostanoligenes group* were decreased in the female animals. The male and the female animals have responded differently to TC-ART exposure. While the exposure in male animals resulted in increase of opportunistic bacteria the female animals showed decrease in the abundance of opportunistic bacterial species. To have a more granular view on the differences we analyzed the changes in the microbiome upon exposure at different taxonomic levels.

Mucosa associated microbiome diversity changes with 16s amplicon sequencing data

The ileal mucosa-associated bacterial population in the adult offspring perinatally exposed to TC-ART was assessed by 16s amplicon sequencing.

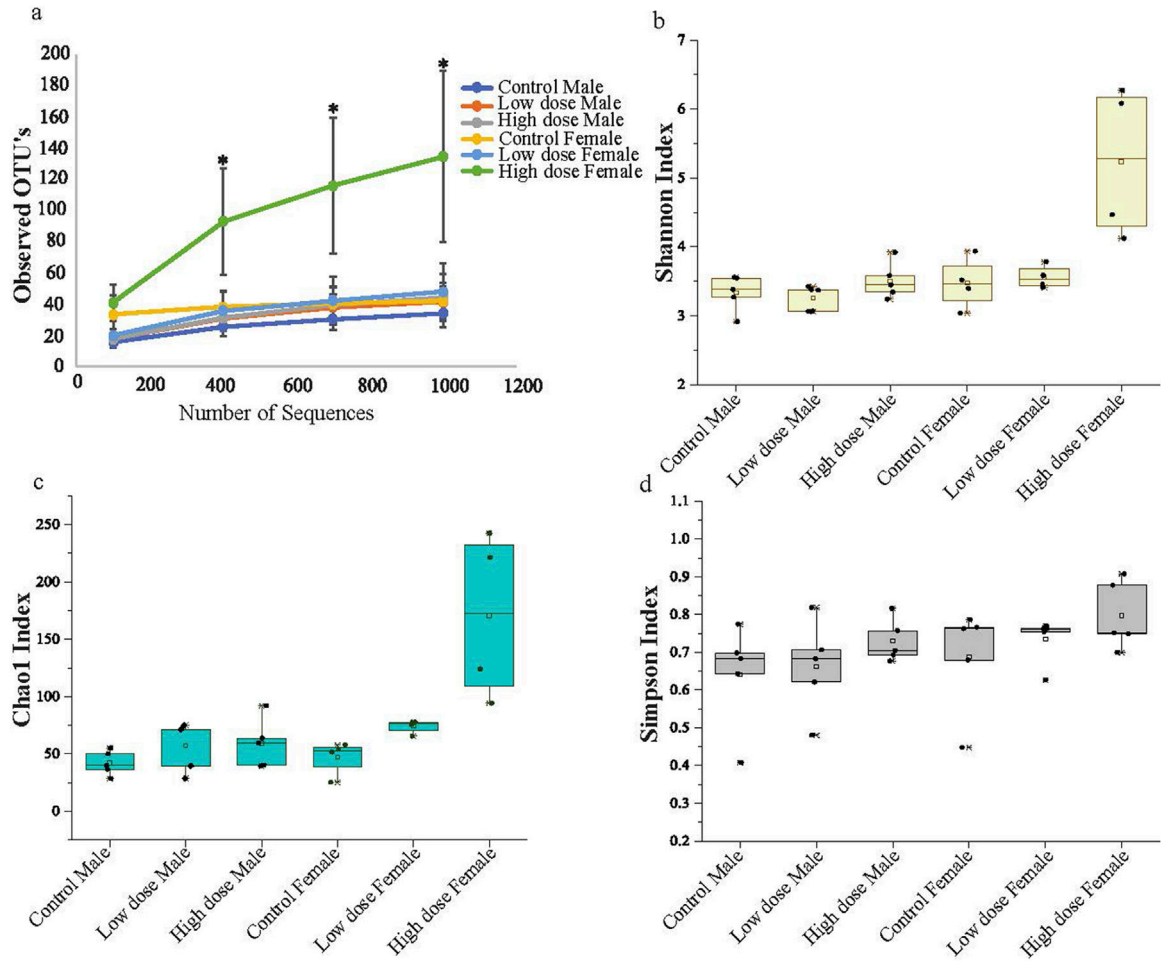

FIGURE 3
Alpha diversity **(a)** Observed OTU abundance over sequence number. The figure shows the observed operational taxonomic unit (OTU) abundance as a function of sequence number for male and female animals across three experimental groups: control, low dose, and high dose treatment. Each line represents the mean OTU abundance for each group. The high dose exposed female animals display a higher OTU abundance compared to the other groups. **(b)** Shannon Diversity Index. **(c)** Chao1 Index **(d)** Simpson Diversity Index. Illustrates the diversity of microbial communities in male and female animals across the groups. The high dose treated female animals show significant differentiation from the other groups, indicating a notable shift in microbial diversity and richness associated with higher treatment levels. The data represents mean with standard deviation (n = 5; *p < 0.05).

The changes in bacterial diversity, richness, and evenness in each group were evaluated by using different alpha diversity indices including total number of observed operational taxonomic units (OTUs), Chao1, Shannon, and Simpson as shown in Figure 3. The female high dose offspring exhibited significantly higher species richness compared to all other groups, with an observed OTU of 132 (Figure 3a); results that were further confirmed when evaluating the Shannon and Chao1 diversity indices (Figures 3b, c). Interestingly, female control animals showed higher species richness compared to male animals, indicating base line sex differences. The microbial species richness in the high dose exposed female offspring were significantly higher compared to other groups (Figures 3a–c; Supplementary Table S2), suggesting that maternal administration of the drugs at the high dose resulted in the enhanced species richness and rare species (low abundant species) in these animals. Conversely, no significant differences between groups were observed using the Simpson Index, which measures richness and evenness between bacterial communities. This suggests a similar level of species dominance within bacterial community among all tested animals (Figure 3d). The rarefaction curves also suggest higher species richness at higher sequence depths in both male and female animals in the high dose-exposed groups (Supplementary Figure S1).

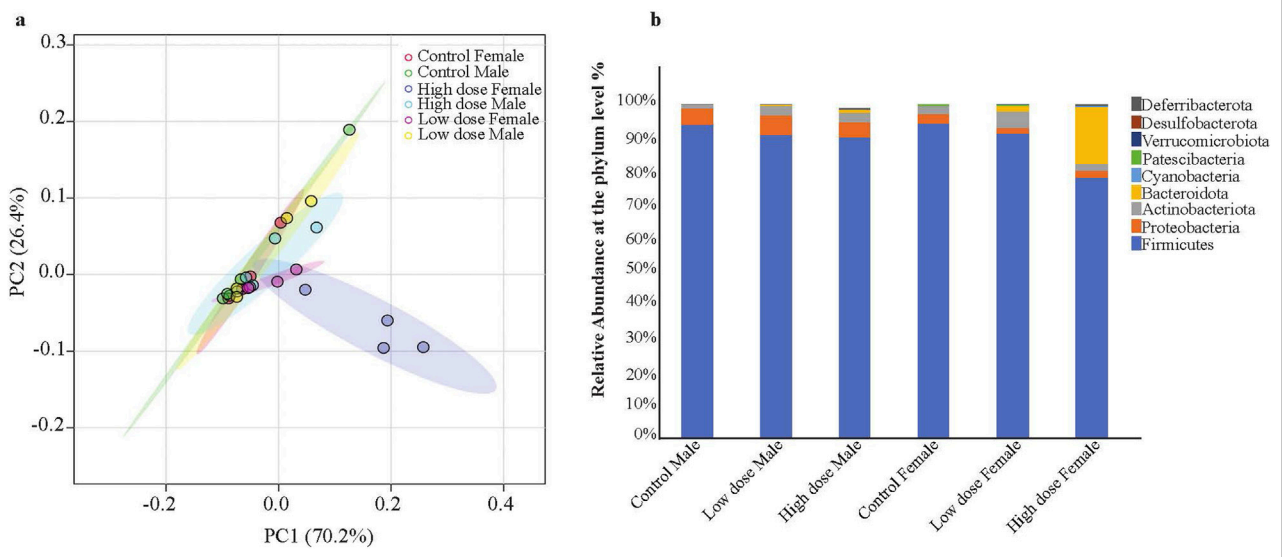

FIGURE 4
Principal Component Analysis (PCA) of microbiome profiles and changes in gut microbiota composition in male and female rat pups exposed to Tricombo drug. **(a)** PCA of the microbial profiles. The PCA score plot illustrates the clustering of microbiome profiles from each group. The plot shows ellipses indicating the 95% confidence intervals with the high dose female (blue) distinctly separated from the other groups. **(b)** Relative abundance of gut microbiota at the phyla level: The bar diagram represents the relative abundance of different bacterial phyla in male and female rat pups exposed to low and high doses of the tricombo drug compared to control animals. The bacterial phyla include Firmicutes, Proteobacteria, Actinobacteriota, Bacteroidota, Cyanobacteria, Patescibacteria, Verrucomicrobiota, Desulfobacterota, and Deferribacterota. The High dose exposed female animals has shown significant variations in *Firmicutes/Bacteroidota* ratio compared to other groups. Data is represented as the percentage of total bacterial abundance for each group Control Male, Low dose Male, High dose Male, Control Female, Low dose Female, High dose Female.

Perinatal exposure to TC-ART leads to taxonomic level changes at phyla, genus, and species levels

The principal component analysis (PCA) at the phylum level showed a distinct shift in the clustering of the high dose exposed female animals (Figure 4a), correlating with significant alterations in Firmicutes/Bacteroidetes ratio (Figure 4b). The low dose showed a substantial increase of Bacteroidetes relative microbial abundance compared to the control animals, while the high dose showed an even greater increase. The Bacteroidetes change was consistent across all the female high dose exposed animals (Figure 4b). The relative abundance of Firmicutes was reduced with the treatment. Although the males also showed a similar trend, the variations were not as prominent as in female animals (Figure 4b; Supplementary Figure S2). Treated male animals had increased Proteobacteria phyla compared to the control animals, while females had a decrease (Figure 4b). Similarly, an increase in the phyla Deferribacterota was observed in the high dose exposed female rats relative to the control animals. Of note, males from the high dose-only and females from both dosed-groups have more unidentified phyla, indicating a diversified bacterial population associated with drug exposure. This, in turn, could potentially lead to metabolic disturbances.

The identified changes in bacterial diversity described above might differentially influence downstream effects. To determine if this was the case, we next analyzed bacteria composition at the genus and species level, which can provide information on their pathogenic or commensal origins. We observed notable sex- and treatment- dependent variabilities. The major genera showed comparable differences between the male and female control animals (Figures 5a, b). Beneficial genera such as *Lactobacillus, Lachnospiraceae, Lactococcus, Romboutsia, and Bifidobacterium,* that promote gut health showed dose-dependent alterations (Figures 5a, b). Interestingly, *Lactobacillus* genera has shown a dose dependent decrease in all groups while *Romboutsia* from Firmicutes phyla showed a decrease in male animals (Figure 5a). Conversely, the genera associated with inflammation or pathogenicity, including *Escherichia (Escherichia schigella), Pseudomonas, Angelakisella,* and *Parabacteroides,* were increased in the groups exposed to TC-ART. Notably, *Pseudomonas*, which is linked to gut dysbiosis and immune activation, showed a dose-dependent increase in both male and female subjects. *Clostridium* sensu stricto1 was decreased in females in both exposed groups but not changed in male groups (Figures 5a, b; Supplementary Figure S3a).

Genera such as *Cupriavidus, Odoribacter*, and *Tyzzerella* were uniquely present in both male and female high dose exposed groups. The abundance of some genera like

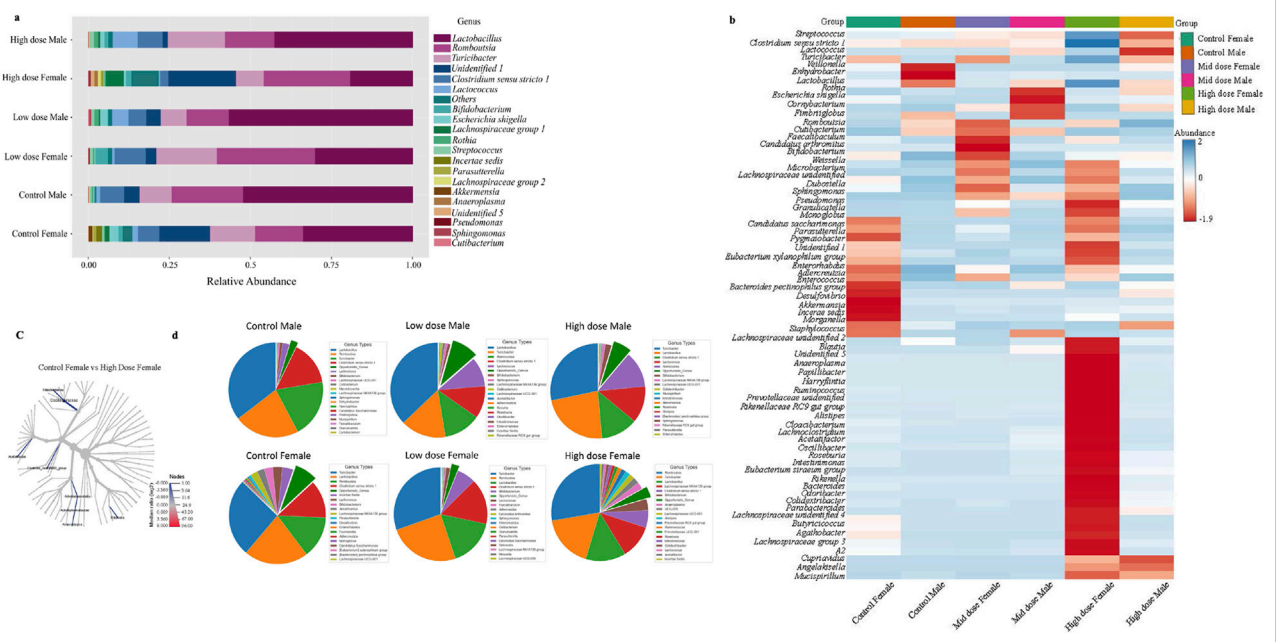

FIGURE 5
Relative abundance of bacterial genus in different TC-ART exposure groups. **(a)** The stacked bar plot illustrates the composition of gut microbiota in male and female subjects across groups: Control Male, Low dose Male, High dose Male, Control Female, Low dose Female, and High dose Female. Each color in the bars represents a different bacterial genus. *Lactobacillus* (yellow), *Romboutsia* (green), and *Turicibacter* (reddish pink), *Lactococcus* (orange), *Clostridium sensu stricto 1* (grey) show significant alterations. High dose treatments decreased *Lactobacillus* and Lactococcus with more pronounced changes in females. These variations highlight the impact of exposure on gut microbiota composition. **(b)** Heatmap of bacterial genera distribution across different exposure doses and in control animals. The rows correspond to bacterial genera, and the columns to the samples within each group. The color scale indicates the abundance of each genus, ranging from blue (low abundance) to red (high abundance). A distinct microbial profile observed in the high dose exposed female animals compared to other groups, indicating a significant shift in bacterial genera due to the exposure. **(c)** The cladogram represents comparison between the control female and the high dose female animals. The blue highlighted branches represent significant taxa and the taxa with higher median log2 ratios in high dose female group are more abundant compared to the control animals indicated by color gradient and intensity. **(d)** The pie chart of top 20 abundance genera with the opportunistic bacterial genera highlighted between the groups (dark green). The abundance of the opportunistic bacteria was added and represented in the pie diagram. The exposed male animals have shown increased abundance of opportunistic bacterial genera while the females have shown low abundance with the exposure to TC-ART.

Bacteroides, Butyricoccus, Turicibacter, and *Eubacterium (Eubacterium ventriosum, Eubacterium siraeum)* showed transient changes in response to treatment indicating sensitivity of the bacterial community following prenatal exposure to the ART (Figure 5b).

When single-factor statistical comparisons were performed using EdgeR, a total of 19 significant features were altered at the genus level between the control female and high dose female animals using PCA analysis (Supplementary Figure S3b). Additionally, 15 microbial features differed, including 9 variations at the genus level, were identified between the control male and the female animals, consistent with the notion of base line sex-specific differences described above. The cladogram (Figure 5c) depicts significant alterations in the relative abundance of several taxa such as *Oscillospiraceae, Intestinimonas, Acettatifactor, Rikenella, Anaeroplasma, Acholeplasmatales*, and *Clostridia VadinBB60* group, are significantly enriched in high dose female group. The shift in Oscillospiraceae and Intestinimonas families in the high dose-exposed animals was notable. Also, females showed higher abundance of *Bifidobacterium* while males showed increased levels of *Clostridia*. Changes were observed in genera within the *Bacteroidetes* and *Bacilli* with more opportunistic genera in the control female animals compared to the male animals, which were further changed in the exposed groups (Figure 5d).

To have a more granular view at the taxonomy, we investigated abundance of bacterial species in each experimental group, which revealed dose- and sex-dependent changes (Figure 6a). Protective bacteria like *Lactobacillus intestinalis and Akkermansia muciniphila* decreased while other commensal bacteria *Bacteroides uniformis, Bacteroides caccae,* and *Mucispirillum schaedleri* were increased in treatment groups (Figures 6a, b). Interestingly, most of the commensal bacteria showed lower abundance in the low dose exposed animals compared to the high dose exposed animals.

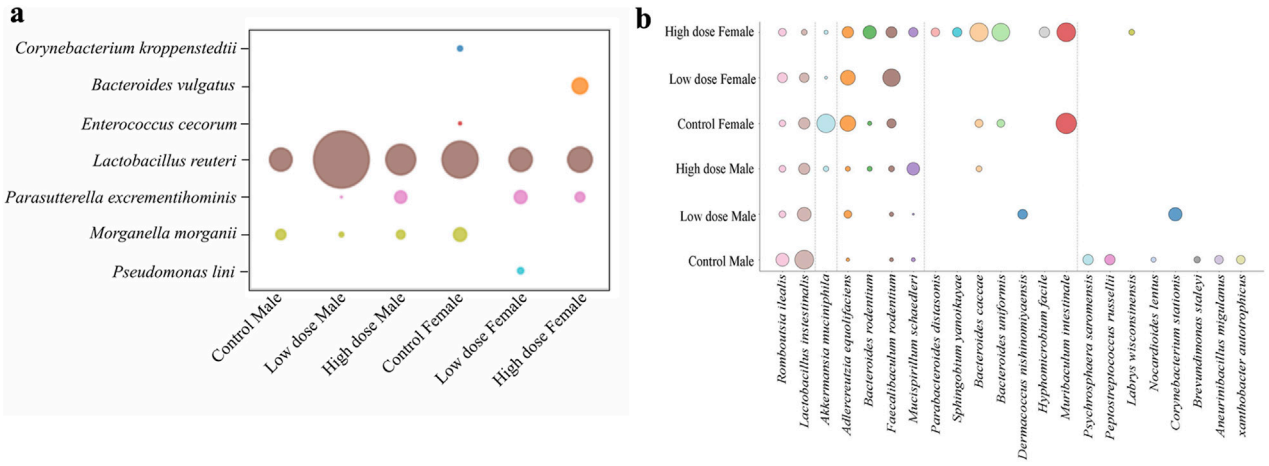

FIGURE 6
Comparative analysis of mucosa associated microbial species across different groups. Bubble plots representing the relative abundance of **(a)** opportunistic bacterial species in mucosa tissue **(b)** commensal bacterial species across the treatment groups in mucosa tissue.

Discussion

The ability of TC-ART to cross the placental barrier and its presence in milk invite a better understanding of the risks associated with their use in pregnancy and lactation [34]. Numerous studies have explored the effects of TC-ART on the mother and the offspring, focusing on aspects like cardiovascular diseases, neuronal development, immune health [35]. These studies focus on the effects of the drugs on these tissues, but often neglect to include analysis on the effects on the gut health of the offspring. Given the importance of gut health and the microbiome in maintaining individual homeostasis, and their association with several pathological conditions when disrupted, it is important to consider how they may be affected by early drug exposure. Perinatal TC-ART exposure may alter the gut microbiome that could impact metabolism, intestinal permeability, and immune system contributing to long-term health outcomes. In this study, by investigating mucosa-associated microbial changes in rats that were exposed to TC-ART solely through placental and lactational transfer, we found significant changes in the composition of intestinal microbiome in adulthood.

Our data aligns with the understanding that the fecal microbiome is more abundant and diverse than the mucosa-associated microbiome. Although both fecal and mucosal microbiomes showed differences, the changes were more pronounced in the mucosal microbiome. This may suggest that the mucosal environment is more sensitive to high-dose exposure and exhibits differential responses, possibly due to the drug being primarily absorbed in the small intestine [27, 36]. Furthermore, several studies have shown that the mucosal environment is crucial for microbiome-immune interactions due to its proximity with the intestinal epithelium and pattern recognition receptors (PRRs) [37, 38]. The combined effect of mucosal environment along with the presence of TC-ART could have significantly contributed to observed shifts in mucosal microbiome. Interestingly, the mucosal data showing a higher proportion of opportunistic bacteria and decreased commensal bacteria, along with the differences in the fecal and mucosal microbiome of the control animals, highlights the importance of studying both to understand the dynamics of drug exposure.

Overall, our data showed sex-dependent and dose-dependent drug-induced changes in the gut microbiome, which were more pronounced in females than males. Notably, sex-dependent microbial variations between male and female control animals were identified, which may provide insights for understanding the sex-specific microbial functions or outcomes. Although female animals exhibited lower microbial abundance, their higher observed OTU counts compared to male samples suggests greater microbial diversity in females. Additionally, treatment in both male and females led to reduced microbial abundance indicating a non-favorable effect of the exposure on the gut microbiome. The opportunistic genera in the male animals increased with the exposure while it decreased in the female animals, suggesting sex-based differences in the effects of the drugs. Sex hormones such as estrogen and testosterone are known to influence gut microbial composition, diversity, and functions [39]. In healthy women, higher estrogen levels are associated with increased Bacteroidetes and microbial diversity, while in healthy men, elevated testosterone levels correlate with higher levels of *Ruminococcus* and *Acinetobacter*. However, in women,

higher testosterone levels are associated with *Escherichia* and *Shigella* species, while *Ruminococcus* species; is negatively associated with elevated testosterone levels [40]. The increased Bacteroidetes and reduced Firmicutes ratio in high dose females observed in our study is often associated with several pathologies including IBS and immune profile alterations [41]. Generally, decreases in Firmicutes and increases in Bacteriodata are considered ideal but high changes in the composition might also disrupt the digestive function and other metabolic pathways. Some studies have revealed that similar microbial changes observed in female animals are associated with disease outcomes in patients with Alzheimer's, refractory epilepsy, and some neurological diseases [42–44]. Alterations in *Actinobacteria* and *Proteobacteria* in the treated groups suggest microbial dysbiosis, which has been linked to inflammatory diseases [41], coronary heart failure, and other cardiac abnormalities [45–47]. For example, *Romboutsia ilealis* species is often linked with better gut health, including improved metabolism, lowering dietary inflammation, and controlling blood sugar and fat [48, 49]. The enrichment of *Romboutsia* in the female animals could contribute to decreased proinflammatory cytokines production. Similarly, the changes in abundance of the *Clostridium sensu stricto1, Escherichia, shigella,* and *Enterococcus* observed in the treated groups have been associated with metabolic dysfunction and fatty acid liver disease [50, 51], as well as heart failure and coronary artery diseases [47]. [52]. Notably, these animals do show cardiac dysfunction later in life (Taube et al., in preparation), but whether the changes in the microbiome reported here play a role in that phenotype remain unclear.

The reduced abundance of *Akkermansia mucinophila* is often associated with vascular inflammation, endotoxemia, and barrier dysfunction [45, 53]. *Akkermansia mucinophila* is a mucin degrading bacterial community that modulates expression of tight junction genes like occludins [53]; thus can influence the intestinal permeability and induce translocation of pathogenic bacteria into the systemic circulation that could contribute the metabolic diseases. Another species, *Faecalibaculum rodentium,* known for its cholesterol degrading activity and protective effects against intestinal tumor growth, was slightly increased with the treatment in both male and female animals. This species is also known to induce oxidative stress and inflammation [54, 55]. The differential abundance of *Aslercreutzia eqyolifaciens* species is related to several disease conditions such as metabolic liver diseases [56]. Given that most of the bacteria are initially acquired from the mother and the surrounding environment, the coprophagy during the co-housing of dam and pups during early development could be another possibility of the transfer of altered microbial population (due to impact of drug on the intestinal microbiota) from dams to pups [57, 58]. These microbial changes may persist into adulthood influencing the microbiome composition of the offspring.

In conclusion, our study shows the effects of TC-ART on the mucosal microbiome of the adult offspring of animals exposed through gestation and lactation. The differences observed highlight the potential sensitivity of the mucosal environment to the drug exposure. The extent to which these changes might affect other phenotypes on the animals, including impacts on their cardiovascular health, is unclear but deserves further investigation. Since our data also suggest sex-specific differences, further studies on the influence of sex hormones to the phenotypes here described are also warranted.

Author contributions

All authors listed have made a substantial, direct, and intellectual contribution to the work and approved it for publication.

Author disclaimer

This article reflects the views of the authors and does not necessarily reflect those of the U.S. Food and Drug Administration. Any mention of a commercial product is for clarification only, it is not an endorsement for the use of it.

Data availability

The datasets presented in this article are not readily available because the work is conducted at the government institute. Requests to access the datasets should be directed to the corresponding author.

Ethics statement

All animals (pregnant female rats and their male and female offspring) were housed in the animal facility at AmplifyBio, West Jefferson, OH, an independent, scientific contract research organization. Rats were approximately 11-14 weeks of age upon receipt. The facility's Institutional Animal Care and Use Committee (IACUC) reviewed the protocol and approved it. The IACUC number for this protocol is T06055. The study was conducted in accordance with the local legislation and institutional requirements.

Funding

The author(s) declare that financial support was received for the research and/or publication of this article. YY, CM, and KK were supported by an appointment to the Postgraduate Research

Program at NCTR administered by the Oak Ridge Institute for Science and Education (ORISE) through an interagency agreement with the U.S. Department of Energy and the U.S. Food and Drug Administration. This study was supported by NIEHS under an interagency agreement between FDA and NIEHS (FDA IAA#224-17-0502 and NIEHS IAA AES23002001/GT&C A2310-075-075-052689). It was also supported by contracts HHSN273201400015C and HHSN273201400022C. VS and HC were supported [in part] by the Intramural Research Program of the National Institutes of Health, NIEHS, under ZIA ES103379.

Acknowledgments

The authors would like to thank Dr. Radwa Hanafy (NCTR), Dr. Jyotshnabala Kanungo (NCTR), and Dr. Kelly Shipkowski (NIEHS) for reviewing the manuscript and providing valuable comments and suggestions.

Conflict of interest

The author(s) declared no potential conflicts of interest with respect to the research, authorship, and/or publication of this article.

Generative AI statement

The author(s) declare that no Generative AI was used in the creation of this manuscript.

Supplementary material

The Supplementary Material for this article can be found online at: https://www.ebm-journal.org/articles/10.3389/ebm.2025.10564/full#supplementary-material

References

1. Douek DC, Roederer M, Koup RA. Emerging concepts in the immunopathogenesis of AIDS. *Annu Rev Med* (2009) **60**(1):471–84. doi:10.1146/annurev.med.60.041807.123549

2. Deeks SG, Lewin SR, Havlir DV. The end of AIDS: HIV infection as a chronic disease. *The lancet* (2013) **382**(9903):1525–33. doi:10.1016/s0140-6736(13)61809-7

3. Arena CT. Triumeq (dolutegravir/abacavir/lamivudine) for the Treatment of HIV (2015). Available online at: https://www.clinicaltrialsarena.com/projects/triumeq-dolutegravirabacavirlamivudine-for-the-treatment-of-hiv/?cf-view. (Accessed April 9, 2024)

4. Amblard F, Patel D, Michailidis E, Coats SJ, Kasthuri M, Biteau N, et al. HIV nucleoside reverse transcriptase inhibitors. *Eur J Med Chem* (2022) **240**:114554. doi:10.1016/j.ejmech.2022.114554

5. Sun Y, Xu M, Duan Q, Bryant JL, Xu X. The role of autophagy in the progression of HIV infected cardiomyopathy. *Front Cell Dev Biol* (2024) **12**:1372573. doi:10.3389/fcell.2024.1372573

6. Balogun K, Serghides L. Comparison of the effects of three dual-nucleos(t)ide reverse transcriptase inhibitor backbones on placenta mitochondria toxicity and oxidative stress using a mouse pregnancy model. *Pharmaceutics* (2022) **14**(5):1063. doi:10.3390/pharmaceutics14051063

7. Patel K, Huo Y, Jao J, Powis KM, Williams PL, Kacanek D, et al. Dolutegravir in pregnancy as compared with current HIV regimens in the United States. *New Engl J Med* (2022) **387**(9):799–809. doi:10.1056/nejmoa2200600

8. Drugs.com. Abacavir/dolutegravir/lamivudine pregnancy and breastfeeding warnings. (2024).

9. Siegfried N, van der Merwe L, Brocklehurst P, Sint TT. Antiretrovirals for reducing the risk of mother-to-child transmission of HIV infection. *The Cochrane database Syst Rev* (2011)(7) CD003510. doi:10.1002/14651858.cd003510.pub3

10. Guinane CM, Cotter PD. Role of the gut microbiota in health and chronic gastrointestinal disease: understanding a hidden metabolic organ. *Therap Adv Gastroenterol* (2013) **6**(4):295–308. doi:10.1177/1756283x13482996

11. Cossarizza A, Moyle G. Antiretroviral nucleoside and nucleotide analogues and mitochondria. *Aids* (2004) **18**(2):137–51. doi:10.1097/00002030-200401230-00002

12. Côté HC. Mechanisms of antiretroviral therapy-induced mitochondrial dysfunction. *Curr Opin HIV AIDS* (2007) **2**(4):253–60. doi:10.1097/coh.0b013e3281df3410

13. Ray S, Narayanan A, Giske CG, Neogi U, Sönnerborg A, Nowak P. Altered gut microbiome under antiretroviral therapy: impact of efavirenz and zidovudine. *ACS Infect Dis* (2020) **7**(5):1104–15. doi:10.1021/acsinfecdis.0c00536

14. Pinto-Cardoso S, Klatt NR, Reyes-Terán G. Impact of antiretroviral drugs on the microbiome: unknown answers to important questions. *Curr Opin HIV AIDS* (2018) **13**(1):53–60. doi:10.1097/COH.0000000000000428

15. Brown K, DeCoffe D, Molcan E, Gibson DL. Diet-induced dysbiosis of the intestinal microbiota and the effects on immunity and disease. *Nutrients* (2012) **4**(8):1095–119. doi:10.3390/nu4081095

16. Stärkel P, Leclercq S, de Timary P, Schnabl B. Intestinal dysbiosis and permeability: the yin and yang in alcohol dependence and alcoholic liver disease. *Clin Sci* (2018) **132**(2):199–212. doi:10.1042/cs20171055

17. Gong X, Ma Y, Deng X, Li A, Li X, Kong X, et al. Intestinal dysbiosis exacerbates susceptibility to the anti-NMDA receptor encephalitis-like phenotype by changing blood brain barrier permeability and immune homeostasis. *Brain Behav Immun* (2024) **116**:34–51. doi:10.1016/j.bbi.2023.11.030

18. Yin J, Liao SX, He Y, Wang S, Xia GH, Liu FT, et al. Dysbiosis of gut microbiota with reduced trimethylamine-N-oxide level in patients with large-artery atherosclerotic stroke or transient ischemic attack. *J Am Heart Assoc* (2015) **4**(11):e002699. doi:10.1161/jaha.115.002699

19. Boursier J, Mueller O, Barret M, Machado M, Fizanne L, Araujo-Perez F, et al. The severity of nonalcoholic fatty liver disease is associated with gut dysbiosis and shift in the metabolic function of the gut microbiota. *Hepatology* (2016) **63**(3):764–75. doi:10.1002/hep.28356

20. Kumari R, Ahuja V, Paul J. Fluctuations in butyrate-producing bacteria in ulcerative colitis patients of North India. *World J Gastroenterol* (2013) **19**(22):3404–14. doi:10.3748/wjg.v19.i22.3404

21. Seo K, Seo J, Yeun J, Choi H, Kim Y-I, Chang S-Y. The role of mucosal barriers in human gut health. *Arch Pharmacal Res* (2021) **44**(4):325–41. doi:10.1007/s12272-021-01327-5

22. Leech B, Schloss J, Steel A. Association between increased intestinal permeability and disease: a systematic review. *Adv Integr Med* (2019) **6**(1):23–34. doi:10.1016/j.aimed.2018.08.003

23. Bischoff SC, Barbara G, Buurman W, Ockhuizen T, Schulzke JD, Serino M, et al. Intestinal permeability--a new target for disease prevention and therapy. *BMC Gastroenterol* (2014) **14**:189. doi:10.1186/s12876-014-0189-7

24. Alwazzan A. The influence of gut microbiome derived neurotransmitters on neonatal immune response. *Pakistan BioMedical J* (2024) 01. doi:10.54393/pbmj.v7i04.1075

25. Willers M, Ulas T, Völlger L, Vogl T, Heinemann AS, Pirr S, et al. S100A8 and S100A9 are important for postnatal development of gut microbiota and immune system in mice and infants. *Gastroenterology* (2020) **159**(6):2130–45.e5. doi:10.1053/j.gastro.2020.08.019

26. Arrieta M-C, Stiemsma LT, Amenyogbe N, Brown EM, Finlay B. The intestinal microbiome in early life: health and disease. *Front Immunol* (2014) **5**: 427. doi:10.3389/fimmu.2014.00427

27. Muthumula CMR, Yanamadala Y, Gokulan K, Karn K, Cunny H, Sutherland V, et al. Effect of *in utero* and lactational exposure to antiretroviral therapy on the gut microbial composition and metabolic function in aged rat offspring. *Exp Biol Med (Maywood)* (2025) **250**:10468. doi:10.3389/ebm.2025.10468

28. Sengupta P. The laboratory rat: relating its age with human's. *Int J Prev Med* (2013) **4**(6):624–30.

29. Khare S, Ficht TA, Santos RL, Romano J, Ficht AR, Zhang S, et al. Rapid and sensitive detection of *Mycobacterium avium* subsp. paratuberculosis in bovine milk and feces by a combination of immunomagnetic bead separation-conventional PCR and real-time PCR. *J Clin Microbiol* (2004) **42**(3):1075–81. doi:10.1128/jcm.42.3.1075-1081.2004

30. Gohl DM, Vangay P, Garbe J, MacLean A, Hauge A, Becker A, et al. Systematic improvement of amplicon marker gene methods for increased accuracy in microbiome studies. *Nat Biotechnol* (2016) **34**(9):942–9. doi:10.1038/nbt.3601

31. Wang Q, Garrity GM, Tiedje JM, Cole JR. Naive Bayesian classifier for rapid assignment of rRNA sequences into the new bacterial taxonomy. *Appl Environ Microbiol* (2007) **73**(16):5261–7. doi:10.1128/aem.00062-07

32. MicrobiomeAnalyst. MicrobiomeAnalyst. (2024).

33. MetaboAnalyst. MetaboAnalyst. (2024).

34. Kobbe R, Schalkwijk S, Dunay G, Eberhard JM, Schulze-Sturm U, Hollwitz B, et al. Dolutegravir in breast milk and maternal and infant plasma during breastfeeding. *AIDS* (2016) **30**(17):2731–3. doi:10.1097/qad.0000000000001259

35. Vannappagari V, Thorne C. Pregnancy and neonatal outcomes following prenatal exposure to dolutegravir. *JAIDS J Acquired Immune Deficiency Syndromes* (2019) **81**(4):371–8. doi:10.1097/qai.0000000000002035

36. Healthcare V. Dolutegravir (DTG) + abacavir (ABC) + lamivudine (3TC) HIV/HCV medications guide: HIV/HCV medications guide (2022). Available online at: https://www.hivmedicationguide.com/medicament/dolutegravir-dtg-abacavir-abc-lamivudine-3tc/. (Accessed April 9, 2024)

37. Tian K, Jing D, Lan J, Lv M, Wang T. Commensal microbiome and gastrointestinal mucosal immunity: harmony and conflict with our closest neighbor. *Immun Inflamm Dis* (2024) **12**(7):e1316. doi:10.1002/iid3.1316

38. Fukata M, Arditi M. The role of pattern recognition receptors in intestinal inflammation. *Mucosal Immunol* (2013) **6**(3):451–63. doi:10.1038/mi.2013.13

39. Lahiani M, Gokulan K, Sutherland V, Cunny HC, Cerniglia CE, Khare S. Early developmental exposure to triclosan impacts fecal microbial populations, IgA and functional activities of the rat microbiome. *J Xenobiotics* (2024) **14**(1):193–213. doi:10.3390/jox14010012

40. d'Afflitto M, Upadhyaya A, Green A, Peiris M. Association between sex hormone levels and gut microbiota composition and diversity-A systematic review. *J Clin Gastroenterol* (2022) **56**(5):384–92. doi:10.1097/mcg.0000000000001676

41. Pittayanon R, Lau JT, Yuan Y, Leontiadis GI, Tse F, Surette M, et al. Gut microbiota in patients with irritable bowel syndrome—a systematic review. *Gastroenterology* (2019) **157**(1):97–108. doi:10.1053/j.gastro.2019.03.049

42. Zhou K, Jia L, Mao Z, Si P, Sun C, Qu Z, et al. Integrated macrogenomics and metabolomics explore alterations and correlation between gut microbiota and serum metabolites in adult epileptic patients: a pilot study. *Microorganisms* (2023) **11**(11):2628. doi:10.3390/microorganisms11112628

43. Li Q, Gu Y, Liang J, Yang Z, Qin J. A long journey to treat epilepsy with the gut microbiota. *Front Cell Neurosci* (2024) **18**:1386205. doi:10.3389/fncel.2024.1386205

44. Hung CC, Chang CC, Huang CW, Nouchi R, Cheng CH. Gut microbiota in patients with Alzheimer's disease spectrum: a systematic review and meta-analysis. *Aging (Albany NY)* (2022) **14**(1):477–96. doi:10.18632/aging.203826

45. Liu L, He X, Feng Y. Coronary heart disease and intestinal microbiota. *Coron Artery Dis* (2019) **30**(5):384–9. doi:10.1097/mca.0000000000000758

46. Khan I, Khan I, Jianye Z, Xiaohua Z, Khan M, Hilal MG, et al. Exploring blood microbial communities and their influence on human cardiovascular disease. *J Clin Lab Anal* (2022) **36**(4):e24354. doi:10.1002/jcla.24354

47. Lu Y-k, Chen T-y, Zhuang X-m, Li J, Jiang X-y, Xu S-s, et al. Mechanism study of sijunzi decoction on rats with heart failure through regulating the imbalance of intestinal flora. (2021).

48. origin L. Romboutsia ilealis: how is this bacteria linked to healthy fats? (2022). Available online at: https://layerorigin.com/blogs/blog-layer-origin-nutrition/romboutsia-ilealis-how-is-the-bacteria-is-linked-to-healthy-fats. (Accessed April 9, 2024)

49. Gerritsen J, Hornung B, Renckens B, van Hijum SA, Martins dos Santos VAP, Rijkers GT, et al. Genomic and functional analysis of Romboutsia ilealis CRIBT reveals adaptation to the small intestine. *PeerJ* (2017) **5**:e3698. doi:10.7717/peerj.3698

50. Lanthier N, Rodriguez J, Nachit MY, Hiel S, Trefois P, Neyrinck AM, et al. Lower abundance of Clostridium sensu stricto is associated with liver steatosis and fibrosis severity in a prospective cohort of obese patients with metabolic dysfunction-associated fatty liver disease. *Acta Gastro-Enterologica Belgica* (2021) **84**:A20.

51. Kwan SY, Jiao J, Joon A, Wei P, Petty LE, Below JE, et al. Gut microbiome features associated with liver fibrosis in Hispanics, a population at high risk for fatty liver disease. *Hepatology* (2022) **75**(4):955–67. doi:10.1002/hep.32197

52. Zhang B, Wang X, Xia R, Li C. Gut microbiota in coronary artery disease: a friend or foe? *Biosci Rep* (2020) **40**(5):BSR20200454. doi:10.1042/bsr20200454

53. Li J, Lin S, Vanhoutte PM, Woo CW, Xu A. Akkermansia muciniphila protects against atherosclerosis by preventing metabolic endotoxemia-induced inflammation in Apoe−/− mice. *Circulation* (2016) **133**(24):2434–46. doi:10.1161/circulationaha.115.019645

54. Zagato E, Pozzi C, Bertocchi A, Schioppa T, Saccheri F, Guglietta S, et al. Endogenous murine microbiota member Faecalibaculum rodentium and its human homologue protect from intestinal tumour growth. *Nat Microbiol* (2020) **5**(3):511–24. doi:10.1038/s41564-019-0649-5

55. Chai X, Wen L, Song Y, He X, Yue J, Wu J, et al. DEHP exposure elevated cardiovascular risk in obese mice by disturbing the arachidonic acid metabolism of gut microbiota. *Sci The Total Environ* (2023) **875**:162615. doi:10.1016/j.scitotenv.2023.162615

56. Oñate FP, Chamignon C, Burz SD, Lapaque N, Monnoye M, Philippe C, et al. Adlercreutzia equolifaciens is an anti-inflammatory commensal bacterium with decreased abundance in gut microbiota of patients with metabolic liver disease. *Int J Mol Sci* (2023) **24**(15):12232. doi:10.3390/ijms241512232

57. Wang M, Zhang Y, Miller D, Rehman NO, Cheng X, Yeo J-Y, et al. Microbial reconstitution reverses early female puberty induced by maternal high-fat diet during lactation. *Endocrinology* (2020) **161**(2):bqz041. doi:10.1210/endocr/bqz041

58. Bo T-B, Zhang X-Y, Kohl KD, Wen J, Tian S-J, Wang D-H. Coprophagy prevention alters microbiome, metabolism, neurochemistry, and cognitive behavior in a small mammal. *The ISME J* (2020) **14**(10):2625–45. doi:10.1038/s41396-020-0711-6

EBM Experimental Biology and Medicine

TYPE Brief Communication
PUBLISHED 14 August 2025
DOI 10.3389/ebm.2025.10524

OPEN ACCESS

*CORRESPONDENCE
Hakon Hakonarson,
hakonarson@email.chop.edu

RECEIVED 12 February 2025
ACCEPTED 01 August 2025
PUBLISHED 14 August 2025

CITATION
Qu H-Q, Goel K, Ostberg K, Slater DJ, Wang F, Snyder J, Hou C, Eister G, Connolly JJ, March M, Glessner JT, Kao C and Hakonarson H (2025) Natural killer cell subpopulations in the peripheral blood of single ventricle/hypoplastic left heart syndrome patients via single-cell RNA sequencing. *Exp. Biol. Med.* 250:10524. doi: 10.3389/ebm.2025.10524

Natural killer cell subpopulations in the peripheral blood of single ventricle/hypoplastic left heart syndrome patients via single-cell RNA sequencing

Hui-Qi Qu[1], Kushagra Goel[1], Kayleigh Ostberg[1], Diana J. Slater[1], Fengxiang Wang[1], James Snyder[1], Cuiping Hou[1], Garnet Eister[1], John J. Connolly[1], Michael March[1], Joseph T. Glessner[1,2,3], Charlly Kao[1] and Hakon Hakonarson[1,2,3,4,5]*

[1]The Center for Applied Genomics, Children's Hospital of Philadelphia, Philadelphia, PA, United States, [2]Department of Pediatrics, The Perelman School of Medicine, University of Pennsylvania, Philadelphia, PA, United States, [3]Division of Human Genetics, Children's Hospital of Philadelphia, Philadelphia, PA, United States, [4]Division of Pulmonary Medicine, Children's Hospital of Philadelphia, Philadelphia, PA, United States, [5]Faculty of Medicine, University of Iceland, Reykjavik, Iceland

Abstract

Natural Killer (NK) cells are integral components of the innate immune system, recognizing and eliminating virus-infected cells. They may play a crucial role in the immune response and contribute to the complications associated with Single Ventricle/Hypoplastic Left Heart Syndrome (SV/HLHS). Utilizing single-cell RNA sequencing (scRNA-seq), NK cells from peripheral blood mononuclear cells (PBMCs) were analyzed in three de-identified SV/HLHS cases and three healthy controls. This study identified two novel NK cell subpopulations that could not be detected by conventional scRNA-seq pipelines or traditional flow cytometry. These subpopulations exhibit distinct gene expression profiles linked to the heterogeneity of immune responsiveness and stress adaptation in NK cells. In SV/HLHS patients, one cluster showed a significant upregulation of androgen response and downregulation of heme metabolism compared to healthy controls. Our study offers new insights into the fine-tuning of immune modulation that could help mitigate complications in SV/HLHS. It suggests that while NK cells in SV/HLHS adapt to support survival in a challenging physiological environment, these adaptations may compromise their ability to effectively respond to additional stresses, such as infections and inflammation.

KEYWORDS

NK cells, peripheral blood mononuclear cells, single-cell RNA sequencing, single ventricle/hypoplastic left heart syndrome, transcriptome

Impact statement

This study identifies two previously unrecognized natural killer (NK) cell subpopulations that were undetectable using conventional methods. By applying single-cell RNA sequencing with sophisticated analytical approaches, we provide definitive molecular evidence of their existence and functional relevance. These subpopulations display distinct gene expression patterns, offering new insights into immune system variability and stress adaptation in NK cells. In patients with single ventricle/Hypoplastic Left Heart Syndrome (SV/HLHS), we identify an NK cell subset with increased androgen signaling and decreased heme metabolism, a shift that is significantly more pronounced compared to healthy controls. These findings advance our understanding of immune adaptation in congenital heart disease and suggest that while NK cells compensate for physiological stress, their altered state may reduce their ability to respond to secondary challenges such as infections and inflammation. This work provides a foundation for future research on immune modulation in SV/HLHS and potential therapeutic interventions.

Introduction

Natural Killer (NK) cells are integral components of the innate immune system, renowned for their ability to identify and eliminate viral-infected cells and tumor cells without prior sensitization [1]. They serve as a first line of defense by exerting cytotoxic effects and producing cytokines that modulate adaptive immune responses [2]. The functionality and population of NK cells are critical for maintaining immune homeostasis and effective immunosurveillance.

Single-ventricle physiology encompasses several rare congenital heart defects and is estimated to occur in approximately 4–8 per 10,000 live births, representing roughly 7.7% of all congenital heart defects [3]. Hypoplastic Left Heart Syndrome (HLHS) is the most common form of functional single-ventricle disease. SV/HLHS results in reliance on the right ventricle to support systemic circulation [4]. Patients with SV/HLHS undergo a series of palliative surgeries to reconstruct the heart's anatomy and improve hemodynamics [4]. Despite surgical advancements, these patients often experience complications such as increased susceptibility to infections, protein-losing enteropathy, thrombosis, and chronic inflammation [5]. NK cell number and function may be compromised in individuals with SV/HLHS due to factors such as chronic hypoxia, repeated surgical trauma, lymphatic dysfunction, and nutritional deficiencies [6, 7]. These issues may impair NK cell development, reduce cytotoxic capacity, and weaken the immune response, which may explain why SV/HLHS patients are more vulnerable to infections and postoperative complications, and may also contribute to systemic inflammation, worsening heart failure and overall morbidity.

In our study of single-cell RNA sequencing (scRNA-seq) from peripheral blood mononuclear cells (PBMCs) of patients with SV/HLHS, we found that gene expression in NK cells is more closely correlated with SV/HLHS than in other cell types by weighted gene co-expression network analysis (WGCNA). In congenital heart diseases (CHD) including SV/HLHS, NK cells play a crucial role in managing infections and mediating complications related to CHD [8]. In our previous study, we identified 1,600 genes that showed differential expression (DE) in NK cells of SV/HLHS patients [9]. Our current investigation suggests that NK cells in SV/HLHS patients are heterogeneous and potentially receptive of different types of immune modulation. We hypothesized that the SV/HLHS-related DE genes might be affected differently across specific NK cell subpopulations, instead of uniformly across all NK cells. To test this hypothesis, we delved into the single cell transcriptome of NK cells in greater detail.

Materials and methods

scRNA-seq of PBMCs

This study received approval from the Institutional Review Board at the Children's Hospital of Philadelphia (CHOP). PBMCs from three de-identified children (2 males and 1 female) with SV/HLHS were compared to those from three healthy controls (2 males and 1 female). The study design included three biologically independent SV/HLHS cases and three matched healthy controls, providing three replicates per group. This level of replication is commonly accepted in exploratory studies, where the primary goal is to identify robust and biologically meaningful patterns. Blood samples were collected in EDTA-coated tubes and promptly processed at the Center for Applied Genomics (CAG) at CHOP. PBMCs were isolated using Ficoll density gradient centrifugation. scRNA-seq for each sample was conducted using the 10X Chromium Single Cell Gene Expression assay (10x Genomics, Single Cell 3' v3) [10]. Sequencing was performed on the Illumina HiSeq2500 SBS v4 platform. The resulting data from the Chromium scRNA-seq were processed with the Cell Ranger 7.1.0 software suite (10x Genomics), with sequencing reads aligned to the GRCh38 reference genome. The number of cells sequenced and analyzed for each sample ranged from 4,598 to 14,298.

Data analysis tools

The scRNA-seq data were analyzed using the Seurat R package (v 5.1.0) [11, 12]. Cells were retained if they had more than 200 and fewer than 5,000 detected genes and <15% mitochondrial-gene reads. Gene expression was normalized with the LogNormalize method (scale factor = 10,000). We identified the top 2,000 variable genes with the variance-stabilizing transformation (vst) method, scaled all genes, and performed principal-component analysis (PCA). The first 10 PCs were used to construct a shared-

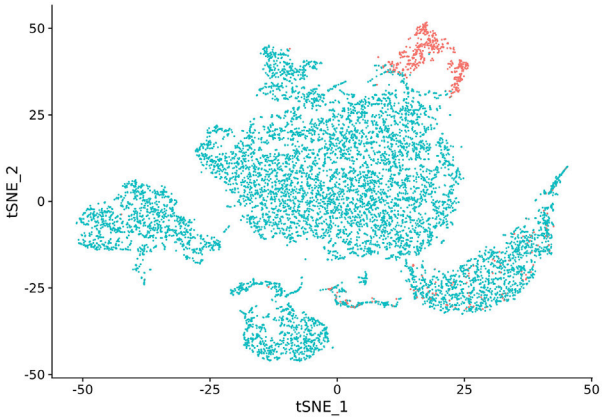

FIGURE 1
NK cell cluster versus other cell types visualized by t-SNE. NK cells are highlighted in red.

nearest-neighbor (SNN) graph, and clusters were called with the Louvain algorithm (resolution = 0.5). Uniform manifold approximation and projection (UMAP) based on the same PCs provided two-dimensional visualization. Marker genes were defined using min.pct = 0.25 and $|\log_2 FC| > 0.25$.

Natural-killer (NK) cells were identified with SingleR in combination with celldex::DatabaseImmuneCellExpressionData () [13], yielding 548 – 939 NK cells per sample after filtering. To resolve NK-cell heterogeneity, we extracted the normalized NK-cell expression matrices, transposed them (rows = cells, columns = genes), and performed unsupervised K-means clustering with scikit-learn (v 1.4.0) [14]. Candidate cluster numbers k = 2 – 10 were evaluated, and the solution with the highest average silhouette score was chosen; clustering was run with random_state = 0 for full reproducibility. Outliers were defined as cells lying more than 2 SD beyond the mean Euclidean distance to their cluster centroid. Cluster structure was visualized with t-distributed stochastic neighbor embedding (t-SNE) [15], and plots were generated in matplotlib [16]. Cluster assignments and outlier flags are provided as Supplementary Data.

Gene-set enrichment analysis (GSEA v 4.3.2) [17] was carried out against the Hallmark collection [18] of the Molecular Signatures Database (MSigDB) [19]. Differential-expression testing between NK-cell clusters (excluding genes used for K-means clustering) was performed on log-transformed counts with a two-sample, two-tailed Student's t-test. We used the CellChat R package (version 1.6.1) [17] to infer intercellular communication networks from our normalized NK cell expression data.

Results

The three cases have been followed at CHOP since birth. The first case is a 13-year-old male with HLHS who has undergone multiple staged cardiac surgeries, including the Fontan and Sano procedures. His clinical course is complicated by feeding difficulties necessitating gastrostomy tube (G-tube) feeding, vocal cord paralysis, developmental delays, and recurrent respiratory infections. He has also experienced atrial flutter, thrombosis, and multiple allergies, requiring ongoing medical management. The second case is a 15-year-old male with HLHS and additional congenital heart defects, including atrioventricular canal and coarctation of the aorta. He has undergone the Fontan and hemi-Fontan operations and presents with feeding difficulties, gastroesophageal reflux, and a hypercoagulable state. Frequent embolic events necessitate chronic anticoagulation therapy. His family history includes congenital anomalies and asthma. The third case, a female who died at age 11, had a single ventricle physiology with an unbalanced atrioventricular canal, Tetralogy of Fallot, congenital heart block, and heterotaxy syndrome. She underwent a bidirectional Glenn shunt and pacemaker placement. Her clinical course was further complicated by developmental delay, feeding difficulties, chronic lung disease, pulmonary hypertension, and recurrent wound complications, requiring nasogastric tube feeding and long-term cardiovascular support.

Heterogeneous NK cell clusters with amplified changes of transcriptomic profiles in SV/HLHS

In our study, we observed that NK cell clusters tend to be heterogeneous (Figure 1). With their function still unknown, there are no definitive gene markers available to classify these NK subpopulations with conventional scRNA-seq pipelines or traditional flow cytometry. To test whether these heterogeneous NK cells are responsible for the DE genes, we examined the 1600 DE genes identified in NK cells from our previous study [9]. K-means clustering with these DE genes yielded high Silhouette scores with 2 clusters in all the 6 samples (Figure 2). As shown in Figure 3, the NK cells within the same sample can be divided into two distinct clusters. Despite clinical heterogeneity among the cases, including differences in anatomical diagnoses, surgical histories, and comorbid conditions, we observed consistent NK cell clustering patterns and transcriptomic signatures across all three samples, suggesting a potentially conserved NK cell transcriptomic signature in SV/HLHS. We then performed GSEA using the averaged difference between the two clusters across the three cases (Table 1; Supplementary Table S1). In one cluster, the gene sets HALLMARK_ANDROGEN_RESPONSE and HALLMARK_HYPOXIA are significantly upregulated, and HALLMARK_HEME_METABOLISM is significantly downregulated.

Compared to the controls, the upregulated androgen response and downregulated heme metabolism are more significant in the cases, as shown by Cluster expression in Cases vs. Controls in Table 1. In addition, upregulation of the gene sets HALLMARK_OXIDATIVE_PHOSPHORYLATION, HALLMARK_INTERFERON_ALPHA_RESPONSE, and HALLMARK_INTERFERON_GAMMA_RESPONSE are more significant in Cluster 1.

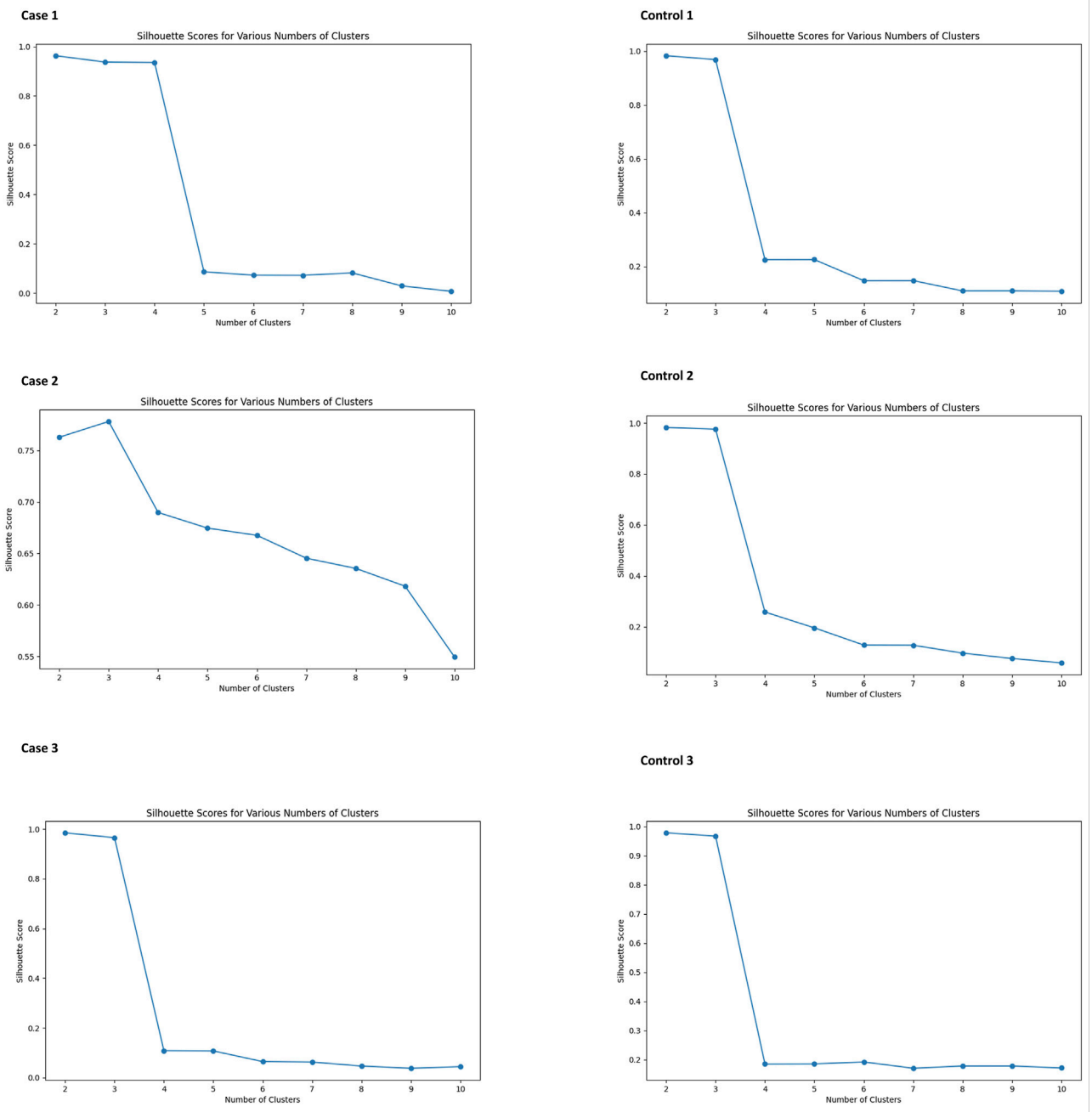

FIGURE 2
Silhouette scores for various numbers of clusters in K-means analysis of NK cells. All subjects show high Silhouette scores with two clusters.

Other gene expression in the two clusters of NK cells

To further characterize the two NK cell clusters, we examined the expression of the two NK cell clusters for genes not used for the clustering. We identified 789 genes with DE between the two clusters in all three cases (Supplementary Table S2). GSEA analysis showed upregulated HALLMARK_ALLOGRAFT_REJECTION and downregulated HALLMARK_UV_RESPONSE_DN in Cluster 1 in cases. The downregulated HALLMARK_UV_RESPONSE_DN in Cluster 1 in cases is more significant than that in controls (Table 1). CellChat-inferred ligand–receptor interactions between Cluster 0 and Cluster 1 are listed in Supplementary Table S3.

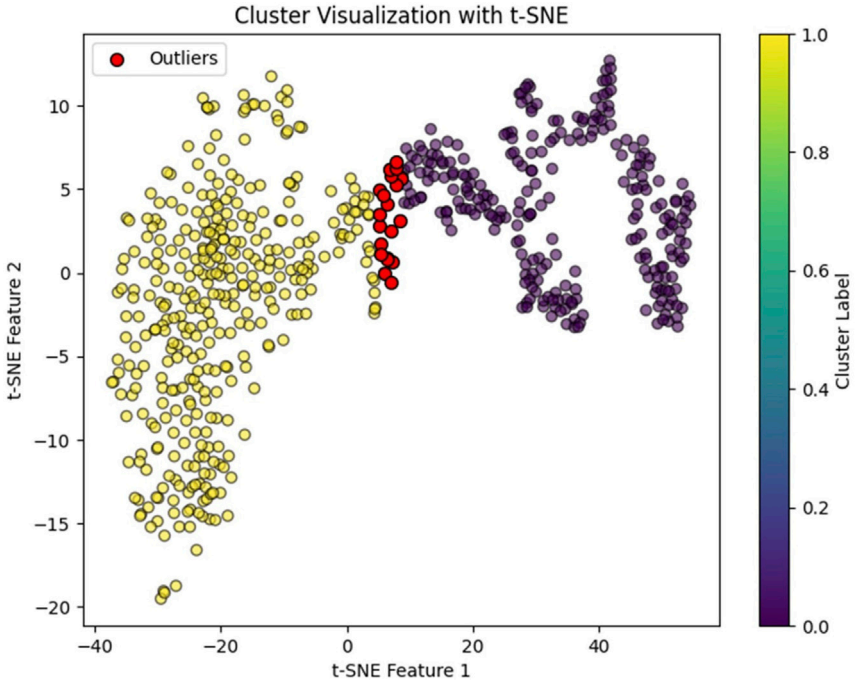

FIGURE 3
NK cell clusters visualized by t-SNE. Red dots indicate identified outliers.

Discussion

In this study, we identified heterogeneous NK cell clusters with amplified transcriptomic changes in SV/HLHS. These gene-expression differences may not only arise as consequences of the cardiac condition but may also shape distinct clinical trajectories, offering potential transcriptomic features and intervention points for infection control, thrombosis, and protein-losing enteropathy.

Distinct functional NK cell populations

In our analysis of NK cell populations, Cluster 1 exhibits distinct transcriptional profiles compared to Cluster 0 in term of the DE genes associated with SV/HLHS, marked by significant upregulation of gene sets including HALLMARK_ANDROGEN_RESPONSE and HALLMARK_HYPOXIA, alongside a notable downregulation of HALLMARK_HEME_METABOLISM. Androgen signaling may modulate NK cell immune functions, potentially tempering their cytotoxic activity while promoting survival and adaptation, particularly under stress [20]. Concurrently, the increased expression of hypoxia-responsive genes likely enhances NK cells' capability to operate in oxygen-deprived environments [21]. The reduced heme metabolism complements the other observed changes by potentially reducing oxidative stress and regulating metabolic responses, including oxidative phosphorylation, amino acid, and xenobiotic metabolism [22], likely shifting towards more energy-conserving processes and potentially linking Cluster 1 to the elevated thrombotic risk observed clinically. Collectively, these transcriptional changes suggest that NK cells in Cluster 1 are likely geared towards adaptation and survival in hypoxic or stress-related conditions. In contrast, Cluster 0 with different gene expression patterns might retain a higher cytotoxic capability and responsiveness, better suited for environments requiring rapid and robust immune reactions without the adaptive pressures of chronic stress.

The distinct overexpression of cytotoxic effector genes *NKG7*, *GNLY*, *GZMB*, and *FGFBP2* in Cluster 1 versus key transcription factors *ZEB1*, *BACH2*, and *BCL11B* in the other reflects divergent, subtype-specific regulatory networks and stable epigenetic landscapes. Studies show *BACH2* loss drives a discrete cytotoxic program with increased granzymes rather than a gradual shift [23], *ZEB1* expression is associated with maintenance/less-cytotoxic states by repressing effector loci [24], and *BCL11B* drives a distinct adaptive-like differentiation incompatible with the cytotoxic program [25]. In addition, epigenetic analyses reveal fixed chromatin states for each subtype [26], and single-cell clustering consistently uncovers separate NK endpoints with no intermediate transcriptional profiles [27]. These marker genes show

TABLE 1 Gene sets with statistical significance identified by GSEA analysis.

HALLMARK gene set	Size	ES	NES	NOM p-val	FDR q-val
1,600 genes for cell clustering with differential expression in NK cells associated with SV/HLHS					
Cluster 1 vs. cluster 0: upregulated					
ANDROGEN_RESPONSE	16	0.81	1.97	0	0
HYPOXIA	20	0.66	1.64	0.009	0.041
Cluster 1 vs. Cluster 0: downregulated					
HEME_METABOLISM	23	−0.74	−1.74	0	0.004
Cluster expression in Cases vs. Controls: upregulated					
ANDROGEN_RESPONSE	16	0.81	1.94	0	0.004
OXIDATIVE_PHOSPHORYLATION	52	0.63	1.8	0.001	0.021
INTERFERON_ALPHA_RESPONSE	23	0.68	1.73	0.006	0.031
INTERFERON_GAMMA_RESPONSE	38	0.63	1.71	0.004	0.027
Cluster expression in Cases vs. Controls: downregulated					
HEME_METABOLISM	23	−0.65	−1.9	0.005	0.03
789 genes with differential expression between two clusters in NK cells[a]					
Cluster 1 vs. Cluster 0: upregulated					
ALLOGRAFT_REJECTION	25	0.68	1.54	0	0.022
Cluster 1 vs. Cluster 0: downregulated					
UV_RESPONSE_DN	15	−0.43	−1.58	0	0
Cluster expression in Cases vs. Controls: upregulated					
Nonsignficant					
Cluster expression in Cases vs. Controls: downregulated					
UV_RESPONSE_DN	15	−0.85	−3.06	0	0

[a]These genes have not been identified as differentially expressed in NK, cells associated with SV/HLHS, and were not used for cell clustering.
ES: enrichment score; NES: normalized enrichment score; NOM p-val: nominal p-value; FDR: false discovery rate.

differential expression in opposite directions between clusters, emphasizing their divergent functional programs without evidence of a gradual transition pattern. Together, these patterns support the interpretation that the subtypes represent two functionally opposite, terminal NK cell states rather than stages along a developmental or activation trajectory.

In addition, our cell–cell communication analysis revealed that the cytotoxic cluster (Cluster 1) preferentially engages inhibitory checkpoints such as HLA-E binding to the CD94/NKG2A heterodimer [28, 29] and TGFB1 signaling through TGFβR1/2 [30], suggesting built-in mechanisms to restrain potent effector activity, whereas the transcription factor–high cluster (Cluster 0) shows alternative contact-mediated interactions (e.g., CLEC2–KLRB1) [31], consistent with niche or maintenance signals. These divergent communication patterns align with the distinct overexpression of the DE genes described above. Together, they reinforce that each subtype represents a terminal NK cell state with its own regulatory network and signaling milieu.

Distinct adaptations in cluster 1 NK cells in SV/HLHS patients

The two clusters of NK cells observed in our study, present in both healthy controls and cases, likely represent distinct functional states tailored to specific immunological needs. Notably, marked differences in the expression profiles of these clusters between cases and controls were observed, as shown by Cluster expression in Cases vs. Controls in Table 1. Cluster 1 in the cases shows significantly heightened androgen response and

more pronounced downregulation of heme metabolism compared to controls. These changes may serve a dual role. This modulation could be protective, reducing potential tissue damage in chronic disease contexts such as seen in SV/HLHS. On the other hand, this reduced cytotoxicity might compromise the NK cells' ability to clear pathogens effectively, potentially increasing the risk of infections. In addition, upregulation of the gene sets related to oxidative phosphorylation, and interferon responses, both alpha and gamma, are more significant in Cluster 1 in cases. Enhanced oxidative phosphorylation indicates that these NK cells have elevated energy production capabilities [32]. Upregulated Interferon responses imply this cluster of NK cells is primed for responding to viral infections and potentially other pathogens [33]. Altogether, upregulated HALLMARK_ANDROGEN_RESPONSE and downregulated HALLMARK_HEME_METABOLISM, plus these additional adaptations, suggest strategic modifications of NK cells to meet the demands of specific pathological states in prolonged exposure to pathogens or inflammatory conditions in SV/HLHS. These findings raise the possibility that pharmacologic modulation of these pathways could help restore a more balanced NK-cell phenotype, enhancing cytotoxicity while preserving protective adaptation in SV/HLHS.

Further characterization of the two NK cell clusters

In our extended analysis, we examined additional gene expressions within the two NK cell clusters beyond those initially used for clustering. This examination revealed 789 genes with DE between the two clusters across all cases. Specifically, Cluster 1 in cases exhibited upregulated HALLMARK_ALLOGRAFT_REJECTION and downregulated HALLMARK_UV_RESPONSE_DN. The upregulation of the allograft rejection gene set in Cluster 1 underscores a heightened immunological readiness to recognize and attack non-self cells, a crucial feature for defending against foreign tissues and potentially harmful pathogens [34]. The downregulation of genes associated with the UV response, including key regulators like *DYRK1A, ATXN1, ATP2B1, NIPBL, RUNX1*, and *SIPA1L1*, presents a complex scenario. These genes are crucial for various NK cell functions such as signaling, development, and effector responses [35, 36]. Their reduced expression might impair the NK cells' capacity for regular immune surveillance and cellular migration. Furthermore, the downregulation of genes associated with the UV response in cases is significantly higher than controls. When considered together, these opposing trends in gene expression paint a picture of a dual nature in NK cells in Cluster 1, which could render these NK cells less effective in handling routine immune tasks, posing risks for viral infections and complicate the management of SV/HLHS.

A focused transcriptomic signature derived from these findings could be developed for longitudinal monitoring, with potential to correlate expression dynamics with postoperative infection rates and lymphatic complications. Functional assays will also be critical to determine whether restoring regulators like *RUNX1* can reverse migratory defects without exacerbating inflammation. This complexity may underlie both the heightened inflammatory tone and reduced immune resilience seen in SV/HLHS patients.

Conclusion

Overall, these findings provide an initial gene expression profile of NK cells in SV/HLHS, suggesting potential adaptations that may support survival in a challenging physiological environment. However, these adaptations could also compromise the cells' ability to manage additional stresses, such as infections and inflammation. Given that this analysis is based solely on gene expression data without proteomic or functional validation, the conclusions should be interpreted with caution. Further studies, incorporating proteomics and functional assays, are necessary to fully understand the immune implications and to develop targeted strategies that support immune function without exacerbating the underlying condition. A longitudinal profiling of NK cells over time, rather than a single timepoint, would provide valuable insights into their role in disease progression and adaptation.

One limitation of this study is the small sample size. However, the consistent identification of two distinct NK cell clusters in all three healthy controls, along with statistically significant findings, supports the robustness of our results. Another limitation is the current lack of knowledge regarding the subpopulations of NK cells in peripheral blood. We hope this study brings attention to the heterogeneity of NK cells in peripheral blood and encourages further research into these subpopulations. An additional important limitation is the clinical heterogeneity among the cases, including differences in sex, associated cardiac anomalies, surgical interventions, and comorbidities such as developmental delays and hypercoagulable states. This heterogeneity reflects the complexity of SV/HLHS patients and poses a challenge to isolating disease-specific transcriptomic signatures. Nonetheless, the reproducibility of NK cell clustering and the consistent enrichment of specific gene expression pathways across all cases support the presence of a shared transcriptomic program. Future studies with larger, stratified cohorts will be essential to investigate how specific clinical variables may shape immune cell behavior.

Author contributions

Conceptualization, H-QQ, CK, and HH; methodology, H-QQ and KG; validation, H-QQ; formal analysis, H-QQ and

KG; investigation, H-QQ, KG, KO, DS, FW, JS, CH, JC, MM, JG, and CK; resources, JG and CK; data curation, H-QQ; writing – original draft preparation, H-QQ; writing – review and editing, H-QQ and HH; visualization, H-QQ; supervision, HH; project administration, H-QQ, CK, and HH; funding acquisition, HH. All authors contributed to the article and approved the submitted version.

Data availability

All data generated or analyzed during this study are included in the article and its Supplementary Material. The raw sequencing datasets presented in this article are not readily available because of privacy and ethical restrictions; requests to access these datasets should be directed to the corresponding author.

Ethics statement

The studies involving humans were approved by Institutional Review Board (IRB) of the Children's Hospital of Philadelphia (CHOP) with the IRB number: IRB 16-013278. The studies were conducted in accordance with the local legislation and institutional requirements. Written informed consent for participation in this study was provided by the participants' legal guardians/next of kin.

Funding

The author(s) declare that financial support was received for the research and/or publication of this article. The study was supported by the Institutional Development Funds from the Children's Hospital of Philadelphia to the Center for Applied Genomics, and The Children's Hospital of Philadelphia Endowed Chair in Genomic Research to HH.

Conflict of interest

The author(s) declared no potential conflicts of interest with respect to the research, authorship, and/or publication of this article.

Generative AI statement

The author(s) declare that no Generative AI was used in the creation of this manuscript.

Supplementary material

The Supplementary Material for this article can be found online at: https://www.ebm-journal.org/articles/10.3389/ebm.2025.10524/full#supplementary-material

References

1. Kiessling R, Klein E, Wigzell H. "natural" killer cells in the mouse. I. Cytotoxic cells with specificity for mouse moloney leukemia cells. Specificity and distribution according to genotype. *Eur J Immunol* (1975) **5**:112–7. doi:10.1002/eji.1830050208

2. Orange JS, Ballas ZK. Natural killer cells in human health and disease. *Clin Immunol* (2006) **118**:1–10. doi:10.1016/j.clim.2005.10.011

3. O'Leary PW. Prevalence, clinical presentation and natural history of patients with single ventricle. *Prog Pediatr Cardiol* (2002) **16**:31–8. doi:10.1016/s1058-9813(02)00042-5

4. Ohye RG, Schranz D, D'Udekem Y. Current therapy for hypoplastic left heart syndrome and related single ventricle lesions. *Circulation* (2016) **134**:1265–79. doi:10.1161/circulationaha.116.022816

5. Kritzmire SM, Cossu AE. Hypoplastic left heart syndrome. (2020).

6. Chang T-D, Chen D, Luo J-L, Wang Y-M, Zhang C, Chen S-Y, et al. The different paradigms of NK cell death in patients with severe trauma. *Cell Death & Dis* (2024) **15**:606. doi:10.1038/s41419-024-06992-0

7. Lubin LN. Multi-systemic consequences of CHD and the impact on perioperative care. In: *Congenital heart disease in pediatric and adult patients: anesthetic and perioperative management*. Springer (2023). p. 323–45.

8. Wienecke LM, Cohen S, Bauersachs J, Mebazaa A, Chousterman BG. Immunity and inflammation: the neglected key players in congenital heart disease? *Heart Fail Rev* (2022) **27**:1957–71. doi:10.1007/s10741-021-10187-6

9. Qu H-Q, Ostberg K, Slater DJ, Wang F, Snyder J, Hou C, et al. Single-cell RNA sequencing of peripheral blood mononuclear cells in patients with single ventricle/hypoplastic left heart syndrome. *medRxiv* (2024).

10. Qu H-Q, Kao C, Garifallou J, Wang F, Snyder J, Slater DJ, et al. Single cell transcriptome analysis of peripheral blood mononuclear cells in freshly isolated *versus* stored blood samples. *Genes* (2023) **14**:142. doi:10.3390/genes14010142

11. Butler A, Hoffman P, Smibert P, Papalexi E, Satija R. Integrating single-cell transcriptomic data across different conditions, technologies, and species. *Nat Biotechnol* (2018) **36**:411–20. doi:10.1038/nbt.4096

12. Satija R, Farrell JA, Gennert D, Schier AF, Regev A. Spatial reconstruction of single-cell gene expression data. *Nat Biotechnol* (2015) **33**:495–502. doi:10.1038/nbt.3192

13. Aran D, Looney AP, Liu L, Wu E, Fong V, Hsu A, et al. Reference-based analysis of lung single-cell sequencing reveals a transitional profibrotic macrophage. *Nat Immunol* (2019) **20**:163–72. doi:10.1038/s41590-018-0276-y

14. Pedregosa F, Varoquaux G, Gramfort A, Michel V, Thirion B, Grisel O, et al. Scikit-learn: machine learning in python. *J machine Learn Res* (2011) **12**:2825–30. doi:10.5555/1953048.2078195

15. Cieslak MC, Castelfranco AM, Roncalli V, Lenz PH, Hartline DK. t-Distributed stochastic neighbor embedding (t-SNE): a tool for eco-physiological transcriptomic analysis. *Mar genomics* (2020) **51**:100723. doi:10.1016/j.margen.2019.100723

16. Hunter JD. Matplotlib: a 2D graphics environment. *Comput Sci & Eng* (2007) **9**:90–5. doi:10.1109/mcse.2007.55

17. Jin S, Guerrero-Juarez CF, Zhang L, Chang I, Ramos R, Kuan C-H, et al. Inference and analysis of cell-cell communication using CellChat. *Nat Commun* (2021) **12**:1088. doi:10.1038/s41467-021-21246-9

18. Liberzon A, Birger C, Thorvaldsdóttir H, Ghandi M, Mesirov JP, Tamayo P. The molecular signatures database (MSigDB) hallmark gene set collection. *Cell Syst* (2015) **1**:417–25. doi:10.1016/j.cels.2015.12.004

19. Subramanian A, Tamayo P, Mootha VK, Mukherjee S, Ebert BL, Gillette MA, et al. Gene set enrichment analysis: a knowledge-based approach for interpreting genome-wide expression profiles, *Proceedings of the National Academy of Sciences*

of the United States of America. (2005) **102**:15545–50. doi:10.1073/pnas.0506580102

20. Liu Q, You B, Meng J, Huang C-P, Dong G, Wang R, et al. Targeting the androgen receptor to enhance NK cell killing efficacy in bladder cancer by modulating ADAR2/circ_0001005/PD-L1 signaling. *Cancer Gene Ther* (2022) **29**:1988–2000. doi:10.1038/s41417-022-00506-w

21. Parodi M, Raggi F, Cangelosi D, Manzini C, Balsamo M, Blengio F, et al. Hypoxia modifies the transcriptome of human NK cells, modulates their immunoregulatory profile, and influences NK cell subset migration. *Front Immunol* (2018) **9**:2358. doi:10.3389/fimmu.2018.02358

22. Dunaway LS, Loeb SA, Petrillo S, Tolosano E, Isakson BE. Heme metabolism in nonerythroid cells. *J Biol Chem* (2024) 300. doi:10.1016/j.jbc.2024.107132

23. Imianowski CJ, Whiteside SK, Lozano T, Evans AC, Benson JD, Courreges CJF, et al. BACH2 restricts NK cell maturation and function, limiting immunity to cancer metastasis. *J Exp Med* (2022) 219. doi:10.1084/jem.20211476

24. Scott CL, Omilusik KD. ZEBs: novel players in immune cell development and function. *Trends Immunol* (2019) **40**:431–46. doi:10.1016/j.it.2019.03.001

25. Holmes TD, Pandey RV, Helm EY, Schlums H, Han H, Campbell TM, et al. The transcription factor Bcl11b promotes both canonical and adaptive NK cell differentiation. *Sci Immunol* (2021) **6**:eabc9801. doi:10.1126/sciimmunol.abc9801

26. Xia M, Wang B, Wang Z, Zhang X, Wang X. Epigenetic regulation of NK cell-mediated antitumor immunity. *Front Immunol* (2021) **12**:672328. doi:10.3389/fimmu.2021.672328

27. de Andrade LF, Lu Y, Luoma A, Ito Y, Pan D, Pyrdol JW, et al. Discovery of specialized NK cell populations infiltrating human melanoma metastases. *JCI insight* (2019) **4**:e133103. doi:10.1172/jci.insight.133103

28. Borst L, van der Burg SH, van Hall T. The NKG2A–HLA-E axis as a novel checkpoint in the tumor microenvironment. *Clin Cancer Res* (2020) **26**:5549–56. doi:10.1158/1078-0432.ccr-19-2095

29. Gaynor LM, Colucci F. Uterine natural killer cells: functional distinctions and influence on pregnancy in humans and mice. *Front Immunol* (2017) **8**:467. doi:10.3389/fimmu.2017.00467

30. Allan DS, Rybalov B, Awong G, Zúñiga-Pflücker JC, Kopcow HD, Carlyle JR, et al. TGF-β affects development and differentiation of human natural killer cell subsets. *Eur J Immunol* (2010) **40**:2289–95. doi:10.1002/eji.200939910

31. Bartel Y, Bauer B, Steinle A. Modulation of NK cell function by genetically coupled C-type lectin-like receptor/ligand pairs encoded in the human natural killer gene complex. *Front Immunol* (2013) **4**:362. doi:10.3389/fimmu.2013.00362

32. Wang Z, Guan D, Wang S, Chai LYA, Xu S, Lam K-P. Glycolysis and oxidative phosphorylation play critical roles in natural killer cell receptor-mediated natural killer cell functions. *Front Immunol* (2020) **11**:202. doi:10.3389/fimmu.2020.00202

33. Gidlund M, Örn A, Wigzell H, Senik A, Gresser I. Enhanced NK cell activity in mice injected with interferon and interferon inducers. *Nature* (1978) **273**:759–61. doi:10.1038/273759a0

34. Hamada S, Dubois V, Koenig A, Thaunat O. Allograft recognition by recipient's natural killer cells: molecular mechanisms and role in transplant rejection. *Hla* (2021) **98**:191–9. doi:10.1111/tan.14332

35. Voon DCC, Hor YT, Ito Y. The RUNX complex: reaching beyond haematopoiesis into immunity. *Immunology* (2015) **146**:523–36. doi:10.1111/imm.12535

36. Matsuura K, Kobayashi S, Konno K, Yamasaki M, Horiuchi T, Senda T, et al. SIPA1L1/SPAR1 interacts with the neurabin family of proteins and is involved in GPCR signaling. *The J Neurosci* (2022) **42**:2448–73. doi:10.1523/jneurosci.0569-21.2022

EBM Experimental Biology and Medicine

TYPE Original Research
PUBLISHED 15 August 2025
DOI 10.3389/ebm.2025.10655

OPEN ACCESS

*CORRESPONDENCE
Stephania A. Cormier,
stephaniacormier@lsu.edu

RECEIVED 01 May 2025
ACCEPTED 04 July 2025
PUBLISHED 15 August 2025

CITATION
Kumar A, Guo C, Sarumi Q, Courtney C, Campagna S, Richmond-Bryant J and Cormier SA (2025) Proximity to a hazardous waste thermal treatment facility alters human physiology: a community-driven pilot study. *Exp. Biol. Med.* 250:10655. doi: 10.3389/ebm.2025.10655

Proximity to a hazardous waste thermal treatment facility alters human physiology: a community-driven pilot study

Avinash Kumar[1,2], Chuqi Guo[3], Qudus Sarumi[4], Christopher Courtney[4], Shawn Campagna[4,5], Jennifer Richmond-Bryant[3] and Stephania A. Cormier[1,2]*

[1]Department of Biological Sciences, Louisiana State University, Baton Rouge, LA, United States, [2]Pennington Biomedical Research Center, Baton Rouge, LA, United States, [3]Department of Forestry and Environmental Resources, North Carolina State University, Raleigh, NC, United States, [4]Department of Chemistry, University of Tennessee, Knoxville, TN, United States, [5]Biological and Small Molecule Mass Spectrometry Core, University of Tennessee, Knoxville, TN, United States

Abstract

Open burn/open detonation (OB/OD) disposes of explosive waste via uncontrolled combustion, releasing harmful pollutants like toxic gases and particulate matter. Colfax, Louisiana, houses the nation's only commercially OB/OD thermal treatment (TT) facility, raising concerns about environmental and public health impacts due to its emissions. In this exploratory pilot study, we investigated metabolic alterations indicative of potential health impacts from exposure to emissions from a TT facility through an untargeted metabolomics analysis of urine samples obtained from local residents. Urine samples were collected from 51 residents living within a 30-km radius of the facility, with proximity, race, and sex as key variables. Samples were analyzed using ultra-high-performance liquid chromatography coupled with high-resolution mass spectrometry (UHPLC-HRMS) to identify metabolic alterations and potential biomarkers of exposure. A total of 217 metabolites were identified, with significant differences in abundance based on proximity to the facility. Key metabolic pathways affected included energy metabolism, amino acid metabolism, and oxidative stress-related pathways. Metabolites associated with oxidative stress, such as glutathione sulfonamide (GSA), were elevated in individuals residing closer to the facility, indicating increased oxidative stress. Alterations in the glutathione/glutathione disulfide (GSH/GSSG) ratio further highlighted redox imbalances. Pathway enrichment analyses revealed perturbations in glycolysis, citric acid cycle, sulfur metabolism, and nucleotide metabolism, which are linked to critical biological functions like energy production and DNA repair. Notable differences in metabolite profiles were also observed between sexes and racial groups, pointing to the interplay of intrinsic biological and environmental factors. These findings demonstrate that exposure to emissions from the TT facility may have significant impacts on human health, including disruptions in cellular metabolism and increased

oxidative stress. Further research is crucial to understand the long-term health implications of these metabolic alterations and to develop strategies to mitigate the environmental and health risks associated with this facility.

KEYWORDS

metabolomics, open burn, hazard waste remediation, environmental exposure, oxidative stress

Impact statement

This study provides critical insights into how environmental exposure to emissions from thermal treatment (TT) facilities can disrupt human metabolism at a cellular level, using urinary metabolomics as a non-invasive monitoring approach. By linking metabolite alterations, particularly in energy, amino acid, and nucleotide pathways, with proximity to the TT facility, this work highlights a potential biochemical signature of exposure. Notably, elevated levels of glutathione sulfonamide (GSA) and disrupted antioxidant balance underscore oxidative stress as a key biological response. The integration of demographic factors such as sex and race adds an important dimension to understanding individual susceptibility. This research advances the field by establishing metabolomics as a sensitive biomonitoring approach for environmental health assessment and by identifying novel metabolite markers of exposure. These findings offer a foundation for future public health strategies, regulatory frameworks, and longitudinal studies, ultimately enhancing our understanding of environmental toxicology and personalized exposure risk evaluation.

Introduction

Colfax, a small rural town in central Louisiana, United States, has a population of 1,442 as of 2023, with 61.1% identifying as Black or African American and 33.1% as White [1] compared with the Parish as a whole, with a population of 22,123 (14.8% identify as Black or African American, 78.2% as White [2]). The community faces economic challenges, with a median individual income of $20,192 and about 35% of residents living below the poverty line. Colfax is notable for housing the country's only commercially operated open burn/open detonation (OB/OD) thermal treatment (TT) facility. In the latest permit application, the Louisiana Department of Environmental Quality (LDEQ) ordered the TT facility to cease OB/OD operations in December 2023 until a closed-burn facility could be constructed; however, the facility is currently appealing this decision in court and remains in operation. The TT facility, in operation since 1985, was previously permitted to treat a wide variety of waste streams, including military ordnances, cylinders, explosives, and propellants, as well as hazardous materials from Superfund sites, fireworks, and ammonium perchlorate [3]. These materials contain toxic components such as metals, explosives, and organohalogens. Without containment or emission control measures, OB/OD operations at the facility released particulate matter (PM) directly into the atmosphere, raising concerns about toxic exposure risks for the Colfax community. Community members living in close proximity to the TT have reported a range of health issues, including thyroid disease, respiratory and cardiovascular disease, skin damage, and cancer [4]. Exposure to certain toxic materials or emitted pollutants has been shown in studies to cause similar health effects [5–16], further amplifying concerns about the impact of the facility's operations on community health.

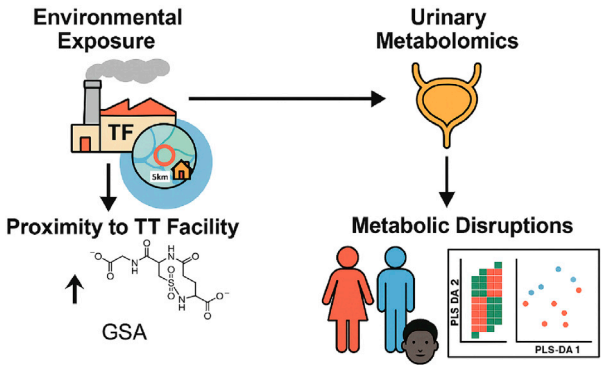

GRAPHICAL ABSTRACT

Metabolomic analysis [17, 18] offers a method for understanding connections between Colfax community members' exposures to PM generated by OB/OD and health outcomes [4, 19] The metabolome is a highly dynamic and individualized biochemical fingerprint that responds rapidly to internal and external influences. It provides a comprehensive snapshot of physiological states of individuals at a particular time, making it a diagnostic tool for changes observed in response to environmental exposure [20]. Metabolites present in tissues or body fluids can serve as intermediate or final products of cellular metabolism, as well as byproducts of energy-producing nutrients, intermediates in the synthesis of biological macromolecules, and waste products that influence normal cellular functions [21]. Since several biomarkers are produced through cellular metabolism and various protein activities, they can indicate the effects of functional changes triggered by external exposures, such as those from OB/OD operation, delineating the potential pathways through which hazardous exposures affect health [22, 23]. Urine is also emerging as a preferred biofluid for the noninvasive monitoring of human health because changes in secreted biomarkers may be easier to detect as there is little to no evolutionary pressure to maintain homeostasis within this waste product [24]. In fact, a recent study conducted in Shanghai, China, demonstrated that short-term exposure to $PM_{2.5}$ can cause significant alterations in urinary metabolomic profiles, potentially leading to disruptions in energy metabolism, oxidative stress, and inflammation [25]. Another study evaluated metabolic response to short-term exposure to airborne $PM_{2.5}$ and bioaerosols using gas chromatography/liquid chromatography-mass spectrometry (GC/LC–MS) with urinary samples [26]. Key findings revealed that 33 out of 155 differential metabolites were associated with $PM_{2.5}$ and bioaerosol exposure. It also revealed potential biomarkers like 16-dehydroprogesterone and 4-hydroxyphenylethanol identified for predicting $PM_{2.5}$ - or bioaerosol-related diseases, highlighting dynamic changes in urinary metabolic profiles in response to air pollution.

Our previous field studies conducted in the same community have included reviews of corporate reports indicating that weapons having metal casings and ammonium perchlorate accelerant and other explosive materials are often burned by ignition with diesel [4], producing PM with complex composition. Measurements have detected environmentally persistent free radicals (EPFRs), metals, and polychlorinated dibenzo-p-dioxins and dibenzofurans (PCDD/Fs) in ambient $PM_{2.5}$ and soil samples [27], with the radical electron localized on carbon with an adjacent oxygen. Residents living near the TT facility have reported several health issues, including thyroid disease, respiratory and cardiovascular conditions, skin damage, and cancer [4]. This study applied an untargeted metabolomics investigation using urine from community members residing near and potentially exposed to emissions from the TT facility in order to identify potential biomarkers of exposure and reflecting a systemic health effect that may help substantiate community members' stated concerns about health effects. Since no established biomarkers exist for exposure to EPFRs and real-world exposures typically involve complex mixtures rather than single agents, this work represents the first attempt to identify biomarkers specific to EPFR exposure.

Materials and methods

Subject recruitment and sample collection

The study population consisted of residents living within a 30-km radius of the facility. Initially, 53 community members (21 male and 32 female) were recruited. However, two participants were unable to provide urine samples, resulting in a final validated sample size of 51 (21 male and 30 female) (Table 1). Participant ages ranged from 24 to 89 years, with a mean age of 65.18 +/−15.26 (SD). Among the 51 individuals providing urine samples, 20 lived within 5 km of the TT facility, and 31 lived further away. A 5 km radius was selected based on our previous work in the community, which identified this distance as encompassing the greatest concentration of reported thyroid, respiratory, and skin conditions members [4]. This boundary is also supported by empirical evidence from prior epidemiological studies demonstrating elevated health risks within similar proximities to environmental pollution sources [28, 29].

This study was reviewed and received approval from the North Carolina State University Institutional Review Board (Protocol #25124) with a reliance agreement to Louisiana State University. All participants signed a consent form agreeing to urine collection. The consent form stipulated that the participants' names were kept on a crosswalk document that is separate from the samples, which were assigned random ID numbers. Address, gender, and race were also recorded on the crosswalk table, and home address was used to obtain distance from the TT facility's burn pads. To ensure confidentiality, the table was de-identified before being sent to the laboratory.

Participants were provided with a urine sample collection kit, including a sterile collection bottle, alcohol wipes, and detailed instructions that followed standard hospital practices. Study participants were furnished with instructions requesting that the urine be collected mid-stream; no special instructions for time of collection were provided. Following collection, samples were kept on ice during the collection period and were stored at −80°C immediately upon transfer to the laboratory. A chain-of-custody form was created for the urine sample collection, and a label containing the sample ID was applied to the sample and entered on the crosswalk table.

TABLE 1 Participant demographics.

Race	F	M	Total
Black	17	8	25
White	13	13	26
Total	30	21	51

Sample analyses

Metabolomics method

Sample preparation and extraction

Stored urine samples were thawed in a cold room at 4°C for 1 h before 100 µL aliquots were prepared for metabolite extraction following established protocols [30, 31]. Briefly, 1.5 mL of extraction solvent (20:40:40 water/methanol/acetonitrile with 0.1 M formic acid) was added to the urine samples in 2-mL microcentrifuge tubes. The tubes were vortexed thoroughly to ensure proper mixing with the extraction solvent. After mixing, the samples were chilled at −20°C for 20 min to enhance metabolite release. The samples were then centrifuged at 15,000 rpm for 5 min at 4°C to separate the supernatant, which contained the extracted metabolites, from the residue. The supernatants were carefully transferred into new microcentrifuge tubes and dried under a stream of nitrogen gas to completely remove the solvent. Once dried, the samples were reconstituted in 300 µL of LC-MS grade water, vortexed, and centrifuged again at 15,000 rpm for 5 min at 4°C to ensure homogeneity. The final extracts were aliquoted into autosampler vials for analysis using ultra-high-performance liquid chromatography coupled with high-resolution mass spectrometry (UHPLC-HRMS). Metabolites were extracted without the addition of internal standards, as the study design focused on relative quantification rather than absolute concentration measurements. Metabolite identification was achieved by matching retention times and mass-to-charge ratios (m/z) to an in-house standard library. Quantification was based on the relative abundances of detected features across sample groups. Given the absence of spiked internal standards, the data is considered semi-quantitative, suitable for comparative analyses. To evaluate extraction efficiency, blank extractions were processed in parallel using identical protocols. Non-specific signals were assessed by comparing metabolite profiles from the blank extractions with those from biological samples, allowing for blank subtraction and recovery estimation to identify background artifacts and assess extraction performance.

UHPLC-HRMS analysis

Metabolite separation and mass analysis were conducted at the University of Tennessee Biological and Small Molecule Mass Spectrometry Core (RRID: SCR_021368) using an UltiMate 3000 RS chromatograph (Dionex, Sunnyvale, CA, United States) coupled to an Exactive™ Plus Orbitrap mass spectrometer (Thermo Fisher Scientific, Waltham, MA, United States). A reversed-phase ion-pairing chromatographic method was employed for separation, utilizing a Synergi Hydro RP column (2.5 µm, 100 × 2.0 mm; Phenomenex, Torrance, CA, United States). The mobile phase consisted of LC-MS grade solvents composed of 97% water, 3% methanol, 11 mM tributylamine as the ion-pairing reagent, and 15 mM acetic acid, with gradient elution performed as previously described by Bazurto et al. [32]. The separation was carried out at a flow rate of 0.2 mL/min for 25 min, with the column temperature maintained at 25°C. The eluted metabolites were ionized using electrospray ionization in negative polarity mode. Mass analysis was performed using the Orbitrap mass analyzer at a resolution of 140,000, with a scan range of 72–1,000 m/z, an injection time of 100 milliseconds, and an automatic gain control (AGC) target of 3×10^6, as detailed in the protocol by Bazurto et al. [32].

Data analysis

The Xcalibur (RAW) files generated from the UHPLC-HRMS analysis were converted to mzML format using the msconvert software, a tool from the ProteoWizard package. This conversion transformed the profile data into centroided data, improving their suitability for downstream analysis. The centroided data were then uploaded to the Metabolomic Analysis and Visualization Engine (MAVEN) [33, 34], an open-source software tool developed at Princeton University. MAVEN was utilized for visualization of extracted ion chromatograms (EICs), peak feature selection, peak area integration, and metabolite identification using an in-house standards library. MAVEN automatically corrected for retention time nonlinearity and aligned peak areas across all samples. Metabolites were identified by comparing chromatographic retention times ±2 min, peak shapes, signal-to-noise ratios, and exact masses within a ±5 ppm mass tolerance to an in-house standard library. Identification was further validated by comparing the natural isotopic abundance patterns of the compounds. Peak intensity data tables were generated from MAVEN for statistical analysis. Metabolite intensities were normalized by the sum to account for differences in the initial concentrations of urine samples and by volume to express metabolite ion counts per mL of urine. Due to the known biological variability of creatinine levels—which can be influenced by factors such as age, sex, muscle mass, diet, and hydration status—samples were normalized using the sum (or Total Useful Signal) approach. This data-driven method assumes that most metabolite intensities remain relatively constant across samples and has been shown in multiple studies to outperform creatinine normalization in untargeted metabolomic analyses [35, 36]. A heatmap was generated using a custom script in R Studio (version 4.2.1, RStudio Team, 2022, Boston, MA, United States). Further downstream data analysis was

performed using Metaboanalyst 6.0. Variance filtering was applied using the interquartile range (IQR), and the data were log-transformed for better visualization and Pareto-scaled. Partial Least Squares-Discriminant Analysis (PLS-DA) was conducted to visualize metabolic profile differences across sample groups. Metabolites showing significant differences and a Variable Importance in Projection (VIP) score greater than 1 were selected for Kyoto Encyclopedia of Genes and Genomes (KEGG) pathway enrichment analyses. All statistical analyses were considered significant at $P < 0.05$, and pathway significance was determined at a False Discovery Rate (FDR) cutoff of <0.05.

Results

Metabolomic analysis was conducted to assess if proximity to the TT facility and exposure to emissions altered the metabolome, as the metabolome is directly related to phenotype. A total of 217 metabolites were identified from 51 urine samples. Among these, 10 metabolites belonged to the vitamin superclass, 2% were neurotransmitters, 9% were related to amino acid metabolism, and 8% were involved in glycolysis, gluconeogenesis, and pentose phosphate pathways. Additionally, 22% were nucleosides, nucleotides, and analogs, 6% were lipid metabolites, 6% were carbohydrates and conjugates, 3% were citric acid cycle metabolites, and 6 metabolites were categorized under bile acids and bile salts. Most of the identified compounds were amino acid precursors and derivatives, which accounted for approximately 25% of the total metabolites, along with carbohydrates involved in nutrient metabolism.

Significant differences in metabolite abundance were observed across urine samples collected from community members (positive fold change ≥2, negative fold change ≤0.5 and P-value cut-offs <0.1). To determine if proximity to the TT facility resulted in metabolome alterations, fold changes were calculated for metabolites between individuals residing less than 5 km vs. those greater than 5 km from the TT facility's burn pads, sex (male vs. female), and race (Black vs. White). Based on our previous discussions with residents [4], a cut-off of 5 km was chosen to differentiate residents living in the Rock community or those in similar proximity to the east, west, and north, from those in the surrounding area living further away. The relative abundance of metabolites varied significantly across these categories, with the greatest differences observed between the less than 5 km and greater than 5 km groups. Most metabolites were found to be higher in abundance in individuals residing closer to the facility (less than 5 km) compared to those farther away (Figure 1).

A p-value threshold of <0.1 was adopted to allow for broader detection of metabolite-level differences in this exploratory study, where the primary aim was to identify potential trends and biologically relevant patterns across sample groups. This approach has been used in similar untargeted metabolomics studies where a balance between sensitivity and specificity is critical in the initial discovery phase [37]. To address the increased risk of false positives associated with this more lenient threshold, false discovery rate (FDR) correction was applied to pathway enrichment analyses, where the biological interpretation of grouped metabolites is most meaningful and informative. The combination of a relaxed p-value threshold and FDR correction at the pathway level provides a balanced strategy for exploratory data interpretation while minimizing the likelihood of spurious associations. In future studies with larger sample sizes, we intend to apply stricter significance thresholds and uniform correction strategies.

Partial least squares discriminant analysis (PLS-DA), a supervised multivariate chemometric tool, was employed to cluster sample groups based on similarities in their metabolic profiles. A 2D PLS-DA score plot was generated to illustrate differences in metabolic profiles between groups by sex (Figure 2A), race (Figure 2B), and proximity to the facility (Figure 2C). The evident separation in the plots indicates distinct differences in metabolic profiles among the groups, suggesting variations in metabolite abundance and distinct metabolic activities, as reflected by clustering along the components. Additionally, the variable importance in projection (VIP) scores are assigned to each metabolite to indicate the extent to which each metabolite contributes to the observed separation in the PLS-DA model. Metabolites with a VIP score greater than 1 are key drivers of global metabolome profile differences between groups. VIP score plots for sex (Figure 3A), race (Figure 3B), and proximity to the facility (Figure 3C) illustrate the metabolites that significantly influence the separation in the PLS-DA plots, underscoring their pivotal role in delineating group differences. To further explore metabolic differences, volcano plots were used to visualize fold changes and statistical significance across the groups. The volcano plot for the female vs. male comparison (Figure 4A) highlights metabolites with fold changes greater than or equal to 2 in red, alongside metabolites with statistical significance ($p \leq 0.1$). Similarly, the volcano plot for the race comparison (Figure 4B) shows metabolites with statistically significant upregulation or downregulation. Proximity to the facility revealed the most pronounced differences, with the volcano plot (Figure 4C) showing several metabolites with fold changes that were substantially elevated in the <5 km group compared to the >5 km group.

A Venn diagram (Figure 5A) was used to analyze the unique and shared metabolites among the sample groups categorized by sex, race, and proximity to the thermal treatment facility. A total of 27 metabolites were common across all three groups. The number of unique metabolites varied, with the proximity-based comparison exhibiting the highest number (33 unique metabolites), followed by the race-based comparison (26 unique metabolites), and the sex-based comparison

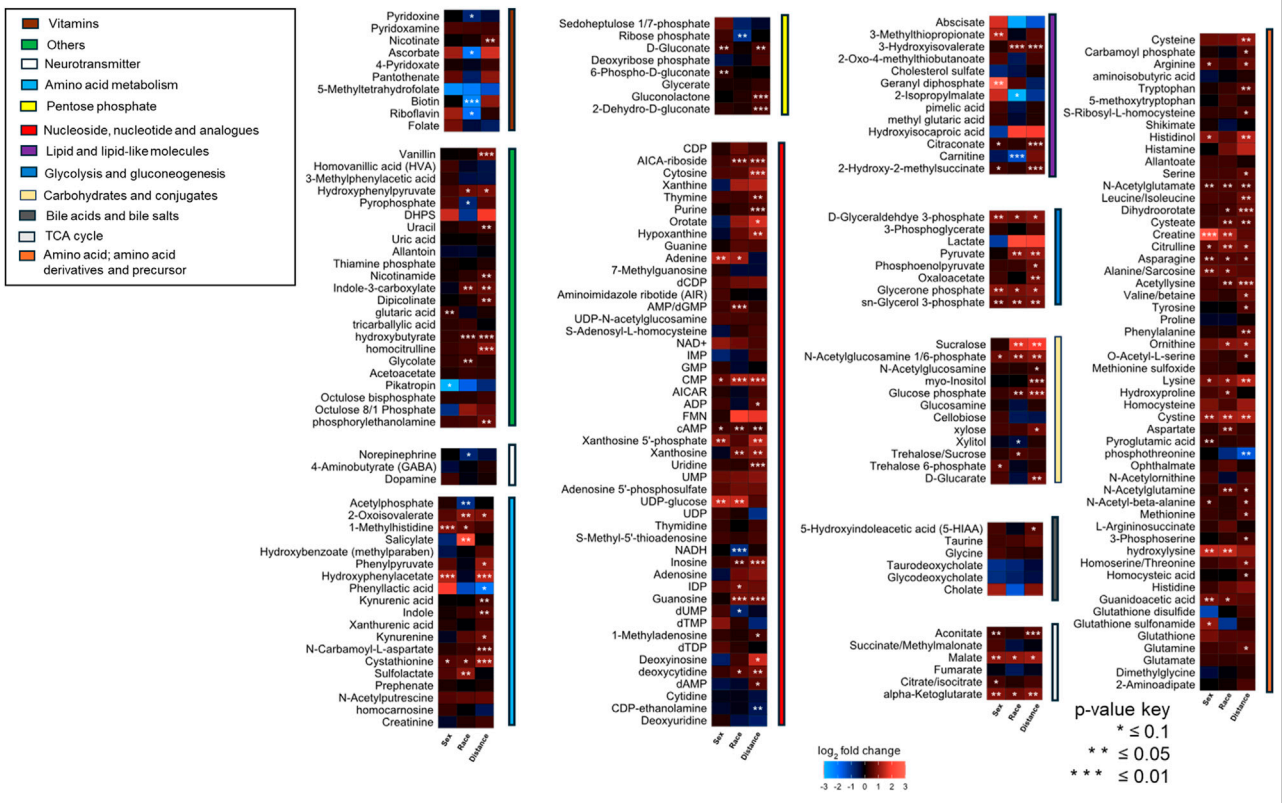

FIGURE 1
A heatmap illustrating fold changes in metabolite abundance, organized by compound class, across sample groups stratified by sex, race, and proximity to the facility. The fold changes include Female/Male, Black/White, and Less than 5 km/Greater than 5 km (n = 51). Statistically significant differences are indicated by asterisks (*P < 0.1, **P < 0.05, ***P < 0.01). Metabolite abundance is represented using a color gradient, with red indicating a higher abundance and blue indicating lower abundance in female for sex-based comparison, Black individuals for race-based comparison, or individuals residing less than 5 km from the facility for proximity-based comparison.

(16 unique metabolites). 10.5% of the metabolites were unique to the sex-based comparison, and they include glutathione sulfonamide, phosphoenolpyruvate, and glutamate. The race-based comparison revealed 17.1% unique metabolites, such as 2-isopropylmalate, phenyl lactic acid, NADH, N-acetyl glutamine, trehalose/sucrose, aspartate, taurine, and glycolate. The proximity-based comparison, which focused on individuals residing less than 5 km versus greater than 5 km from the facility, identified 21.7% unique metabolites. These included uridine, cholate, myo-inositol, indole, uracil, gluconolactone, phenylalanine, N-carbamoyl-L-aspartate, oxaloacetate, purine, nicotinamide, nicotinamide, S-ribosyl-L-homocysteine, tyrosine, homoserine/threonine, and glutamine (Table 2). Additionally, 3.9% of metabolites were shared between the sex and race groups, 17.8% between the sex and proximity groups, and 11.2% between the race and proximity groups. A total of 17.8% of metabolites were shared across all three groups. These included UDP-glucose, creatine, UMP, alpha-ketoglutarate, glutathione, CMP, malate, cystine, cysteine, glucose phosphate, lysine, cytosine, lactate, taurodeoxycholate, and cystathionine.

Enrichment analysis for metabolic pathways across the sample groups was visualized in a clustered bar graph (Figure 5B), with the pathways' significance evaluated based on their false discovery rate (FDR) plotted on a logarithmic scale. The bar graph revealed that the most significant pathways in the proximity-based groups were pyrimidine and purine metabolism, as well as phenylalanine, tyrosine, and tryptophan biosynthesis. In the race-based comparison, arginine biosynthesis and pyrimidine metabolism were prominent, while glycolysis and arginine biosynthesis pathways showed significant enrichment in the sex-based groups. These findings highlight the distinct metabolic activities and pathway perturbations across the groups, potentially linked to demographic and environmental factors.

Metabolic pathway enrichment analysis was performed using metabolites with a VIP score greater than 1. Pathways with an FDR <0.05 and high impact factors were selected for detailed enrichment analysis (Figures 6A–D). Metabolites associated with amino acid metabolism pathways demonstrated significant sex-based differences. Enrichment analysis revealed that metabolites

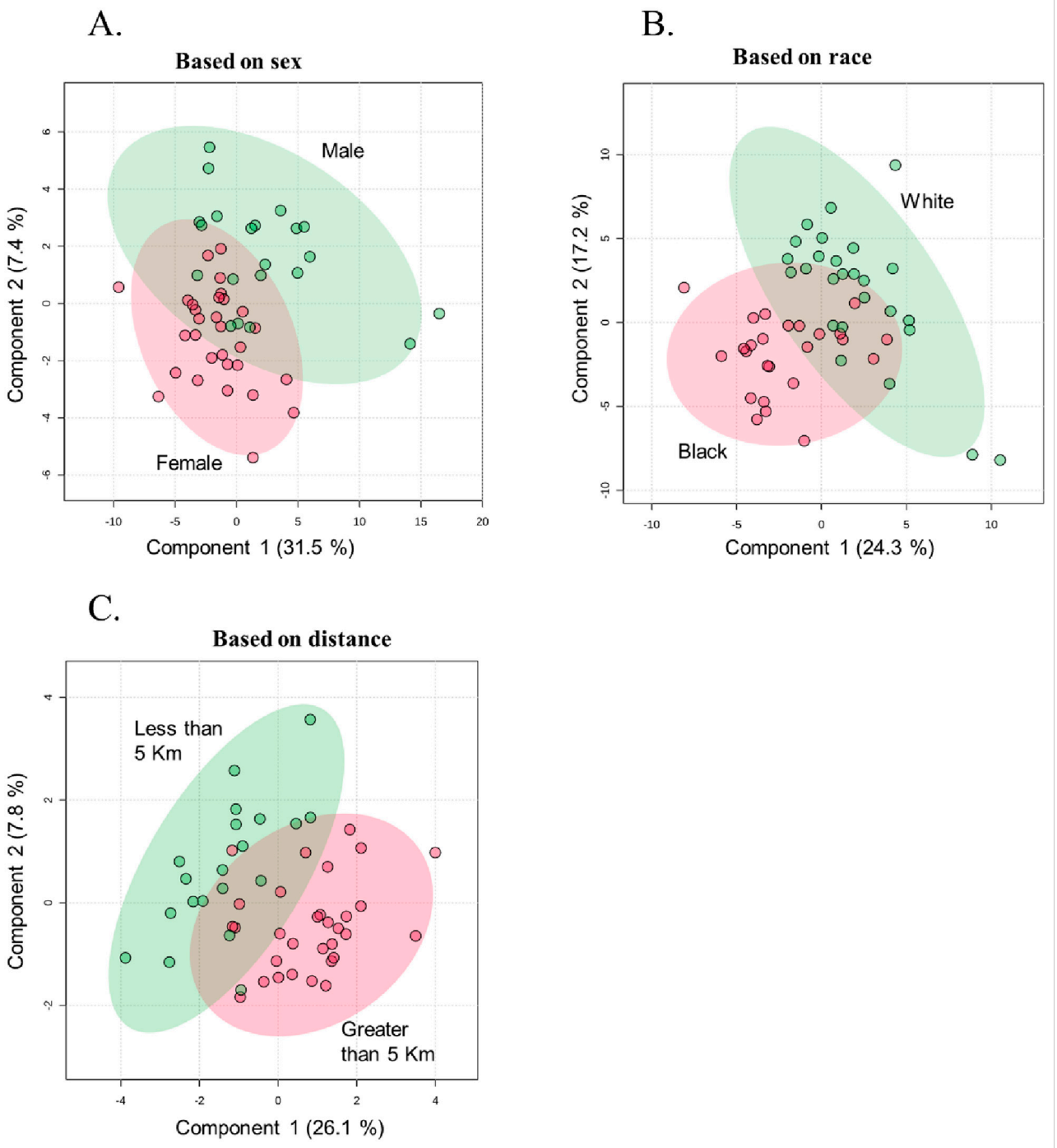

FIGURE 2
Partial Least Squares-Discriminant Analysis (PLS-DA) plots illustrating metabolic profile separations with 95% confidence intervals, grouped by: **(A)** Sex (Female vs. Male), **(B)** Race (Black vs. White), and **(C)** Distance from the facility (Less than 5 km vs. Greater than 5 km) (n = 51).

such as glutathione sulfonamide, UDP glucose, geranyl diphosphate, alanine/sarcosine, guanidinoacetate, alpha-ketoglutarate, and creatine were significantly more abundant in females ($P < 0.1$), whereas metabolites such as lactate, glycodeoxycholate, taurodeoxycholate, 5-methyl tetrahydrofolate, and hydroxyisocaproic acid were less abundant. All significantly altered metabolites in arginine, phenylalanine, tyrosine, tryptophan, alanine, aspartate, and glutamate metabolism and biosynthesis had a higher abundance in females (Figure 6A). When comparing

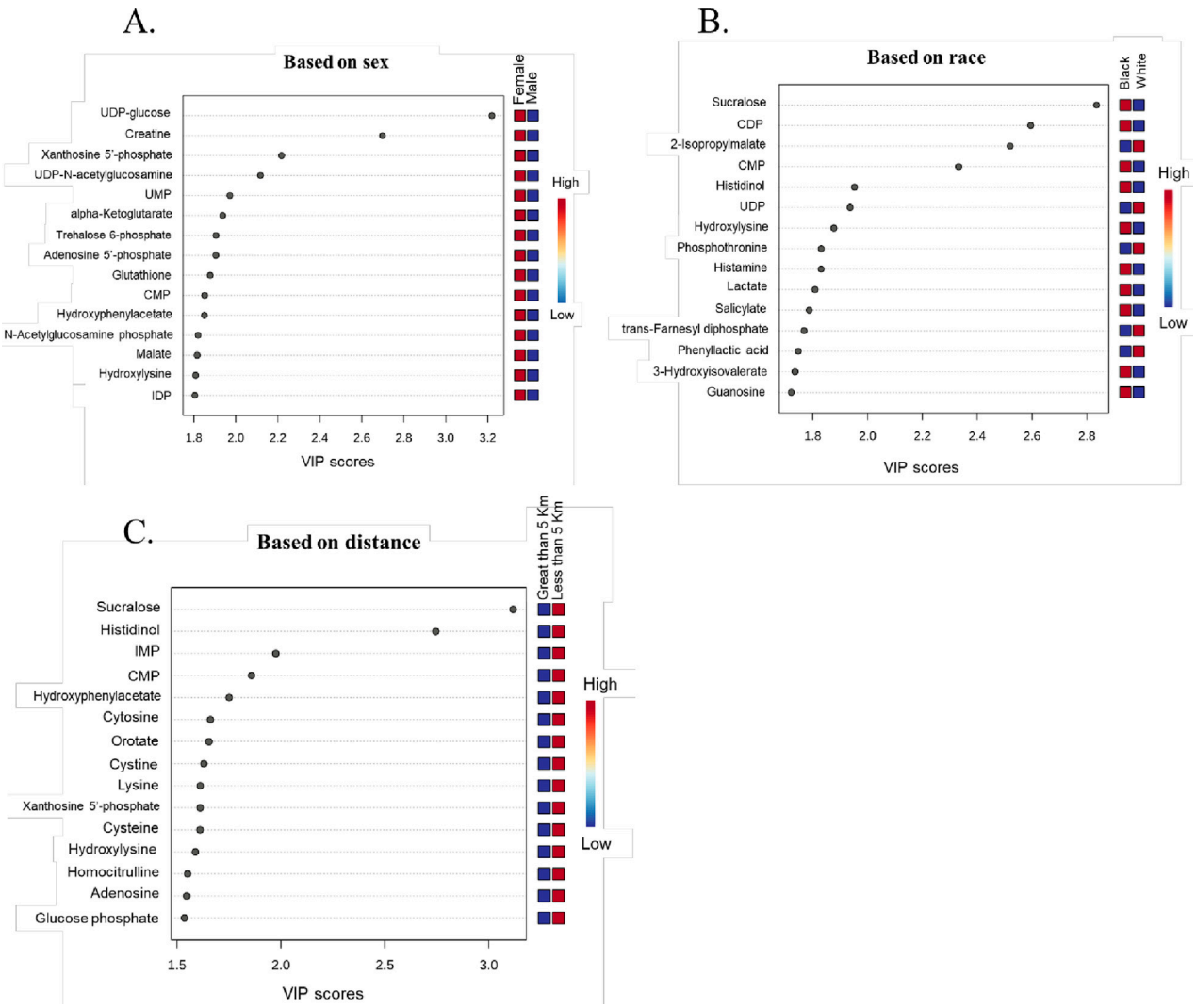

FIGURE 3
Variable Importance in Projection (VIP) score plots highlighting metabolites with 15 highest VIP scores. All metabolites with a VIP score greater than 1 significantly contribute to the observed group separations. These metabolites drive the differences across **(A)** Sex (Female vs. Male), **(B)** Race (Black vs. White), and **(C)** Distance from the facility (Less than 5 km vs. Greater than 5 km) (n = 51).

individuals residing less than 5 km from the TT facility to those living farther than 5 km, notable differences in energy and sulfur compound metabolism were observed (Figure 6B). Metabolites such as pyruvate, serine, alanine/sarcosine, guanidinoacetate, valine/betaine, glutathione, glutathione disulfide, glutathione sulfonamide, homoserine/threonine, cystine, cystathionine, cysteine, and tryptophan were significantly upregulated in the Less than 5 km group (highlighted in red), while phosphothreonine and abscisate were downregulated. These differences suggest potential metabolic adaptations or disruptions linked to proximity to the TT facility. Energy and carbohydrate metabolism pathways were also significantly impacted by proximity to the TT facility (Figure 6C). Metabolites upregulated in the Less than 5 km group included lactate, pyruvate, glycerate, oxaloacetate, malate, alpha-ketoglutarate, aconitate, glyceraldehyde phosphate, phosphoenolpyruvate, glycerone phosphate, and glucose phosphate ($P < 0.1$). Conversely, metabolites such as phenyl lactic acid and 2-isopropyl malate were downregulated. These findings highlight shifts in energy metabolism are likely driven by exposure to emissions from the TT facility. Additionally, metabolites involved in nucleotide and amino acid metabolism exhibited significant differences between the Less than 5 km and Greater than 5 km groups (Figure 6D). Red-highlighted metabolites, such as tyrosine, phenylalanine, pyruvate, cytosine, histamine, taurine, thymine, glutamine, guanine,

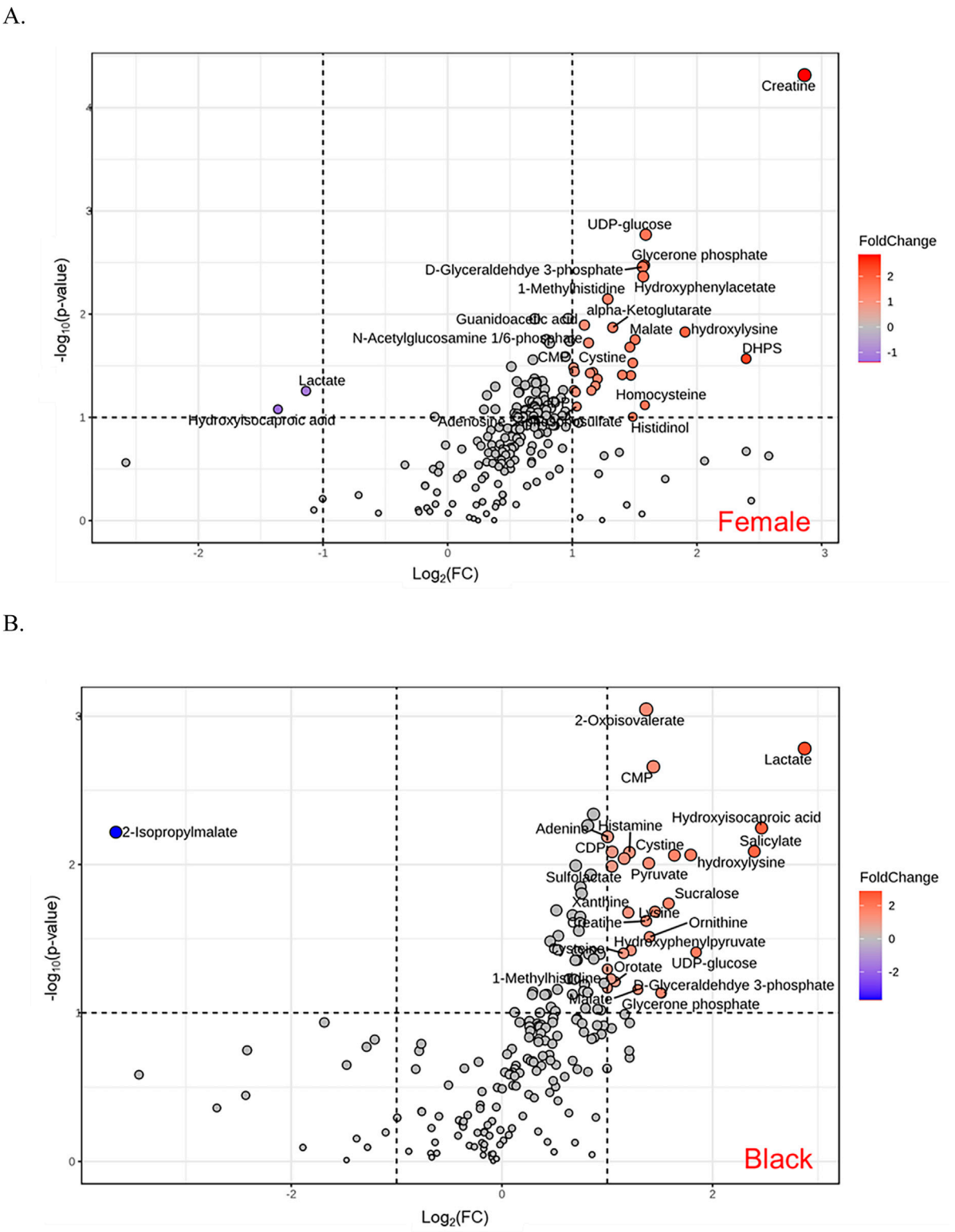

FIGURE 4
(Continued).

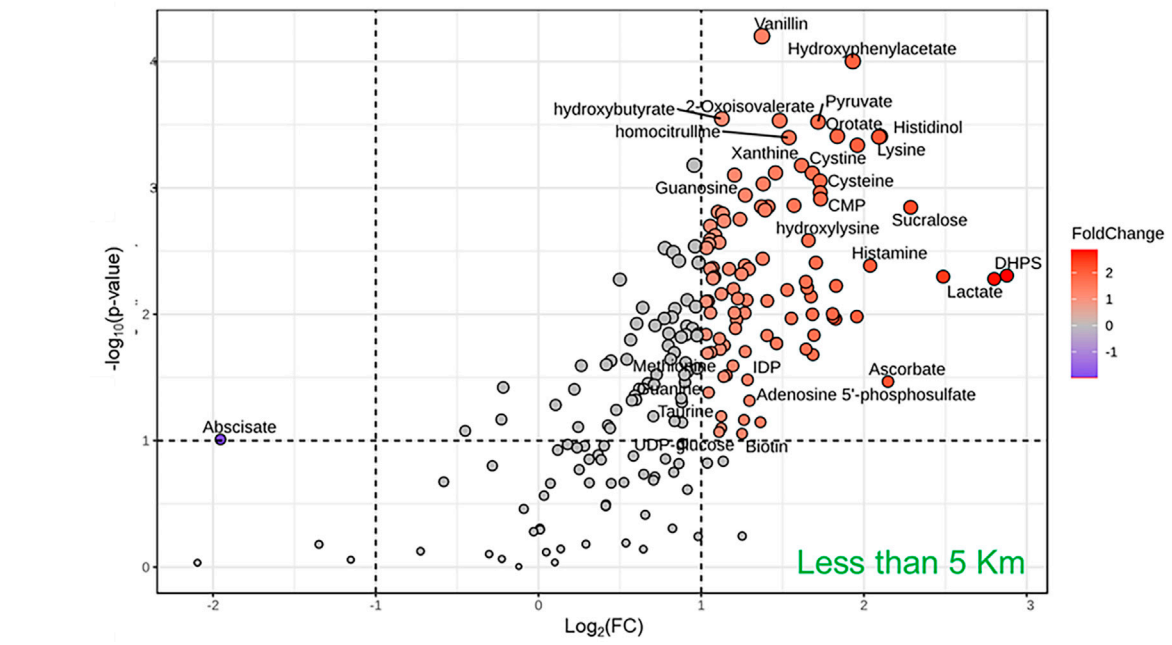

FIGURE 4
(Continued). Volcano plots illustrating the differentially abundant metabolites across groups: **(A)** Sex (Female vs. Male), **(B)** Race (Black vs. White), and **(C)** Distance from the facility (<5 km vs. >5 km). Metabolites with a fold change ≥2 and P-value <0.1 are highlighted with red spot, while those with a fold change ≤0.5 and P-value <0.1 are highlighted with blue spot.

DHPS, dihydroorotate, carnitine, cysteate, carbamoyl aspartate, hydroxyphenyl pyruvate, uridine, adenosine, guanosine, inosine, CMP, UMP, and ADP, were significantly more abundant in the Less than 5 km group ($P < 0.1$). In contrast, metabolites such as dTMP and 5-methyltetrahydrofolate, highlighted in blue, were less abundant. These findings indicate potential disruptions in fundamental metabolic processes in individuals residing closer to the TT facility. There were significant metabolic pathway perturbations influenced by both sex and proximity to the TT facility. Amino acid metabolism pathways showed prominent sex-based differences, while energy and carbohydrate metabolism pathways, as well as nucleotide and amino acid metabolism pathways, were most affected by proximity to the TT facility.

Biomarkers for systemic inflammation and oxidative stress were evaluated across all sample groups (Figures 7A–F). The relative abundances of glutathione sulfonamide (GSA) displayed significant variations based on sex, race, and proximity to the thermal treatment facility. A study demonstrated that urinary GSA levels correlate with GSA levels in BAL and other markers of neutrophilic inflammation, suggesting that GSA could serve as a biomarker for tracking disease activity in the population [38]. Female samples exhibited higher levels of GSA compared to male samples (33,500 ± 8,337.38 vs. 14,600 ± 1,570.03) (Figure 7A). Similarly, white individuals showed significantly elevated levels of GSA compared to black individuals (18,000 ± 1812.71 vs. 33,200 ± 8,953.52) (Figure 7B). Additionally, individuals residing within 5 km of the facility exhibited higher abundances of GSA than those living farther away, indicating a potential relationship between proximity to the facility and increased metabolite levels (18,000 ± 3,161.67 vs. 37,600 ± 9,546.69) (Figure 7C). To examine antioxidant status in the groups, the glutathione/glutathione disulfide (GSH/GSSG) ratio, a critical marker of oxidative stress, was calculated across all groups. A GSH/GSSG ratio of less than 1 reflects an imbalance between reduced glutathione (GSH) and oxidized glutathione (GSSG). The relative abundances of GSH and GSSG, as well as their calculated ratio, revealed significant group-specific differences. Females demonstrated a higher GSH/GSSG ratio compared to males (18.82 ± 3.17 vs. 4.78 ± 0.79) (Figure 7D). In contrast, Black individuals exhibited elevated GSH levels and a higher GSH/GSSG ratio compared to White individuals (12.68 ± 2.57 vs. 8.96 ± 1.17) (Figure 7E). Furthermore, individuals residing closer to the thermal treatment facility (less than 5 km) displayed a slightly higher GSH/GSSG ratio compared to those living farther away (10.57 ± 1.35 vs. 11.54 ± 2.58) (Figure 7F).

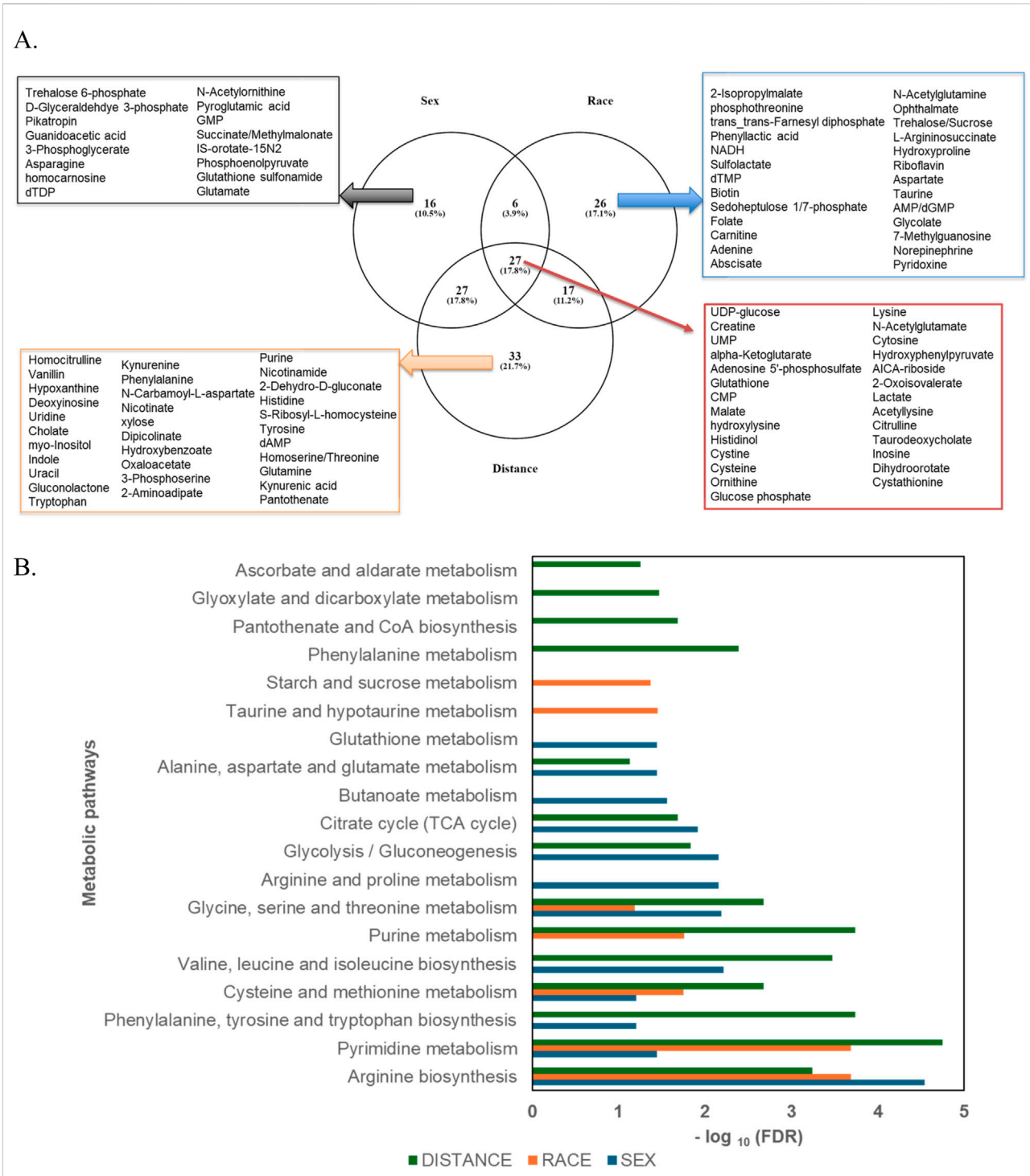

FIGURE 5
(A) Venn diagram depicting the distribution of differentially abundant metabolites uniquely identified in each group—Sex (n = 16), Race (n = 26), and Distance (n = 33)—as well as the metabolites shared across all groups (n = 27). **(B)** Clustered bar graph illustrating the enriched metabolic pathways across the sample groups, with logarithmically transformed FDR values. Pathway significance was determined using P-values, with a false discovery rate (FDR) threshold of <0.05.

TABLE 2 Differential abundance of metabolites across sample groups.

List of metabolites that are uniquely present in sample groups categorized by sex, race, and proximity to the thermal treatment facility			
Sex-based unique metabolites	**Race-based unique metabolites**	**Distance-based unique metabolites**	**Metabolites common across race, sex, and distance**
Trehalose 6-phosphate	2-Isopropylmalate	Homocitrulline	UDP-glucose
D-Glyceraldehyde 3-phosphate	Trans-trans-farnesyl diphosphate	n-Carbamoyl-l-aspartate	Hydroxyphenylpyruvate
Pikatropin	Phosphothreonine	Vanillin	UMP
Guanidoacetic acid	Phenyl lactic acid	Hypoxanthine	Alpha-ketoglutarate
3-Phosphoglycerate	NADH	Deoxyinosine	Glutathione
Asparagine	Sulfolactate	Uridine	CMP
Homocarnosine	Biotin	Cholate	Malate
dTDP	dTMP	Myo-inositol	Hydroxylysine
n-Acetylornithine	n-Acetyl glutamine	Indole	Histidinol
Pyroglutamic acid	Folate	Uracil	Cystine
GMP	Carnitine	Gluconolactone	Cysteine
Succinate/Methylmalonate	Sedoheptulose 1/7-phosphate	S-Ribosyl-L-homocysteine	Adenosine 5′-phosphosulfate
Orotate	Adenine	Kynurenine	Ornithine
Phosphoenolpyruvate	Abscisate	Phenylalanine	Glucose phosphate
Glutathione sulfonamide	Ophthalmate	Nicotinate	Lysine
Glutamate	Trehalose/Sucrose	Xylose	N-Acetylglutamate
	L-Arginosuccinate	Dipicolinate	Cytosine
	Hydroxyproline	Hydroxybenzoate	AICA-riboside
	Riboflavin	Oxaloacetate	Creatine
	Aspartate	3-Phosphoserine	2-Oxoisovalerate
	Taurine	2-Aminoadipate	Lactate
	AMP/dGMP	Purine	Acetyl lysine
	Glycolate	Nicotinamide	Citrulline
	7-Methylguanosine	Histidine	Tauro deoxycholate
	Norepinephrine	Tyrosine	Inosine
	Pyridoxine	dAMP	Cystathionine
		Homoserine/threonine	Dihydroorotate
		Glutamine	
		Kynurenic acid	
		Pantothenate	
		2-dehydro-d-gluconate	
		Tryptophan	

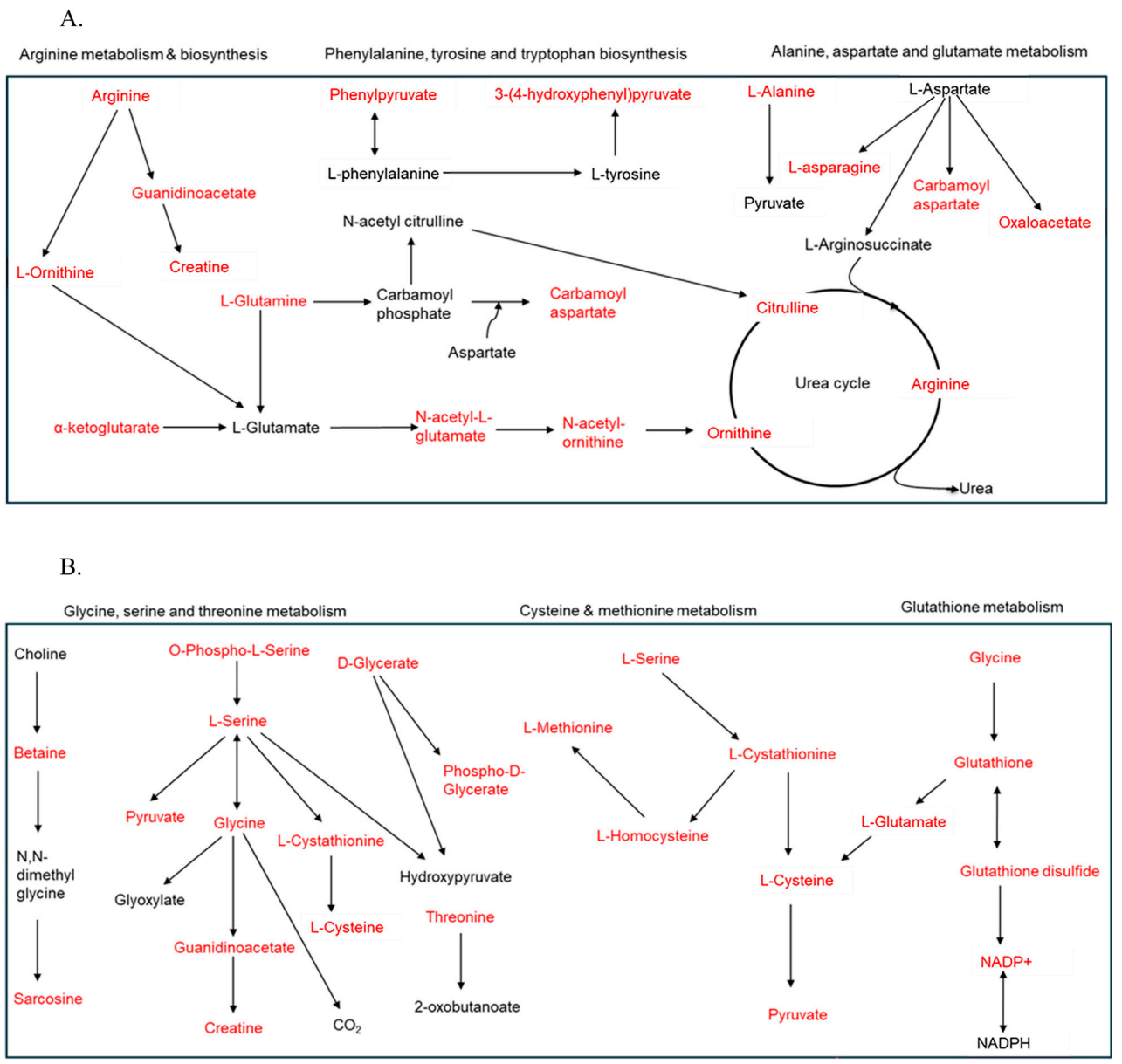

FIGURE 6
(Continued).

Discussion

The TT facility in Colfax, LA experienced a substantial increase in energetic waste processing volume in 2014, raising concerns about potential environmental and public health impacts from exposure to hazardous air pollutants. Residents described experiencing adverse health conditions or symptoms potentially linked to exposure to air pollutants, including thyroid disease, respiratory distress, skin lesions, hair loss and cancers [4, 39]. The metabolomics analysis of urine samples provided valuable insights into the metabolic disruptions potentially associated with environmental exposure to emissions from the hazardous waste thermal treatment facility. The identification of 217 metabolites spanning various biochemical pathways underscores the diversity of metabolic responses influenced by proximity, sex, and race. From the two-way Anova analysis, 94 metabolites out of the 217 were significantly altered by distance when compared to sex Supplementary Figure S1). Notably, the results highlight significant differences in metabolite abundance among individuals residing closest to

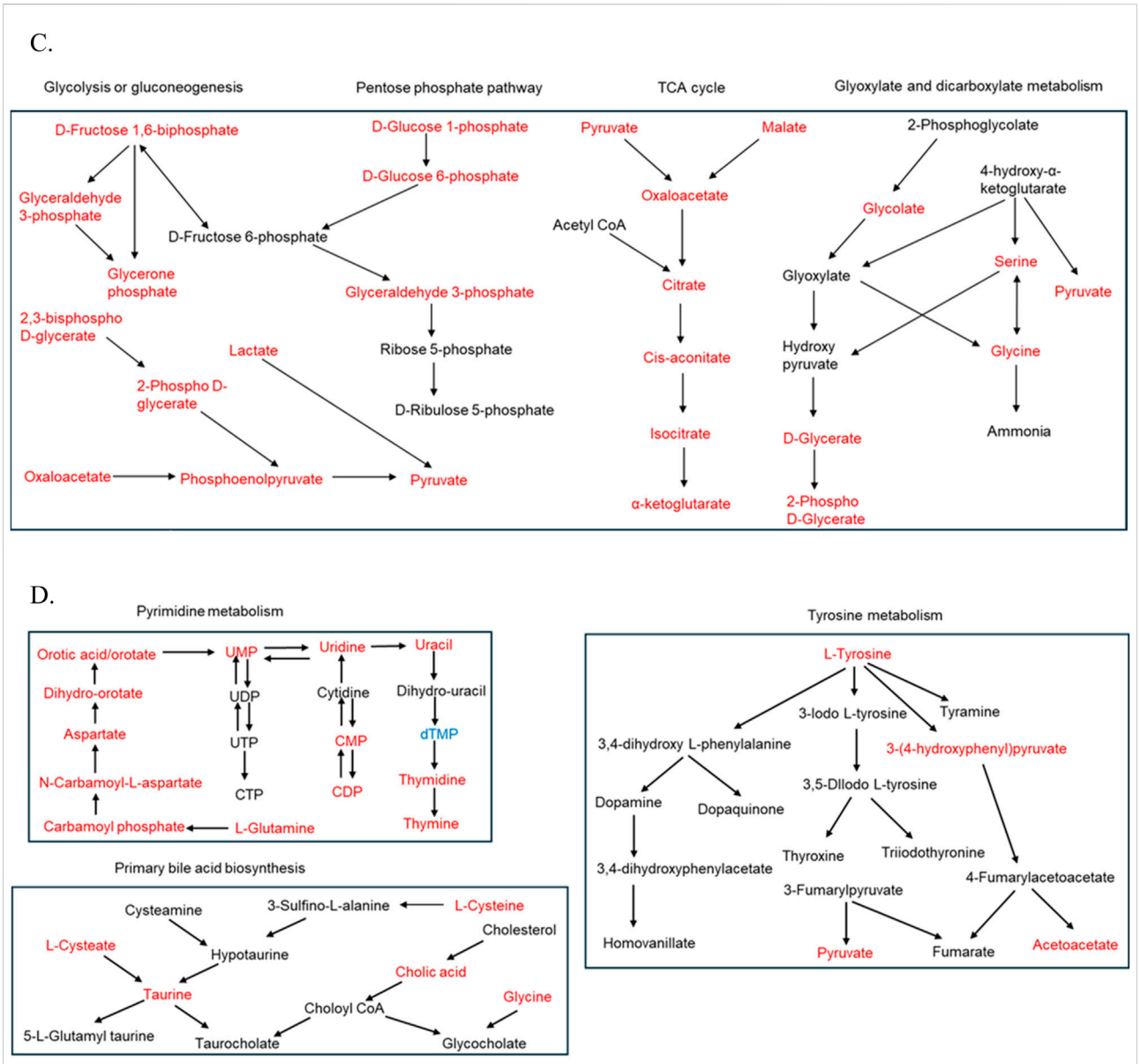

FIGURE 6
(Continued). **(A)** Schematic representation of amino acid metabolism pathways enriched with metabolites that exhibit differential abundance between females and males. Metabolites highlighted in red are significantly more abundant in females, while those in blue are significantly less abundant ($P < 0.1$). **(B–D)** Illustrating the most impacted pathways for differentially abundant metabolites in the Less than 5 km vs. Greater than 5 km groups. Metabolites highlighted in red are significantly upregulated, while those in blue are significantly downregulated in the Less than 5 km group ($P < 0.1$) **(B)** Schematic representation of energy and sulfur compound metabolism pathways. **(C)** Schematic representation of energy and carbohydrate metabolism pathways. **(D)** Schematic representation of nucleotide and amino acid metabolism pathways.

(less than 5 km from) the facility compared to those living farther away, suggesting an environmental impact on metabolic activity.

The impact of living near thermal treatment facilities has been a subject of concern, with several studies investigating potential health effects [40–45]. These effects include cancer, respiratory diseases, cardio-cerebrovascular disease, and adverse pregnancy outcomes [40]. In this study as well, we observed that individuals residing closer to the TT facility exhibited perturbation in the pathways involved in energy and nucleotide metabolism. We observed alterations in pathways related to glycolysis, the citric acid cycle, and oxidative phosphorylation in individuals residing closer to the facility (Figure 1). These shifts may indicate altered cellular energy production and utilization, potentially impacting cellular function and overall health [46, 47]. These pathways are important in evaluating potential health risks [48]. Studies

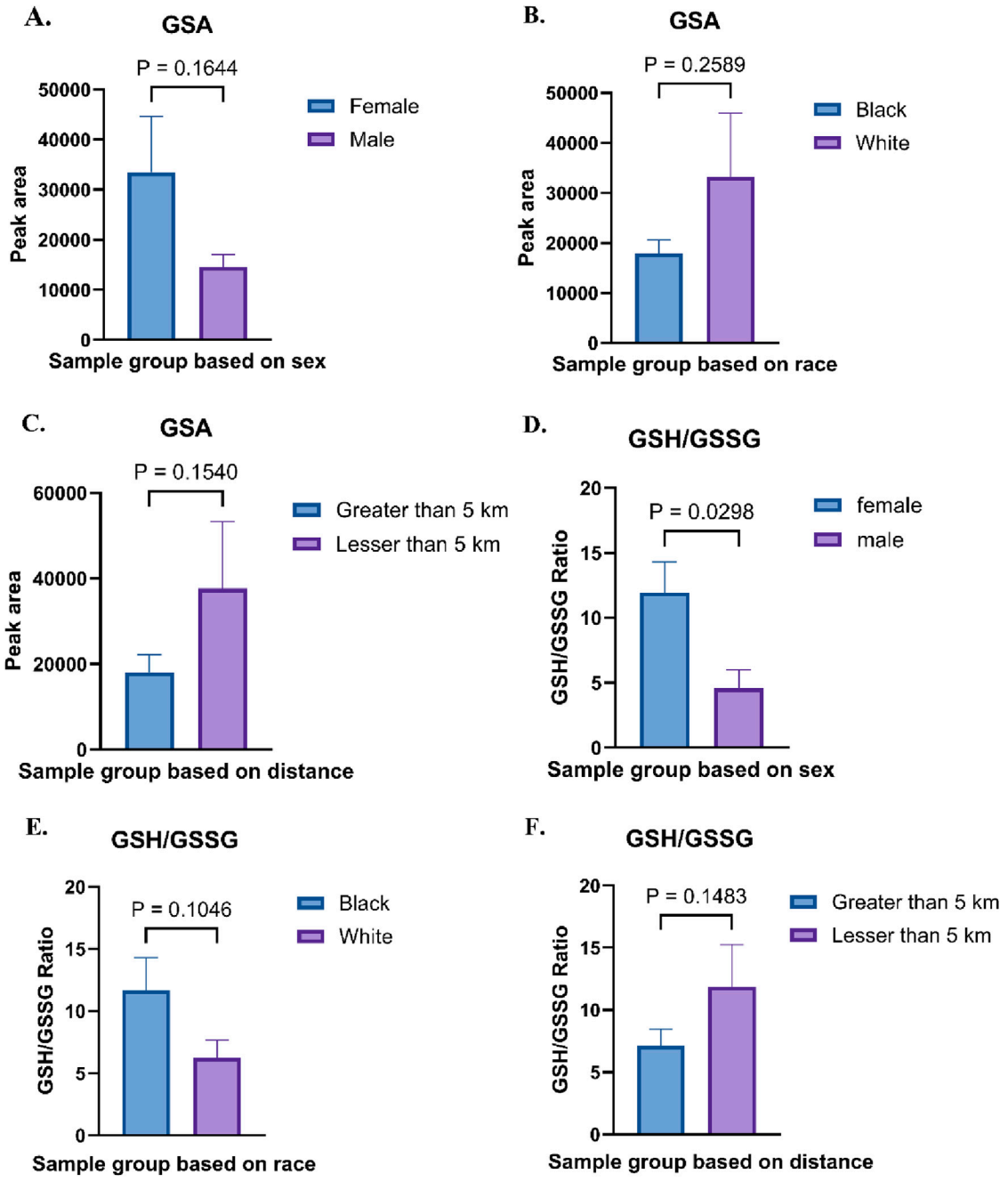

FIGURE 7
(A) Relative abundances of glutathione sulfonamide (GSA) in Female vs. Male sample groups. **(B)** Relative abundances of GSA in Black vs. White sample groups. **(C)** Absolute abundances of GSA in Less than 5 km vs. Greater than 5 km sample groups **(D)** Relative abundances of glutathione (GSH) and glutathione disulfide (GSSG), along with their ratio, in Female vs. Male sample groups. **(E)** GSH/GSSG abundance ratio in Black vs. White sample groups. **(F)** GSH/GSSG abundance ratio in Less than 5 km vs. Greater than 5 km sample groups.

have suggested that exposure to ambient air pollution and traffic-related air pollutants is associated with dysregulated metabolism of fatty acids, amino acids, leukotrienes and glucose [49, 50]. Similarly, we observed significant alterations in carbohydrate metabolism pathways, suggesting potential disruptions in glucose utilization and energy production. Disruptions in

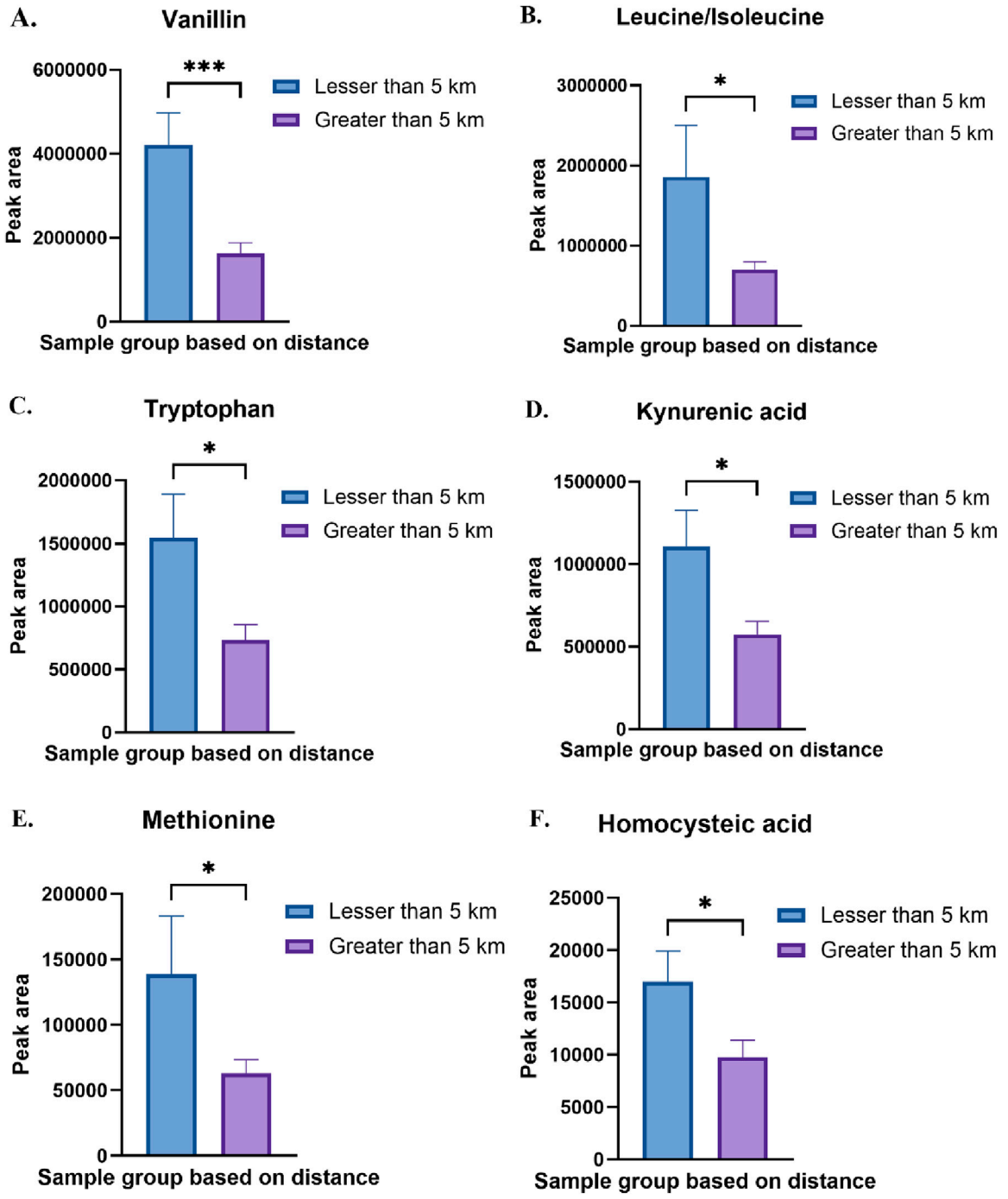

FIGURE 8
(A) Relative abundance of vanillin in Less than 5 km vs. Greater than 5 km sample group. **(B)** Relative abundance of leucine/isoleucine in Less than 5 km vs. Greater than 5 km sample group. **(C)** Relative abundance of tryptophan in Less than 5 km vs. Greater than 5 km sample group **(D)** Relative abundance of kynurenic acid in Less than 5 km vs. Greater than 5 km sample group **(E)** Relative abundance of methionine in Less than 5 km vs. Greater than 5 km sample group **(F)** Relative abundance of homocysteic acid in Less than 5 km vs. Greater than 5 km sample group. *$p < 0.05$, ***$p < 0.001$.

sulfur metabolism, particularly alterations in glutathione metabolism, as observed in our study (Figure 7) suggest increased oxidative stress in individuals closer to the facility. Glutathione plays a crucial role in cellular antioxidant defense, and its dysregulation can lead to oxidative damage to cellular components [51]. We also found that nucleoside and nucleotide metabolism pathways were impacted (Figures 5, 6). Altered nucleotide metabolism could potentially impact DNA replication and repair [52]. Altered nucleotide metabolism can also contribute to cancer development and progression. Cancer cells have an increased need for nucleotides, which are used in the synthesis of DNA and RNA. This altered metabolism can help cancer cells grow quickly, resist chemotherapy, and spread to other parts of the body [53].

Several amino acid metabolism pathways were enriched due to the differences in distance, race and sex. Few amino acid metabolism pathways such as glycine, serine and threonine metabolism, cysteine and methionine metabolism, pyrimidine metabolism and arginine metabolism were enriched in all the three groups. Valine, leucine and isoleucine biosynthesis and phenylalanine, tyrosine and tryptophan metabolism were changed in two groups due to distance and sex. Perturbations in different amino acid metabolism pathways can have implications for cellular growth, repair, and protein synthesis. Methionine, an essential amino acid, in excess also acts as precursor for homocysteine. We observed a significant increase in methionine and homocysteic acid in individuals residing closer to the TT facility (Figure 8). Increased homocysteine or hyperhomocysteinemia is a known risk factor for cardiovascular disease, Parkinson's disease, Alzheimer's disease and stroke [54]. Glycine and serine are biosynthetically linked together and are essential metabolite for the survival of cancer cells [55]. Chronic dysregulation of glycine and serine metabolism can lead to cancer as these amino acids also play an important role in cellular antioxidant capacity, one-carbon metabolism and help in protein, lipid and nucleic acid synthesis. Branched-chain amino acid (BCAA) leucine, isoleucine and valine were also increased significantly in the residents due to proximity to the TT facility (Figures 1, 8). Elevated levels BCAAs observed in our study may reflect increased protein catabolism and muscle wasting, which are indicators of chronic metabolic stress. This has been consistently reported in both animal models and patients with Type 1 Diabetes Mellitus (T1DM), where plasma BCAAs are significantly elevated compared to healthy controls [56–58]. These results suggest that the elevated BCAAs in our exposed group may represent not only a consequence of environmental stress but also an early metabolic indicator of disrupted energy homeostasis. Our findings align with a previous mouse study showing that exposure to $PM_{2.5}$-induced asthma, was associated with elevated levels of BCAAs [59]. We also found vanillin was significantly high in the residents residing closer to the TT facility (Figure 8). In a study using high-resolution metabolomics analysis of human bronchial epithelial cells exposed to vanillin, revealed disruptions in energy, amino acid, antioxidant, and sphingolipid pathways linked to lung diseases [60].

Another important amino acid pathway that was enriched due to distance and sex is tyrosine and tryptophan metabolism. We observed a significant increase in tryptophan and its metabolite kynurenic acid in the group which was close to facility (Figure 8). Tryptophan metabolism is involved in many physiological functions, including inflammation, metabolism, and immune response. Dysregulation of these metabolic pathways can contribute to the development of a number of diseases such as respiratory, nervous, digestive disorders and cancers [61]. Tryptophan and its metabolites, particularly kynurenine, can act as reactive oxygen species (ROS) scavengers by directly neutralizing ROS such as hydrogen peroxide and superoxide, converting them into less reactive or more stable compounds [62, 63]. Thus, the observed increase in tryptophan and kynurenic acid near the facility may also indicate elevated oxidative burden, given the known susceptibility of the indole ring of tryptophan to oxidation. Tyrosine is a non-essential amino acid that serves as the precursor for several crucial neurotransmitters, including epinephrine, norepinephrine, and dopamine, as well as hormone thyroxine. Dysregulation in tyrosine metabolism has been implicated in the development of several diseases, including cancers and chronic disorders [64]. Increased tyrosine in urine or dysregulated tyrosine metabolism is associated with altered thyroid function [65]. This can partially explain the increased thyroid diseases reported by the several Colfax residents [4].

We further evaluated the changes in urinary metabolites based on sex and race. Sex-specific differences revealed distinct patterns of amino acid metabolism, with females exhibiting higher levels of metabolites like glutathione sulfonamide and UDP glucose, while males displayed elevated levels of lactate and bile acids. These findings may reflect physiological differences in metabolic processing and stress response mechanisms. Similarly, race-based comparisons highlighted unique metabolic signatures, with Black individuals showing elevated levels of glutathione and a higher GSH/GSSG ratio compared to White individuals. While some of these differences may be due to inherent biological variation, they may also reflect socio-environmental disparities. Factors such as unequal exposure to environmental pollutants, differences in healthcare access, diet, and chronic stress, can influence metabolic profiles and oxidative stress responses. These observations emphasize the importance of interpreting metabolomic data within a broader social and environmental context, accounting for both biological and non-biological determinants of health.

The observed shifts in the GSH/GSSG ratio suggest potential oxidative stress and it requires detailed investigation. Under normal conditions, the GSH:GSSG ratio in mammalian cells

exceeds 100:1, but this ratio decreases to 10:1 or even 1:1 under oxidative. This imbalance reflects an increase in oxidized glutathione (GSSG) relative to reduced glutathione (GSH), signifying a shift in the cellular redox state. The relative abundances glutathione sulfonamide (GSA) displayed significant variations based on proximity to the thermal treatment facility, with individuals residing within 5 km exhibiting higher abundances than those living farther away, indicating increased oxidative stress (Figure 7). Oxidative stress arises when the production of reactive oxygen species (ROS) surpasses the capacity of antioxidant defense systems, either due to insufficiency or dysfunction. This imbalance leads to significant damage to several biological macromolecules such as cellular membranes, lipids, proteins, and nucleic acids. An increase in oxidative stress is associated with onset and pathogenesis of several diseases such as thyroid disorders [66], diabetes [67], Parkinson's disease [68], Alzheimer's disease [69] and cancer [70]. While GSA levels and GSH/GSSG ratios are reliable biomarkers of redox status, it is important to consider potential confounding factors such as diet, medication use, renal function, and smoking, which may independently affect glutathione metabolism and oxidative balance. Future studies should incorporate detailed individual exposure histories and lifestyle data to better delineate the sources and implications of oxidative stress in environmentally exposed populations.

The study's findings are indicative of the potential health risks associated with exposure to emissions from the TT facility. Emissions from the TT facility contain a variety of pollutants, including PM, volatile organic compounds, heavy metals and EPFRs. These pollutants can directly or indirectly interfere with cellular metabolism, leading to the observed metabolic changes. The disruption of key metabolic pathways and the association with oxidative stress biomarkers suggest that long-term exposure could lead to adverse health outcomes. Identifying unique metabolites and pathway perturbations linked to proximity highlights the need for further epidemiological studies and regulatory measures to mitigate environmental health risks.

Limitations of the study

While the study provides compelling evidence of metabolic alterations, several limitations should be noted. First, this is an exploratory study with a relatively small sample size. However, this is a rural community, and 51 participants actually represents 3.5% of the population. Statistical analyses were performed using appropriate multivariate methods. To enhance reliability, data normalization, quality control filtering, and multiple testing corrections such as false discovery rate were also applied. For PLS-DA and VIP score analyses, model quality was assessed using Q2 values, calculated via cross-validation (CV) with thresholds above 0.5 indicating good predictive performance and model validity. Future studies involving larger cohorts and longitudinal sampling are obviously necessary to confirm these results and support their broader applicability. Power analysis for our exploratory study shows that significance of $\alpha = 0.10$ could be achieved with a power of $\beta = 0.72$ for a 1.75-fold difference, which was observed for 16 compounds among those living within 5 km of the facility and 2 compounds for those living at least 5 km away. Second, due to challenges of conducting the research in a rural community (older population, low educational attainment), first-void urine samples were not collected. It is not expected that bias in the sample collection method was systematic [71]. Third, self-selection bias may have resulted in a less healthy population, especially near the TT facility, because sick participants may have been more willing to tell their stories. This error could have the potential to introduce systematic bias [72] into the results if the health of those living closer to the facility was different from those living farther away and associated with their exposure. Additionally, integrating other omics approaches, such as transcriptomics and proteomics, could provide a more comprehensive understanding of the biological impacts of environmental exposure.

Conclusion

The metabolomic analysis of urine samples from the Colfax community members near the thermal treatment facility provides critical insights into potential environmental exposures and their impact on human health. With metabolomic profiling we found strong evidence of significant metabolic alterations in individuals residing closer to the thermal treatment facility compared to those living further away. The observed shifts in metabolite abundances and pathway perturbations, particularly in energy metabolism, oxidative stress pathways, and nucleotide and amino acid metabolism, suggest potential adverse health impacts associated with exposure to emissions from the facility. These findings highlight the importance of further investigation into the long-term health implications of these metabolic changes and the need for continued monitoring of the environmental and health impacts of the TT facility.

Author contributions

AK analyzed the data. AK, CG, QS, and CC wrote the manuscript. QS and CC performed the experiments and analyzed the data. SC, JR-B, and SC reviewed and edited the manuscript. SC conceived and designed the experiments. All authors contributed to the article and approved the submitted version.

Data availability

The original contributions presented in the study are included in the article/Supplementary Material, further inquiries can be directed to the corresponding author.

Ethics statement

The studies involving humans were approved by North Carolina State University IRB. The studies were conducted in accordance with the local legislation and institutional requirements. The participants provided their written informed consent to participate in this study.

Funding

The author(s) declare that no financial support was received for the research and/or publication of this article.

Conflict of interest

The author(s) declared no potential conflicts of interest with respect to the research, authorship, and/or publication of this article.

Generative AI statement

The author(s) declare that no Generative AI was used in the creation of this manuscript.

Supplementary material

The Supplementary Material for this article can be found online at: https://www.ebm-journal.org/articles/10.3389/ebm.2025.10655/full#supplementary-material

References

1. U.S. Census Bureau. S0601: selected characteristics of the total and native populations in the United States. *5-year Am Community Surv Colfax town, La* (2023). Available online at: https://data.census.gov/table/ACSST5Y2023.S0601?q=colfax,%20la (Accessed December 27, 2024).

2. U.S. Census Bureau. *S0601: selected characteristics of the total and native populations in the United States*. 2023 5-year American Community Survey, Grant Parish, Louisiana (2025). Available online at: https://data.census.gov/table/ACSST5Y2023.S0601?q=grant+parish+la (Accessed March 26, 2025).

3. Louisiana Department of Environmental Quality (LDEQ). *Hazardous waste permit application R&D*, **1** (2024). Available online at: https://edms.deq.louisiana.gov/app/doc/view?doc=673338 (Accessed July 1, 2024).

4. Richmond-Bryant J, Odera M, Subra W, Vallee B, Tucker C, Oliver C, et al. A community-integrated geographic information system study of air pollution exposure impacts in Colfax, LA. *Local Environ* (2022) **27**:728–46. doi:10.1080/13549839.2022.2075840

5. U.S. EPA. *Supplement to the 2019 integrated science assessment for particulate matter*. Final Report (2022). United states environmental protection agency. EPA/635/R-22/028, 2022.

6. Pelucchi C, Negri E, Gallus S, Boffetta P, Tramacere I, La Vecchia C. Long-term particulate matter exposure and mortality: a review of European epidemiological studies. *BMC Public Health* (2009) **9**:453. doi:10.1186/1471-2458-9-453

7. Hogervorst JGF, de Kok TMCM, Briedé JJ, Wesseling G, Kleinjans JCS, van Schayck CP. Relationship between radical generation by urban ambient particulate matter and pulmonary function of school children. *J Toxicol Environ Health A* (2006) **69**:245–62. doi:10.1080/15287390500227431

8. Saravia J, Lee GI, Lomnicki S, Dellinger B, Cormier SA. Particulate matter containing environmentally persistent free radicals and adverse infant respiratory health effects: a review. *J Biochem Mol Toxicol* (2013) **27**:56–68. doi:10.1002/jbt.21465

9. Harmon AC, Noël A, Subramanian B, Perveen Z, Jennings MH, Chen Y-F, et al. Inhalation of particulate matter containing free radicals leads to decreased vascular responsiveness associated with an altered pulmonary function. *Am J Physiology-Heart Circulatory Physiol* (2021) **321**:H667–H683. doi:10.1152/ajpheart.00725.2020

10. Mahne S, Chuang GC, Pankey E, Kiruri L, Kadowitz PJ, Dellinger B, et al. Environmentally persistent free radicals decrease cardiac function and increase pulmonary artery pressure. *Am J Physiology-Heart Circulatory Physiol* (2012) **303**:H1135–H1142. doi:10.1152/ajpheart.00545.2012

11. Wang Y, Yao K, Fu X, Zhai X, Jin L, Guo H. Size-resolved exposure risk and subsequent role of environmentally persistent free radicals (EPFRs) from atmospheric particles. *Atmos Environ* (2022) **276**:119059. doi:10.1016/j.atmosenv.2022.119059

12. Aryal A, Noël A, Khachatryan L, Cormier SA, Chowdhury PH, Penn A, et al. Environmentally persistent free radicals: methods for combustion generation, whole-body inhalation and assessing cardiopulmonary consequences. *Environ Pollut* (2023) **334**:122183. doi:10.1016/j.envpol.2023.122183

13. Zhang Z, Zhou M, He J, Shi T, Zhang S, Tang N, et al. Polychlorinated dibenzo-dioxins and polychlorinated dibenzo-furans exposure and altered lung function: the mediating role of oxidative stress. *Environ Int* (2020) **137**:105521. doi:10.1016/j.envint.2020.105521

14. Bertazzi PA, Consonni D, Bachetti S, Rubagotti M, Baccarelli A, Zocchetti C, et al. Health effects of dioxin exposure: a 20-year mortality study. *Am J Epidemiol* (2001) **153**:1031–44. doi:10.1093/aje/153.11.1031

15. McLean J, Anderson D, Capra G, Riley CA. The potential effects of burn pit exposure on the respiratory tract: a systematic review. *Mil Med* (2021) **186**:672–81. doi:10.1093/milmed/usab070

16. Liu J, Lezama N, Gasper J, Kawata J, Morley S, Helmer D, et al. Burn pit emissions exposure and respiratory and cardiovascular conditions among airborne hazards and open burn pit registry participants. *J Occup & Environ Med* (2016) **58**:e249–e255. doi:10.1097/jom.0000000000000776

17. Bedia C. Metabolomics in environmental toxicology: applications and challenges. *Trends Environ Anal Chem* (2022) **34**:e00161. doi:10.1016/j.teac.2022.e00161

18. Deng P, Li X, Petriello MC, Wang C, Morris AJ, Hennig B. Application of metabolomics to characterize environmental pollutant toxicity and disease risks. *Rev Environ Health* (2019) **34**:251–9. doi:10.1515/reveh-2019-0030

19. Richmond-Bryant J, Odera M, Subra W, Vallee B, Rivers III L, Kelley B, et al. Oral histories document community mobilisation to participate in decision-making regarding a hazardous waste thermal treatment facility. *Local Environ* (2024) **29**:57–73. doi:10.1080/13549839.2023.2249498

20. Gonzalez-Covarrubias V, Martínez-Martínez E, del Bosque-Plata L. The potential of metabolomics in biomedical applications. *Metabolites* (2025) **12**. doi:10.3390/metabo12020194

21. Wishart DS. Metabolomics for investigating physiological and pathophysiological processes. *Physiol Rev* (2019) **99**:1819–75. doi:10.1152/physrev.00035.2018

22. Johnson CH, Ivanisevic J, Siuzdak G. Metabolomics: beyond biomarkers and towards mechanisms. *Nat Rev Mol Cell Biol* (2016) **17**:451–9. doi:10.1038/nrm.2016.25

23. Johnson CH, Patterson AD, Idle JR, Gonzalez FJ. Xenobiotic metabolomics: major impact on the metabolome. *Annu Rev Pharmacol Toxicol* (2012) **52**:37–56. doi:10.1146/annurev-pharmtox-010611-134748

24. Xue C, Yang B, Fu L, Hou H, Qiang J, Zhou C, et al. Urine biomarkers can outperform serum biomarkers in certain diseases. *URINE* (2023) **5**:57–64. doi:10.1016/j.urine.2023.10.001

25. Chen C, Li H, Niu Y, Liu C, Lin Z, Cai J, et al. Impact of short-term exposure to fine particulate matter air pollution on urinary metabolome: a randomized, double-blind, crossover trial. *Environ Int* (2019) **130**:104878. doi:10.1016/j.envint.2019.05.072

26. Li G, Duan Y, Wang Y, Bian L, Xiong M, Song W, et al. Potential urinary biomarkers in young adults with short-term exposure to particulate matter and bioaerosols identified using an unbiased metabolomic approach. *Environ Pollut* (2022) **305**:119308. doi:10.1016/j.envpol.2022.119308

27. Guo C, Mathieu-Campbell ME, Blanchard T, Khachatryan L, Yu Q, Al-Mamun MA, et al. *Persistent chemicals in particulate matter (PM) near a hazardous waste thermal treatment facility*. preparation (2025).

28. Brender JD, Maantay JA, Chakraborty J. Residential proximity to environmental hazards and adverse health outcomes. *Am J Public Health* (2011) **101**:S37–S52. doi:10.2105/ajph.2011.300183

29. Oyinloye MA. *Environmental pollution and health risks of residents living near ewekoro cement factory*, **9**. Nigeria: Ewekoro (2025).

30. Rabinowitz JD, Kimball E. Acidic acetonitrile for cellular metabolome extraction from *Escherichia coli*. *Anal Chem* (2007) **79**:6167–73. doi:10.1021/ac070470c

31. Lu W, Clasquin MF, Melamud E, Amador-Noguez D, Caudy AA, Rabinowitz JD. Metabolomic analysis via reversed-phase ion-pairing liquid chromatography coupled to a stand alone Orbitrap mass spectrometer. *Anal Chem* (2010) **82**:3212–21. doi:10.1021/ac902837x

32. Bazurto JV, Dearth SP, Tague ED, Campagna SR, Downs DM. Untargeted metabolomics confirms and extends the understanding of the impact of aminoimidazole carboxamide ribotide (AICAR) in the metabolic network of *Salmonella enterica*. *Microb Cell* (2018) **5**:74–87. doi:10.15698/mic2018.02.613

33. Melamud E, Vastag L, Rabinowitz JD. Metabolomic analysis and visualization engine for LC–MS data. *Anal Chem* (2010) **82**:9818–26. doi:10.1021/ac1021166

34. Clasquin MF, Melamud E, Rabinowitz JD. LC-MS data processing with MAVEN: a metabolomic analysis and visualization engine. *Curr Protoc Bioinformatics* (2012) **Chapter 14**:Unit14.11–4.11.23. doi:10.1002/0471250953.bi1411s37

35. Mahmud I, Wei B, Veillon L, Tan L, Martinez S, Tran B, et al. Ion suppression correction and normalization for non-targeted metabolomics. *Nat Commun* (2025) **16**:1347. doi:10.1038/s41467-025-56646-8

36. Nam SL, de la Mata AP, Dias RP, Harynuk JJ. Towards standardization of data normalization strategies to improve urinary metabolomics studies by GC×GC-TOFMS. *Metabolites* (2020) **10**:376. doi:10.3390/metabo10090376

37. Zaparte A, Christopher CJ, Arnold C, Richey L, Castille A, Mistretta K, et al. Effects of E-cigarettes on the lung and systemic metabolome in people with HIV. *Metabolites* (2024) **14**:434. doi:10.3390/metabo14080434

38. Blake TL, Sly PD, Andersen I, Wainwright CE, Reid DW, Bell SC, et al. Changes in urinary glutathione sulfonamide (GSA) levels between admission and discharge of patients with cystic fibrosis. *J Cystic Fibrosis* (2024) **23**:1163–6. doi:10.1016/j.jcf.2024.04.009

39. Odera M, Kelley B, Rivers L, Wilson A, Tran J, Patel K, et al. A community-engaged oral history study as a tool for understanding environmental justice aspects of human exposures to hazardous waste thermal treatment emissions in Colfax, LA. *Environ Justice* (2023) 0003.

40. Negri E, Bravi F, Catalani S, Guercio V, Metruccio F, Moretto A, et al. Health effects of living near an incinerator: a systematic review of epidemiological studies, with focus on last generation plants. *Environ Res* (2020) **184**:109305. doi:10.1016/j.envres.2020.109305

41. Parkes B, Hansell AL, Ghosh RE, Douglas P, Fecht D, Wellesley D, et al. Risk of congenital anomalies near municipal waste incinerators in England and Scotland: retrospective population-based cohort study. *Environ Int* (2020) **134**:104845. doi:10.1016/j.envint.2019.05.039

42. Mohan AK, Degnan D, Feigley CE, Shy CM, Hornung CA, Mustafa T, et al. Comparison of respiratory symptoms among community residents near waste disposal incinerators. *Int J Environ Health Res* (2000) **10**:63–75. doi:10.1080/09603120073018

43. Mattiello A, Chiodini P, Bianco E, Forgione N, Flammia I, Gallo C, et al. Health effects associated with the disposal of solid waste in landfills and incinerators in populations living in surrounding areas: a systematic review. *Int J Public Health* (2013) **58**:725–35. doi:10.1007/s00038-013-0496-8

44. Comba P, Ascoli V, Belli S, Benedetti M, Gatti L, Ricci P, et al. Risk of soft tissue sarcomas and residence in the neighbourhood of an incinerator of industrial wastes. *Occup Environ Med* (2003) **60**:680–3. doi:10.1136/oem.60.9.680

45. Ashworth DC, Elliott P, Toledano MB. Waste incineration and adverse birth and neonatal outcomes: a systematic review. *Environ Int* (2014) **69**:120–32. doi:10.1016/j.envint.2014.04.003

46. Ahmad F, Cherukuri MK, Choyke PL. Metabolic reprogramming in prostate cancer. *Br J Cancer* (2021) **125**:1185–96. doi:10.1038/s41416-021-01435-5

47. Liu H, Wang S, Wang J, Guo X, Song Y, Fu K, et al. Energy metabolism in health and diseases. *Sig Transduct Target Ther* (2025) **10**:69–71. doi:10.1038/s41392-025-02141-x

48. Yusa V, Ye X, Calafat AM. Methods for the determination of biomarkers of exposure to emerging pollutants in human specimens. *Trac Trends Anal Chem* (2012) **38**:129–42. doi:10.1016/j.trac.2012.05.004

49. Liao J, Goodrich J, Walker DI, Lin Y, Lurmann F, Qiu C, et al. Metabolic pathways altered by air pollutant exposure in association with lipid profiles in young adults. *Environ Pollut* (2023) **327**:121522. doi:10.1016/j.envpol.2023.121522

50. Mann JK, Lutzker L, Holm SM, Margolis HG, Neophytou AM, Eisen EA, et al. Traffic-related air pollution is associated with glucose dysregulation, blood pressure, and oxidative stress in children. *Environ Res* (2021) **195**:110870. doi:10.1016/j.envres.2021.110870

51. Kurutas EB. The importance of antioxidants which play the role in cellular response against oxidative/nitrosative stress: current state. *Nutr J* (2016) **15**:71. doi:10.1186/s12937-016-0186-5

52. Uboveja A, Aird KM. Interplay between altered metabolism and DNA damage and repair in ovarian cancer. *BioEssays* (2024) **46**:2300166. doi:10.1002/bies.202300166

53. Mullen NJ, Singh PK. Nucleotide metabolism: a pan-cancer metabolic dependency. *Nat Rev Cancer* (2023) **23**:275–94. doi:10.1038/s41568-023-00557-7

54. Kumar A, Palfrey HA, Pathak R, Kadowitz PJ, Gettys TW, Murthy SN. The metabolism and significance of homocysteine in nutrition and health. *Nutr Metab (Lond)* (2017) **14**:78. doi:10.1186/s12986-017-0233-z

55. Amelio I, Cutruzzolá F, Antonov A, Agostini M, Melino G. Serine and glycine metabolism in cancer. *Trends Biochem Sci* (2014) **39**:191–8. doi:10.1016/j.tibs.2014.02.004

56. Rodríguez T, Alvarez B, Busquets S, Carbó N, López-Soriano FJ, Argilés JM. The increased skeletal muscle protein turnover of the streptozotocin diabetic rat is associated with high concentrations of branched-chain amino acids. *Biochem Mol Med* (1997) **61**:87–94. doi:10.1006/bmme.1997.2585

57. Borghi L, Lugari R, Montanari A, Dall'Argine P, Elia GF, Nicolotti V, et al. Plasma and skeletal muscle free amino acids in type I, insulin-treated diabetic subjects. *Diabetes* (1985) **34**:812–5. doi:10.2337/diab.34.8.812

58. Holeček M. Why are branched-chain amino acids increased in starvation and diabetes? *Nutrients* (2020) **12**:3087. doi:10.3390/nu12103087

59. Wang Z, Gao S, Xie J, Li R. Identification of multiple dysregulated metabolic pathways by GC-MS-based profiling of lung tissue in mice with PM2.5-induced asthma. *Chemosphere* (2019) **220**:1–10. doi:10.1016/j.chemosphere.2018.12.092

60. Smith MR, Jarrell ZR, Orr M, Liu KH, Go Y-M, Jones DP. Metabolome-wide association study of flavorant vanillin exposure in bronchial epithelial cells reveals disease-related perturbations in metabolism. *Environ Int* (2021) **147**:106323. doi:10.1016/j.envint.2020.106323

61. Xue C, Li G, Zheng Q, Gu X, Shi Q, Su Y, et al. Tryptophan metabolism in health and disease. *Cell Metab* (2023) **35**:1304–26. doi:10.1016/j.cmet.2023.06.004

62. Genestet C, Le Gouellec A, Chaker H, Polack B, Guery B, Toussaint B, et al. Scavenging of reactive oxygen species by tryptophan metabolites helps *Pseudomonas aeruginosa* escape neutrophil killing. *Free Radic Biol Med* (2014) **73**:400–10. doi:10.1016/j.freeradbiomed.2014.06.003

63. Christen S, Peterhans E, Stocker R. Antioxidant activities of some tryptophan metabolites: possible implication for inflammatory diseases. *Proc Natl Acad Sci U S A* (1990) **87**:2506–10. doi:10.1073/pnas.87.7.2506

64. Tanguay RM, Jorquera R, Poudrier J, St-Louis M. Tyrosine and its catabolites: from disease to cancer. *Acta Biochim Pol* (1996) **43**:209–16. doi:10.18388/abp.1996_4530

65. Bélanger R, Chandramohan N, Misbin R, Rivlin RS. Tyrosine and glutamic acid in plasma and urine of patients with altered thyroid function. *Metabolism* (1972) **21**:855–65. doi:10.1016/0026-0495(72)90009-1

66. Lassoued S, Mseddi M, Mnif F, Abid M, Guermazi F, Masmoudi H, et al. A comparative study of the oxidative profile in graves' disease, hashimoto's thyroiditis, and papillary thyroid cancer. *Biol Trace Elem Res* (2010) **138**:107–15. doi:10.1007/s12011-010-8625-1

67. Cerielo A, Motz E, Cavarape A, Lizzio S, Russo A, Quatraro A, et al. Hyperglycemia counterbalances the antihypertensive effect of glutathione in diabetic patients: evidence linking hypertension and glycemia through the

oxidative stress in diabetes Mellitus. *J Diabetes its Complications* (1997) **11**:250–5. doi:10.1016/s1056-8727(97)00021-4

68. Burke WJ. The progression of Parkinson disease: a hypothesis. *Neurology* (2007) **69**:710–1. doi:10.1212/01.wnl.0000285430.23876.c5

69. Liu H, Wang H, Shenvi S, Hagen TM, Liu R-M. Glutathione metabolism during aging and in Alzheimer disease. *Ann New York Acad Sci* (2004) **1019**:346–9. doi:10.1196/annals.1297.059

70. Li K, Deng Z, Lei C, Ding X, Li J, Wang C. The role of oxidative stress in tumorigenesis and progression. *Cells* (2024) **13**:441. doi:10.3390/cells13050441

71. Ginsberg JM, Chang BS, Matarese RA, Garella S. Use of single voided urine samples to estimate quantitative proteinuria. *N Engl J Med* (1983) **309**:1543–6. doi:10.1056/nejm198312223092503

72. Heckman JJ. Selection bias and self-selection. In: *The new palgrave dictionary of economics*. London: Palgrave Macmillan (2025). p. 1–18.

EBM Experimental Biology and Medicine

TYPE Original Research
PUBLISHED 20 August 2025
DOI 10.3389/ebm.2025.10611

OPEN ACCESS

*CORRESPONDENCE
Jin Li,
jimlijin76@126.com

†These authors have contributed equally to this work

RECEIVED 01 April 2025
ACCEPTED 06 August 2025
PUBLISHED 20 August 2025

CITATION
Hou J, Zhang S, Luo S, Zuo X, Ma F, Wang H, Han P, Zhu P, Wang N, Hou X and Li J (2025) Csf1⁺ AD-MSCs promote stroke repair by activating the resident microglia.
Exp. Biol. Med. 250:10611.
doi: 10.3389/ebm.2025.10611

Csf1⁺ AD-MSCs promote stroke repair by activating the resident microglia

Jiguang Hou[1†], Sunfu Zhang[2†], Shuang Luo[3], Xiao Zuo[4], Fei Ma[4], Huizhen Wang[4], Pengfei Han[4], Ping Zhu[4], Ning Wang[4], Xiaoming Hou[5] and Jin Li[1*]

[1]Department of Neurosurgery, West China Hospital of Sichuan University, Chengdu, China, [2]Department of Neurosurgery, Third People's Hospital of Chengdu, Chengdu, China, [3]Department of Neurosurgery, Fifth People's Hospital of Chengdu, Chengdu, China, [4]Tasly Stem Cell Biology Laboratory, Tasly Group, Tianjin, China, [5]Regenerative Medicine Research Center, West China Hospital of Sichuan University, Chengdu, China

Abstract

The potential of mesenchymal stromal cells (MSCs) in the treatment of hemorrhagic stroke has been demonstrated; however, their clinical efficacy remains inconsistent and further comprehensive studies on their mechanism of action are warranted. In this study, the intracerebral hemorrhage (ICH) rat model was used for intravenous infusion of adipose-derived mesenchymal stromal cells (AD-MSCs) 24 h after modeling. Histopathological techniques and single cell transcriptome sequencing techniques were used to study the mechanism of AD-MSCs promoting the repair of damaged brain tissue. The results indicated that AD-MSCs markedly promote the repair of damaged brain tissues and restored neural function. Single-cell transcriptome sequencing further revealed that this therapeutic effect is specifically through the inhibition of monocyte infiltration in injured brain tissue, promotion of resident microglia proliferation and signaling pathways linked to immune response and neuroprotection. These processes are closely tied to the Csf1⁺ subgroup of AD-MSCs. For acute hemorrhagic stroke, Csf1⁺ AD-MSCs promote the repair of damaged brain tissue by activating resident microglia and inhibiting monocyte infiltration. This study offers novel insights into the mechanisms underlying MSC-based stroke treatment and supports the potential for stable and efficacious MSC therapies.

KEYWORDS

stroke, MSCs, microglia, single-cell transcriptome sequencing, subgroup

Impact statement

This study uncovers a critical mechanism by which adipose-derived mesenchymal stromal cells (AD-MSCs) promote brain repair in hemorrhagic stroke, revealing that the Csf1⁺ AD-MSCs subgroup enhances neuroprotection by activating resident microglia while suppressing monocyte infiltration. By integrating single-cell

transcriptomics with functional validation, we resolve longstanding inconsistencies in MSC therapeutic efficacy and identify cellular heterogeneity as a key determinant of treatment outcomes. These findings provide a roadmap for optimizing MSC-based therapies through targeted enrichment of functional subpopulations, paving the way for standardized, high-efficacy treatments in stroke and potentially other neuroinflammatory disorders. This work bridges mechanistic insights with clinical translation, offering a transformative strategy to improve regenerative medicine for neurological injuries.

Introduction

Hemorrhagic stroke is a common subtype of stroke, characterized by high rates of disability and mortality [1, 2]. With the development of cell therapy technology, MSCs have shown potential to promote the repair of injured nerve tissue. Animal studies haves shown that MSCs promote nerve regeneration, restore motor function, and hold promise for stroke treatment [3, 4]. However, clinical trials have identified a significant challenge–the inconsistent therapeutic effects of MSCs, limiting their widespread use [5–7]. More efforts are needed to elucidate the therapeutic mechanisms of MSCs.

Numerous studies have reported that MSCs exert therapeutic effects by participating in immune regulation at the site of injury [8, 9]. Microglia, as resident immune cells in brain tissue, play a crucial role in the repair of neural tissue damage. Under normal physiological conditions, microglia remain in a quiescent state, contributing significantly to maintaining brain tissue homeostasis [10, 11]. Following injury, resident microglia become activated and recruit bone marrow-derived inflammatory cells to infiltrate the area, resulting in the production of substantial inflammatory factors that cause severe damage to neural cells [12]. A pile of evidence demonstrated the immunomodulatory effects of MSCs on microglia in stroke model [13–15]. Results based on a model of traumatic brain injury in rats showed that intraventricular injection of MSCs 24 h after injury significantly inhibited the activity of microglia and promoted injury repair [16]. However, other studies have found that intravenous MSCs infusion 2 days after middle cerebral artery occlusion (MCAO) modeling does not suppress immune response, but aggravate inflammation and brain tissue damage, manifested by the increase of microglia and increased secretion of inflammatory factors such as TNF-α and IL-1β [17, 18]. These paradoxical phenomena suggest that the 24 h after injury may be the key time window for MSCs to play the role of immune regulation and promote the repair of damaged tissues.

Additionally, a considerable amount of research has shown that MSCs promote the transformation of microglia from the M1 type to the M2 type, promoting the repair of damaged brain tissue [19, 20]. Although the activation of M1 microglia is generally considered to be associated with the occurrence of inflammation and neurological injury, however, studies suggest that M1 microglia is necessary for clearing necrotic tissue debris and promoting tissue repair in the early stages of injury. Research by David et al. demonstrated that depleting microglia cell in brain tissue before inducing injury exacerbates the damage [21]. Studies based on single-cell RNA sequencing technology have revealed that during the repair of neural tissue injury, microglia cells exhibit dynamically changing and diverse cell phenotypes that cannot be simply categorized as M1 or M2 [22, 23]. Consequently, the mechanism of MSCs in promoting the repair of injured neural tissue cannot be simply defined as immune suppression; rather, it involves a complex interplay of immune modulation and tissue repair processes.

In this study, we constructed ICH experimental animal models utilizing Sprague-Dawley (SD) rats. To more accurately analyze the role of MSCs in damaged brain tissue, allogeneic AD-MSCs were administered via intravenous injection 24 h post-model establishment. By integrating histopathological techniques with single-cell transcriptome sequencing, we systematically analyzed the impact of AD-MSCs on brain microglial and the repair mechanisms of injured brain tissue. Furthermore, we elucidated the underlying molecular mechanisms. The findings from this research will offer a significant foundation for future clinical treatments.

Materials and methods

Animals

All animal procedures described here were approved by the Institutional Animal Care and Use Committee at Sichuan University West China Hospital.

The work has been reported in line with the ARRIVE guidelines 2.0.

Hemorrhagic stroke model in rats

Experimental animals

Male rats were exclusively used in this study to preclude the neuroprotective effects of estrogen on brain injury and to circumvent operational variability associated with the estrous cycle in females. This approach eliminates confounding hormonal protection (e.g., reduced hematoma volume, accelerated recovery) and ensures model reproducibility by avoiding fluctuations in blood-brain barrier permeability and coagulation function inherent to the female estrous cycle [24–26]. The experimental animals were healthy male SD rats, 8–10 weeks old, weighing 220–280 g.

TABLE 1 Modified Neurological Severity Score (mNSS) tests and scoring values.

Motor test score values and descriptions	
(Normal score = 0; maximum possible summary score = 6)	
0 or 1[a]	Flexion of forelimb after raising rat by the tail
0 or 1*	Flexion of hindlimb after raising rat by the tail
0 or 1*	Head moved >10° to vertical axis within 30 seconds after raising rat by the tail
0	Normal walk after placing rat on the floor
1	Inability to walk straight after placing rat on the floor
2	Circling toward paretic side after placing rat on the floor
3	Falls down to paretic side after placing rat on the floor
Sensory test score values and descriptions	
(Normal score = 0; maximum possible summary score = 2)	
0 or 1[a]	Placing test (visual and tactile test)
0 or 1[a]	Procioceptive test (deep sensation, pushing paw against table to stimulate limb muscles)
Beam and balance test score values and descriptions	
(Normal score = 0; maximum possible summary score = 6)	
0	Balances with steady posture
1	Grasps side of beam
2	Hugs beam and 1 limb falls down from beam
3	Hugs beam and 2 limbs fall down from beam, or spins on beam (60 seconds)
4	Attempts to balance on beam, but falls off (>40 seconds)
5	Attempts to balance on beam, but falls off (>20 seconds)
6	Falls off; no attempt to balance or hang on to beam (<20 seconds)
Reflex absence and abnormal movements test score values and descriptions	
(Normal score = 0; maximum possible summary score = 4)	
0 or 1[a]	Pinna reflex (head shakes when auditory meatus is touched with cotton)
0 or 1[a]	Corneal reflex (eye blink when cornea is lightly touched with cotton)
0 or 1[a]	Startle reflex (motor response to a brief noise from snapping a clipboard paper)
0 or 1[a]	Seizure, myoclonus, myodystony

[a]Score value of 1 was given for the inability to perform a test, or for the lack of a tested reflex, or for abnormal movement as described by Chen et al [26].

Modeling methods

The ICH model of the right striatum of rats was established by using the collagenase-induced ICH model reported by Rosenberg et al.

Anesthesia of animals

The rats were first induced with isoflurane at 4% concentration, the head surgical site was shaved and the surgical area was disinfected with iodophor, then the rats were fixed on a stereoscope, and the anesthesia was maintained with isoflurane at 2% ± 1% concentration for modeling surgery.

Modeling operation procedure

The skin was cut 1.0 cm at the median sagittal position of the head, and the periosteum was cut to the skin to reveal. Then a sterile cotton swab dipped in 3% hydrogen peroxide was used to corrode the outer mold of the skull, exposing the coronal suture and the fontanel. According to the brain atlas, the position of the right striatum was 3 mm beside the bregma, 0.2 mm behind it, and 5.6 mm deep. At the location, drill a small round hole with a dental drill to reach the surface of the hard membrane. Type VII collagenase was extracted with a microsyringe of 0.5 U/μL, and the microsyringe was fixed on the stereoscope, the needle was vertically inserted into the subdural 5.6 mm along the drilling hole, and the collagenase was slowly pushed into the brain for about 2 min, and the needle was slowly withdrawn to the extracranial for about 2 min after the needle was stopped. Finally, the bone holes were closed with bone wax, and the scalp was sutured and disinfected with iodophor.

Model identification and enrollment criteria

Neurological score (NS) was performed at different time points after rats were awake, as shown in Table 1. In this study, the 18-point Neurological score (NS) system was used 24 h after modeling, and animals with moderate and severe neurological impairment ranging from 7 to 14 points were selected into the group.

The successful establishment of a hemorrhagic stroke model in SD rats was evaluated using MRI

SD rats underwent cranial scanning using a 3.0T S magnetic resonance imaging (MRI) device to assess the hemorrhage status in a model of hemorrhagic stroke. Prior to MRI scanning, the rats were anesthetized via intraperitoneal injection of Sufentanil citrate (Sufentanil) at a dosage of 0.1 mL per 100 g of body weight, ensuring the animals remained sedated and pain-free during the scanning process. The scanning sequence employed was T2-weighted imaging, with a slice thickness of 1 mm. This sequence is particularly sensitive to changes in water content within brain tissue, and acute cerebral hemorrhage areas will appear as hypointense regions. This feature facilitates clear identification of brain edema and hemorrhage areas caused by hemorrhagic stroke, thereby confirming the successful establishment of the cerebral hemorrhage model.

Amplified culture of AD-MSCs

AD-MSCs were isolated from rats as follows: Approximately 2 g adipose tissue was harvested from the lateral hypogastric region of rat by aseptic surgery. AD-MSCs were isolated following a procedure described previously [27, 28]. Briefly, the adipose tissue was treated with collagenase type I (Life Technologies, Grand Island, NY, United States), and then cultured in α-MEM (Gibco, United States, 41061-029) with 10% FBS (Gibco, United States, 12664025) for 1 day in a T-25 flask (Thermo Fisher, Carlsbad, CA, United States). Floating cells were removed the next day by replacing the medium. Verification of isolated AD-MSCs was performed using antibodies against CD90-BV786, CD105-PE, CD44-PE-CF594, CD29-APC, CD73-BV421, CD14-FITC, CD34-FITC, CD45-FITC, CD31-FITC and HLA-FITC. The isolated AD-MSCs did not express CD14, CD31, CD34, CD45 and HLA. Surface type analysis of the AD-MSCs was performed using a FACSelesta flow cytometer (BD, Germany). The isolated AD-MSCs were propagated for 3 generations within 14 days, and the propagated AD-MSCs were cryopreserved until the use.

Cell differentiation

The induced differentiation of AD-MSCs was performed by culturing the AD-MSCs in conditioned induction medium (Cyagen, US). The osteogenic differentiation of AD-MSCs was observed by alizarin red staining. Adipogenic differentiation of AD-MSCs was observed by oil Red O staining. The chondrogenic differentiation of AD-MSCs was observed by Alcian blue staining.

Fluorescent labeling of AD-MSCs by PKH26

AD-MSCs were fluorescently labeled using the PKH26 reagent according to the provided instructions. Reagents were prepared, including 1% human albumin normal saline, complete medium, and PKH26 working liquid (prepared to avoid light and used immediately). AD-MSCs were centrifuged, cleaned, and resuspended in normal saline for sampling and counting. The PKH26 working fluid was prepared according to cell count results, and cells were labeled, stained at room temperature for 5 min with gentle mixing, and then centrifuged. After staining cessation with FBS, AD-MSCs were cleaned, resuspended, passed through a 70 μm cell screen, and centrifuged again. The AD-MSCs concentration was adjusted to 5×10^6 cells/mL using human blood albumin and normal saline, and the cell preparation was stored at 2–8°C for later use. AD-MSCs from 1-month-old and 12-month-old SD rats were prepared similarly for treatment.

Cell viability assay

LIVE/DEADTM cell imaging kit (Cat No. R37601, Thermo Fisher Scientific, United States) and NucBlueTM live cell stain (Cat No. R37605, Thermo Fisher Scientific, United States) were prepared and added into the medium of AD-MSCs as per manufacturer reference. The cells were then incubated at room temperature for 20 min in darkness. After incubation, the cells were imaged by Nikon A1 laser confocal microscope (Nikon, Japan).

Caudal venous transfusion of AD-MSCs

The SD rats in the treatment group were treated with AD-MSCs 24 h after intracranial hemorrhage modeling. After the SD rats were fixed with a rat fixation device, the tail vein was disinfected with alcohol, and 5×10^6 cells/mL of AD-MSCs were slowly injected into the rats through the tail vein at a dose of 1×10^7 cells/kg. The injection time is controlled at 1–2 min. During the treatment of ICH rats, AD-MSCs derived from young rats and aged rats were administered at identical doses.

Neural function score

Neurological function scores were performed 24 h after modeling before treatment, 7, 14, 21 and 28 days after treatment. The neural function scores were mainly from the following four aspects listed in Table 1 [29]: 1. Motor function (6 points): lifting the rat tail and observing the flexion of the contralateral forelimb; The rats were placed on the floor and observed to walk. 2. Sensation test (2 points): mainly deep sense. 3. Balance beam test (6 points): mainly observe the balance of rats after cerebral ischemia, so as to judge the degree of neurological dysfunction. 4. Reflex (4 points): including auricle, cornea, fright, convulsive reflex, etc. 0 is normal, 18 is the most serious. A score of 1-6 indicates mild damage; 7-12 points indicate moderate damage; A score of 13–18 indicates serious damage.

Euthanasia of rats using carbon dioxide

Rats were euthanized using carbon dioxide. The rats are placed in a transparent, airtight anesthetic chamber, and the valve of the carbon dioxide tank is slowly opened to fill the chamber with carbon dioxide at a flow rate of 10%–30% of the container's volume per minute for 3–5 min. The rats will initially exhibit agitation, followed by gradual anesthesia, collapse, and cessation of breathing. After stopping the gas supply, the rats are observed for an additional 2–3 min to

confirm death by palpating the chest for a heartbeat and observing for the absence of respiration. Immediately after confirming the animals' death, they are dissected for tissue collection.

Immunohistochemistry/ immunofluorescence staining

HE and immunohistochemical tests were performed 28 days after treatment to evaluate the therapeutic effect of allogeneic young and old AD-MSCs. The collected rat brain tissue was fixed with 4% paraformaldehyde, embedded in paraffin by the usual method, sliced to a thickness of 4 μm, stained with HE and Masson according to the manufacturer's instructions. All sections were histologically analyzed and photographed with an optical microscope.

The homing of AD-MSCs at brain injury sites was observed by immunofluorescence (PKH26) detection at 24 h, 48 h and 72 h after AD-MSCs treatment.

Rat derived AD-MSCs and brain tissue single cell RNA-seq library generation and sequencing

The brain tissue of the infarct margin area was collected from rat with a scalpel (or surgical scissors). Under sterile conditions, wash twice with pre-cooled RPMI 1640 + 0.04% BSA medium. The tissue was fully cut into small pieces of about 0.5 mm^3 with surgical scissors and put into freshly prepared enzymatic solution (enzymatic solution composition, concentration, brand), and digested by enzymatic digestion in a constant temperature incubator at 37°C for 30–60 min (references), and mixed inversely every 5–10 min. The digested cell suspension was filtered by BD 40 μm cell screen for 1-2 times, centrifuged at 4°C and 300 g for 5 min. After the precipitation was suspended with appropriate medium, the same volume of red blood cell lysate (MACS, No. 130-094–183) was added, mixed, left for 10 min at 4°C, cell suspension 300 g centrifuged for 5 min, and the supernatant was discarded. The precipitation was washed in the medium once, centrifuged at 300 g for 5 min, and the supernatant was discarded. The cell precipitation was suspended in the medium of 100 μL, and the cell concentration and viability were calculated by Luna cell counter.

The freshly prepared single-cell suspension was adjusted to 700-1,200 cell/μL according to the 10 × Genomics Chromium Next GEM Single Cell 3′ Reagent Kits v3.1 (No. 1000268) Operation manual for computer and library construction. The constructed library was sequenced using Illumina Nova 6000 PE150 platform.

Single cell RNA-seq data pre-processing and quality control

Single-cell RNA sequencing data generated using the 10x Genomics platform was processed with Cell Ranger version 8.0.0 (10x Genomics). Raw sequencing reads were aligned to the rat reference genome and assigned to individual cells of origin according to the cell-specific barcodes using the Cell Ranger pipeline (10× Genomics). The rat genome used in this analysis was obtained from the NCBI database, specifically version GCF_015227675.2. The output gene expression matrix was then imported into the Seurat (v4.3.0) R package for downstream analysis. SoupX R package (v1.6.2) was employed to removes ambient RNA contamination from droplet-based single-cell RNA sequencing data. DoubletFinder R package (v2.0.4) was employed to identify the poorly dissociated doublets in the single-cell suspension preparation process. Low-quality cells (<200 genes/cell and >10% mitochondrial genes) were excluded. Low-quality genes detected in less three cells were excluded. Gene expression levels for each cell were normalized by total expression, multiplied by a scale factor (10,000), and log-transformed. Top 2000 highly variable features (HVGs) in a sample were identified by "FindVariableFeatures" Seurat function. Brain samples and AD-MSCs samples were merged respectively, and variable features per sample were merged correspondingly. Gene expression data was scaled according to UMI number using the "ScaleData" Seurat function, meanwhile, nUMI and percent.mito were regressed out, ensuring that each gene's expression is centered and scaled to facilitate downstream dimensionality reduction and clustering analyses. We reduced the dimensionality of the data by performing the principal component analysis (PCA) on HVGs. Harmony R package (v0.1.1) was used to remove batch effect. To display data, the Unsupervised Uniform Manifold Approximation and Projection (UMAP) was applied to cell loadings of selected PCs. The "FindClusters" Seurat function was employed to identify distinct cell clusters based on gene expression patterns, using a shared nearest neighbor (SNN) modularity optimization algorithm to group cells with similar profiles. To identify differentially expressed genes between two clusters, we used the "find.markers" Seurat function with logfc. threshold = 0.25 and test. use = "wilcox".

Subcluster identification steps was same to the above cluster identification steps.

Celltype indentification

For brain samples, we divided cells into 31 clusters using the "FindClusters" Seurat function in with resolution 0.6. We identified 18 cell types including two unknown populations. The identified cell types are: Astrocytes (Gfap, Aqp4, Rorb), Microglial cells (Tmem119, P2ry12, Cx3cr, Sall),

Oligodendrocytes (Mbp, Plp1, Mog, Olig1, Olig2), Neurons (Gria1, Syt1), OPCs (Vcan, Pdgfra, Sox10), Neuroblasts (Ccnd2, Dcx, Sox4, Sox11, Stmn2), T cells (Cd3e, Cd3g), Monocytes (Cd74, Plac8, Ccr2), Macrophages (Cd14, Cd68, Lyz2, Gpnmb), Myeloid derived cells (Lilrb4), Neutrophils (S100a9, S100a8), Endothelial cells (Vwf, Pecam1), SMCs (Myh11, Acta2), Pericytes (Pdgfrb, Vtn, Cspg4), Fibroblasts (Col1a1, Col1a2, Col3a1), Epithelial cells (Kl, Folr1, Sostdc1), Ependymal cells (Ccdc153, Tmem212, Dnah11), Cycling cells (Top2a, Mki67).

Enrichment analysis

Enriched KEGG terms of marker genes were identified using the enrichKEGG function from the clusterProfiler package (v4.6.0), with gene annotations provided by the org.Rn.eg.db database in the org.Rn.eg.db R package (v3.16.0).

Statistical analysis

Data were obtained from three separate experiments and expressed as means ± standard error of the mean (SEM). A single factor design was applied to this study. After a significant interaction was detected by the analysis of variance (SPSS), the significance of the main effects was further determined by T-test (2 groups) and Kruskal-Wallis test (3 groups). The Mann-Whitney U test (Bonferroni correction) was used for *post hoc* statistical testing. The level of significance was considered when $P < 0.05$.

Results

AD-MSCs significantly promote the repair of damaged brain tissues in ICH rats

The rat model of ICH was established by intraventricular injection of collagenase (Figure 1A), the result of nuclear magnetic test 24 h after operation showed that the mold was made successfully (Supplementary Figure S1). The neural function score indicated a significant loss of neural function in the rats following ICH modeling, which gradually recovered to a certain extent during the subsequent 28-day observation period (ICH group: n = 6). Compared to the ICH group, rats treated with AD-MSCs exhibited more pronounced recovery of neural function (Figure 1B). (AD-MSCs group: n = 5). The gross observation results of brain tissue sampling showed that there were significant defects in the rat brain tissue after ICH modeling, and AD-MSCs treatment significantly limited the expansion of the damage (Figure 1C). Further histopathological results showed that, compared with the ICH group, AD-MSCs treatment significantly reduced collagen formation and apoptosis in the injured brain tissue, and significantly increased the formation of blood vessels (Figure 1D). These results showed that the treatment of AD-MSCs significantly promote the repair of damaged brain tissue and recover the nerve function. Next, we analyzed the effects of AD-MSCs by single-cell sequencing.

AD-MSCs promote the damaged brain tissues repair by increasing and activating the resident microglia

After 3 days of AD-MSCs treatment, brain tissues were sampled and sequenced by 10×Genomics. The brain tissue cells were divided into 18 subgroups by unsupervised clustering. The classification of each cell subgroup was identified by characteristic markers (Supplementary Figure S2), and the results were shown in Figure 2A. Compared with the ICH group, AD-MSCs treatment significantly reduced the proportion of fibroblasts and moderately increased the proportion of endothelial cells as well as the proportion of neuronal cells (Figure 2B).

In terms of the effect on immune cells, AD-MSCs significantly reduced the invasion of mononuclear/macrophage cells. However, compared with the ICH group, AD-MSCs did not affect the transformation of macrophage subgroups (Figure 2C). In addition, AD-MSCs significantly increased the proportion of microglia (Figure 2B). It is generally believed that the increase of microglia leads to increased brain tissue damage. Therefore, we conducted an in-depth analysis of the increase of microglia induced by AD-MSCs. Unsupervised cluster analysis showed that microglia could be divided into three subgroups (Figure 2D). In order to explore the function of these three subgroups, we first detected the expression of microglia cells homeostasis genes Tmem119, P2ry12, Csf1r, Cx3cr1 and Hexb in each subpopulation. The results showed that these genes were highly expressed in subpopulations 0 (Figure 3A), which constituted 70% of the total microglia population in the control group (Figure 2E). Therefore, we determined that subgroup 0 was a resting microglia. We further analyzed subpopulations 1 and 2 of microglia. It has been proved that there are active microglia with anti-inflammatory and pro-inflammatory phenotypes in injured brain tissue [30]. Therefore, we examined the expression of related genes in microglia cells subgroups 1 and 2. The results showed that the genes closely related to proinflammation were highly expressed in subpopulation 2, including Lgals3, Plau, Ankrd33b, Fam129b, Vat1, Ccl2, Ccl3, Ccl4, Cxcl2 and Cxcl16, however, which were not expressed in subpopulation 1 (Figure 3C). It suggested that subpopulation 1 and subpopulation 2 are two completely different activated microglia cells.

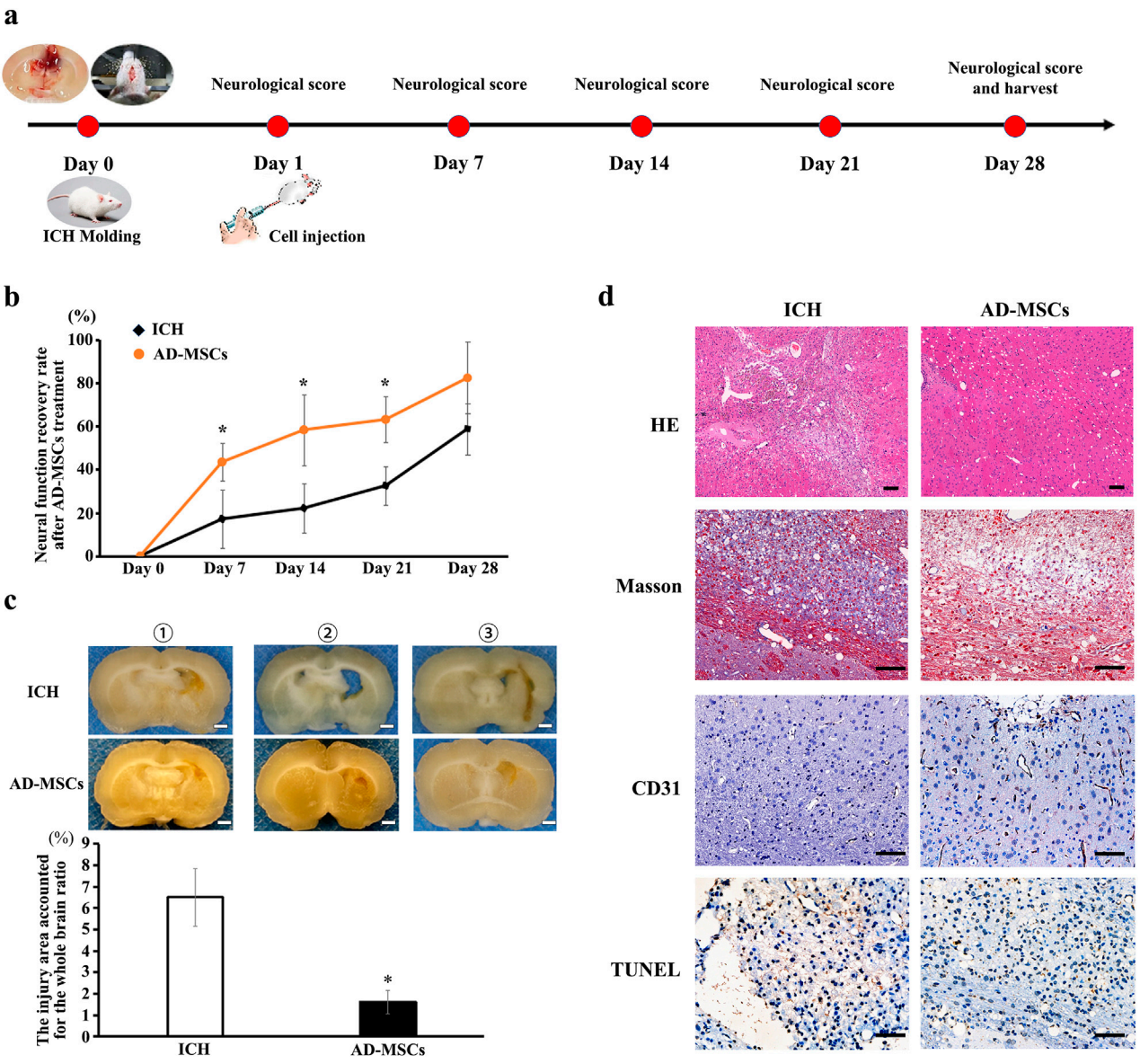

FIGURE 1
Intravenous infusion of allogeneic AD-MSCs significantly inhibited brain injury 24 h after ICH modeling. **(a)** Experimental procedure of treating ICH rats with AD-MSCs. **(b)** Neural function scores of rats at different time points after AD-MSCs treatment (ICH group: n = 6, AD-MSCs group: n = 5). **(c)** General observation of brain tissue. * indicated significant difference compared with the control group ($P < 0.05$). Bar = 1 mm. ①, ②, ③ represent different experimental batches. **(d)** HE staining and immunohistochemical staining of brain tissue were performed. HE results indicated the gross structural changes after brain tissue injury and AD-MSCs treatment. Masson test results indicated the degree of fibrosis in brain tissue. CD31 test results indicate the formation of blood vessels in brain tissue. TUNEL test results indicate the apoptosis of neurons in brain tissue. Bar = 200 μm.

Studies have shown that when brain tissue injured, the recruited monocytes can also transform into microglia, which mainly play a pro-inflammatory role [31]. Therefore, we detected the expression of the Sall1 and Adgre1, which are characteristic microglia-resident gene, in subgroup 1 and subgroup 2. The results showed that Sall1 and Adgre1, which were specifically expressed only in resident microglia, were only highly expressed in subgroup 1 (Figure 3A). Thus, the proinflammatory phenotype of subgroup 2 may be derived from the transformation of bone marrow-derived monocyte, while the anti-inflammatory subgroup 1 is derived from resident microglia. We further examined the proportion of 3 microglia subgroups in each rat group. The results showed that brain injury significantly increased the proportion of activated microglia, including the conversion of recruited monocytes into microglia. The treatment with AD-MSCs significantly increased the overall ratio of

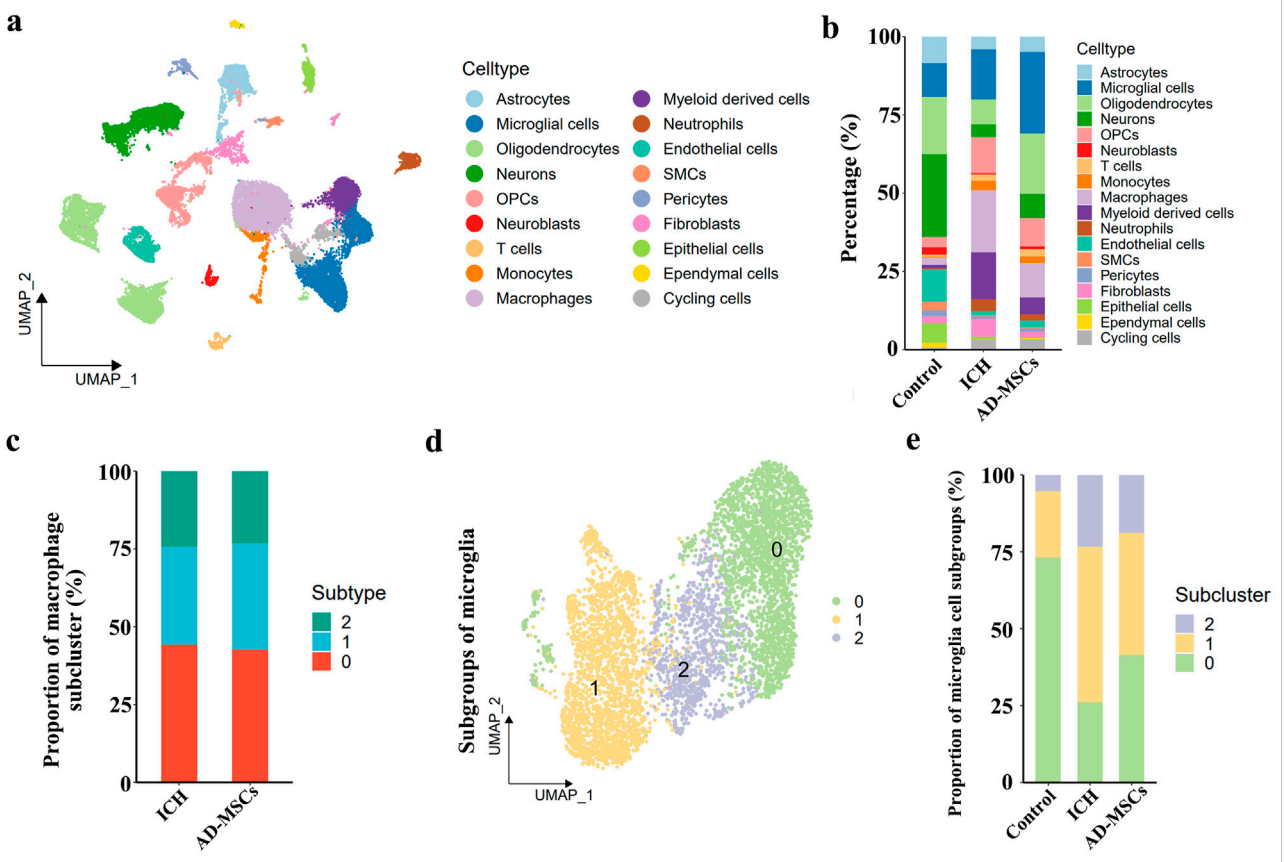

FIGURE 2
Single cell transcriptome sequencing and analysis of brain tissue. **(a)** The analysis of brain tissue cells based on unsupervised clustering showed that brain tissue cells could be divided into 18 categories. **(b)** The classification of each cell subgroup was identified by characteristic markers. **(c)** Subpopulation ratio analysis of macrophages in ICH group and AD-MSCs treatment group. **(d)** Subpopulation analysis of microglial cells in brain tissue. **(e)** The proportion of microglia subsets in the normal control group, ICH group and AD-MSCs treatment group.

microglia in brain tissue. Moreover, the increase in activated microglia was primarily derived from resident microglia and displayed an anti-inflammatory phenotype (Figure 3B). The signaling pathway enrichment of the up-regulated genes in microglia was further analyzed. The results demonstrated that AD-MSCs treatment significantly enhanced the expression of microglial signaling pathways associated with cellular proliferation, immune response, and neuroprotection compared to the ICH group (Figure 3D). Therefore, changes in the proportion and subgroups of microglia may be the root cause of AD-MSCs limiting brain tissue damage.

Csf1$^+$ AD-MSCs are the key to the regulation of microglia

We administered various qualities of AD-MSCs to ICH rats in order to investigate the mechanism of action of AD-MSCs in promoting damaged brain tissue repair through microglia regulation. AD-MSCs obtained from 1-month-old rats (termed young AD-MSCs) and 12-month-old rats (termed old AD-MSCs) were expanded and cultured *in vitro*, followed by single-cell transcriptome sequencing analysis. The results showed that despite the identical viability, surface markers and capacity for differentiation into osteoblasts, lipoblasts, and chondroblasts between young AD-MSCs and old-AD-MSCs (Figures 4A–C; Supplementary Figure S3), significant disparities were observed at the transcriptome level. AD-MSCs were divided into two subgroups, and the proportion of subgroup 1 of young AD-MSCs was significantly higher than that of old AD-MSCs (Figures 4D,E). We examined the expression of genes related to microglia proliferation, homeostasis maintenance and chemotaxis in different subgroups of AD-MSCs. The results showed that there was no significant difference in the expression of Il34, Ccl2, Tnfaip6 and Cx3cl1 between the two AD-MSCs subgroups, while Csf1 was highly expressed in subgroup 1 of AD-MSCs (Figure 4F), which suggests that the expression of Csf1 in young AD-MSCs is significantly higher

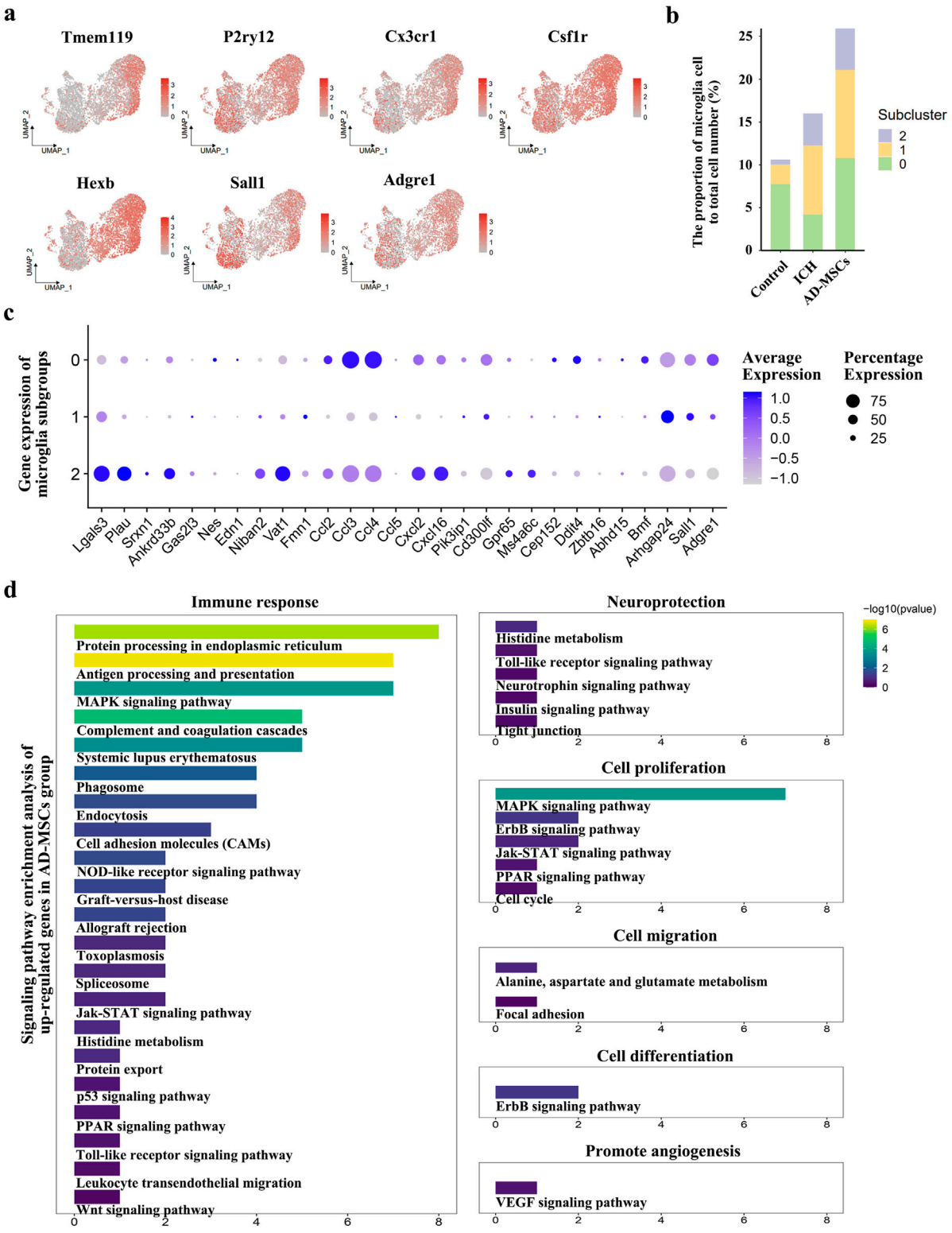

FIGURE 3
Based on the results of single cell transcriptome sequencing, the categories and functions of microglia subsets were analyzed. **(a)** The expression of genes related to resting state of microglia and genes specific to resident microglia in microglia subgroups. **(b)** The proportion of microglia and their subsets in the total cell volume of brain tissue in the normal control group, ICH group and AD-MSCs treatment

(*Continued*)

FIGURE 3 (Continued)
group. **(c)** Expression of genes associated with inflammation and anti-inflammatory in various subpopulations of microglia. **(d)** Signaling pathway enrichment analysis of genes that cause microglial hyperexpression after AD-MSCs treatment compared with ICH group.

than that in Old AD-MSCs. Since Csf1 plays an important role in promoting the proliferation of microglia, we treated ICH rats with these two types of cells respectively to observe their effects on microglia and the therapeutic effect on injured brain tissue.

Young AD-MSCs and old AD-MSCs were injected through the caudal vein 24 h after ICH modeling. Single cell sequencing of rat brain tissue showed that young AD-MSCs significantly increased the number of microglia and inhibited the number of monocyte-derived macrophages and fibroblasts compared with ICH group. The promotion effect of old AD-MSCs on microglia cells and the inhibition effect on monocyte-derived macrophages were significantly weaker than that of young AD-MSCs (Figure 4G). We further evaluated the therapeutic effects of two types of AD-MSC. Neural function scores showed that young AD-MSCs could significantly restore the neural function of ICH rats, while old AD-MSCs had no therapeutic effect (Figure 4H). The histopathological results showed that young AD-MSCs significantly inhibited the expansion of injury, while the brain injury of old AD-MSCs was consistent with that of the ICH group, and had no therapeutic effect (Figure 4J). Homing of AD-MSCs is an important factor in determining the therapeutic effect of AD-Mscs. We used PKH26-labeled AD-MSCs to perform reinfusion at 24 h after ICH modeling, and the homing of cells in brain tissue was simplified at 24 h and 48 h after reinfusion. The results showed that there was no significant difference in homing ability between young AD-MSCs and old AD-MSCs (Figure 4I).

Discussion

In this study, we utilized an ICH rat model to investigate the mechanism of action of AD-MSCs in the treatment of stroke. Our results demonstrate that AD-MSCs exert their therapeutic effects by regulating the number and phenotype of resident microglia, thereby promote the repair of damaged brain tissues.

As resident macrophage cells, microglia are the principal immune cells of the brain, and the first to respond to the pathophysiological changes induced by stroke. Previous research has suggested that microglia activation leads to exacerbated neural tissue damage. In this study, however, we observed that AD-MSCs facilitate the proliferation and activation of microglia, thereby mitigating brain tissue damage. Following brain tissue injury, monocytes are recruited to the injured site and contribute to the inflammatory response. It has been demonstrated that monocytes can differentiate into microglia-like cells, predominantly expressing pro-inflammatory cytokines that exacerbate neural impairment. In this study, microglia in injured brain tissue transition from a quiescent to an activated state, and nearly 50% of activated microglia are derived from monocytes. AD-MSCs significantly inhibit the infiltration of monocytes. More importantly, AD-MSCs treatment notably increases the proportion of innately developed resident microglia while inhibiting the transformation of recruited monocytes into microglia. This increase in the proportion of resident microglia, along with an increase in anti-inflammatory phenotypes, is closely associated with the therapeutic effect of AD-MSCs in inhibiting brain tissue damage. When AD-MSCs derived from 12-month-old rats were used for treatment, they were ineffective in increasing microglia numbers and inhibiting the number of recruited monocytes/macrophages, resulting in poor therapeutic outcomes. Therefore, increasing the number of innately developed resident microglia in brain tissue after injury may be an important direction, the underlying molecular mechanisms need further elaboration. Additionally, the correlation between AD-MSCs increasing the number of resident microglia and inhibiting the infiltration of monocyte-derived macrophages remains unclear, and the relevant molecular mechanisms should be investigated in future work.

The heterogeneity of *in vitro* cultured MSCs may significantly contribute to the inconsistent clinical therapeutic outcomes observed in stroke treatment [32, 33]. This heterogeneity refers to the variations in morphology, protein expression, transcriptome expression, staining characteristics, ultrastructure, and function among individual cells within primary MSC cultures. These variations are influenced by factors such as donor age and health status, tissue type, tissue microenvironment, and *in vitro* culturing techniques [34]. As a result, primary MSC cultures contain multiple cell subgroups with distinct functions. Studies have demonstrated that these different cell subgroups exhibit unique biological functions [35, 36]. Therefore, identifying functional subgroups of MSCs is crucial for the development of effective stroke treatments. In this study, single-cell transcriptome sequencing revealed distinct cell subpopulations in AD-MSCs derived from 1-month-old and 12-month-old rats. Compared to AD-MSCs from older rats, those from younger rats had a higher proportion of the Csf1 subpopulation, which is closely associated with microglial cell proliferation. *In vivo* studies showed that AD-MSCs from 1-month-old rats significantly promoted an increase in resident microglia cell within injured brain tissue and facilitated nerve function recovery. Consequently, enhancing the proportion of AD-MSCs expressing high levels of Csf1 may be pivotal in

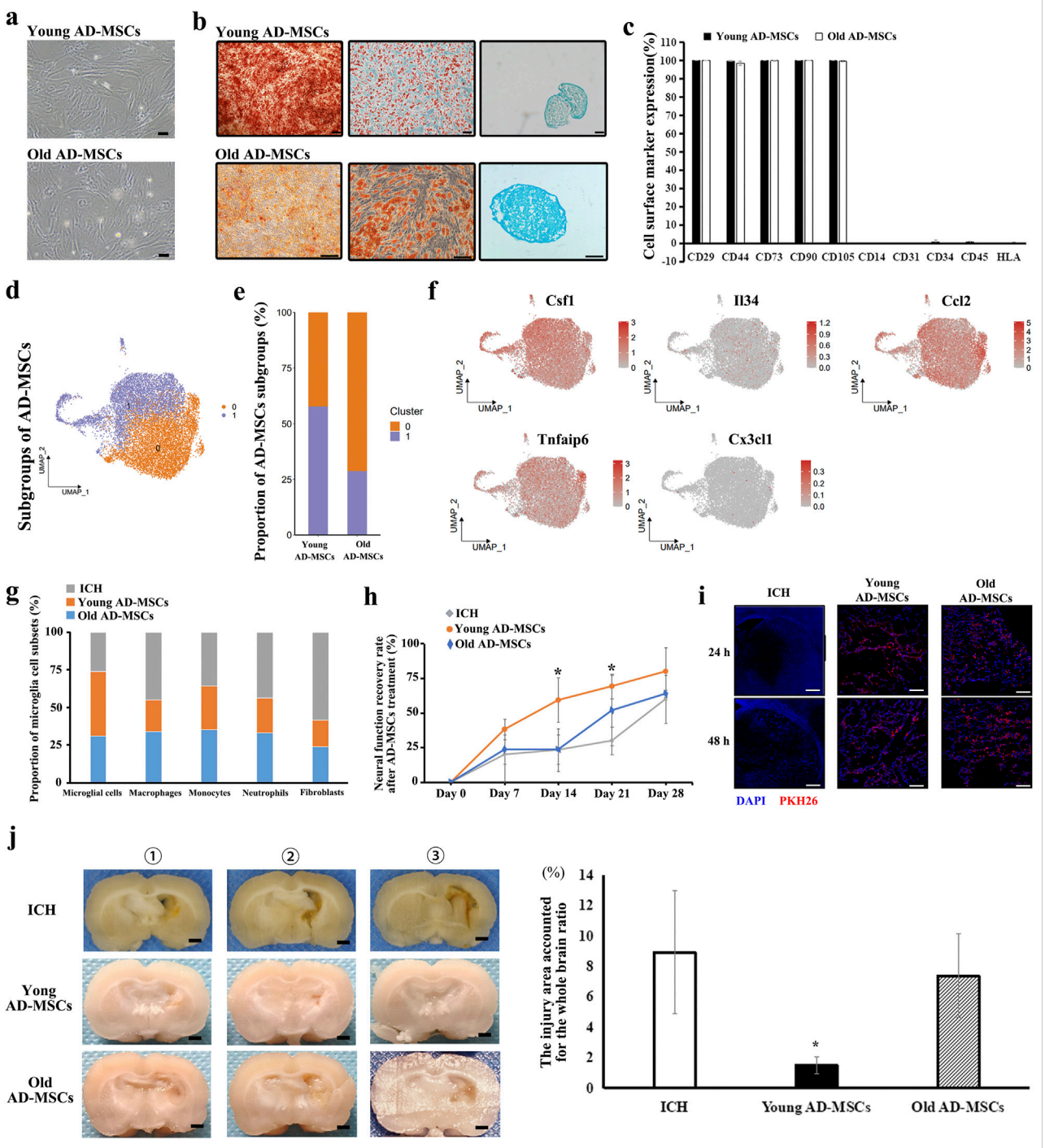

FIGURE 4
Therapeutic effect of Young AD-MSCs and Old AD-MSCs on ICH rats and analysis of key cell subgroups. **(a)** Cell morphology of Young AD-MSCs and Old AD-MSCs expanded *in vitro*. Bar = 200 μm. **(b)** Induction differentiation of Young AD-MSCs and Old AD-MSCs into osteoblasts, lipoblasts and chondroblasts. Bar = 100 μm. **(c)** Surface marker detection of Young AD-MSCs and Old AD-MSCs by flow cytometry. **(d, e)** Subpopulation analysis of Young AD-MSCs and Old AD-MSCs was performed based on single-cell transcriptome sequencing. **(f)** Expression of genes closely related to microglia proliferation, chemotaxis and phenotypic transformation in AD-MSCs subgroups. **(g)** Effects of Young AD-MSCs and Old AD-MSCs on the proportion of immune-associated cells and fibroblasts in brain tissue. **(h)** Neural function scores of Young AD-MSCs and Old AD-MSCs treated rats (n = 4 for each group). **(i)** Homing detection of PKH26-labeled Young AD-MSCs and Old AD-MSCs in damaged brain tissue of rats. **(j)** General observation of brain tissue (n = 4 for each group). Bar = 1 mm * indicated significant difference compared with the control group ($P < 0.05$). (n = 3 for each group) ①, ②, ③ represent different experimental batches.

ensuring the therapeutic efficacy of stroke treatment products during their development.

This study has several limitations. Specifically, we only investigated the effects of AD-MSC transfusions administered 24 h after the induction of ICH modeling. It remains unclear whether treatments administered at different time points following modeling (e.g., 3, 7, or 21 days post-injury) would exhibit comparable therapeutic efficacy and operate through similar mechanisms. Furthermore, the precise mechanisms underlying the homing of MSCs to injured tissue and their subsequent promotion of resident microglia proliferation following injury warrant further investigation.

Conclusion

This study investigated the interaction between AD-MSCs and microglia in ICH models, as well as their therapeutic impact on damaged brain tissue. Our findings revealed that intravenously injected allogeneic AD-MSCs inhibited the infiltration of recruited monocytes by stimulating an increase in resident microglia and promoting an anti-inflammatory phenotype transformation within injured brain tissue, thereby promote the repair of damaged tissues. A subgroup of AD-MSCs expressing Csf1 emerged as a crucial functional component in stroke treatment. Future research will focus on elucidating the mechanisms underlying the enhancement of resident microglia by AD-MSCs and its subsequent influence on the damage repair process.

Author contributions

Conceptualization: JL. Investigation: JGH, XZ, PFH, XMH and PZ. Methodology: SFZ, SL, FM, HZW and PZ. Formal analysis: JL, XZ, PFH, FM and NW. Supervision: JL. Writing – original draft: JL, XZ, PFH and PZ. Writing – review and editing: JL. All authors contributed to the article and approved the submitted version.

Data availability

The datasets presented in this study can be found in online repositories. The names of the repository/repositories and accession number(s) can be found in the article/ Supplementary Material.

Ethics statement

All animal procedures described were approved by the Institutional Animal Careand Use Committee of Sichuan University West China Hospital following national regulations and guidelines (The regulation of experimental animals, the Ministry of Science and Technology of China, 2005, and Guidance suggestion of caring laboratory animals, The Ministry of Science and Technology of China, 2006).

Funding

The author(s) declare that financial support was received for the research and/or publication of this article. This work is funded by Sichuan Natural Science Foundation Project (2023YFQ0038).

Acknowledgments

The authors declare that they have not use AI-generated work in this manuscript.

Conflict of interest

Authors XZ, FM, HW, PH, PZ, and NW were employed by Tasly Group.

The remaining author(s) declared no potential conflicts of interest with respect to the research, authorship, and/or publication of this article.

Generative AI statement

The author(s) declare that no Generative AI was used in the creation of this manuscript.

Supplementary material

The Supplementary Material for this article can be found online at: https://www.ebm-journal.org/articles/10.3389/ebm.2025.10611/full#supplementary-material

References

1. Feigin VL, Lawes CMM, Bennett DA, Barker-Collo SL, Parag V. Worldwide stroke incidence and early case fatality reported in 56 population-based studies: a systematic review. *The Lancet Neurol* (2009) **8**:355–69. doi:10.1016/s1474-4422(09)70025-0

2. An SJ, Kim TJ, Yoon BW. Epidemiology, risk factors, and clinical features of intracerebral hemorrhage: an update. *J Stroke* (2017) **19**(1):3–10. doi:10.5853/jos.2016.00864

3. Quertainmont R, Cantinieaux D, Botman O, Sid S, Schoenen J, Franzen R. Mesenchymal stem cell graft improves recovery after spinal cord injury in adult rats through neurotrophic and pro-angiogenic actions. *PLoS ONE* (2012) **7**(6):e39500. doi:10.1371/journal.pone.0039500

4. Tetzlaff W, Okon EB, Karimi-Abdolrezaee S, Hill CE, Sparling JS, Plemel JR, et al. A systematic review of cellular transplantation therapies for spinal cord injury. *J neurotrauma* (2011) **28**(SP8):1611–82. doi:10.1089/neu.2009.1177

5. Chung JW, Chang WH, Bang OY, Moon GJ, Kim SJ, Kim SK, et al. Efficacy and safety of intravenous mesenchymal stem cells for ischemic stroke. *Neurology* (2021) **96**(7):e1012–e1023. doi:10.1212/wnl.0000000000011440

6. Law ZK, Tan HJ, Chin SP, Wong CY, Wan Yahya WNN, Muda AS, et al. The effects of intravenous infusion of autologous mesenchymal stromal cells in patients with subacute middle cerebral artery infarct: a phase 2 randomized controlled trial on safety, tolerability and efficacy. *Cytotherapy* (2021) **23**(9):833–40. doi:10.1016/j.jcyt.2021.03.005

7. de Celis-Ruiz E, Fuentes B, Alonso de Leciñana M, Gutiérrez-Fernández M, Borobia AM, Gutiérrez-Zúñiga R, et al. Final results of allogeneic adipose tissue–derived mesenchymal stem cells in acute ischemic stroke (AMASCIS): a phase II, randomized, double-Blind, Placebo-Controlled, Single-Center, pilot clinical trial. *Cell Transplant* (2022) **31**:09636897221083863. doi:10.1177/09636897221083863

8. Bernardo M, Fibbe W. Mesenchymal stromal cells: sensors and switchers of inflammation. *Cell stem cell* (2013) **13**(4):392–402. doi:10.1016/j.stem.2013.09.006

9. Lu D, Xu Y, Liu Q, Zhang Q. Mesenchymal stem cell-macrophage crosstalk and maintenance of inflammatory microenvironment homeostasis. *Front Cel Dev Biol* (2021) **9**:681171. doi:10.3389/fcell.2021.681171

10. Colonna M, Butovsky O. Microglia function in the central nervous System during health and neurodegeneration. *Annu Rev Immunol* (2017) **35**(35):441–68. doi:10.1146/annurev-immunol-051116-052358

11. Alsbrook DL, Di Napoli M, Bhatia K, Biller J, Andalib S, Hinduja A, et al. Neuroinflammation in acute ischemic and hemorrhagic stroke. *Curr Neurol Neurosci Rep* (2023) **23**(8):407–31. doi:10.1007/s11910-023-01282-2

12. Borst K, Dumas AA, Prinz M. Microglia: immune and non-immune functions. *Immunity* (2021) **54**(10):2194–208. doi:10.1016/j.immuni.2021.09.014

13. Li Y, Dong Y, Ran Y, Zhang Y, Wu B, Xie J, et al. Three-dimensional cultured mesenchymal stem cells enhance repair of ischemic stroke through inhibition of microglia. *Stem Cell Res Ther* (2021) **12**(1):358. doi:10.1186/s13287-021-02416-4

14. Liu Y, Zeng R, Wang Y, Huang W, Hu B, Zhu G, et al. Mesenchymal stem cells enhance microglia M2 polarization and attenuate neuroinflammation through TSG-6. *Brain Res* (2019) 1724. doi:10.1016/j.brainres.2019.146422

15. Noh MY, Lim SM, Oh KW, Cho KA, Park J, Kim KS, et al. Mesenchymal stem cells modulate the functional properties of Microglia *via* TGF-β secretion. *Stem Cells Translational Med* (2016) **5**(11):1538–49. doi:10.5966/sctm.2015-0217

16. Zanier ER, Pischiutta F, Riganti L, Marchesi F, Turola E, Fumagalli S, et al. Bone marrow mesenchymal stromal cells drive protective M2 microglia polarization after brain trauma. *Neurotherapeutics* (2014) **11**(3):679–95. doi:10.1007/s13311-014-0277-y

17. Liang ZH, Gu JJ, Yu WX, Guan YQ, Khater M, Li XB. Bone marrow mesenchymal stem cell transplantation downregulates plasma level and the microglia expression of transforming growth factor β1 in the acute phase of cerebral cortex ischemia. *Chronic Dis Translational Med* (2020) **6**:270–80. doi:10.1016/j.cdtm.2020.05.005

18. Li X, Huang M, Zhao R, Zhao C, Liu Y, Zou H, et al. Intravenously delivered allogeneic mesenchymal stem cells bidirectionally regulate inflammation and induce neurotrophic effects in distal middle cerebral artery occlusion rats within the first 7 days after stroke. *Cell Physiol Biochem* (2018) **46**:1951–70. doi:10.1159/000489384

19. Xu C, Fu F, Li X, Zhang S. Mesenchymal stem cells maintain the microenvironment of central nervous system by regulating the polarization of macrophages/microglia after traumatic brain injury. *Int J Neurosci* (2017) **127**(12):1124–35. doi:10.1080/00207454.2017.1325884

20. Liu W, Yu M, Xie D, Wang L, Ye C, Zhu Q, et al. Melatonin-stimulated MSC-derived exosomes improve diabetic wound healing through regulating macrophage M1 and M2 polarization by targeting the PTEN/AKT Pathway. *Stem Cell Res and Ther* (2020) **11**:259. doi:10.1186/s13287-020-01756-x

21. Fernández-López D, Faustino J, Klibanov AL, Derugin N, Blanchard E, Simon F, et al. Microglial cells prevent hemorrhage in neonatal focal arterial stroke. *The J Neurosci* (2016) **36**(10):2881–93. doi:10.1523/jneurosci.0140-15.2016

22. Ransohoff RM. A polarizing question: do M1 and M2 microglia exist? *Nat Neurosci* (2016) **19**:987–91. doi:10.1038/nn.4338

23. Masuda T, Sankowski R, Staszewski O, Prinz M. Microglia heterogeneity in the single-cell era. *Cell Rep* (2020) **30**:1271–81. doi:10.1016/j.celrep.2020.01.010

24. Haast RA, Gustafson DR, Kiliaan AJ. Sex differences in stroke. *J Cereb Blood Flow Metab* (2012) **32**(12):2100–7. doi:10.1038/jcbfm.2012.141

25. Tang T, Hu L, Liu Y, Fu X, Li J, Yan F, et al. Sex-associated differences in neurovascular dysfunction during ischemic stroke. *Front Mol Neurosci* (2022) **15**:860959. doi:10.3389/fnmol.2022.860959

26. Li Y, Zhang J. Animal models of stroke. *Anim Models Exp Med* (2021) **4**:204–19. doi:10.1002/ame2.12179

27. Lee RH, Kim B, Choi I, Kim H, Choi HS, Suh K, et al. Characterization and expression analysis of mesenchymal stem cells from human bone marrow and adipose tissue. *Cell Physiol Biochem* (2004) **14**(4-6):311–24. doi:10.1159/000080341

28. Zuk PA, Zhu M, Mizuno H, Huang J, Futrell JW, Katz AJ, et al. Multilineage cells from human adipose tissue: implications for cell-based therapies. *Tissue Eng* (2001) **7**(2):211–28. doi:10.1089/107632701300062859

29. Chen J, Sanberg PR, Li Y, Wang L, Lu M, Willing AE, et al. Intravenous administration of human umbilical cord blood reduces behavioral deficits after stroke in rats. *Stroke* (2001) **32**(11):2682–8. doi:10.1161/hs1101.098367

30. Li H, Liu P, Zhang B, Yuan Z, Guo M, Zou X, et al. Acute ischemia induces spatially and transcriptionally distinct microglial subclusters. *Genome Med* (2023) **15**:109. doi:10.1186/s13073-023-01257-5

31. Chen HR, Chen CW, Kuo YM, Chen B, Kuan IS, Huang H, et al. Monocytes promote acute neuroinflammation and become pathological microglia in neonatal hypoxic-ischemic brain injury. *Theranostics* (2022) **12**(Issue 2):512–29. doi:10.7150/thno.64033

32. Mendicino M, Bailey A, Wonnacott K, Puri R, Bauer S. MSC-Based product characterization for clinical trials: an FDA perspective. *Cell Stem Cell* (2014) **14**(2):141–5. doi:10.1016/j.stem.2014.01.013

33. Dent E, Martin FC, Bergman H, Woo J, Romero-Ortuno R, Walston JD. Management of frailty: opportunities, challenges, and future directions. *The Lancet* (2019) **394**(10206):1376–86. doi:10.1016/s0140-6736(19)31785-4

34. Costa LA, Eiro N, Fraile M, Gonzalez LO, Saá J, Garcia-Portabella P, et al. Functional heterogeneity of mesenchymal stem cells from natural niches to culture conditions: implications for further clinical uses. *Cell Mol Life Sci* (2021) **78**(2):447–67. doi:10.1007/s00018-020-03600-0

35. Li X, Guo W, Zha K, Jing X, Wang M, Zhang Y, et al. Enrichment of CD146+ adipose-derived stem cells in combination with articular cartilage extracellular matrix scaffold promotes cartilage regeneration. *Theranostics* (2019) **9**(17):5105–21. doi:10.7150/thno.33904

36. Liang ZX, Liu HS, Xiong L, Zeng ZW, Zheng XB, Kang L, et al. GAS6 from CD200+ adipose-derived stem cells mitigates colonic inflammation in a macrophage-dependent manner. *J Crohn's Colitis* (2023) **17**(2):289–301. doi:10.1093/ecco-jcc/jjac123

EBM Experimental Biology and Medicine

TYPE Correction
PUBLISHED 23 July 2025
DOI 10.3389/ebm.2025.10735

OPEN ACCESS

*CORRESPONDENCE
Anya Maan-Yuh Lin,
myalin@nycu.edu.tw

RECEIVED 02 July 2025
ACCEPTED 08 July 2025
PUBLISHED 23 July 2025

CITATION
Tseng YJ, Huang H-J, Lin C-H and Lin AM-Y (2025) Corrigendum: A double-edged effect of hypoxia on astrocyte-derived exosome releases. *Exp. Biol. Med.* 250:10735. doi: 10.3389/ebm.2025.10735

Corrigendum: A double-edged effect of hypoxia on astrocyte-derived exosome releases

Yang Jie Tseng[1], Hui-Ju Huang[2], Chien-Hui Lin[3] and Anya Maan-Yuh Lin[1,2,4]*

[1]Ph.D. Program in Regulatory Science and Policy, National Yang-Ming Chiao-Tung University, Hsin-Chu, Taiwan, [2]Department of Medical Research, Taipei Veterans General Hospital, Taipei, Taiwan, [3]Institute of Physiology, National Yang-Ming Chiao-Tung University, Hsin-Chu, Taiwan, [4]Department of Pharmacy, National Yang-Ming Chiao-Tung University, Hsin-Chu, Taiwan

KEYWORDS

hypoxic preconditioning, double-edged role, exosomes, hemin, CTX-TNA2

A Corrigendum on
A double-edged effect of hypoxia on astrocyte-derived exosome releases

by Tseng YJ, Huang H-J, Lin C-H and Lin AM-Y (2025). Exp. Biol. Med. 250:10559. doi: 10.3389/ebm.2025.10559

In the original article, there was a mistake in Figure 6 as published. The error was due to the inadvertent insertion of an incorrect version of the figure during the final submission process. Specifically, the published figure mistakenly displayed HO-1 (A, B) and GPX4 (C, D), instead of the correct picture, which should show GPX4 (A, B) and active-caspase 3 (C, D), as measured by Western blot assay. The corrected Figure 6 appears below.

The authors apologize for this error and state that this does not change the scientific conclusions of the article in any way. The original article has been updated.

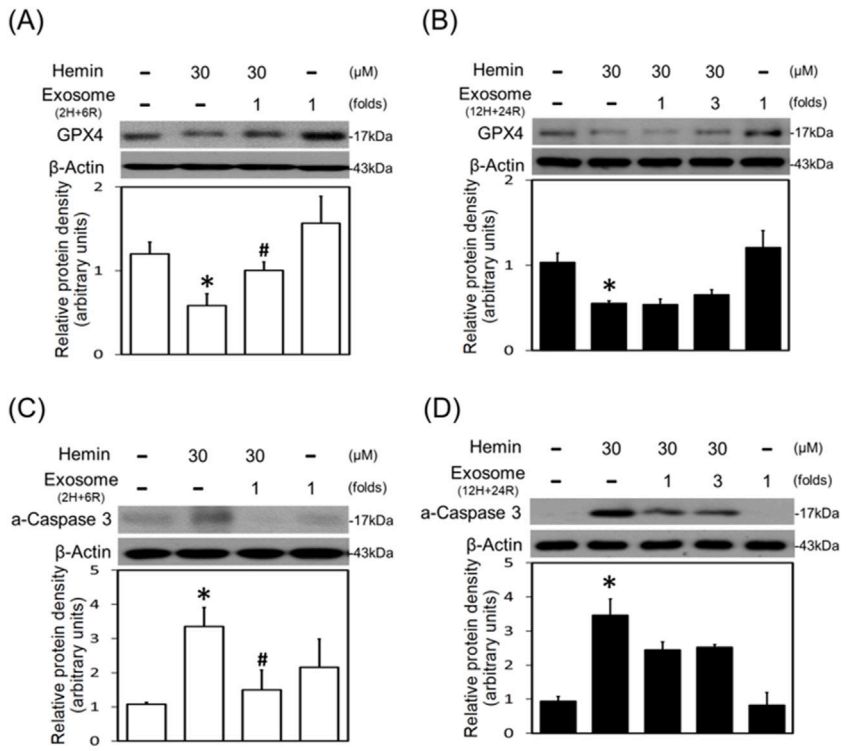

FIGURE 6
Differential effects of 2H/6R exosomes and 12H/24R exosomes on hemin-induced programmed cell death in primary cultured cortical neurons. **(A,C)** Primary cultured cortical neurons were treated with hemin (30 μM) plus 2H/6R exosomes obtained from 1×10^6 CTX-TNA2 cells (as 1 fold) for 16 h **(B,D)** Primary cultured cortical neurons were treated with hemin (30 μM) plus 12H/24R exosomes (1 fold and 3 folds) for 16 h. Western blot assay was employed to measure GPX4 **(A,B)** and active-caspase 3 **(C,D)**. Each lane contained 30 μg protein for all experiments. Graphs show statistic results from relative optical density of bands on the blots. Values are the mean ± S.E.M. (n = 3/each group). *, $p < 0.05$ statistically significant in the hemin groups compared with the control groups; #, $P < 0.05$ in hemin plus exosomes compared with hemin alone by one-way ANOVA followed by the LSD test as *post hoc* method.

Scope

Experimental Biology and Medicine (EBM) is a global, peer-reviewed journal dedicated to the publication of multi- and interdisciplinary research in the biomedical sciences. The journal covers the spectrum of translational research from T0, basic research, to T4, population health. EBM is particularly appropriate for manuscripts that are multidisciplinary in nature, are of interest to a wide audience, and represent experimental medicine in the broadest sense of the term.

EBM publishes Research, Reviews, Mini Reviews, and Brief Communications in the following categories.

- Anatomy/Pathology
- Artificial Intelligence/ Machine Learning Applications to Biomedical Research
- Biochemistry and Molecular Biology
- Bioimaging
- Biomedical Engineering
- Bionanoscience
- Cell and Developmental Biology
- Clinical Trials
- Endocrinology and Nutrition
- Environmental Health/Biomarkers/ Precision Medicine
- Genomics, Proteomics, and Bioinformatics
- Immunology/Microbiology/ Virology
- Mechanisms of Aging
- Neuroscience
- Pharmacology and Toxicology
- Physiology and Pathophysiology
- Population Health
- Stem Cell Biology
- Structural Biology
- Synthetic Biology
- Systems Biology and Microphysiological Systems
- Translational Research

Submit your work to Experimental Biology and Medicine at
ebm-journal.org/submission

More information
ebm-journal.org/journals/experimental-biology-and-medicine

EBM Experimental Biology and Medicine

EBM is the official journal of the Society for Experimental Biology and Medicine

Experimental Biology and Medicine (EBM) is a global, peer-reviewed journal dedicated to the publication of multidisciplinary and interdisciplinary research in the biomedical sciences.

Discover more of our Special Issues

See more →

Contact

development@ebm-journal.org

See more

ebm-journal.org

publishingpartnerships.frontiersin.org/our-partners